Active scalar mixing in turbulent jet flows

Yacine Brahami

To cite this version:

Yacine Brahami. Active scalar mixing in turbulent jet flows. Fluids mechanics [physics.class-ph]. Normandie Université, 2020. English. NNT : 2020NORMR093 . tel-03187940

HAL Id: tel-03187940
https://theses.hal.science/tel-03187940

Submitted on 1 Apr 2021

Normandie Université

THÈSE

Pour obtenir le diplôme de doctorat

Spécialité Mécanique Des Fluides

Preparée au sein de l'Université de Rouen

Active scalar mixing in turbulent jet flows

Presentée et soutenue par

Yacine BRAHAMI

Thèse soutenue publiquement le 08 Octobre 2020 **devant le jury composé de**		
M. Malek ABID	Maître de conférences, HDR, IRPHE, Marseille	Rapporteur
M. Fabien ANSELMET	Professeur, IRPHE, Marseille	Examinateur
M. Mickaël BOURGOIN	Directeur de Recherche, ENS Lyon	Rapporteur
Mme Luminita DANAILA	Professeur, CORIA, Rouen	Directrice de thèse
M. Michael GAUDING	Post-doctorant, CORIA, Rouen	Examinateur
M. Jean-François KRAWCZYNSKI	Maître de conférences, Institut ∂'Alembert, Paris	Examinateur
M. Jean-Charles SAUTET	Professeur, CORIA, Rouen	Examinateur
M. Emilien VAREA	Maître de conférences, CORIA, Rouen	Co-encadrant

Thèse dirigée par Luminita DANAILA, laboratoire CORIA UMR 6614

UNIVERSITÉ DE ROUEN NORMANDIE

ED PSIME

CORIA UMR 6614

Contents

Résumé

Le mélange de scalaire actif, qui implique une rétroaction du champ scalaire sur les champs de vitesses, a attiré beaucoup moins d'attention dans la littérature que le mélange du scalaire passif où le champ scalaire se laisse transporter cinématiquement par le champ de vitesse. Dans cette thèse, nous nous intéressons à quelques questions ouvertes au sujet du mélange de scalaire actif. En particulier, on observe une accélération de la transition vers la turbulence pour : un jet léger, et un jet plus visqueux, par rapport au fluide hôte. Nous abordons deux types d'écoulements :

I. Jet rond à masse volumique variable : Nous avons conçu et réalisé une expérience permettant la mesure simultanée des champs de vitesses et scalaire dans le champ très proche d'un jet rond à masse volumique variable. Nous utilisons la Vélocimétrie par Images de Particules Stéréoscopique, couplée à la Fluorescence Induite par Laser Planaire. La première question consiste à connaitre l'influence des variations de masse volumique sur les toutes premières structures qui apparaissent après l'injection. La seconde question concerne le transfert d'énergie dans l'écoulement. Nous utilisons une approche statistique en deux-points, et analysons les transferts d'énergie et de variance du scalaire dans l'espace des échelles. Enfin, le mélange est quantifié par une approche de statistiques conditionnées à la périphérie du jet, au voisinage de l'Interface Turbulent/Non-Turbulent. Cette méthode révèle des informations qui sont inaccessibles par des moyennes dans un repère de coordonnées cylindriques classique.

II. Jet plan temporel à viscosité et diffusivité massique variables : Nous utilisons des données de Simulations Numériques Directes, produites par le Dr. M. Gauding au sein de notre groupe. Le but de ces simulations est d'étudier l'influence de la variation de viscosité et de la diffusivité de masse sur les taux de dissipation de l'énergie cinétique et du scalaire. Pour traiter cette question, nous utilisons une approche de statistiques conditionnées à l'Interface Turbulent/Non-Turbulent. Dans cette région de l'écoulement, nous évaluons le bilan en un point de l'amplitude du vecteur gradient du scalaire, ainsi que le bilan en deux points de la fonction de structure d'ordre deux du scalaire. Nous montrons que les inhomogénéités initiales du scalaire actif ont un effet intense et persistant sur le mélange dans le voisinage de l'Interface Turbulent/Non-Turbulent, et ceci même tard, dans le régime auto-similaire du jet.

Abstract

Active scalar mixing, which modifies the velocity field through variations of either density or viscosity, received much less attention than passive scalars. This thesis aims at unravelling some open questions pertaining to active scalar mixing. Whilst some results point to the facts that mixing occurs faster for i) light jets than for heavy jets, and ii) more viscous fluid released in a less viscous environment. This simple example reveals the necessity of a systematic study of the problem. We focus on two aspects of these very vast questions.

I. Variable density round jet. We designed an experimental set-up, which allows measuring both velocity and scalar fields, using simultaneous Stereo Particle Image Velocimetry and Planar Laser Induced Fluorescence. The first question concerns mixing immediately after injection. Therefore, the very near field of the jet was particularly sought. One-point statistics were used to evaluate the large-scale effect of momentum and density variations on the initiation of turbulence. Also, two-point turbulent statistics for velocity and scalar have been appraised. Through this approach, the effects on transition were assessed through scales of turbulent motion. Mixing was also evaluated at the edge of the flow, in the vicinity of the Turbulent/Non-Turbulent Interface. We found additional specificity to variable density mixing, that is inaccessible by averaging on a cylindrical frame of reference.

II. Temporally evolving turbulent jet flow with variable viscosity and mass diffusivity. The data consists in Direct Numerical Simulation performed in our group by Dr. M. Gauding. The purpose of these simulations is to study the kinetic energy and scalar dissipation rates in flows with variable momentum and mass diffusivities. We focused on conditional averaging in the vicinity of Turbulent/Non-Turbulent Interface. This data is confronted to one-and-two point transport equations for the momentum and scalar. It is shown that initial gradients of both viscosity and mass diffusivity have an intense and persistent impact on both kinetic energy and scalar dissipation rates, in the vicinity of the Turbulent/Non-Turbulent Interface, albeit a rapidly trend of the jet core towards self-preservation.

List of Symbols

Annotations

$(.)_a$	At the axis or at the center-plane
$(.)_I$	Conditionned on the distance to the Turbulent/Non-Turbulent Interface
$(.)_j$	Jet inlet
$(.)_c$	Co-flow
$(.)_{crit}$	Critical value
$(.)_e$	Entrainment
$(.)_m$	Momentum
$(.)_p$	Particle
$(.)_s$	Sound
$(.)_r$	Radial
$(.)_x$	Axial
$(.)_V$	Volume average
$()^*$	Reference scale
$\langle . \rangle$	Statistical average
$(.)'$	Reynolds fluctuation
$\tilde{(.)}$	Infinitesimal perturbation
$\hat{(.)}$	Perturbation spectral amplitude
$(.)^+$ and $(.)^-$	At physical space location
$\Delta(.)$	Increment between the quantity at point $(.)^+$ and point $(.)^-$
$\Sigma(.)$	Sum of the quantity at points $(.)^+$ and $(.)^-$

Differential operators

$\partial_t \equiv \frac{\partial}{\partial t}$	derivative with respect to time
$\partial_i \equiv \frac{\partial}{\partial x_i}$	derivative with respect to spatial direction x_i
$\partial^2_{ik} \equiv \frac{\partial^2}{\partial x_i \partial x_k}$	second derivative with respect to spatial directions x_i and x_k
	index not repeated when $i = k$.
$d_\phi \equiv \frac{d}{d\phi}$	total derivative with respect to the mass fraction ϕ

Dimensional quantities

D	$[L]$	Diameter
u	$[L][T]^{-1}$	Velocity
ρ	$[M][L]^{-3}$	Density
μ	$[M][L]^{-1}[T]^{-1}$	Dynamic viscosity
$\mathcal{D}$	$[L]^2[T]^{-1}$	Mass diffusivity
δ	$[L]$	Characteristic thickness
Q	$[M][T]^{-3}$	Mass flow rate
r	$[L]$	Distance in homogeneous component in scale space
X	$[L]$	Distance in inhomogeneous component in scale space
α, β, k	$[L]^{-1}$	Wave numbers
c	$[T]^{-1}$	Wave phase speed
λ	$[L]$	Monochromatic light wavelength
ψ	$[M]^2[L]$	Diffusivity of both momentum and chemical species
ε	$[L]^2[T]^{-3}$	Kinetic energy pseudo dissipation rate
χ	$[L]^2[T]^{-3}$	Scalar dissipation rate
L	$[L]$	Integral length-scale

Dimensionless quantities

$Re = \frac{\rho_j D_j u_j}{\mu_j}$	Reynolds number
$Ar = \frac{g\rho_j(\rho_c - \rho_j)D_j^3}{\mu_j^2}$	Archimedes number
$Fr = \frac{\sqrt{gL}}{u_j}$	Froude number
$At = \frac{\rho_c - \rho_j}{\rho_c + \rho_j}$	Atwood number
$Pe = \frac{D_j u_j}{\mathcal{D}}$	Peclet number
$Ma = \frac{u_j}{a_0}$	Mach number
$\mathcal{R}$	Thermo-physical property ratio
$\mathcal{I}$	Turbulence intensity
γ_e	Entrainment coefficient
M	Mie parameter
ϕ	Mass fraction
φ	Pseudo mass fraction
σ	Fluorescence quantum yield

List of Figures

List of Tables

General Introduction

Fluids and their motion surround us, ranging from the atmosphere down to inside our cells. In very specific configurations, flows can be very organised and are referred to as *laminar*. Laminar flows are an exception amongst all flows that take place in our daily life. They are characterized by very slow motion and generally occur close to solid boundaries, whereas the vast majority of flows are not very slow and potentially take place far from solid boundaries.

The quantitative criterion that discriminates laminar from non-laminar flows is the Reynolds number, Re. This number compares momentum to friction, so that, laminar flows are dominated by friction and present low Reynolds numbers. When the Reynolds number is large, the fluid motion is more difficult to predict, and the dynamics are more dependent on the specific flow configuration. These very different dynamics are referred to as *regimes*, and dimensionless numbers like the Reynolds number are used to distinguish these regimes.

The Navier-Stokes equations, which result from the application of Newton's second law to a fluid, govern fluid motion. Phenomenological observations translate into mathematics, as the Reynolds number appears explicitly in the equations when suitably normalized. Flow configurations correspond to specific initial and boundary conditions. Theoretically, the motion of a continuous medium is governed by an infinity of degrees of freedom, as each infinitesimal parcel of medium contributes individually to the solution.

The Navier-Stokes equations are nonlinear. Except in some rare cases, fluid flows are not composed of a combination of simple elementary solutions. Each specific non-laminar flow is unique. The surprising consequence of nonlinearity when combined to a large number of degrees of freedom is *deterministic chaos*. This particularity leads to an even more counter-intuitive property. In addition to the uniqueness of each non-laminar flow configuration, each realization of a specific flow is unique.

When supplementary physical mechanisms contribute to the dynamics of a flow, additional dimensionless numbers are to be used. Fluid mechanics deals with the study and classification of regimes, regarding all the dimensionless numbers that govern a specific flow.

Turbulence

When the Reynolds number is large, flows are chaotic and occur over a wide range of temporal and spatial scales. Said differently, large Reynolds number flows are composed of a continuous distribution of energy containing structures of different sizes, which interact nonlinearly and collectively. The ratio of the size of the largest to smallest structure is a function of the Reynolds number. These concepts are to be seen only statistically, as chaos prohibits any local and instantaneous prediction after some time.

Turbulence is the branch of fluid mechanics that studies very large Reynolds number flows. The chaotic nature of such flows enforces any approach to be statistical, as it is fundamentally impossible to make any deterministic prediction. Most of the theory of turbulence is due to A. Kolmogorov in a series of papers in 1941, and is therefore called K41 theory in the literature. K41 is asymptotically valid for $Re \to +\infty$. Experiments have shown that some predictions of K41 are recovered in this limit, and others are not because of implicit hypotheses in the Kolmogorov theory. At high Reynolds numbers, the departure due to these implicit hypotheses is referred to as *internal intermittency*. When the Reynolds number is not large enough, the departure from K41 is referred to as *finite Reynolds number effects*.

Active scalar turbulent flows

Farther from fundamental aspects, turbulent flows are very efficient when it comes to homogenize a temperature or a chemical species field faster than diffusion alone. This feature is referred to as *turbulent mixing*, and temperature or chemical species are *scalar fields*, which can either be passive or active. A passive scalar is transported by the velocity field, with negligible feedback, whereas an active scalar has a substantial contribution to the dynamics.

For example, any living human being emits 100 Watts of heat. If a person is still, the temperature field close to its skin is larger by a few degrees than the ambient air. If this temperature difference is large enough, a plume rises. In this case, the temperature field is active, because the acceleration that buoyancy force causes on the fluid is non-negligible, compared to the overall momentum in the flow. Now if this person is walking, the wake behind the body is mostly caused by the walking speed relative to ambient air. Buoyancy force is negligible and the temperature field in this case is passive.

Stating if a scalar field is passive or active is a matter of dimensionless numbers. Regarding the human skin heat release taught experiment, we compared the characteristic momentum to buoyancy force, which is the Froude number.

The K41 theory hypotheses lead to strong mathematical simplifications, but the predictions of this theory were found to be valid in a hypothetical context. Similarly, turbulent mixing theory is designed for large Reynolds numbers and mostly for passive scalars. In real turbulent mixing, the Reynolds number is not necessarily large, and the scalar generally contributes to the dynamics.

As a turbulent flow with an active scalar evolves, mixing leads to a homogenization of the scalar which becomes passive. The effect of active scalars on turbulent mixing is therefore necessarily transitional, and stronger on a low to moderate Reynolds number flow. Studying these flows intrinsically involves finite Reynolds number effects.

Active scalar fields contribute to the dynamics through density and/or viscosity variations. The coupling that these two thermo-physical properties offer is different. For example in jets, when compared to the passive scalar case, an active scalar jet can either transit faster or slower to a fully turbulent regime.

Jets are generally injected in a quiescent fluid, creating two distinct regions. Inside the jet, the flow is fully turbulent, whereas the flow is laminar in the outer flow. These two regions are separated by a thin layer that is referred to as the *Turbulent/Non-Turbulent Interface*. This interface is the place where momentum and mass exchanges occur.

Overview of this work

We assess some aspects of active scalar turbulent flows. Apart from the introduction and conclusion, the manuscript is organized as follows. A comparison of active and passive scalar jets, and a Turbulent/Non-Turbulent Interface literature review are presented, in Chapter 1. We focus on two types of flows. A variable density jet, during its transition to turbulence, and a variable viscosity and mass diffusivity jet late in its development. In Chapter 2, the governing equations for incompressible flows with multiple active scalars are shown. The variable density and variable viscosity and mass diffusivity cases are then derived and discussed. Each of these specific problems receives some argued simplifications.

The variable density jet case was studied using experimental measurements, from a setup that we designed and built. In Chapter 3, we expose the details of the experiment. This setup allows to measure simultaneously the three components of velocity, together with the scalar field in the very near-field of a variable density round jet. Experimental data is studied using one-point, two-point, and Turbulent/Non-Turbulent Interface statistics. In Chapter 4, we detail the processing techniques together with the results of these three approaches. The variable viscosity and mass diffusivity jet is assessed using Direct Numerical Simulations of temporally evolving plane jet, performed by Dr M.Gauding in our group. Chapter 5 is dedicated to the comparison between the fully turbulent core and the flow in the vicinity of the Turbulent/Non-Turbulent Interface.

In this thesis, two main questions are addressed. First, it is known that active scalars alter the transition to turbulence, by enhancing or diminishing the growth of fluctuations right after injection. The variable density jet aims at evaluating the effect of density deficit combined to momentum variations on the growth of turbulence. Second, turbulence is believed to smooth active scalar effects quickly, so that the scalar becomes passive early after injection. The variable viscosity and mass diffusivity jet aims at evaluating the decoupling of the scalar field from the velocity field, in the large time dynamics of the flow.

Chapter 1

Literature review and motivation

In this chapter, we expose the literature review for our study. First, we describe the effect of momentum variations at the injection of a passive scalar jet. Then, we assess the effect of density and viscosity variations on turbulent statistics of round jets. Second, we discuss the state of the art in momentum and mass exchanges in shear flows, through the Turbulent/Non-Turbulent Interface. Finally, we conclude this chapter by the overall motivation of this thesis.

1.1 Active scalar turbulent jets

In this section, we first make a short introduction to the phenomenology of passive scalar jets. Then, we provide a literature review on the more general problem of jets with variable thermo-physical properties, that we will refer to as active scalar jets.

1.1.1 Passive scalar jets, Reynolds number effects

Figure 1.1 shows a passive scalar field, in a jet flowing through a circular orifice. Passive scalar jets are governed by momentum and viscosity. Different flow regimes are governed by the Reynolds number. The jet development can be separated into multiple regions in the rescaled stream-wise direction x/D_j, where x is the distance to the orifice and D_j is the diameter of the orifice, respectively.

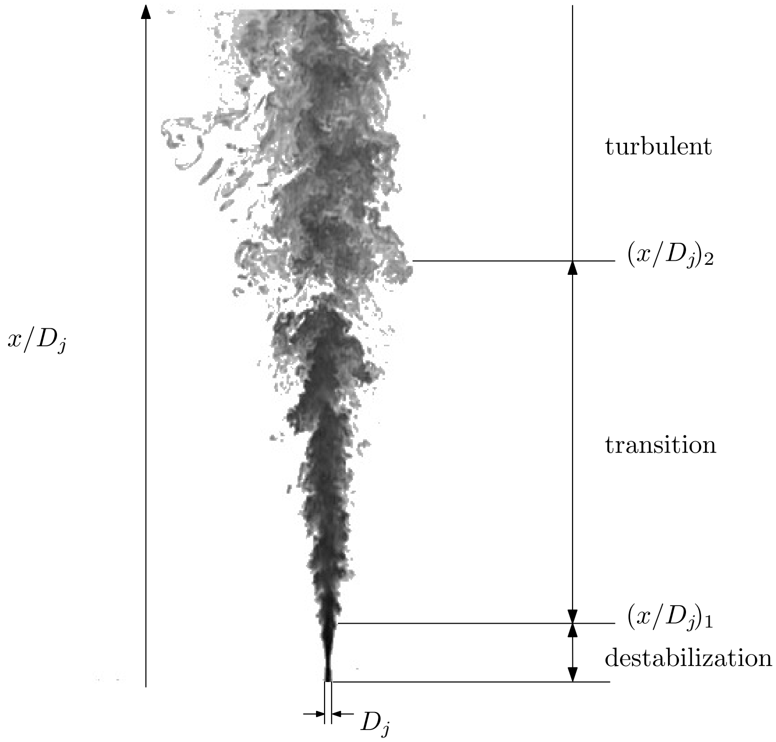

Figure 1.1: A water turbulent jet at $Re = 10000$. Gray intensity corresponds to jet mass fraction. Reproduced from Dimotakis *et al.* (1983).

In the very near field, $(x/D_j)_1 \leq 1$, the jet is still very similar to the one just before the injection and consists in an annular shear layer. This shear layer destabilises and grows until it contaminates the center of the jet. On average, this is represented by a cone that is called the potential core, where the velocity statistics are very similar to the injected flow field.

If the Reynolds number is larger than a critical value Re_{crit}, the flow dynamics changes dramatically in the far-field at a distance $(x/D_j) \geq (x/D_j)_2$ downstream (illustrated in Figure 1.1). The mean velocity in this regime is self-similar[1], which means that a single length scale a radial profile are enough to describe the average dynamics. A separation of variables applies as follows

$$\langle u \rangle(x,r) = \langle u \rangle_a(x)\, h\left(\frac{r}{\delta(x)}\right), \tag{1.1}$$

---

[1] This feature is shared by many free shear flows (Pope, 2000, Chapter 5)

where $\langle u \rangle_a$ is the streamwise mean velocity at the axis, $\delta(x)$ is the characteristic length-scale, and h is the radial self-similar profile. This simple hypothesis allows a transformation of the governing set of partial differential equations to ordinary differential equations. Adding the hypothesis that momentum flux is conserved along the streamwise direction (Chen & Rodi, 1980; Burattini *et al.*, 2005), the mean streamwise velocity, the jet velocity half-width and the mean passive scalar write as

$$\frac{\langle u \rangle_a}{u_j} = A_U \left(\frac{x - x_U}{D_j} \right)^{-1} \quad ; \quad \delta_{1/2} = A_\delta \left(\frac{x - x_\delta}{D_j} \right) \quad ; \quad \langle \phi \rangle_a = A_\phi \left(\frac{x - x_\phi}{D_j} \right)^{-1} , \tag{1.2}$$

where u_j is the injection velocity, x_U, x_δ and x_ϕ are the virtual origins for the velocity, jet half-velocity width and scalar, respectively. These quantities are not necessarily equal. The constants A_U, A_δ and A_ϕ, together with the virtual origins, depend on the specific injection conditions of the jet. Scaling laws (1.2) suggest that at the injection, the average streamwise velocity and scalar fraction diverge, whereas the jet half-velocity radius vanishes. This is why this approach is referred to as the point-source approximation, and is only valid in the far-field.

According to George (1989), the profile $h(r/\delta(x))$ is common to all classical jets that share the same boundary conditions. Therefore, the equivalence class of these mean profiles contains very few elements. Nevertheless, according to this author, the decay rate should be a function of the details of the injection conditions. In other words, Equation (1.2) is particular for a certain class of round jets, but the function $h(r/\delta(x))$ is common to all free round jets.

Between the potential core and the self-similar regime, the dynamics follow a transition between the two asymptotic states described above. There is little hope to find any general laws that govern this region of the flow, as it is highly unsteady and extremely dependent on the injection and boundary conditions. The above description is very generic, and the actual dynamics of particular jet flows can be very different from the above cartoon, even if $Re \geq Re_{crit}$. Except the Reynolds number, five parameters can modify the dynamics of the jet, especially in the transition region, that is the most sensitive. These are as follows,

1. **The geometry of the orifice.** Two jet flows have extensively been studied in the literature, the round jet issuing from a circular orifice, and the plane jet issuing from a rectangle with a very large aspect ratio. Other geometries have also been considered (Aleyasin *et al.*, 2017). Moreover, the pipe thickness has been shown to have an effect on the transition of round jets (Aihara *et al.*, 1974).

2. **The geometry of the discharging environment.** Confined jets, that issue close to solid boundaries, and free jets that issue far from solid boundaries have different dynamics (Becker *et al.*, 1963). Confinement generally has the effect of damping mean velocities and therefore enhancing turbulence intensities (Risso & Fabre, 1997).

3. **The inlet velocity distribution.** The geometry of the pipe before the injection is a key parameter. A jet issuing with a laminar Poiseuille will transit differently to turbulence than a fully developed Laufer's profile. In some experiments, a particular geometry is manufactured precisely to generate a laminarized top-hat velocity profile at the injection with a large Reynolds number (Antonia & Zhao, 2001; Xu & Antonia, 2002; Voivenel *et al.*, 2017). The whole routing of the injected fluid is to be considered, as any bending in the pipe can create very persistent Dean vorticies that can survive for tens of jet diameters in the pipe (Jimenez-Gonzalez & Brancher, 2017).

4. **The surrounding velocity distribution.** The presence of a slight co-flow, counter-flow or cross-flow can highly alter the jet dynamics. If the surrounding fluid is flowing in the same direction of the jet, the structures that appear in the beginning of the transition region are advected together with the co-flow, and the transition can take place over larger downstream distances (Antonia & Bilger, 1973). In the co-flowing configuration, the external boundary layer on the injection pipe also plays a role Matsumoto *et al.* (1973). The counter and cross-flow configurations give rise to different dynamics that are out of the scope of our study (Yoda & Fiedler, 1996; Kelso *et al.*, 1996).

5. **The displacement of the inlet nozzle.** Studies shown that a vibration of the nozzle can influence the transition and induce a very rich phenomenology, like vortex pairing (Broze & Hussain, 1994; Shaabani-Ardali *et al.*, 2019).

All these effects influence the value of the critical Reynolds number Re_{crit}, the distance that separates the different regimes $(x/D_j)_1$ and $(x/D_j)_2$, the self-similarity prefactors and the virtual origins (Equation (1.2)). Mi *et al.* (2013) performed an extensive study of the Reynolds number effect on the dynamical fields in a top-hat free round jet. The definition of their Reynolds number is $Re = \rho_j u_j D_j/\mu_j$, where ρ_j and μ_j are the density and dynamic viscosity of the injected fluid, respectively. These authors studied the low-order statistics of both large scales and small scales of turbulence. Friehe *et al.* (1971) derived self-preserving scaling for the dissipation rate. These authors method is applicable to any second order quantity. Following this assumption, Mi *et al.* (2013) also derived scaling laws analogous to Equation (1.2), for the streamwise turbulence intensity, length scales of turbulent motion. They found two distinct regimes separated by $Re_{crit} = 10^4$, so that the statistics become independent of the Reynolds number above this value.

Figure 1.2 shows the decay of the streamwise mean velocity and turbulence intensity at this axis, for given Reynolds numbers. It is clear that there is a slight effect of the Reynolds number on the decay of the mean streamwise in Fig 1.2(a). The authors reported a dependence of the self-similarity prefactor $A_U = 0.028\ Re^{1/2} + 3.54$ for $Re \leq 10^4$ and $A_U = 5.85$ for Re$> 10^4$. This correlation indicates that the higher the Reynolds number, the farther the transition to turbulence. Regarding the streamwise turbulence intensity, a plateau of 23% is reached quite fast at $10D_j$, almost independently of the Reynolds number.

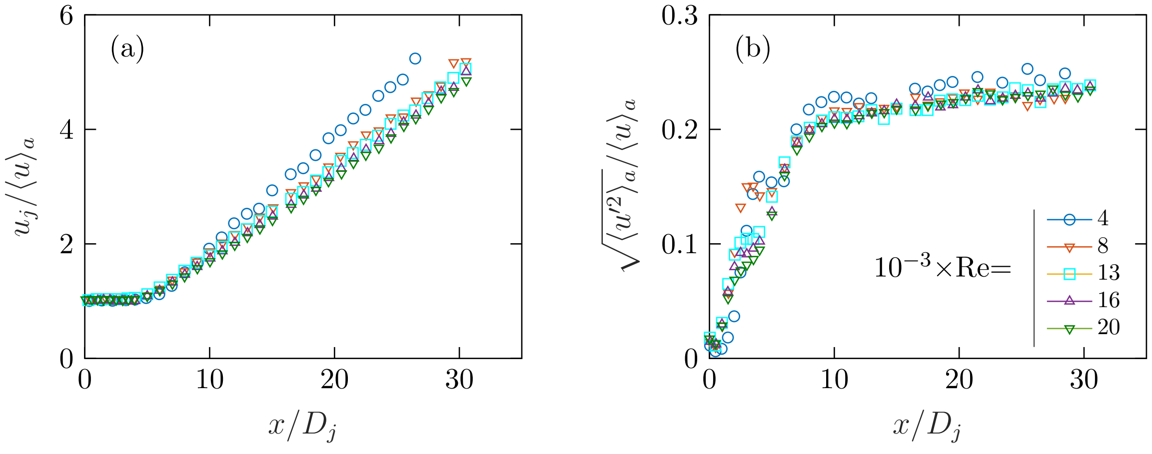

Figure 1.2: Axial variation of inverse of mean axial velocity (a) and turbulence intensity (b), for different Reynolds numbers. Figure reproduced from Mi *et al.* (2013).

Unfortunately, Mi *et al.* (2013) did not report passive scalar measurements, in the same spirit of their extensive study on the dynamic field. A frequent lack in the literature is a detailed coupled measurement of both the scalar and the dynamic fields. This feature is even more important for variable thermo-physical properties flows, because the scalar actively modifies to the flow dynamics. This lack is generally due to the technical difficulty of measuring the dynamic and the scalar fields simultaneously. We will discuss in detail this aspect in Chapter 3.

1.1.2 Active scalar jets, Archimedes number and viscosity ratio effects

Variable density jets

A variable density jet is a jet that has a different density than the hosting fluid. This density difference causes an additional forcing on momentum through two contributions. Buoyancy, which is an algebraic quantity, and changing the local inertia of the fluid, which is generally referred to as *inertial flows*. Buoyancy is always a vertical force, together the fact that it can be negative or positive, gives rise for very rich nonlinear dynamics (Mashayek & Peltier, 2012*a*,*b*). We will only focus on vertically oriented jets where the buoyancy is co-linear with momentum. If buoyancy is in the same (resp opposite) direction, the jet is said to be positively (negatively) buoyant. The phenomenology of these two configurations is very different and we will focus on positively buoyant jets.

An additional dimensionless number is required to classify the different dynamics of variable density jets, compared to constant density jets which are referred to as pure jets. Multiple choices for this dimensionless number can be made. In the literature, the Froude number (buoyancy/momentum) is employed to compare momentum to buoyancy. We will use the Archimedes number defined as $Ar = g\rho_j(\rho_c - \rho_j)D_j^3/\mu_j^2$, where subscritps $_j$ and $_c$ refer to the jet injection and co-flow conditions, respectively.

Variable density turbulent jets are to be seen as the competition of momentum and buoyancy, with the two limiting cases of the pure jet (momentum only) and pure plume (buoyancy only). Pure plumes are also self-similar if the initial Archimedes number is above a critical value, following different scaling laws than Equation (1.2) (Chen & Rodi, 1980, Table 1). Buoyant jets self-similar dynamics is always separated into three regions. Right after the self-similar regime is reached ($(x/D_j)_2$ in Figure 1.1), the jet is momentum dominated, and very far downstream the jet is buoyancy dominated. In between, an intermediate region between the pure jet and pure plume occurs. Papantoniou & List (1988) (in their Figure 9) demonstrated the separation between these regimes. The characteristic length that separates the pure jet from the pure plume regimes is the momentum length $(x/D_j)_m$, which expression for a round buoyant jet is

$$(x/D_j)_m = \left(\frac{\pi}{4}\right)^{1/4} \frac{1}{\sqrt{Fr}}, \tag{1.3}$$

where $Fr = \frac{g|\rho_c - \rho_j| D_j}{\rho_j u_j^2}$ is the Froude number. This characteristic length scale measures the length of the inertial self-preserving regime. The pure jet regime is referred to as inertial regime, and the pure plume regime is the buoyant regime. In this study, we will focus on the inertial regime, close enough from the injection.

As explained in Section 1.1.1, pure turbulent jets are very sensitive to external sources of change in the transition region to turbulence. It is intuitive that density effects add even more sensitivity to turbulent jets in this transition region. To the list of five factors that govern the dynamics of pure jets, one has to add density related factors

1. **The inlet density distribution and, closely linked, the physical mechanism responsible for density variations.** If density variations are due to temperature differences and a heat flux is flowing through the pipe, the thermal boundary layer inside the pipe can alter the dynamics. If density variations are due to the different chemical species, say perfect gases, then the distribution in a hermetic pipe is homogeneous and the gradient at the edge of the jet is very sharp. The density gradient relative intensity and orientation compared to the velocity gradient at the injection affects the transition.

2. **The surrounding density distribution.** The injection density ratio together with the density distribution in the surrounding fluid play an important role. Such a situation is encountered in volcanic eruptions, where the atmospheric density stratification cannot be neglected. The case of negative buoyancy will not be discussed in this study. See Hunt & Burridge (2015) for a recent review on this topic.

The classification of buoyant turbulent jets are to be done on a two dimensional regime diagram in the (Re, Ar) plane. The combination of the five effects on the jet transient dynamics, together with the two density effects should be taken into account. The regime diagram depends on all the seven parameters (5 for momentum and 2 for density variations).

Buoyancy variations are indeed negligible in the inertial regime, nevertheless, density variations still have a large impact on the momentum transfer.Figure 1.3 shows the decay of the dynamical quantities, subject to both Reynolds and Archimedes numbers variations. The flow is a buoyant round jet in a co-flow of velocity u_c, in the inertial and intermediate regimes. It is clear in Figure 1.3 that the trends are the same as for Figure 1.2, so that increasing Reynolds numbers pushed the self-similar regime farther downstream, for both the dynamical quantities. Nevertheless, the magnitude of this variation is much larger in Amielh *et al.* (1996) experiment, and this can only be due to density variations. We observe, in Figure 1.3, a very large effect on the downstream evolution of the dynamical quantities at the axis, especially for the lightest case. These measurements suggest that the transition to turbulence is faster when the injected fluid is lighter, and slower when the jet is heavier. This effect is widely observed in the literature (Keagy & Weller, 1949; Way & Libby, 1971; Chen & Rodi, 1980; Pitts, 1991*a*; Panchapakesan & Lumley, 1993*b*; Chassaing *et al.*, 1994; Djeridane *et al.*, 1996; **?**; Amielh *et al.*, 1996; Djeridane *et al.*, 1996).

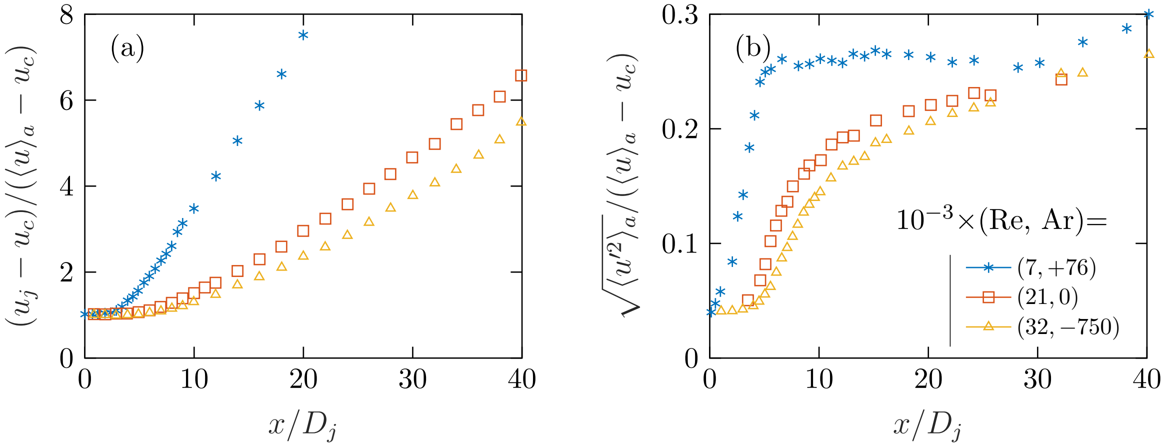

Figure 1.3: Axial variation of the mean axial velocity (a) and axial turbulence intensity (b), for different couples (Re, Ar). Figure reproduced from Amielh *et al.* (1996).

Variable density jets have been shown to never be identically self-similar in the inertial regime (Chen & Rodi, 1980). Nevertheless, there is empirical evidence (?) that a particular scaling is suitable to re-scale the mean streamwise velocity decay (Amielh *et al.*, 1996, Figure 3(a)). Figure 1.3(b) shows that the streamwise turbulence intensity reaches the usual plateau of 25% but at different downstream distances. Notice that the turbulence intensity is taken as $\sqrt{\langle u_i'^2 \rangle}/\langle u \rangle_a$. This definition does not take into account the density variations. There are, a priori, multiple possible definitions for turbulent statistics. This aspect will be discussed in Section 2.2.3.

The density variations are non-linearly coupled with the dynamical field of the flow. Considering the velocity field alone is therefore insufficient to describe the effect of density variations on the flow. Figure 1.4 shows the decay of the scalar statistics at the axis for six different turbulent round jets from Pitts (1991*a*). All six jets share the same Reynolds number $Re = 3950$ (except the heaviest one, for which $Re = 7890$). The $Ar = -240$ case is a pure jet. The trend is the same as for the dynamic fields (Figure 1.3), so that the transition is faster for the active scalar field when the jet is lighter ($Ar > 0$), and slower when the jet is heavier ($Ar < 0$). The turbulence intensity of the scalar also reaches a plateau at a typical value of $\sqrt{\langle \phi'^2 \rangle_a}/\langle \phi \rangle_a \sim 25\%$, at a distance that can vary a lot depending on the density ratio, Figure 1.4(b), similarly to the turbulent turbulence intensity, Figure 1.3(b).

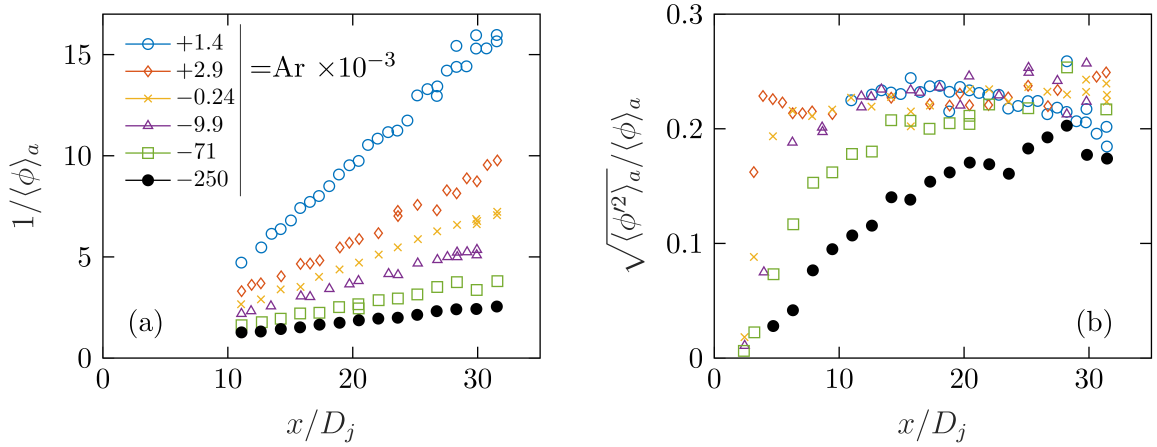

Figure 1.4: Axial variation of the mean scalar (a) and scalar turbulence intensity (b), for different Archimedes numbers. Figure reproduced from Pitts (1991*a*).

Confinement effects in co-flowing variable density jets

It is difficult to perform laboratory controlled experiments with free jets. It is preferable to use confined jets. It has been shown that a slight co-flow can isolate a confined jet from the solid boundary effect. Craya & Curtet (1955) derived a theoretical criterion for a confined jet with co-flow to evolve like free jets. The criterion is quantified through a dimensionless number named the Craya-Curtet number. The corresponding criterion has been refined by Becker *et al.* (1963), who extensively performed experimental measurements to evaluate the effect of Craya-Curtet number on the statistics of co-flowing pure jets. These authors showed that the flow dynamics are indeed a unique function of the Ct number.

Density variations have been taken into account by Steward & Guruz (1977), who generalized the Craya & Curtet (1955) criterion to variable density jets. The so-called *non-isothermal Craya-Curtet number*, noted Ct_{ni}, is a parameter that gives a criterion to compare between confined and free buoyant jets. The analytical expression of Ct_{ni} is

$$Ct_{ni} = \frac{u_k}{(u_d^2 - \frac{1}{2}u_k^2)^{1/2}}, \tag{1.4}$$

with

$$\begin{aligned} u_k &= \frac{\rho_j u_j D_j^2 + \rho_c u_c (D_c^2 - D_j^2)}{\rho_0 D_c^2}, \\ u_d^2 &= \frac{\rho_j u_j^2 D_j^2 + \rho_c u_c^2 (D_c^2 - D_j^2)}{\rho_0 D_c^2} - \frac{1}{2}\frac{\rho_c}{\rho_0} u_c^2, \\ \rho_0 &= \frac{\rho_j u_j D_j^2 + \rho_c u_c (D_c^2 - D_j^2)}{u_j D_j^2 + u_c (D_c^2 - D_j^2)}, \end{aligned}$$

where subscript c indicates the co-flow. Steward & Guruz (1977) found that $Ct_{ni} = 0.7$ is the suitable value to reproduce free buoyant jet dynamics in a co-flowing confined configuration. This value for Ct_{ni} has been successfully employed by many authors (Steward & Guruz, 1977; Pitts, 1991*a*,*b*; Amielh *et al.*, 1996). Equation (1.4), knowing the confinement diameter and density D_c and ρ_c, the jet velocity and density u_j and ρ_j, allows to compute the suitable co-flow velocity u_c for the jet to behave like a free jet. We, as explained in Chapter 3, will also use the particular value $Ct_{ni} = 0.7$ and employ it as a design criterion for our experimental setup. The determination of the dimensional variables from the dimensionless numbers is explained in Appendix A.

Variable viscosity jets

Variable viscosity jets have marginally been studied in the literature, when compared to the variable density jets. This is mainly due to the fact that viscosity is considered to be confined to the small-scales. The variations of this property were long believed to be insignificant in the turbulent cascade. Some studies have proved this argument to be wrong, as the viscosity changes can highly alter the transition of free shear flows. The first variable viscosity study was performed by Campbell & Turner (1985, 1986*b*,*a*). These authors studied the mixing in magmatic chambers. Here, we only focus on velocity statistics. Talbot (2009) showed the effect of viscosity variations on the near field statistics of a co-flowing round jet, issuing with a fully developed turbulent pipe flow velocity profile.

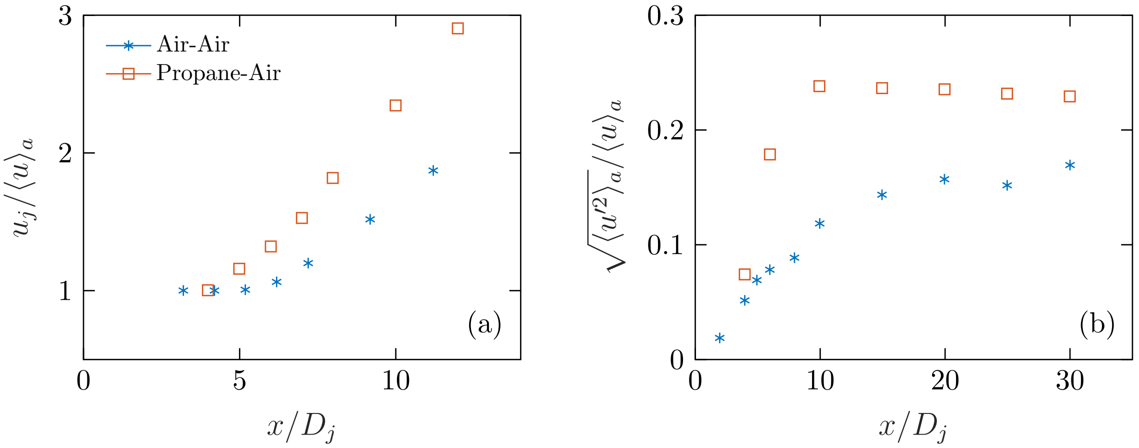

Figure 1.5: Axis decay of the mean streamwise velocity (a) and streamwise turbulence intensity (b). See text for dimensionless numbers. Figure reproduced from Talbot (2009).

Figure 1.5 shows the axis evolution of the velocity statistics of Talbot (2009). The cases are an Air-Air jet, with Re = 5400, and a Propane-Oxidizer ($30\% O_2 + 70\% Ne$) jet, with $Re = 1.54\ 10^4$, $Ar = -3.5\ 10^4$ and the dynamic viscosity ratio is $\mathcal{R}_\mu = 0.28$. First, the Reynolds number of the Propane-Oxidizer jet is large. Second, the Archimedes number is large and negative. As seen in the above sub-sections, both variations should delay the transition. Nevertheless, it is clear in Figure 1.5 that the transition is much faster in the Propane-Oxidizer jet, than in the Air-Air jet, in both the average and turbulence intensity of the streamwise velocity at the axis. This is a clear effect of dynamic viscosity variations. This inverse trend has also been observed by Voivenel (2016) in a top-hat velocity profile round jet. This suggests that the variable viscosity trend is robust to injection conditions changes.

Mini conclusion

In this section, we reviewed some effects of density and viscosity variations on the turbulent statistics of round jets. We exposed that a lower density or a higher viscosity leads to faster growth of the turbulent statistics after injection. Surprisingly, the combination of a lighter and more viscous jet has been shown to delay the growth of these statistics, which is the opposite trend to each part thermo-physical property alone.

Turbulent statistics at the axis are a robust indication of the transition of the flow, but a finer study is desired to quantify the active scalar contribution to the dynamics of such flows. To do so, we use the statistics conditioned on the very thin interface that separates the jet flow from its surroundings. The next section covers a recent literature review on this topic, with a focus on active scalar flows.

1.2 Turbulent/Non-Turbulent Interface

When a fluid is injected into another quiescent irrotational fluid, the flow is separated into two instinct regions. The injected fluid is turbulent, and is characterized by a distribution of eddies of various length and velocity scales. As this fluid spreads, vorticity contaminates the outer fluid. The rotational and irrotational regions are separated by a very thin layer, through which the vorticity jumps from zero outside to a large amount inside. This surface that separates the two regions is the so-called Turbulent/Non-Turbulent Interface (TNTI). The first study on the TNTI was performed by Corrsin & Kistler (1955), who performed hot-wire measurements in a boundary layer, a plane wake and a round jet. This work is the foundation of the TNTI knowledge. The recent improvement of experimental techniques and direct numerical simulations allows to study the TNTI in detail, and the last two decades have been extremely active in the topic. In this section, we review some results on the TNTI, and point the role of active scalars in its dynamics.

1.2.1 Turbulent/Non-Turbulent Interface detection methods

The most natural quantity to use to locate the TNTI is the magnitude of the vorticity vector $\|\omega_k\|$ (or enstrophy ω^2). Indeed, it is a quantity that is inherent to hydrodynamic turbulence, and is directly related to the small scales as it is a function of the velocity gradients only. Nevertheless, the vorticity magnitude is not the only necessary scalar field for a flow to be turbulent. For this reason, many fields have been employed in the literature as criteria for discriminating the turbulent from the non-turbulent regions, and locate the TNTI.

The requirement for the choice of the criterion field is rather linked to the particular purpose of the study than to the crude definition of a turbulent flow. Using particle tracking velocimetry, Holzner *et al.* (2007) considered the turbulent kinetic energy as a threshold in the configuration of a particle that is drawn from the laminar region towards the turbulent core through the mass entrainment mechanism. In the regard of turbulent mixing, the scalar field is generally employed as a criterion field. One should keep in mind that the scalar gradients are not necessarily sharp precisely where the TNTI is located, and this is due to the diffusivity of the scalar. To justify the use of the scalar field as a criterion, Westerweel *et al.*

(2005) applied this approach on a highly non-diffusive scalar ($Sc \gg 1$). As we are interested in turbulent mixing, we will focus on the scalar field criterion, even is our Schmidt number is not very high. We will justify the use of this method hereinafter.

Consider a blob of tracers, say a small sphere of pure ink, is plunged into a large volume of clear water in turbulent motion. Figure 1.6 represents a typical transitional distribution of such a scalar mixing. Initially, the scalar distribution consists in two Dirac distributions[2] $\mathbb{P}(\phi) = \frac{1}{2}\delta(0) + \frac{1}{2}\delta(1)$, representing pure water $\delta(0)$ and pure ink $\delta(1)$. Because ink is extremely minoritary compared to clear water, the high peak $\delta(1)$ disappears very fast, whereas the low peak $\delta(0)$ is very persistent. As ink is diluted by the turbulent motion of water, the higher concentration become fewer and fewer occurring in the flow, until they eventually disappear. The distribution then evolves by converging towards an increasing probability of very dilute ink. The asymptotic fully mixed state of this system is a single Dirac function on the dilute and homogeneous scalar value[3], say ϕ_{hom}, $\mathbb{P} = \delta(\phi_{\text{hom}})$ (not represented on the figure).

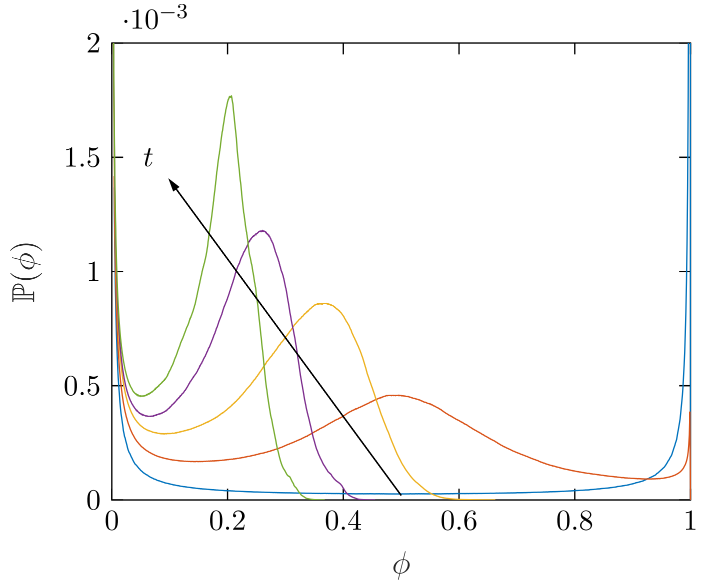

Figure 1.6: Distribution of the scalar concentration of a very dilute contaminant. The arrow indicates increasing time (data from our group).

---

[2] We use the symbol δ for the Dirac operator only on this page.

[3] This homogeneous scalar value is equal to the ratio of initial volume of the blob and the total volume.

In a turbulent jet injected into a quiescent reservoir, the scalar ϕ represents the dilution of the jet into the surrounding fluid. If the distribution of this scalar is evaluated over the whole cross-sectional plane at fixed downstream positions, the distribution evolves similarly with the downstream distance as the toy picture of Figure 1.6 through time. The jet spreads, and the scalar decays, globally following the decay rate depicted in Figure 1.4. Small scalar values therefore represent the radial edge of the jet, an choosing a suitable threshold value ϕ_0 allows to locate with good accuracy the TNTI. The requirement for a suitable TNTI detection method is the sensitivity of the interface position to ϕ_0. Prasad & Sreenivasan (1989) suggested to use the local minimum of the distribution in the neighborhood of the small scalar values (Figure 1.6), which ensures that this method is suitable. In this approach, the threshold value is a function of the actual distribution of the scalar field, so that ϕ_0 depends on the downstream position and on the flow configuration.

Figure 1.7 shows a small part of a shear flow, where the color-map represents the scalar fraction. The application of the Prasad & Sreenivasan (1989) method leads to the blue line on the Figure, which seems to accurately distinguish between the inner and outer regions of the flow. The threshold value for this particular frame is $\phi_0 = 0.08$.

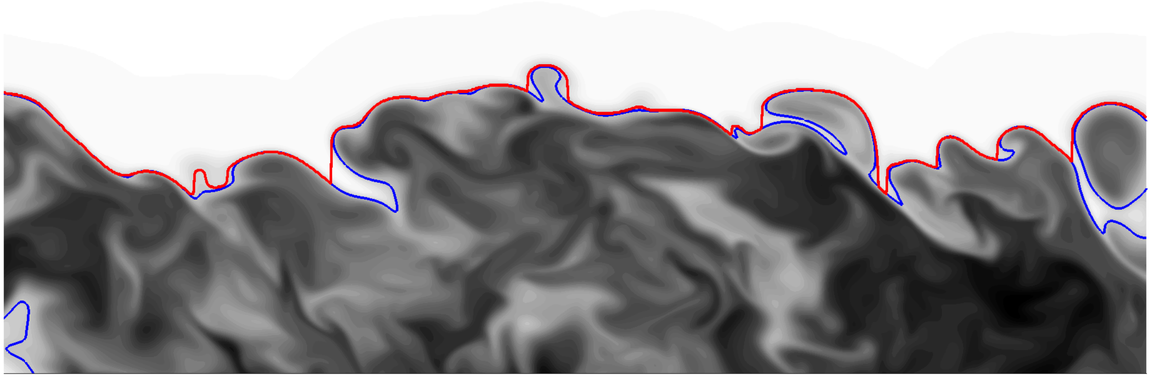

Figure 1.7: Small part of a turbulent free shear flow. The TNTI is represented by the blue line (data from our group).

Special care is to be taken regarding the diffusive effects of the scalar on the accuracy of the TNTI estimation. In order to establish conditions for which the scalar criterion is suitable, Gampert *et al.* (2014) performed a quantitative comparison of the interface position with both the vorticity and scalar fields as criteria. These authors found that the two interfaces located in a temporally evolving mixing layer converge one towards another in the limit of vanishing threshold values. This is an indication that the scalar field can be used as a criterion for flows with $Sc \geq 1$, which generalizes the Westerweel *et al.* (2005) approach to smaller Schmidt numbers. Nevertheless, this result has been evaluated with a passive scalar in a particular flow configuration. As we will be interested in active scalar mixing in a different flow, special care will be taken to ensure that the scalar criterion and threshold value are correctly chosen.

1.2.2 Turbulent statistics in the TNTI frame of reference

As explained in the previous section, the statistics show a bump through the thickness of the TNTI. In order to reveal this feature of free shear flows, Bisset *et al.* (2002) elaborated a procedure that can be described as follows. First, we choose a criterion and a suitable threshold value ϕ_0 as described in the previous section. Then, the threshold is applied to the scalar field, which leads to a scalar ϕ_0 iso-surface. The corresponding step is represented by the blue line in Figure 1.7. Next, this iso-surface is converted to a single valued function by taking only the out-most values in the cross-TNTI direction. This new surface is a single valued function of the two other coordinates of the flow location, $z_I(x, y)$. This is represented by the red line in Figure 1.7. The following step is to perform a change of frame of reference from (x, y, z) to $(x, y, z - z_I)$, the frame that is attached to the TNTI in the cross-wise direction. In the following, we will call this direction the cross-TNTI direction. We are left with a local frame of reference that is attached to the TNTI and the crosswise coordinate is positive towards the inner region, and negative towards the irrotational flow. Finally, the last step consists in averaging over the x and y directions at fixed cross-TNTI distance $z - z_I$. This method offers the possibility to evaluate statistical quantities through the thickness of the TNTI. We will refer at this kind of statistics as **conditional statistics**, as opposed to the averages along Cartesian lines of the laboratory frame that are referred to as **conventional statistics**.

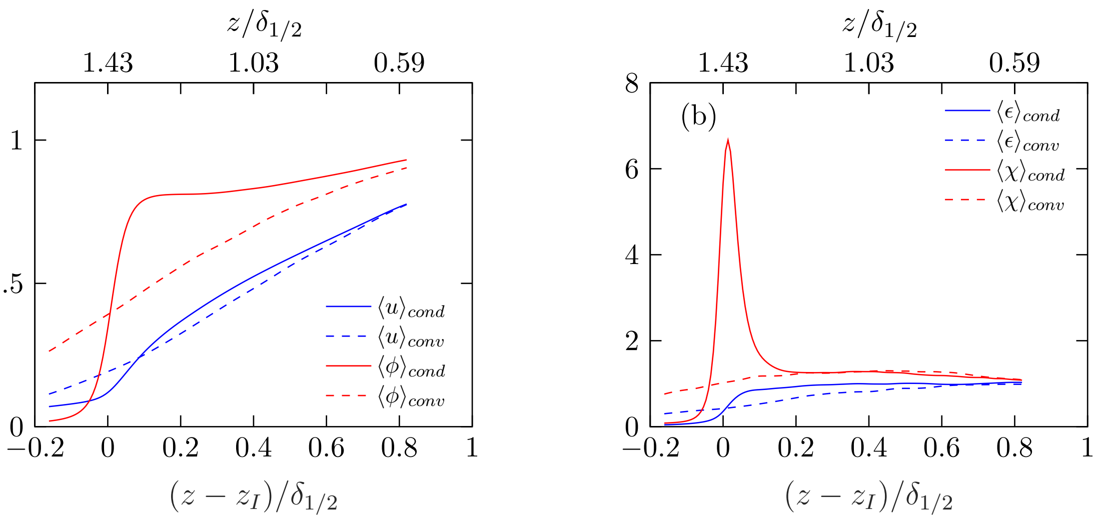

Figure 1.8: Conditional and conventional statistics of mean streamwise velocity and scalar (a) and dissipation rates (b). The conditional statistics are plotted in the TNTI frame (lower x-axis), and the conventional statistics are plotted in the Cartesian cross-stream coordinate (upper x-axis). All the statistics are normalized by the core value (data from our group).

Figure 1.8 shows the conventional and conditional statistics of (a) streamwise velocity and scalar fraction (b) kinetic energy and scalar dissipation rates. The conditional statistics are represented in the local instantaneous TNTI frame (solid lines), whereas the conventional statistics are plotted in the frame of the cross-stream direction (dashed lines).

The considered flow here is a temporally evolving plane turbulent jet, transporting a passive scalar. These statistics are normalized by the fully turbulent center-plane value, so they converge to 1 deep in the core. There clearly is a strong variation between the non-turbulent region where the turbulent statistics almost vanish, and the turbulent core where the statistics reach a fully turbulent value.

Regarding the mean quantities conditional statistics (Figure 1.8(a) solid lines), the streamwise velocity does not show a sharp increase compared to the scalar fraction. Moreover, the scalar fraction presents a small overshoot in the inner neighborhood of the TNTI. This is an indication of the accumulation of the scalar fraction just inside the TNTI. The responsible mechanism for this accumulation of passive scalar is related to the intense velocity gradients at the vicinity of the TNTI, which generate large passive scalar gradients in this region.

The kinetic energy and scalar dissipation rates behave very differently through TNTI (Figure 1.8(b) solid lines). The former endures a sharp increase and reaches its fully turbulent value very close in the turbulent region, whereas the latter shows a very large peak, that is an order of magnitude larger than the fully turbulent value, then quickly decays to this value. The kinetic energy dissipation rate behavior is related to the absence of turbulent fluctuations outside the TNTI, whereas the velocity gradients are intense and relatively homogeneous in the core. On the other hand, the scalar dissipation rate peak is directly related to the intense generation of passive scalar gradients at the edge of the TNTI. The local sharp increase of the kinetic energy dissipation rate indicates that the velocity gradients undergo a large variation, in other words, the shear is very large through the TNTI. The passive scalar is totally enslaved to this shear increase, and the scalar gradients are therefore very large very locally, which leads to a peak in the scalar dissipation rate. The dependence of the scalar field to the velocity gradient field will be assessed in Chapter 5.

In Figure 1.8, we also represent the conventional statistics of the considered quantities, in the frame of the average TNTI (upper x-axis, dashed lines). It is important to notice that the conventional averaging approach is unable to reveal the local statistical behavior of the scalar quantities. The mean scalar fraction and scalar dissipation rate are underestimated by a factor of 2 and 6 at the TNTI, respectively. The correct estimation of the scalar dissipation rate is of very high relevance in the turbulent mixing modeling perspective, and a mis-estimation of a factor 6 on this quantity is, of course, not desired. This large difference between conditional and conventional statistics has been observed by many authors (Bisset *et al.*, 2002; Westerweel *et al.*, 2009; Hunger *et al.*, 2016).

This ineffectiveness of the conventional statistics to capture the local behavior of the statistics at the edge of the jet is related to the arbitrary choice of the frame of coordinates within the average is performed. The flow does not know or feel the Cartesian coordinates, this frame is just the most efficient way that we found to solve the governing equations with these particular boundary conditions. The natural frame of coordinates of the flow is related to the local velocity and velocity gradients eigen-frame, which is globally better captured by the conditional statistics approach. In this regard, Elsinga & da Silva (2019) studied in the alignment of the velocity and passive scalar gradients, in the vicinity of the TNTI.

These authors show that there is a strong dependence of the scalar gradient magnitude on the orientation of the velocity gradient eigen-frame, so that the gradient is mostly aligned with the most compressive strain direction. This particular alignment plays the role of a source term for the scalar gradient magnitude.

1.2.3 Effects of active scalars on entrainment in jet flows

Entrainment is the process by which a jet flow encompasses the surrounding fluid towards the core. It is also the way a jet expands, as the surrounding fluid is entrained, the mass content of a very thin disk increases along the downstream direction. Using a statistical approach, Morton *et al.* (1956) pioneered the field of mass entrainment through a simple hypothesis. These authors supposed that, in the self-similar regime, the radial entrainment velocity u_e is linearly proportional to a mean streamwise jet velocity $u_e(x) = \gamma_e \langle u \rangle_x(x)$. This closure entails the prefactors A_U, A_δ and A_ϕ in Equations (1.2). Ricou & Spalding (1961) developed a direct measurement technique for the entrainment coefficient. This technique consists in adjusting the flow injected radially in a porous wall chamber to recover free jet statistics. The net mass flow rate injected through the wall at each downstream position is therefore the entrained mass flow rate. This technique was applied to variable density jets, and the authors showed that a correction similar to Thring & Newby (1953) should be included, proportionally to $(\rho_j/\rho_c)^{1/2}$. A light jet entrains more than a heavy jet.

The Morton *et al.* (1956) closure is very handy, as it requires the determination of a single constant to adjust all the mean quantities streamwise evolution. Unfortunately, the precise value of the entrainment coefficient has been found to be very sensitive to the particular configuration of the considered flow, as a consequence of the strong dependence of the decay of the self-similar solutions (as discussed in Section 1.1 (George, 1989)). Generally, this coefficient is $\gamma_e \sim 0.08 - 0.13$.

Entrainment in the Morton *et al.* (1956) sens is a statistical average of all the mass fluxes that cross the edge of the jet. Other authors focused on the case where the net average of these mass fluxes was directed towards the outer region, this is called detrainment. Cotel & Breidenthal (1997) evaluated the detrainment of a fountain crossing a stable density interface. The authors identified many regimes, varying the density ratios and the height of the density interface compared to the jet diameter (Cotel & Breidenthal, 1997, Figure 4). In particular, one of the regimes consisted on the regular ejection of heavy jet fluid into the stratified fluid, which is detrainment. The authors identify the physical mechanism that causes this effect as the baroclinic torque, which appears as a forcing term in the vorticity transport equation. Adjusting the height of the interface for a certain density ratio permits a resonating interaction that forces vorticity away from the core of the fountain.

The above models consider a conical jet, with uniform velocity in it for a point-source jet. This picture is very simplified and valid only in a statistical sens, far enough downstream. At a lower level description, the jet exchanges mass with the surrounding fluid through the TNTI. Many recent studies considered mass fluxes through the TNTI in classical free shear flows and boundary layers (Mistry *et al.*, 2019, and references therein). Local normal velocity to the TNTI has a wide probability density function, that is skewed towards the negative values. Local mass exchanges are therefore an equilibrium between entrainment and detrainment, where the entrainment is generally dominant. This is in adequacy with the observed statistical entrainment (Morton *et al.*, 1956). Recently, local mass exchanges at the TNTI of classical shear flows has been proven to depend on the local curvature of the TNTI (Wolf *et al.*, 2012, 2013) and on the orientation relative to flow direction (Watanabe *et al.*, 2014). The local dynamics of the TNTI are closely linked to the vortex stretching mechanism, that maintains very fine scales at the edge of the flow.

As the topic is still new, very few studies focus on the TNTI mass exchanges in active scalar turbulence. Regarding Boussinesq stably stratified turbulence, Watanabe *et al.* (2016*b*, 2017, 2018) studied mixing layers and Watanabe *et al.* (2016*a*) looked at a turbulent wake. Jahanbakhshi *et al.* (2015); Jahanbakhshi & Madnia (2016) performed a direct numerical simulation of a compressible shear layer and van Reeuwijk *et al.* (2018) studied an inclined gravity current.

Stably stratified turbulence and gravity currents have very distinct phenomenology compared to the problem of active scalar mixing, we will therefore focus on the compressible shear layer from Jahanbakhshi & Madnia (2016), even so our considerations are incompressible. These authors wrote an enstrophy transport equation and identified two groups of terms. The inviscid group contains a strain, baroclinic torque and a dilatation term. The viscous group contains diffusion, dissipation rate, and shear/density-gradient terms. One of the results of this study is the variation of the average entrained mass flux at the TNTI with the Mach number. The authors found that, as the Mach number increases, the global entrainment mass decreases, and that the contribution from the viscous group decreases whereas the contribution of the inviscid group increases. This is an indication that at large March number, the main source of enstrophy at the TNTI are strain and variable density driven, instead of viscosity or variable viscosity driven.

An analogy with the incompressible variable density mixing is delicate, but one could expect that the strain and baroclinic terms should be important regarding the average entrainment. We recall that Cotel & Breidenthal (1997) linked the detrainment effect they observed to the baroclinic torque. Strain and the baroclinic torque therefore seem to be an important feature of variable density entrainment.

Voivenel (2016) performed experimental measurements of entrainment characteristics in a variable viscosity and density jet. The flow configuration is a laminarized top-hat velocity profile of Propane-Nitrogen jet. The corresponding dimensionless numbers $(Re, Ar, \mathcal{R}_\mu)$ are $(2.4\,10^4, -5.7\,10^6, 0.45)$. The conditions are very similar to Talbot (2009), except the fluids and the injection velocity profile. The main result of Voivenel (2016) is that entrainment is enhanced in this variable viscosity density configuration, even in the very near field of the jet. The average statistics show a much faster transition compared to a Nitrogen-Nitrogen jet. The entrainment coefficient is evaluated through the statistical approach (Ricou & Spalding, 1961), and at locally at the TNTI. Both approaches reveal that some regions of the flow are dominated by detrainment instead of entrainment.

The vicinity of the TNTI is considered to be the least favorable location in a turbulent shear flow for the turbulence classical theory to be valid. As this theory rests on conventionally averaged statistics, and the TNTI is the most inhomogeneous region of this type of flows, one could expect that the failure of conventional statistics to capture the kinetic energy and scalar dissipation rates.

Mini conclusion

In this section, we reviewed the literature concerning the Turbulent/Non-Turbulent Interface (TNTI) phenomenology. Averaging along Cartesian lines and planes is convenient in the post-processing point of view, but imposing the laboratory frame of reference to the statistics is artificial. The *natural* frame of reference of the flow is local, and consists in the eigen-frame of the velocity gradient tensor. In addition, momentum and mass exchanges occur at the edge of free shear flows. Using the magnitude of the enstrophy to locate the edge of the flow is not biased, as the flow dictates the location where we should observe it. Evaluating statistics in the neighborhood of the TNTI is therefore more representative of momentum and mass exchanges than conventional averaging. The effect of density and viscosity variations has not been addressed directly in incompressible flows. Our aim is to use this approach to study mixing at the vicinity of the TNTI, as we will do for a variable density jet in Chapter 4, and for a variable viscosity and mass diffusivity jet in Chapter 5.

1.3 Motivation and methodology of the thesis

The main observed effect of active scalars on the dynamics of jets is the dissymmetry of the transition to turbulence. This feature depends on the density or viscosity ratios between the jet and the surrounding fluid. Decreasing the density or increasing the viscosity of the jet accelerates the transition. On the contrary, increasing the density or lowering the viscosity decelerates the transition. The dynamics of such flows is not trivial, and a separate study is required to each specific flow configuration in terms of geometry and of the scalar feedback mechanism.

Figure 1.9 shows a typical scalar field, in the near-field of a round jet. We will focus on two regions of these flows, using specific methodologies, 1) the fully developed turbulent core, where we will evaluate one-point and two-point statistics, to quantify the transition and energy transfers inside the jet and 2) the Turbulent/Non-Turbulent Interface, where we evaluate momentum and mass exchanges with the surrounding fluid. In this thesis, we assess the effect of active scalars on the dynamics in two particular flows, a variable density jet and a variable viscosity and mass diffusivity jet.

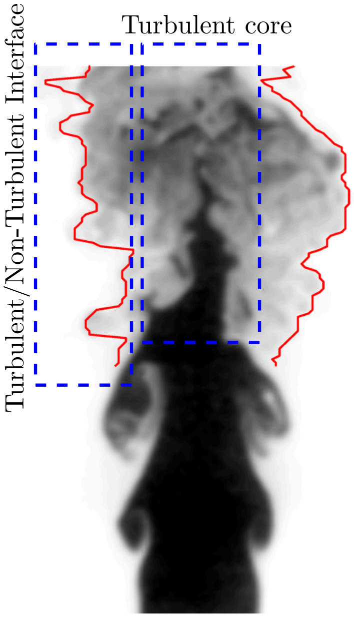

Figure 1.9: Typical scalar field in the very-near field of a turbulent round jet (data from our measurements, see Chapter 3). The red lines correspond to the TNTI.

Chapter 2

Analytical formalism

In this chapter, we introduce the theoretical grounds for studying the flows of interest. Then, we show the two isothermal particular problems that we will treat, non-Boussinesq variable density flows, and variable viscosity and mass diffusivity flows. This chapter is limited to the derivation of local and instantaneous equations, as each flow configuration has a dedicated chapter. We also derive equations for the second-order velocity and scalar structure functions in the framework of the fully turbulent two-point approach.

2.1 Governing equations for flows with active scalars

First, we will introduce the general set of equations for our study. We briefly discuss the significance of these equations and the physical problem that they model. The following equations are derived from the application of fundamental invariance principles of mass, momentum and energy, in the context of continuum mechanics. In addition, we use the low-Mach number approximation. To further simplify, we consider a Newton-Stokes fluid and neglect the second viscosity[1], with Fourier-Fick diffusion laws for heat and mass, respectively. We do not consider any chemical reaction, or heat release. The problem concerns the mixing of two different chemical species, initially at different temperatures. The corresponding equations read (Chassaing *et al.*, 2002),

---

[1] See Buresti (2015) for a recent justification of this hypothesis.

Mass conservation

$$\partial_t \rho + \partial_k(\rho u_k) = 0, \tag{2.1}$$

where ρ and u_j are the density and the velocity component in direction x_j, respectively. The Einstein summation convention is applied over repeated indices.

Momentum conservation

$$\partial_t(\rho u_i) + \partial_k(\rho u_k u_i) = -\partial_i p + \partial_k \left(\mu \left(\partial_k u_i + \partial_i u_k - \frac{2}{3}\partial_n u_n \delta_{ik} \right) \right) + \rho g_i, \tag{2.2}$$

where p, μ and g_i represent the dynamic pressure, the dynamic viscosity and the component gravity vector in the x_i direction, respectively.

Internal energy conservation

$$\partial_t(\rho T) + \partial_k(\rho u_k T) = \partial_k(\kappa \, \partial_k T), \tag{2.3}$$

where T and κ represent the temperature and the thermal diffusivity, respectively. The heat capacity is supposed to be constant.

Chemical species conservation

$$\partial_t(\rho \phi) + \partial_k(\rho u_k \phi) = \partial_k(\rho \mathcal{D} \partial_k \phi), \tag{2.4}$$

where ϕ and $\mathcal{D}$ are the mass fraction and the binary mass diffusivity, respectively.

State equations

$$\rho = f_1(T, \phi); \qquad \mu = f_2(T, \phi); \qquad \kappa = f_3(T, \phi); \qquad \mathcal{D} = f_4(T, \phi), \tag{2.5}$$

where f_i are state equations. Equations (2.1)-(2.4) result from the application of fundamental physical conservation laws of mass, momentum, internal energy and chemical species, respectively. This set contains 6 equations over 10 scalar fields. In order to close the problem, it is necessary to add 4 equations (2.5). The equations of state represent the link between the mass fraction and temperature (ϕ, T) together with the thermo-physical properties $(\mu, \rho, \mathcal{D}, \kappa)$.

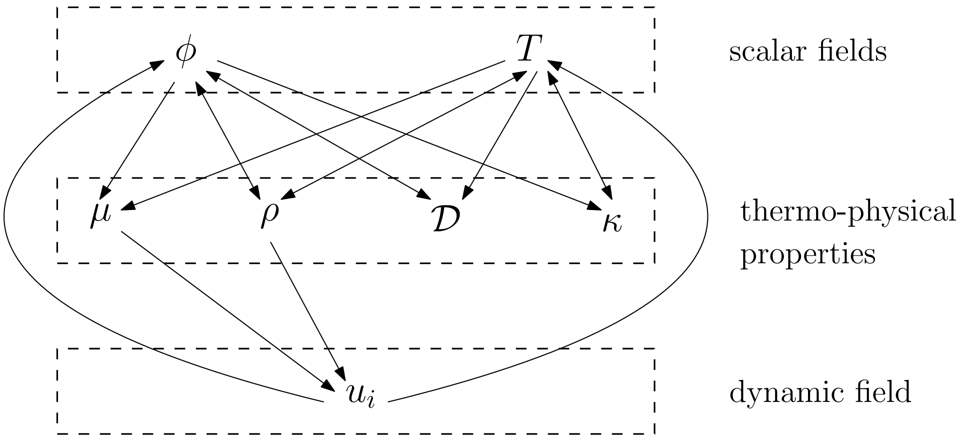

Figure 2.1: Scheme of the interaction of the different fields in the incompressible binary mixing case, corresponding to the set of equations (2.1)-(2.5)

It is necessary to distinguish passive from active scalar fields. Passive scalars are kinematically transported by the velocity field, without any contribution to the dynamics, whereas active scalars act through a feedback mechanism on the dynamical field. Figure 2.1 is a schematic view of the fields involved in the set of equations (2.1)-(2.5). The highest row represents the conservation equations of chemical species and internal energy, (2.4) and (2.3), respectively. The bottom row represents the generalized Navier-Stokes equation (2.2). The middle row is the thermo-physical properties. The arrows separating the scalar fields from the thermo-physical properties are the state equations (2.5), whereas the arrows from the thermo-physical properties to the dynamic fields represent the coupling of the thermo-physical properties with the Navier-Stokes equations.

The scalar fields that can be qualified of active or passive are the first raw. The dynamic viscosity μ and density ρ are the only thermo-physical properties that can act on the momentum equation. These quantities are coupling variables that allow the scalar fields ϕ and T to have a feedback mechanism on the dynamics. The mass and heat diffusivities, $\mathcal{D}$ and κ respectively, cannot do be a feedback mechanism, as they do not appear explicitly in the generalized Navier-Stokes equation (2.2). This precise distinction between the physically invariant scalar fields and the thermo-physical properties is necessary when treating particular situations encountered in active scalar flows. Precise examples will be given in Chapter 4 for variable density flows, and in Chapter 5 for variable viscosity/diffusion flows.

When writing the transport equations for multi-species flows, some subtle hypotheses have to be made. In particular, each substance obeys a distinct Navier-Stokes equation. Multiple methods have been developed for the combination into a single Navier-Stokes equation. In this thesis, we restrict ourselves to a mass-weighted velocities. For a detailed discussion of these considerations, see (Williams, 2018, Appendix C), and Guillén-González *et al.* (2007) for an alternative formulation.

In Figure 2.1, two sub-problems emerge, isothermal binary chemical species flows, and non-isothermal single species flows. These two problems seem to be very analogous, but the diffusive terms of the energy conservation equation (2.3) and the chemical species conservation equation (2.4) are different. This subtle dissimilarity has large consequences when studying particular flows (Livescu, 2020). The state equations (2.5) depend on which scalar is active and on the fluids involved. We will consider only isothermal mixing.

2.2 Non-Boussinesq variable density flows

We write the particular case of the set (2.1)-(2.5) for isothermal, constant viscosity and mass diffusivity, leaving the density variable. The corresponding dimensionless equations read

$$\partial_t\rho + \partial_k(\rho u_k) = 0, \tag{2.6}$$

$$\partial_t(\rho u_i) + \partial_k(\rho u_k u_i) = -\partial_i p + \frac{1}{Re}\left(\partial_k^2 u_i + \frac{1}{3}\partial_{ik}^2 u_k\right) + Fr^2 g_i \rho, \tag{2.7}$$

$$\partial_t(\rho\phi) + \partial_k(\rho u_k \phi) = \frac{1}{Pe}\partial_k(\rho\partial_k\phi), \tag{2.8}$$

$$\rho = f_1(\phi; \mathcal{R}_\rho), \tag{2.9}$$

where $Re = \rho_2 U^* L^*/\mu$, $Fr = \sqrt{gL^*}/U^*$, $Pe = \rho_2 U^* L^*/\mathcal{D}$, $\mathcal{R}_\rho = \rho_1/\rho_2$, g_i ρ_1 and ρ_2, U^* and L^* are the Reynolds number, the Froude number, the Peclet number, the density ratio, the projection of the gravitational acceleration orientation vector in i direction, reference densities, and the reference velocity and length scale, respectively. The equations are made dimensionless by multiplying the dimensional set by $L^*/(\rho_2 U^{*2})$. In equations (2.6)-(2.9), the density ρ is a unique function of the mass fraction ϕ, through the state equation (2.9). The density ratio $\mathcal{R}_\rho$ is a control parameter for this equation so that the density is constant when $\mathcal{R}_\rho = 1$. The viscous term in equation (2.7) compared to (2.2) by consideration that the dynamic viscosity is constant.

2.2.1 Large density variations and acoustic waves

In Equations (2.6)-(2.9), the flow is incompressible. Nevertheless, the velocity field is not necessarily divergence free. In order to clarify this point, we discuss what compressiblity is, and what are the conditions the velocity field to be divergence free. The Navier-Stokes equations are non-local. The quantity that allows any variation of the velocity fields to impact distant regions within a flow is pressure. Lighthill (1952, 1954) introduced the so-called hydro-acoustic analogy. In these papers, M. J. Lighthill derived a D'Alembert equation for pressure fluctuations, starting from the fully compressible Navier-Stokes system (Chassaing *et al.*, 2002). This equation is called the Lighthill equation, and reads

$$\left[\frac{1}{c_s^2}\partial_t^2 - \partial_k^2\right] p' = \partial_{ik}^2(\rho u_i u_k - \tau_{ik}), \tag{2.10}$$

where p', c_s, ρ and τ_{ik} are the pressure fluctuation, the speed of sound, a background reference density and the shear stresses, respectively. Equation (2.10) is a wave equation over the pressure fluctuation, that is forced by the dynamic fields. This equation demonstrates how turbulent motion generates noise, in a compressible flow.

The derivation of equation (2.10) consists in the combination of the mass and momentum conservation equations, together with the assumptions that the density turbulence intensity is small and that the pressure and density fluctuations are linked through $p' = c_s^2\,\rho'$. This last assumption gives a physical mechanism to small pressure fluctuations to behave as waves.

In any flow, a displacement at instant t_1 of a fluid parcel located at x_1 generates acoustic waves that propagate at the speed of sound c_s in all directions. If we consider a distant fluid parcel located at x_2 that is also in motion, it is reached by the waves at a characteristic time $t_2 = ||x_2 - x_1||/c_s + t_1$. In compressible flows, the displacement of the x_2 parcel is non-negligible within the time $t_2 - t_1$. The incompressiblity hypothesis consists in neglecting the displacement of all fluid parcels within the domain compared to the speed of sound, so that the flow is frozen in time as acoustic waves propagate. The consequence is an instantaneous adaptation of the whole pressure field to any displacement within the flow.

Mathematically, starting from the general compressible Navier-Stokes equations Chassaing *et al.* (2002), it is possible to make an asymptotic expansion into the Mach number for all variables of the equations. The leading order in this parameter decouples the pressure into two components, the thermodynamic pressure, and the dynamic pressure, respectively.

The corresponding set of equations is the same as for (2.6)-(2.9), with an additional equation that ensures that the thermodynamic pressure is homogeneous in space (i.e. its gradient is zero). The pressure that is present in the variable density Navier-Stokes equation (2.7) is the dynamic pressure. When the low-Mach number assumption applies, we split the pressure into two components, the thermodynamic pressure, which is a passive scalar field, and the dynamic pressure field, which is an active scalar field. The dynamic pressure is active through the variable density Poisson equation (i.e. ∂_i (2.7)), that reads

$$\partial_i^2 p = -\partial_{ik}^2(\rho u_k u_i) + \frac{1}{Re}\partial_i \left(\partial_k^2 u_i + \frac{1}{3}\partial_{ik}^2 u_k\right) + Fr^2 g_i \partial_i \rho. \tag{2.11}$$

If the fluid accelerates in some region of the flow, the pressure drop is transmitted to the whole domain instantaneously, through equation (2.11), but the induced displacement will be affected by the surrounding density variations. Density here affects the response of the fluid to dynamic pressure variations, only. This precise configuration of variable density incompressible flows is called dynamic incompressiblity (Chassaing *et al.*, 2002).

Compressibility is quantified through the isentropic compressibility coefficient, which is defined by

$$\beta_s = \left(\frac{\partial \rho}{\partial p}\right)_S = \frac{1}{c_s^2}, \tag{2.12}$$

where ρ and p denote thermodynamic variables[2]. The mathematical formulation of this hypothesis is to assume that sound is infinitely fast, i.e. $\beta_s = 0$. In the Lighthill equation (2.10), the assumption of proportionality $p' = c_s^2\, \rho'$ requires the speed of sound to be finite. It is not possible to derive a Lighthill equation in the dynamic incompressiblity context.

The continuity equation (2.6) is not modified by the incompressiblity hypothesis, and the velocity field is not divergence free. Nevertheless, we will derive, in the next section, sufficient conditions for the velocity field to be divergence free in this configuration.

---

[2] We do not use a different notation because we will not invoke these variables elsewhere. In the rest of the document, this notation is used for dynamical fields.

2.2.2 Pseudo mass fraction and state equation

The temporal terms of equations (2.7) and (2.8) are quadratic, whereas the advection terms are cubic. In order to reduce the non-linearity of the problem, one can replace the state equation (2.9) into the chemical species conservation equation (2.8). By use of continuity we find

$$f_1(\phi;\mathcal{R}_\rho)(\partial_t\phi + u_k\partial_k\phi) = \frac{1}{Pe}\partial_k(f_1(\phi;\mathcal{R}_\rho)\partial_k\phi), \tag{2.13}$$

then, by employing the chain rule on the primitive function of the state equation $\varphi(\phi,\mathcal{R}_\rho) = \int f_1 d\phi = \int \rho d\phi \Rightarrow \rho\partial_k\phi = \partial_k\varphi$. The chemical species transport equation (2.8) reduces to

$$\partial_t\varphi + u_k\partial_k\varphi = \frac{1}{Pe}\partial_k^2\varphi. \tag{2.14}$$

The variable φ obeys a usual advection-diffusion equation, which is linear. The non-linearity of the problem, when formulated with φ, is therefore reduced. Informations on the mass fraction as well as on the density fields are contained in φ. In addition, we notice that

$$\lim_{\mathcal{R}_\rho\to 1}\varphi = \int \lim_{\mathcal{R}_\rho\to 1} f d\phi = \int d\phi = \phi + C, \tag{2.15}$$

where C is an integration constant than has to be zero so the passive scalar lower bound is zero. Because the passive scalar case can be recovered by adjusting the control parameter $\mathcal{R}_\rho$, we call φ the pseudo mass fraction.

The pseudo mass fraction is therefore a natural field to consider in the set (2.6)-(2.9). Notice that we did not specify the analytical expression of the state equation (2.9) to make this simplification. Introducing φ in the whole set of equations leads to

$$\partial_k u_k = \frac{1}{Pe} d_\phi\left(\frac{1}{d_\phi\varphi}\right)\partial_k^2\varphi, \tag{2.16}$$

$$d_\phi\varphi(\partial_t u_i + u_k\partial_k u_i) = -\partial_i p + \frac{1}{Re}\left(\partial_k^2 u_i + \frac{1}{3}\partial_{ik}^2 u_k\right) + Fr^2 g_i d_\phi\varphi, \tag{2.17}$$

$$\partial_t\varphi + u_k\partial_k\varphi = \frac{1}{Pe}\partial_k^2\varphi, \tag{2.18}$$

where $d_\phi \equiv d/d\phi$ and $d_\phi\varphi = \rho$ by definition. The set of equations (2.16)-(2.18) is closed, provided the analytical expression of the state equation.

Equation (2.16) shows the sufficient conditions for the velocity field to be divergence free in this context. Either the density is constant $d_\phi(1/d_\phi\varphi) = 0$, or mass diffusivity is neglected $Pe \to +\infty$. We recall that this property is specific to the mass-weighted velocity (Williams, 2018, Appendix C).

The set (2.16)-(2.18) can be further simplified. If the density variations are small, one can apply the Boussinesq approximation. This approximation consists in considering the density constant in all terms, except the buoyancy term. This simplification is valid only for buoyancy-driven flows, as it requires the Froude number to be non-negligible. If mass diffusivity and buoyancy are neglected ($Fr \to +\infty$ and $Pe \to +\infty$), the set (2.16)-(2.18) is analogous to the passive scalar Navier-Stokes equations, with the difference that the left-hand-side of the momentum conservation equation (2.17) is multiplied by $d_\phi\varphi$.

The specific form of the state equation is a key to the dynamics of the flow, as it controls the coupling between the pseudo mass fraction and the velocity field. If the thermodynamical properties of a fluid are constant, the volume occupied by a substance is an extensive property. Therefore, mixing N species of respective volume V_i and mass m_i the share the same pressure and temperature leads to a final mixture of volume $V = \sum_{i=1}^N V_i$ and mass $m = \sum_{i=1}^N m_i$. Defining the densities as $\rho_i = m_i/V_i$, one finds

$$\frac{m}{\rho} = \sum_{i=1}^{N} \frac{m_i}{\rho_i}, \tag{2.19}$$

then dividing by m, introducing the mass fractions $\phi_i = m_i/m$ and inverting

$$\rho = \left(\sum_{i=1}^{N} \frac{\phi_i}{\rho_i} \right)^{-1}. \tag{2.20}$$

For a binary mixture, one finds the dimensionless form

$$\rho = \frac{1}{1 + a\phi}, \tag{2.21}$$

where ρ is normalized by ρ_2 and $a = (\rho_2 - \rho_1)/\rho_1 = 1/\mathcal{R}_\rho - 1$. This equation has been derived for perfect gases by Chassaing (1979), and has extensively been used in variable density mixing literature (Shih *et al.*, 1987; Panchapakesan & Lumley, 1993*b*; Sandoval, 1995; Cook & Dimotakis, 2001; Livescu & Ristorcelli, 2007).

The underlying hypothesis to derive the state equation (2.21) is the additivity of volumes of the mixed species. For perfect gases, this is the Amagat law of the additivity of partial volumes (Winterbone & Turan, 2015). This law is the equivalent of the Dalton law for the additivity of partial pressures. This is valid for ideal non-reacting fluids, that initially share the same pressure and temperature. For example, in fast combustion processes, heat release causes a local expansion of the mixture. The volume of the burned gases is larger than the sum of the fuel and oxidizer initial volumes.

We will consider this state equation in our study, which is representative of a large variety of non-reacting mixing processes. Using (2.21), the pseudo mass fraction is obtained by integration

$$\varphi = \frac{1}{a}\ln(1 + a\phi). \tag{2.22}$$

Introducing this function in the set (2.16)-(2.18) leads to the set that we will consider in our study of non-Boussinesq variable density jet flows in Chapter 4

$$\boxed{\begin{aligned} \partial_k u_k &= -\frac{a}{Pe}\partial_k^2\varphi, & (2.23)\\ e^{-a\,\varphi}(\partial_t u_i + u_k\partial_k u_i) &= -\partial_i p + \frac{1}{Re}\left(\partial_k^2 u_i + \frac{1}{3}\partial_{ik}^2 u_k\right) + Fr^2 g_i e^{-a\,\varphi}, & (2.24)\\ \partial_t\varphi + u_k\partial_k\varphi &= \frac{1}{Pe}\partial_k^2\varphi. & (2.25)\end{aligned}}$$

In literature, it is common to use the change of variables $\theta = \ln\rho$ for this type of flows (Sandoval, 1995; Livescu & Ristorcelli, 2007; Rao *et al.*, 2017; Viciconte, 2019). The apparent equivalence of θ and φ is due to the particular analytical expression of the state equation (2.21), so by considering the logarithm of this equation

$$\ln\rho = -\ln(1 + a\phi) \Rightarrow \theta = -a\varphi. \tag{2.26}$$

Even if θ and φ are linearly linked, the mathematical behavior of these fields is different. The pseudo mass fraction allows a control of the variable density effects through the explicit parameter a (or $\mathcal{R}_\rho$) in the set (2.23)-(2.25). This difference is of primary importance when comparing passive and active scalar dynamics. As $\mathcal{R}_\rho \to 1$, θ vanishes, whereas $\varphi \to \phi$. Moreover, if the flow is largely diluted, the pseudo mass fraction dynamically converges towards mass fraction, $\lim_{t\to\infty}\varphi \to \phi$. Pseudo mass fraction φ is valid for any state equation, and θ is valid only for the particular case of equation (2.21).

2.2.3 Statistical filtering

The statistical approach of variable density flows is not straightforward. The filtering of the equations is not unequivocal, as multiple choices are possible to define a decomposition. In classical Navier-Stokes equations, the only nonlinearity is the quadratic advection term. When applying the classical Reynolds decomposition $u_i = \langle u_i \rangle + u_i'$, the nonlinear term generates 6 additional terms in the mean momentum transport equation, which are the unclosed Reynolds stresses $\langle u_k' u_i' \rangle$.

In the variable density case, the temporal term is quadratic and the convective term is cubic. A systematic use of the Reynolds decomposition on the all the fields leads to a large number of additional terms. To this extent, A. Favre developed a mass weighted averaging that reduces drastically the number of unknown correlations in the variable density closure problem. This method is suitable for modeling and is widely used in engineering. The drawback of the Favre decomposition is the difficulty to physically interpret the generated terms and to make an analogy with the constant density case. A comparison of the Reynolds and Favre approaches can be found in (Chassaing *et al.*, 2002, chapter 5).

In addition to the choice of the statistical decomposition of the flow field, many choices can also be made for the kinetic energy. There is, a priori, no physically favored choice for this definition. Each particular choice generates a different analytical form for the viscous dissipation rate. Zhao & Aluie (2018) showed that for some definitions of the turbulent kinetic energy, the viscous dissipation rate is not negligible at large scales, when the density ratio is large enough. This feature is in contradiction with the inviscid criterion, that postulates that when the Reynolds number is large enough, large to intermediate scales are inertial. In particular, these authors showed that the Favre average respects the inviscid criterion.

The Reynolds decomposition quickly generates many terms, even for low-order equations. Nevertheless, this method has the advantage of strictly generalizing the constant density equations with additional terms. In the perspective of a quantitative evaluation of the influence of density variations, we choose to use the Reynolds decomposition.

2.2.4 Variable density scale-by-scale budget equations

One of the classical turbulence approaches consists in evaluating the non-local energy transfer through two-point statistics. In this context, we focus on two points that are separated by a distance r within a turbulent flow, noted as $(.)^+$ and $(.)^-$ respectively. The first transport equations of this type were derived by Kármán & Howard (1938) for the two-point velocity correlation $\langle u_i^+ u_i^- \rangle$, and Kolmogorov (1941*a*,*b*) for the velocity increment second-order moment $\langle (\Delta u_i)^2 \rangle$, where $\Delta(.) = (.)^+ - (.)^-$. The passive scalar equivalent of the Kolmogorov equation has been derived by Yaglom (1949), for $\langle (\Delta \phi)^2 \rangle$. We will focus the mathematical aspects of the second-order increment equations, without going into the theoretical aspects of the Kolmogorov theory on the velocity and passive scalar higher-order increments (see Nelkin (1994); Frisch (1995); Sreenivasan & Antonia (1997); Warhaft (2000); Danaila *et al.* (2012*a*); Dubrulle (2019) for those aspects).

Kolmogorov and Yaglom original equations present the very handy property of being scalar equations, containing only a few terms which have a clear physical interpretation. The simplicity of these equations originates from the hypothesis that, when the Reynolds number is large enough, the flow is statistically homogeneous and isotropic. This property motivates the coordinate transformation

$$X_k = \frac{1}{2}(x_k^+ + x_k^-)\,, \quad r_k = x_k^+ - x_k^-, \tag{2.27}$$

$$\text{and} \quad \partial_{X_k} \equiv +\partial_k^+ + \partial_k^-\,, \qquad \partial_{r_k} \equiv \frac{1}{2}(\partial_k^+ - \partial_k^-), \tag{2.28}$$

where r_k is the vector ranging from point $(.)^-$ towards point $(.)^+$, and X_k is the position of the mid-point of this segment. In statistically Homogeneous and Isotropic Turbulence (HIT), the differential operators $\partial_{r_k}\langle . \rangle$ and $\partial_{X_k}\langle . \rangle$ respectively reduce to ∂_r and 0, when applied to statistical quantities. Here, r is the the separation distance between the two points.

Invoking HIT reduces the increment dependencies from 7 variables (r_k^+, X_k^-, t) to only 2 variables (r, t). In addition, if statistical stationnarity is invoked, the structure function depends to the separation distance alone.

Unfortunately, the hypothetical context where the HIT approximation is valid requires Reynolds numbers that are large. In most turbulent flows, the classical Kolmogorov and Yaglom equations are not valid in their homogeneous and isotropic form. Many generalizations of these equations, that account for inhomogeneity and/or anisotropy have been developed (Hill, 2002; Danaila *et al.*, 2004; Gomes-Fernandes *et al.*, 2015). These equations are frequently referred to in the literature as generalized Kármán-Howarth-Monin equations. To avoid confusion, we will speak of generalized Kolmogorov equations for momentum related budgets, and of generalized Yaglom equations for scalar related budgets.

Analytically, the cost of the departure from HIT can be important, regarding the number of terms in the scale-by-scale budget equations, or regarding their physical interpretation. The difficulty in generalizing the Kolmogorov and Yaglom equations is to exploit as much as possible the statistical symmetries of specific canonical flows (horizontally a channel flow (Danaila *et al.*, 2001), spherically in rotating turbulence (Campagne *et al.*, 2014), axisymmetry of a round jet (Danaila *et al.*, 2012*b*) or decay in streamwise direction of grid turbulence (Danaila *et al.*, 1999), for example).

Active scalar flows received very little attention in the two-point framework. In addition to finite Reynolds number effects, active scalars add a source of inhomogeneity and anisotropy. Kolmogorov equation has been generalized to take into account compressibility (Galtier & Banerjee, 2011), magnetohydrodynamics (Politano & Pouquet, 1998), and regarding incompressible mixing, viscosity variations (Danaila *et al.*, 2017), and large density variations by (Lai *et al.*, 2018). The latter authors used a combined Favre-fluctuation/Reynolds-averaging technique to define their momentum increment.

To our knowledge, no variable density generalization of the Yaglom equation has been published in the literature. In this section, we aim at deriving such an equation, and expose the derivation of a new variable density Kolmogorov equation. We will use either the pseudo mass fraction or the density, depending on the calculation step. Next, we briefly describe the analytical derivation of the generalized Kolmogorov and Yaglom equations, for variable density flows.

Variable density Yaglom equation

We will formulate the problem using local and instantaneous fields, without any statistical filtering. The derivation of this equation is straightforward, thanks to the change of variables introducing the pseudo mass fraction into the dynamic equations. The scalar budget (2.25) is simply an advection-diffusion equation. We start by writing this equation at two positions $(.)^+$ and $(.)^-$

Step 0

$$\partial_t\varphi^+ + u_k^+\partial_k^+\varphi^+ = \frac{1}{Pe}\partial_k^{2+}\varphi^+, \tag{2.29}$$

$$\partial_t\varphi^- + u_k^-\partial_k^-\varphi^- = \frac{1}{Pe}\partial_k^{2-}\varphi^-, \tag{2.30}$$

We substract one equation from the other in order to use the definition of the increment. Then we multiply by $2\Delta\varphi$. Also, we split the right-hand-side into a diffusive and a dissipative term. We find

Step 1

$$\partial_t(\Delta\varphi)^2 + [u_k^+\partial_k^+ + u^-\partial_k^-](\Delta\varphi)^2 = \frac{1}{Pe}\Big([\partial_k^{2+} + \partial_k^{2-}](\Delta\varphi)^2 - (\chi_\varphi^+ + \chi_\varphi^-)\Big), \tag{2.31}$$

where $\chi_\varphi^+ = 2(\partial_k^+\varphi^+)^2$ is the pseudo mass fraction dissipation rate at point $(.)^+$. In order to exploit statistical symmetries, we want to include as many terms as possible inside derivatives. Also, we make use of the continuity equation, in the pseudo mass fraction form Equation (2.23). This introduces variable density terms in the equation, as follows

Step 2

$$\begin{aligned}\partial_t(\Delta\varphi)^2 + \partial_k^+[u_k^+(\Delta\varphi)^2] + \partial_k^-[u_k^-(\Delta\varphi)^2] =& \frac{1}{Pe}\Big([\partial_k^{2+} + \partial_k^{2-}](\Delta\varphi)^2 - (\chi_\varphi^+ + \chi_\varphi^-)\Big)\\ &-\frac{a}{Pe}(\Delta\varphi)^2[\partial_k^{2+} + \partial_k^{2-}]\Delta\varphi,\end{aligned} \tag{2.32}$$

Introducing the scale-space transformation, we find

Step 3

$$\boxed{\begin{aligned}&\partial_t(\Delta\varphi)^2 + \partial_{r_k}[(\Delta u_k)(\Delta\varphi)^2] + \partial_{X_k}\Big[\frac{u_k^+ + u_k^-}{2}(\Delta\varphi)^2\Big] =\\ &\qquad\frac{1}{Pe}\Big(2[\partial^2_{r_k} + \frac{1}{4}\partial^2_{X_k}]((\Delta\varphi)^2 - a(\Delta\varphi)^3)\Big) - \frac{1}{Pe}(1 - 3a\Delta\varphi)(\chi_\varphi^+ + \chi_\varphi^-),\end{aligned}} \tag{2.33}$$

Equation (2.33) is the variable density Yaglom equation. Density variations introduce additional terms, which are colored in blue. When $a \to 0$, the classical Yaglom equation for a passive scalar is recovered, because the pseudo mass fraction tends to the passive mass fraction $\varphi \to \phi$ and the blue terms vanish.

Variable density Kolmogorov equation

We write the variable density Navier-Stokes equation (2.7) normalized by density, at two distinct and independent spatial locations in the flow. These two points are considered at the same instant. Analytically, the independence of the two frames writes $\partial_j^+(.)^- = \partial_j^-(.)^+ = 0$. We also make use of continuity (2.6), in order to get the density in or out the temporal and convective terms, simultaneously. The variable density Navier-Stokes equations, written at two separate points $(.)^+$ and $(.)^-$, read

$$\textbf{Step 0}\quad \partial_t u_i^+ + u_k^+\partial_k^+ u_i^+ = -\frac{1}{\rho^+}\partial_i^+ p^+ + \frac{1}{Re}\left(\frac{1}{\rho^+}\partial_k^{2+}u_i^+ + \frac{1}{3}\frac{1}{\rho^+}\partial_{ik}^{2+}u_k^+\right) + Fr^2 g_i \tag{2.34}$$

$$\partial_t u_i^- + u_k^-\partial_k^- u_i^- = -\frac{1}{\rho^-}\partial_i^- p^- + \frac{1}{Re}\left(\frac{1}{\rho^-}\partial_k^{2-}u_i^- + \frac{1}{3}\frac{1}{\rho^-}\partial_{ik}^{2-}u_k^-\right) + Fr^2 g_i, \tag{2.35}$$

We substract Equation (2.35) from Equation (2.34), and use the definition of increments

$$\textbf{Step 1}\quad \partial_t\Delta u_i + [u_k^+\partial_k^+ + u_k^-\partial_k^-]\Delta u_i = -\left[\frac{1}{\rho^+}\partial_i^+ + \frac{1}{\rho^-}\partial_i^-\right]\Delta p + \frac{1}{Re}\left[\frac{1}{\rho^+}\partial_k^{2+} + \frac{1}{\rho^-}\partial_k^{2-}\right]\Delta u_i \\ \frac{1}{3Re}\left[\frac{1}{\rho^+}\partial_{ik}^{2+} + \frac{1}{\rho^-}\partial_{ik}^{2-}\right]\Delta u_k, \tag{2.36}$$

We multiply this equation by the average density $(\Sigma\rho)/2 = (\rho^+ + \rho^-)/2$. After rearranging, we find

$$\textbf{Step 2}\quad \frac{1}{2}\Sigma\rho\,\partial_t\Delta u_i + \frac{1}{2}\Sigma\rho[u_k^+\partial_k^+ + u_k^-\partial_k^-]\Delta u_i = \\ -\frac{1}{2}[\partial_i^+ + \partial_i^-]\Delta p - \frac{1}{2}\left[\frac{\rho^-}{\rho^+}\partial_i^+ + \frac{\rho^+}{\rho^-}\partial_i^-\right]\Delta p \\ \frac{1}{2Re}\left([\partial_k^{2+} + \partial_k^{2-}]\Delta u_i + \left[\frac{\rho^-}{\rho^+}\partial_k^{2+} + \frac{\rho^+}{\rho^-}\partial_k^{2-}\right]\Delta u_i\right) \\ + \frac{1}{6Re}\left([\partial_{ik}^{2+} + \partial_{ik}^{2-}] + \left[\frac{\rho^-}{\rho^+}\partial_{ik}^{2+} + \frac{\rho^+}{\rho^-}\partial_{ik}^{2-}\right]\right)\Delta u_k, \tag{2.37}$$

We colored this equation so that, the black terms are present in the classical equation derivation, and the blue ones are the terms that are due to density variations. At this stage, if density is set to a constant, all blue terms equate their constant density counterpart [3], and the we recover the constant density case at this step of calculation.

---

[3] The last blue term equates zero if the density is constant, as it is only due to the velocity non zero divergence.

As a next step, we multiply the equation by $2\Delta u_i$, and apply the continuity at each point. Notice that $\rho^- u_k^+ \partial_k^+ \Delta u_i \neq \partial_k^+ \rho^- u_k^+ \Delta u_i$. We also make use of the independence of the frames of reference. The temporal and convective terms are

Step 2*

$$\begin{aligned}\frac{1}{2}\Sigma\rho\,\partial_t(\Delta u_i)^2+\frac{1}{2}\Sigma\rho\,[u_k^+\partial_k^+ + u_k^-\partial_k^-](\Delta u_i)^2 = \\ \frac{1}{2}\partial_t[\Sigma\rho\,(\Delta u_i)^2] + \frac{1}{2}\partial_k^+[\Sigma\rho\, u_k^+(\Delta u_i)^2] + \frac{1}{2}\partial_k^-[\Sigma\rho\, u_k^-(\Delta u_i)^2] \\ -\frac{1}{2}(\Delta u_i)^2[\rho^-\partial_k^+ u_k^+ + \rho^+\partial_k^- u_k^-],\end{aligned}\tag{2.38}$$

In order to use the coordinate transformation and the statistical symmetries described in the previous section, as many terms as possible have to be inside derivatives. Applying the scale-space coordinate transformation, we find

Step 3

$$\boxed{\begin{aligned}&\frac{1}{2}\partial_t[\Sigma\rho\,(\Delta u_i)^2] + \frac{1}{2}\partial_{r_k}[\Sigma\rho\,\Delta u_k(\Delta u_i)^2] + \frac{1}{4}\partial_{X_k}[\Sigma\rho\,\Sigma u_k\,(\Delta u_i)^2] = \\ &\quad -\Delta u_i[\partial_i^+ + \partial_i^-]\Delta p - \Delta u_i\left[\frac{\rho^-}{\rho^+}\partial_i^+ + \frac{\rho^+}{\rho^-}\partial_i^-\right]\Delta p \\ &\quad \frac{1}{2Re}\left(2[\partial_{r_k}^2 + \frac{1}{4}\partial_{X_k}^2](\Delta u_i)^2 - (\varepsilon^+ + \varepsilon^-) + 2\Delta u_i\left[\frac{\rho^-}{\rho^+}\partial_k^{2+} + \frac{\rho^+}{\rho^-}\partial_k^{2-}\right]\Delta u_i\right) \\ &\quad -\frac{1}{2}(\Delta u_i)^2[\rho^-\partial_k^+ u_k^+ + \rho^+\partial_k^- u_k^-] \\ &\quad +\frac{1}{3Re}\Delta u_i\left([\partial_{ik}^{2+} + \partial_{ik}^{2-}] + \left[\frac{\rho^-}{\rho^+}\partial_{ik}^{2+} + \frac{\rho^+}{\rho^-}\partial_{ik}^{2-}\right]\right)\Delta u_k,\end{aligned}}\tag{2.39}$$

where $\varepsilon^+ = 2(\partial_k^+ u_i^+)^2$ is the kinetic energy dissipation rate, at point $(.)^+$. Equation (2.39) is a generalization of inhomogeneous and anisotropic Kolmogorov equation to variable density flows. The derivation of Equation (2.39) contains subtle nuances compared to the constant density equation derivation, that we clarify hereinafter.

The variable density Navier-Stokes equation (2.7) is a transport equation for a local momentum ρu_i, and is a consequence of conservation of momentum applied to an infinitesimal fluid parcel. In **Step 0**, this equation is divided by the density, which changes the physical quantity that is described by the equation. Equations (2.34)-(2.35) describe the evolution of an infinitesimal fluid parcel by evaluating its change in volume. This mathematical difference has implications on the physical interpretation of the subsequent calculation steps.

Step 1 consists in using the definition of the increment, which involves a non-local velocity Δu_i. **Step 2** dimensionally results in a momentum quantity, but using the average density leads to a hybrid momentum increment between the points $(.)^+$ and $(.)^-$. This quantity, when distributed, is $\rho^+\partial_t u_i^+ - \rho^-\partial_t u_i^- - \rho^+\partial_t u_i^- + \rho^-\partial_t u_i^+$. The motivation to take such a definition of the increment instead of simply using $\Delta(\rho u_i)$ is related to the shape of the variable density Navier-Stokes equation. The right-hand-side concerns the momentum transport by the velocity, whereas the left-hand-side pressure and viscous terms contain the velocity alone. This feature does not appear in the classical Navier-Stokes equations, as all the terms concern only velocity. If the momentum increment is chosen as $\Delta(\rho u_i)$, we have to make a choice in **Step 3** on whether we multiply the whole equation by $\Delta(\rho u_i)$ or Δu_i. The former is useful for the right-hand-side and makes the treatment of the left-hand-side difficult, and vice-sersa for the latter. Introducing the hybrid momentum $\Sigma\rho\,\Delta u_i/2$ is the best compromise that found between these two choices, to define a kinetic energy $\Sigma\rho\,(\Delta u_i)^2/2$.

Notice that, starting from **Step 1**, buoyancy does not appear explicitly in the velocity increment budget. Equation (2.39) is therefore not suitable for buoyancy driven flows, because the Froude number does not explicitly appear in it[4] In that case, if Boussinesq approximation is not applicable, it is necessary to start from the variable density Navier-Stokes equation, and consider a kinetic energy of the form $(\Delta(\rho u_i))^2$.

Strictly speaking, Equations (2.39) and (2.33) are not generalized Kolmogorov and Yaglom equations. This reference is only made after the application of statistical homogeneity and isotropy, and an integration in scale-space over a sphere. This integration leads to the so-called $-4/3$ law for both Kolmogorov and Yaglom equations (Frisch, 1995), which we do not consider here. As explained in the previous section, shear flows have been observed to break the HIT approximation at low to moderate Reynolds numbers. Density variations in Equation (2.39) are an additional source of inhomogeneity and anisotropy, so the HIT approximation is even more restrictive than in the constant density case. For this reason, we do not apply this hypothesis. In Chapter 4, we will evaluate some terms of both variable density Kolmogorov and Yaglom equations, using our round jet experimental measurements.

---

[4] even if density variations are taken into account in the additional terms.

2.3 Variable viscosity and mass diffusivity flows

In order to span a wide range of active scalar turbulent flows, we complete our study of variable density flows by an investigation of variable viscosity and mass diffusivity flows. We write the set of equations (2.1)-(2.5) for isothermal, constant density ρ^* and variable kinematic viscosity $\nu = \mu/\rho^*$ and diffusion coefficient $\mathcal{D}$. Dimensionless forms of these equations are

$$\partial_k u_k = 0, \tag{2.40}$$

$$\partial_t u_i + u_k \partial_k u_i = -\partial_i p + \frac{1}{Re} \partial_k (\nu(\partial_k u_i + \partial_i u_k)), \tag{2.41}$$

$$\partial_t \phi + u_k \partial_k \phi = \frac{1}{Pe} \partial_k (\mathcal{D} \partial_k \phi), \tag{2.42}$$

$$\nu = f_2(\phi,\mathcal{R}_\nu)\ ; \quad \mathcal{D} = f_4(\phi, \mathcal{R}_\mathcal{D}), \tag{2.43}$$

where $Re = U^* L^*/\nu^*$ and $Pe = U^* L^*/\mathcal{D}^*$ are the Reynolds and Peclet numbers, respectively. The dimensional Navier-Stokes equation (2.2) is multiplied by $L^*/(\rho^* U^{*2})$. The density being constant, it is included as such in the expression of the kinematic viscosity and pressure, respectively. The kinematic viscosity (respectively mass diffusivity) is then normalized by a reference viscosity ν^* (respectively mass diffusivity $\mathcal{D}^*$), which subsequently appears in the Reynolds number (respectively Peclet number).

When density is constant in the general set of equations (2.1)-(2.5), the internal energy (equation (2.3)) and chemical species (equation (2.4)) conservation equations become analogous, as their respective diffusive terms become identical. The set (2.40)-(2.43) is therefore suitable to represent non-isothermal single species mixing, if the state equations (2.43) are chosen accordingly. For consistency with the rest of the study, we will keep using the mass fraction ϕ as an active scalar in this part.

2.3.1 State equations and retained problem

The state equations (2.43) strongly influence the dynamics of variable viscosity/diffusion flows. As for variable density flows (Equation (2.9)), these equations allow to control the coupling between the active scalar and the dynamic fields through the control parameters $\mathcal{R}_\nu$ and $\mathcal{R}_\mathcal{D}$. These parameters allow to recover the constant viscosity and mass diffusivity for $\mathcal{R}_\nu = 1$ and $\mathcal{R}_\mathcal{D} = 1$, respectively.

The influence of the kinematic viscosity on the flow strongly constrasts with that of mass diffusivity. The viscosity allows an interaction of the scalar ϕ with the diffusive term of the Navier-Stokes equation (2.41), whereas mass diffusivity modifies the governing equation of the scalar itself through an anomalous diffusion. In the case $\mathcal{R}_{\mathcal{D}} \neq 1$ and $\mathcal{R}_{\nu} = 1$, the scalar remains passive, independently of the form of the state equation $\mathcal{D} = f_4(\phi, \mathcal{R}_{\mathcal{D}})$.

Many state equations for viscosity have been developed in the literature for very different situations, depending on the type of the chemical substances involved, and on whether the viscosity changes by mixing or temperature variations (Reid *et al.*, 1987). The wide variety of laws that have been developed are either fully empirical, semi-analytical or analytical. For ideal gases, semi-analytical and analytical predictions can be made using the Chapman & Enskog method (Chapman *et al.*, 1990), whereas for liquids, all state equations are empirical. In particular, the *Wilke formula* (Wilke, 1950) is a semi-analytic law that is valid for the mixing of N perfect gases, taking into account their respective mass fractions. This relation reads

$$\mu = \sum_{i=1}^{N} \frac{c_i \mu_i}{\sum_{j=1}^{N} c_k \zeta_{ik}}, \tag{2.44}$$

where

$$\zeta_{ik} = \frac{(1 + (\mu_i/\mu_k)^{1/2}(\mathcal{M}_k/\mathcal{M}_i)^{1/4})^2}{(8(1 + \mathcal{M}_i/\mathcal{M}_k))^{1/2}} \tag{2.45}$$

and ν_i, c_i and $\mathcal{M}_i$ are the kinematic viscosity, molar fraction and molar mass of species i, respectively. The Wilke law (2.44) offers a very good precision over a large thermodynamic variables values.

In a single species, when temperature increases, the dynamic viscosity of liquids decreases whereas the dynamic viscosity of gases increases. Special care is be to be taken depending on the chemical species considered. For perfect gases, the usual method is the Sutherland law (Sutherland, 1893), whereas for liquids, a Nahme-type temperature is generally considered (Nahme, 1940). The Nahme-type relationship reads

$$\mu = \mu_0 e^{-\beta \frac{(T - T^*)}{T^*}}, \tag{2.46}$$

where superscript $(.)^*$ denotes reference quantities and β is a positive dimensionless number that depends on the liquid chemical composition.

Mass diffusivity can also vary a lot from one species to the other. When the species are dilute, the diffusion coefficient is independent of the mass fraction ϕ. On the contrary, if the species are very concentrated, anomalous diffusion can be observed, especially in non-ideal fluids and liquids (Cussler, 2009). Various laws exist for predicting mass diffusivities of mixtures. In particular, Vignes (1966) empirically suggested that the binary diffusion coefficient varies exponentially with the mass fraction of non-ideal solutions, with very good experimental agreement. This relation reads

$$\mathcal{D} = \mathcal{D}_1^{\phi}\mathcal{D}_2^{1-\phi} \Rightarrow \frac{\mathcal{D}}{\mathcal{D}_2} = \mathcal{R}_{\mathcal{D}}^{\phi} \quad \text{where} \quad \mathcal{R}_{\mathcal{D}} = \frac{\mathcal{D}_1}{\mathcal{D}_2}. \tag{2.47}$$

The choice of these state equations (2.43) remains an open degree of freedom for the problem (2.40)-(2.43), that could consistently affect the dynamics of the flow. As we saw in section 1.3.3, Wall & Wilson (1996, 1997) showed that the state equation can have a strong effect on the linear stability properties plane Couette and flat-plate Boundary layers. This result suggests that there can be a persistent effect of this parameter on the fully nonlinear dynamics of shear flows.

Regarding anomalous diffusion, Straughan (2007) investigated convection with a temperature dependent heat conductivity. This author found that the linear stability, together with the weakly nonlinear dynamics of such a flow is very affected by the nonlinearity of the considered state equation for heat conductivity.

In order to reduce the complexity of the problem, we make the choice of equating both state equations, with a Vignes like relation (2.47). The final set of equations that we will consider in Chapter 5 is as follows

$$\boxed{\begin{aligned} \partial_k u_k &= 0, && (2.48)\\ \partial_t u_i + u_k \partial_k u_i &= -\partial_i p + \frac{1}{Re}\partial_k(\psi(\partial_k u_i + \partial_i u_k)), && (2.49)\\ \partial_t \phi + u_k \partial_k \phi &= \frac{1}{Pe}\partial_k(\psi \partial_k \phi), && (2.50)\\ \psi &= \mathcal{R}_{\psi}^{\phi-1}, && (2.51) \end{aligned}}$$

where, for the sake of lightness, ψ represents both the kinematic viscosity and mass diffusivity and $\mathcal{R}_{\psi}$ is the control parameter for the magnitude of ψ variations.

2.3.2 Scalar gradient magnitude transport equation

In active scalar flows, the velocity field is affected by the scalar through a feedback mechanism. The velocity and scalar gradients therefore interact nonlinearly. At the vicinity of the TNTI, this interaction is particularly intense, as we exposed in Section 1.2.2. To this regard, we derive a transport equation for the magnitude of the scalar gradient vector $g^2 = g_n^2$, with variable mass diffusivity. We start by applying the gradient scalar transport equation with variable diffusivity (2.51)

$$\partial_t g_n + u_k \partial_k g_n + g_k \partial_n u_k = \frac{1}{Pe}\Big[\psi \partial_k^2 g_n + \partial_n \psi \partial_k g_k + \partial_n (g_k \partial_k \psi)\Big] \tag{2.52}$$

We then perform a scalar product of this equation with $2g_n$ and find

$$\partial_t g^2 + u_k \partial_k g^2 + 2 g_n g_k \partial_n u_k = \frac{2}{Pe}\Big(\psi g_n \partial_k^2 g_n + g_n \partial_n \psi \partial_k g_k + g_n \partial_n (g_k \partial_k \psi)\Big) \tag{2.53}$$

Then, we split the usual diffusive term using the classical diffusion-dissipation form, and make use of the chain rule on the diffusivity gradients, through $\partial_k \psi = \frac{df}{d\phi} g_k = \log \mathcal{R}\, \psi\, g_k$. We find after rearranging

$$\boxed{\begin{aligned} \underbrace{\partial_t g^2}_{\text{temporal}} + \underbrace{u_k \partial_k g^2}_{\text{advection}} + \underbrace{2 g_n g_k \partial_n u_k}_{\text{strain}} = \frac{1}{Pe}\Big[\underbrace{\psi \partial_k^2 g^2}_{\text{diffusion}} - \underbrace{2\psi (\partial_k g_n)^2}_{\text{dissipation}}\Big] \\ + \frac{2}{Pe} \log \mathcal{R} \psi \Big[\underbrace{g^2 \partial_k g_k}_{\text{accretion}} + \underbrace{g_k \partial_k g^2}_{\text{drift}} + \underbrace{\log \mathcal{R} (g^2)^2}_{\text{variable diffusivity dissipation}}\Big] \end{aligned}} \tag{2.54}$$

In Equation (2.54), the temporal term represents the local variation of the gradient magnitude through time, whereas the advection term is a transport of this quantity by the velocity field. The strain term is the production by which the velocity gradients stretch the scalar locally, and amplify the scalar gradients. This term is responsible for the large magnitude of the scalar gradients at the vicinity of the TNTI. The right-hand-side of Equation (2.54) contains terms that are related only to the diffusivity gradients, on the second line of this equation. We interpret these terms as follows from left to right, an accretion, because this term depends on the divergence of the scalar gradient, a drift, because the scalar gradient transports itself, a variable diffusivity dissipation. We will evaluate these terms in Chapter 5, in the vicinity of the TNTI in a variable diffusivity jet.

2.4 Conclusion

The purpose of this chapter was to settle theoretical grounds for the flow configurations of interest. We described a general set of equations that is valid for the incompressible turbulent mixing of two active scalars, namely the temperature and mass fraction in a binary substance. These two active scalars can be coupled with the dynamics through four thermo-physical properties, under certain conditions that we exposed. We limited ourselves in this study to flows with a single active scalar, choosing mass fraction. Then, we derived two particular problems, namely the non-Boussinesq variable density case, and the variable viscosity and mass diffusivity case.

In the non-Boussinesq variable density case, we discussed the relevance of acoustic waves and their role when large density variations occur in an incompressible flow. Then, we derived a natural change of variables for the case of binary chemical species mixing, and found a simplification for the isochoric configuration. We discussed the statistical averaging of this type of flows, with the particularity that many arbitrary choices can be made for the definition of statistical quantities. Finally, we chose a specific form for two-point statistics, and derived generalizations for the Kolmogorov and Yaglom equations, for flows with large density variations.

In the variable viscosity and mass diffusivity case, we discussed the wide variety of state equations that have been developed in the literature for both viscosity and mass diffusivity. We made a particular choice of equating both these quantities in order to reduce the degrees of freedom of the problem. Finally, we focused on the scalar gradients, deriving a transport equation for the magnitude of the mass fraction gradient vector.

Chapter 3

Experimental measurements in a variable density round jet

In this chapter, we describe the flow configuration that we experimentally investigated in this thesis. Then, the complete experimental design is exposed, showing the constraints and their consequences on the retained setup. The experimental techniques consist in simultaneous measurements of velocity and scalar fields, in the very-near field of the variable density round jet. We elaborate a shot-to-shot calibration procedure for the scalar measurements. Finally, we decribe a validation of these techniques, for different considered parameters.

3.1 Design of the experiment

3.1.1 Objectives and constraints

Fluid constraints

The aim is to measure the velocity and scalar fields in an isothermal variable density round turbulent jet, surrounded by a co-flow, for which equations (2.23)-(2.25) are valid. We choose to mix two different chemical substances injected at the same temperature. The constrains on these substances are

1. Densities as different as possible and dynamic viscosities and mass diffusivities as close as possible.

2. Optical measurement techniques are used, therefore the refractive indices of the two substances have to be very nearly equal. For the same reason, non reactivity to optical illumination, especially with ultra-violet light is required.
3. Neither toxic nor greenhouse gases should be involved.
4. Low prize and availability in large amounts.

In order to satisfy the requirement of chemical non-reactivity, we focused on rare gases together with Air. We found that Helium is a good candidate, with a Helium to Air density ratio of $\mathcal{R}_\rho = 1/7$. Another possibility was Xenon, with a density ratio of $\mathcal{R}_\rho = 5$, but Xenon is very hard to be produced, and is therefore $\sim$ 4000 times more expensive than Helium.

The dynamic viscosity ratio between Helium and Air is $\mathcal{R}_\mu = 0.93$. Because Air is not a pure substance, we ensured that there is no differential diffusion of Helium into the different components of Air. To do so, we used the Champman-Enskog formula for binary mixing of perfect gases (Reid *et al.*, 1987). We found that the ratio of the binary diffusion coefficients of Helium with Oxygen and Helium with Nitrogen is $\mathcal{R}_\mathcal{D} = \mathcal{D}_{He-O_2}/\mathcal{D}_{He-N_2} = 1.06$.

The refractive index of Helium and Air are both close up to 10^{-4} to 1, which guarantees the use of optical measurement techniques through a medium composed of a mixture of these species. The toxicity of Helium is nonexistent when inhaled in small amounts. All these arguments motivate our choice of employing Helium-Air mixtures injected into Air to perform our experiments.

Flow constraints

As shown in Chapter 1, a large number of parameters may influence the dynamics of a round jet. Moreover, most studies in the literature focus on a limited number of points in their flow parameters. The flow constraints to be achieved are

1. The have a large variability in the Reynolds and Archimedes numbers.
2. To control density variations as precisely as possible.
3. To respect dynamic incompressiblity $Ma \leq 0.2$.
4. To avoid confinement effect, by adjusting the co-flow velocity.
5. Getting a good compromise between large and small scales, for the velocity measurements.

3.1.2 Experimental device

The experimental set-up is sketched in Figure 3.1. The injector is a pipe of $D_j = 10$ mm inner diameter and 12 mm outer diameter, which ensures no effect from the nozzle lip boundary layer. The pipe is 120 D_j long so the velocity profile is a Laufer's profile in all flow conditions (Laufer, 1954). The jet pipe is set in a 800 mm duct, where co-flowing air is injected from below through 18 pipes of 2 inches diameter. Co-flow turbulent fluctuations are damped upstream the jet nozzle, using iron fillings together with multiple grids.

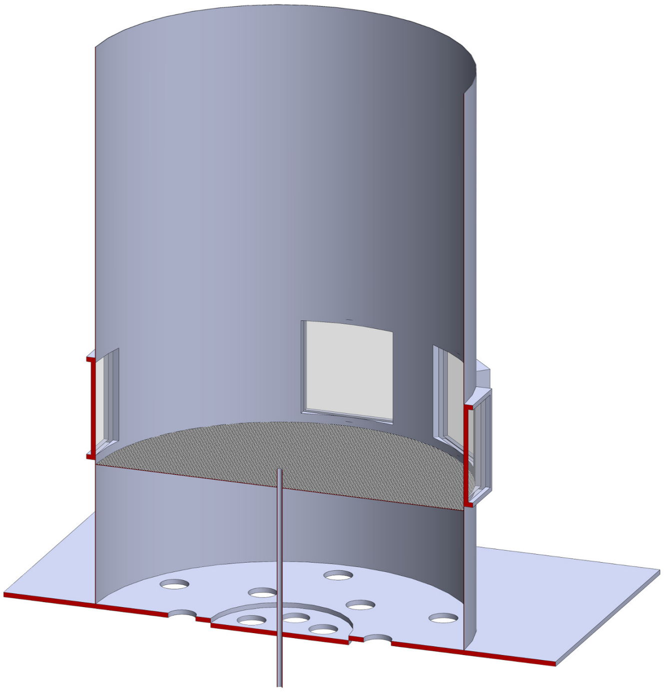

Figure 3.1: Sketch of the experimental set-up.

The jet is composed of pure air, pure helium, seeded air for velocity measurements and seeded air for mass fraction measurements. Each of these fluids are separately controlled through *Bronkorst* mass flow meters. The Helium mass flow rates span a very wide range, so we used separate mass flow meters for the Boussinesq and non-Boussinesq regimes, respectively. The jet content was homogenized in a small cylindrical mixing box. The co-flow mass flow rate was controlled though a static pressure measurement with a *Kimo Instruments CP114* manometer. The flow was regulated by six mass flow meters.

For the different air components of the jet, we used the air supply network of our laboratory facility. The jet Helium was derived from bottles. We used a turbine to inject the experiment room air into the co-flow. The heat losses inside the co-flow routing were so large, that the turbine Joule effect warmed up the co-flow up to 43° at the largest co-flow mass flow rates. The facility air was generally at a temperature of 17°. To avoid this temperature difference, both the jet and the co-flow were heated up at a fixed temperature of 50°C for all experimental measurements. The seeded air for mass concentration measurements is highly flammable (see section 3.2.2). For safety reasons, we choose to warm the pure air part of the jet before it enters the mixing box, with a suitable temperature threshold at the box entrance. All jet and co-flow pipes are insulated to avoid thermal losses. Figure 3.2 sketches the gases routing, together with the location of heating and seeding systems.

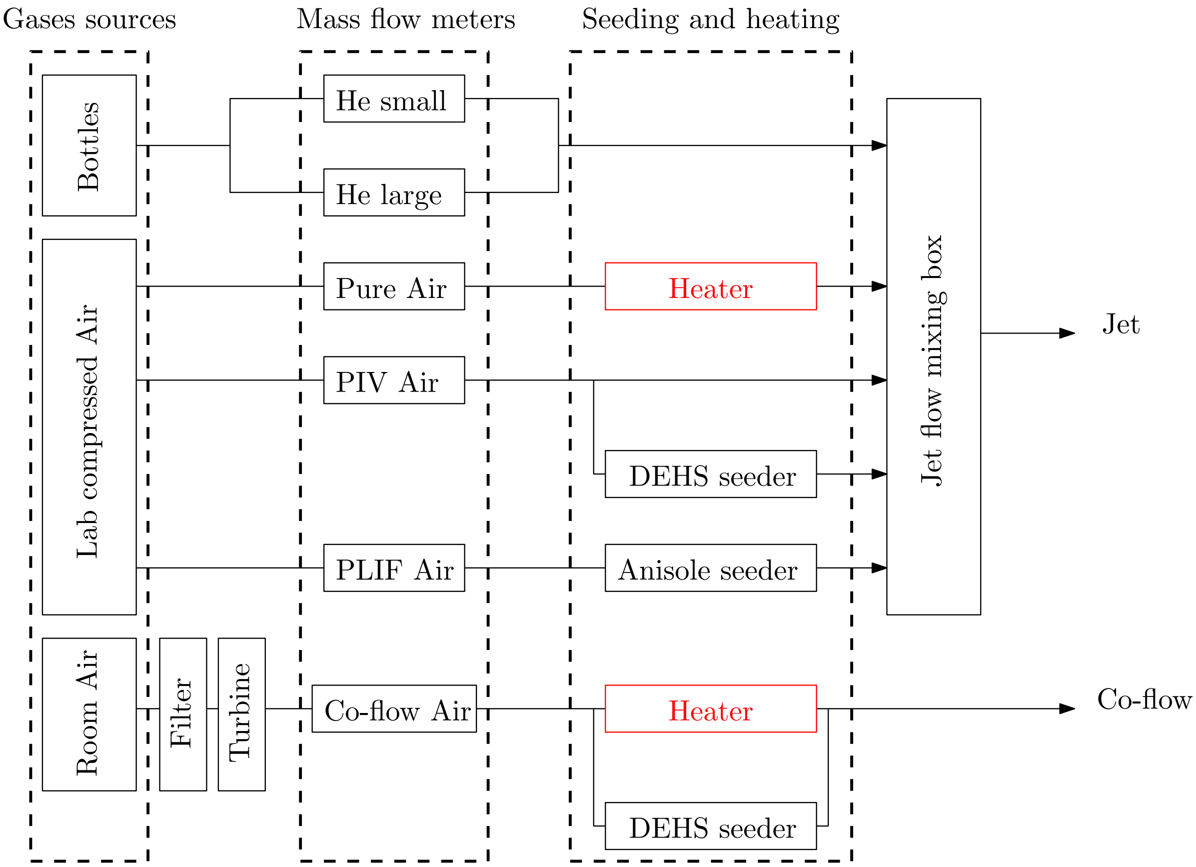

Figure 3.2: Sketch of the gas routing, heating and seeding systems.

3.1.3 Flow conditions

Table 3.1 summarises the definitions of the dimensionless numbers involved in our study. The Reynolds number controls momentum, whereas the Archimedes number controls density variations. The confinement effects are avoided by adjusting the co-flow velocity. In the literature, it is well known that a confined variable density jet behaves like a free jet when $Ct_{\mathrm{ni}} \in [0.67, 0.8]$ (Pitts, 1986; Amielh *et al.*, 1996). We choose the value of $\mathrm{Ct}_{\mathrm{ni}} = 0.7$.

Re	Ar	At	Fr	$\mathcal{R}_\rho$	a	Ma
$\frac{\rho_j(u_j-u_c)D_j}{\mu_j}$	$\frac{g\rho_j D_j^3(\rho_c-\rho_j)}{\mu_j^2}$	$\frac{\rho_c-\rho_j}{\rho_c+\rho_j}$	$\frac{gD_j(\rho_c-\rho_j)}{\rho_j(u_j-u_c)^2}$	$\frac{\rho_j}{\rho_c}$	$\frac{\rho_c-\rho_j}{\rho_j}$	$\frac{u_j}{a_0}$

Table 3.1: Definition of various dimensionless numbers pertaining to the jet experiment. The non-isothermal Craya-Curtet number definition is provided by Equation (1.4).

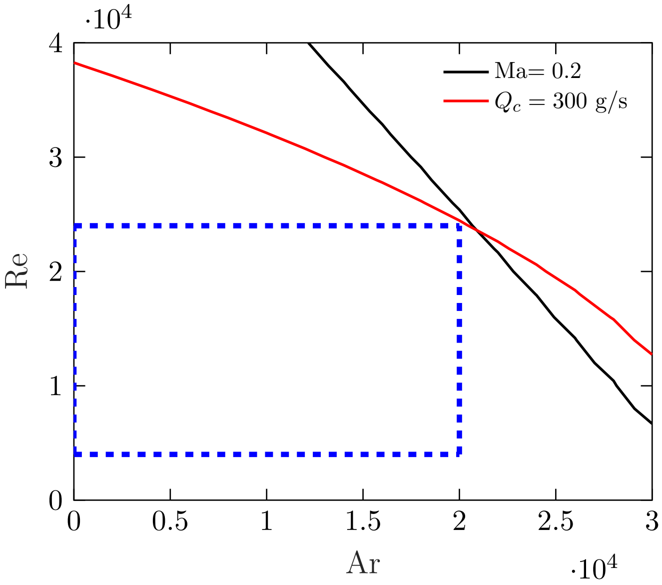

Figure 3.3: Retained parameter space in the (Re, Ar) plane, represented by a blue dashed rectangle.

The determination of the dimensional quantities (u_j, u_c, ρ_j) for a particular triplet of the dimensionless numbers (Re, Ar, Ct_{ni}) requires the resolution of a nonlinear set of equations. We used a Newton-Raphson method to solve this problem (see Appendix A for details on the resolution).

The major constraints for the design of our experimental facility are the mass flow rate of the co-flow, limited to $Q_c = 300$ g/s, and the jet injection Mach number $Ma \leq 0.2$. The dynamic incompressiblity condition is limited by the co-flowing Air, because the speed of sound in air is lower than in Helium-Air mixtures. Figure 3.3 illustrates iso-lines of Mach number $Ma = 0.2$ and co-flow mass flow rate $Q_c = 300$ g/s in a (Re, Ar) diagram, with $Ct_{ni} = 0.7$. We chose the dashed blue rectangle for our measurement campaigns. The measurement conditions span from $Re = 4000$ to 24000, with a step of 4000, and from $Ar = 0$ to 20000 with a step of 5000. The choice of the Archimedes number for variable density effects allows to evaluate all density effects with the single knowledge of this number. We consider the case $Ar = 5000$ as a Boussinesq regime, and higher value of this number as non-Boussinesq regime. Tables 3.2 and 3.3 summarise all the flow conditions that we considered.

Ar	At	$\mathcal{R}_\rho$	a	φ_j
0	0	1	0	1
5000	0.08	0.851	0.175	0.9215
10000	0.175	0.702	0.4245	0.8335
15000	0.288	0.553	0.808	0.7329
20000	0.425	0.404	1.475	0.6144

Table 3.2: Archimedes number variations of some relevant dimensionless quantities.

Ar \ Re	4000	8000	12000	16000	20000	24000
0	0.0590	0.1181	0.1771	0.2361	0.2951	0.3542
5000	0.0639	0.1279	0.1918	0.2558	0.3197	0.3836
10000	0.0703	0.1407	0.2110	0.2813	0.3516	0.4220
15000	0.0791	0.1582	0.2374	0.3165	0.3956	0.4747
20000	0.0924	0.1847	0.2771	0.3694	0.4618	0.5542

Table 3.3: Co-flow velocity (m/s) variation with both Reynolds and Archimedes numbers.

3.2 Experimental techniques

With the appearance of lasers in the 1960's, and the development of computational capabilities in the late 1990's, new measurement techniques emerged in fluid mechanics. Regarding our experiment, we are interested in simultaneous measurements of both velocity and scalar fields. These fields are non-linearly coupled in two-ways. The velocity fields was measured using Stereoscopic-Particle Image Velocimetry (stereo-PIV), and the scalar field was measured by a Planar Laser Induced Fluorescence (PLIF) technique. This section closely followed the Handbook Tropea & Yarin (2007).

3.2.1 Stereoscopic-Particle Image Velocimetry

3.2.1.1 General principle of PIV

This technique consists of the pattern tracking formed by a large number of particles diven into a fluid flow. We need these particles to follow as accurately as possible the trajectory of the fluid that surrounds them. Assuming a spherical shape for the particles and Stokes regime for the flow in their neighborhood, it is possible to predict the time response of the particles to acceleration caused by the fluid motion. The characteristic response time-scale of the particle can than be compared to the smallest fluid time-scale, through the Stokes number, as follows

$$St = \frac{1}{18}\frac{D_p^2(\rho_p - \rho)}{\mu\,\tau_\eta} \tag{3.1}$$

where τ_η, μ, ρ, D_p and ρ_p refer to the Kolmogorov time-scale, the dynamic viscosity and density of the fluid, and the particle diameter and density, respectively. A small Stokes number guarantees a very short response time of the particle. For PIV, the usual values for the Stokes number should be $\mathrm{St} < 0.1$.

The particles can either be liquid or solid. For gas flows, it is customary to employ liquid droplets, when possible. Assuming that $\rho_p \sim 10^3$ kg/m^3, $\mu \sim 10^{-5}$ Pa.s and $\tau_\eta \sim 10^{-5}$ s, one finds that the diameter has to be of the order $D_p \sim 10^{-6}$ m. In practice, we generate droplets of diameter $D_p \sim 5$ µm, using an atomizer. Numerous atomized designs have been developed in the literature.

The light scattered form spherical objects depends on numerous parameters, including the ratio of refractive indices of the gas and the object, the angle between the observer and the incident light, and the Mie parameter M, which is defined as

$$M = \frac{\pi D_p}{\lambda} \tag{3.2}$$

where λ is the wavelength of the monochromatic incident light. The scattered light intensity is a strong function of the Mie parameter M. Particles of the order of the micron in diameter scatter very little light. In order to observe the droplets in PIV for gaseous flows, it is necessary to illuminate them using an intense and brief light source. The development of lasers unlocked this problem. The droplets are generally illuminated using a thin laser sheet, and observed using a Charge Couple Device (CCD) camera.

PIV uses two images of the distribution of particles within a light sheet that illuminates a flow. These two images are separated by a controllable time interval. Then, both images are split on a grid, where each node of the grid is analysed on an interrogation window of a few pixels wide. An algorithm evaluates the most probable displacement of each node within, in order to map the pattern from the first frame onto the second. Finally, evaluating the velocity on a node consists in dividing the most probable displacement by the time interval between the two images.

3.2.1.2 Application to our experimental device

Particle Image Velocimetry, as described above, allows measuring two components of the velocity vector, as projected on the laser sheet. This technique is referred to as 2-dimensional 2-component PIV (2D2C). Stereoscopic-Particle Image Velocimetry (2D3C) consists in measuring the velocity on the laser sheet simultaneously at two angles of view. This measurement is possible using the Scheimpflug principle. In the stereo-PIV configuration, the 2D2C procedure is applied on each camera individually. The projection plane of the resulting vector fields is different. Therefore, it is possible to build the three dimensional velocity vector by a projection.

In our experiment, we used two *LaVision* Imager Pro X cameras, each of them is positioned apart from the Laser sheet at an angle of 45°. Two object lenses of type *Nikkor*

105$f/2.8$ were used, which allowed to observe a field of view of 60x60 mm^2. The field of view of each camera projected onto the laser sheet results in a trapezium, that we centered at the injection nozzle. We used Di-Etylhexyl-Sebacate (DEHS) oil as seeding for both jet and co-flow. This substance is commonly used in non-reactive gaseous flows, as it forms a very large amount of droplets of $D_p \sim 5$ µm. We used an in-house atomizer of the Laskin type (Echols & Young, 1963). The Laser pulses were generated using a *Quantel* Twin CFR200 laser, emitting at a wavelength of 532 nm and with an average energy of 150 mJ/shot. The Laser sheet was created using successively a cylindrical lens with focal length -40mm, then a spherical lens with focal length of 500 mm. We made sure that the Laser sheet is the thinnest at the measurement field of view.

As shown in Figure 3.4, we checked that the injection velocity profile is weakly dependent on the Reynolds and Archimedes numbers. We also plot the classical Laufer's fully developed turbulent pipe flow profile. The agreement is good, considering that we start measuring at $x/D_j = 0.5$[1]. We consider that the pipe is long enough to neglect the establishment length effects.

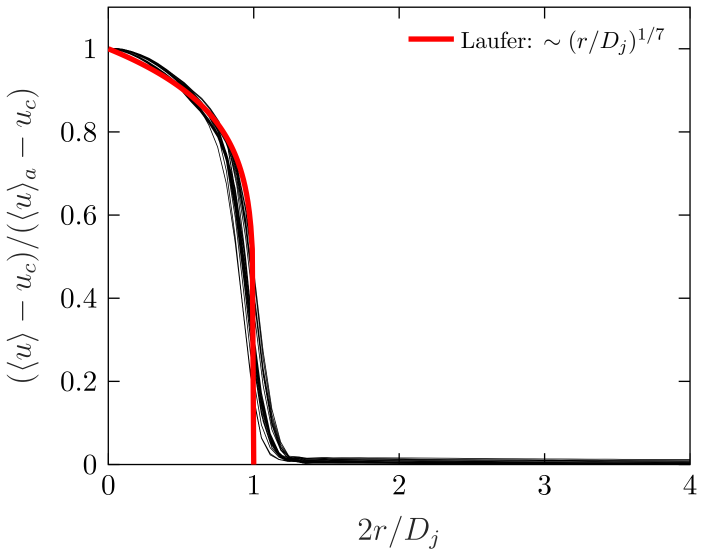

Figure 3.4: Radial variation of the mean axial velocity at $x/D_j = 0.5$, for all measured cases (black), and Laufer's fully developed pipe flow profile (red).

---

[1] Comparing with (Amielh *et al.*, 1996, Figure 7.a), we would need to measure at $x/D_j = 0.2$ to have a better collapse.

3.2.1.3 Stereo-PIV calibration procedure

The acquisition and processing of the data was performed using *LaVision* Davis 6. The calibration procedure for stereo-PIV consists in using a pre-designed *LaVision* 3D-target, that is placed parallel to the laser sheet. This target contains multiple planes and the markers on each side are asymmetric. Davis is implemented to distinguish each side of the Laser sheet through a few reference images. Then we computed, for each camera individually, a mapping of the field of view onto the measurement plane.

When superimposing the two trapezoids on the measurement field, small misalignments are very likely to appear. Reference flow images are used to correct these misalignments of the two cameras through a self-calibration. This step is necessary for the precise re-projection of the separate 2D2C measurements onto 2D3C fields. Self-calibration was performed after the measurements, to ensure the faithfulness of the calibration to the measurement conditions.

The time delay between the two laser pulses depends on the injection velocity of the jet u_j and on the size of the interrogation window that we use for processing. In our case, we mainly used 24×24 square interrogation windows, and adapted the time delay between the 532nm laser shots to have an average displacement of 4 pixels at the injection.

3.2.2 Planar Laser Induced Fluorescence

3.2.2.1 General principle of PLIF

Fluorescence consists in the absorption of a photon by a chemical substance, which is quickly followed by the emission of a photon at a different wavelength. Planar Laser Induced Fluorescence is fluorescence stimulated by a laser sheet. The classical scenario for PLIF is a two levels model, which is sketched in Figure 3.5.

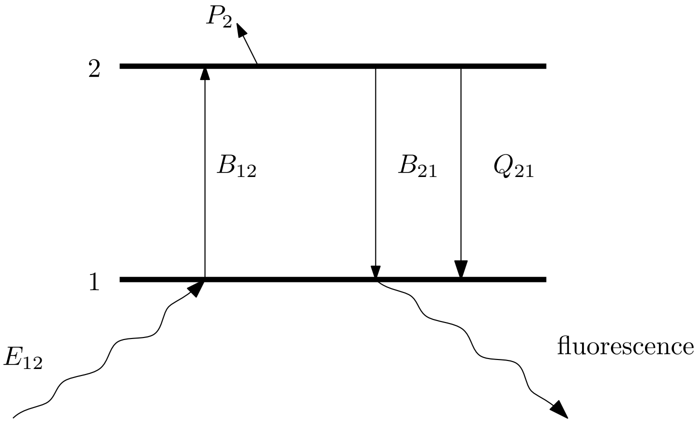

Figure 3.5: Laser Induced Fluorescence two levels model.

Level 1 is a non-excited state, and level 2 is electronically excited. If the incident photon has the right energy E_{12}, the $1 \rightarrow 2$ transition has a certain probability of occurrence, represented by the Einstein coefficient B_{12}. In the excited state, the molecule can be altered, through ionization or photo-dissociation. Both these events are summed up and represented by probability P_2. The $1 \rightarrow 2$ transition is evaluated by a pure electronic excitation in this model.

The backwards transition $2 \rightarrow 1$ occurs with a probability B_{21}, and is accompanied by an energy transfer to vibrational energy levels of the molecule, which explains the Stokes shift of the emitted photon compared to the absorbed one. A wide shift is particularly desirable for optical measurements. Fluorescence can generally be inhibited by quenching, that is a loss of energy through the collision with another molecule and is represented by Q_{21} in figure 3.5. The collision molecule can be a different chemical species.

In the limit of low laser intensity, pre-dissociation can be neglected. The fluorescence intensity is then modeled by

$$S_{LIF} = cB_{12}E_{12}f(P,T)N(P,T)\sigma \tag{3.3}$$

where c, $f(P,T)$, $N(P,T)$ and σ are a setup-dependent constant, the Boltzmann distribution function for the population of level 1, the number density of the molecules in the measurement region and the quantum yield, respectively. After some hypotheses, it is reasonable to evaluate the quantum yield as $\sigma = \frac{B_{21}}{B_{21}+Q_{21}}$.

Equation (3.3) shows that the fluorescence response to weak laser light is linear. If the laser light is intense, pre-dissociation cannot be neglected anymore, and the fluorescence response is non-linear and reaches a plateau. The laser energy limit between the linear regime and the plateau depends on many parameters and is to be determined experimentally. In order to maximize the precision of the concentration field measurement, it is preferable to maintain all measurements within the linear regime of the PLIF.

The choice of the target molecule is very case-specific, and requires a lot of attention. Each molecule has its advantages and disadvantages in terms of quantum yield, quenching with some present molecules in the flow, thermo-physical properties, spectra of absorption and emission and toxicity.

The advantage of PLIF is its large cross section for many chemical substances, which yields to large signal-to-noise ratios (SNR). Nevertheless, PLIF does not allow for precise quantitative measurements, even in non-reacting flows. In many cases, it is necessary to apply multiple successive corrections to the external variations of the signal.

3.2.2.2 Application to our experimental device, choice of the seeding

In order to select a suitable seeding substance for our PLIF, we compared different seeding candidates at 50°C, and summarize the results in table 3.4.

Gas	σ	λ_{abs} (nm)	λ_{fluo} (nm)	ρ/ρ_{Air}	P_{sat} at 25°C (mbar)	Note	Source
Acetone	0.2%	250 – 320	350 – 550	2	306	Poor SNR	Lozano *et al.* (1992)
3-pentanone	0.08%	220 – 320	350 – 550	3	49	Slightly toxic	Schulz & Sick (2005)
Toluene	17%	220 – 290	270 – 370	3.14	37	Toxic Quenches with 0_2	Schulz & Sick (2005)
Anisole	29%	240 – 280	270 – 350	3.72	4	Quenches with O_2	Berlman (2012)

Table 3.4: Comparison of some properties at 50°C of seeding substances for PLIF.

From Table 3.4, we notice that multiple substances are suitable candidates for seeding our PLIF. As we are interested in variable density flows, it is preferable to modify the jet density as slightly as possible. The most common substance for non-reacting gaseous flows is Acetone (Lozano *et al.*, 1992). Acetone and 3-pentanone have very small quantum yields. Obtaining reasonable SNR with these substances requires large seeding mass flow rates. The use of Acetone and 3-pentanone in our experiment highly alters the density of the jet, so these should be avoided in our case. Contrariwise, the quantum yield of Anisole and Toluene are two orders of magnitude larger. Very low mass flow rates of these substances are required to obtain very satisfactory SNR. Toluene fluorescence is very sensitive to quenching with oxygen. This feature might alter the fluorescence signal in our experiment because we use Helium/Air mixtures injected into co-flowing Air. The oxygen mass fraction slightly varies between the jet core and the co-flow. Anisole also quenches with oxygen, but to a much smaller extent. We consequently chose Anisole in our experiment.

The drawback of Anisole is its narrow spectral overlap. Careful optical filtering should be done to isolate the fluorescence signal from the laser radiation. Pasquier-Guilbert (2004) developed a liquid optical filter, composed of a volume of 5% toluene and 95% iso-octane. This liquid filter is a very sharp low-pass filter with a cutoff scale of 270 nm. This method allows to absorb the laser radiation and collect only the fluorescence signal. Moreover, this optical filter is also suitable to absorb the Mie scatter UV light from the DEHS droplets that we simultaneously used for stereo-PIV measurements.

The PLIF signal was collected using a *Princeton Instruments* PIMAX4 EM intensified CCD camera, with a *Sodern* UV $100f/28$ objective . The images are 1024×1024 matrices encoded in 16 bits. On this camera, the maximum intensification gain is 10000. The behavior of the sensor can be non-linear at high gains, and the SNR decreases when increasing the value of the gain. We will discuss this aspect in section 3.2.2.4. The Anisole molecules were illuminated using a *Quantel* QSmart 850 laser, emitting at 266nm with a maximum energy of 100mJ. The UV beam was merged with the PIV 532nm beam using a dichroic lens. The adjustment of the cylindrical and spherical lenses for the generation of the bi-chromatic sheet was conditioned by the parallelism of the UV sheet, because the PLIF signal requires a homogeneous illumination of Anisole.

3.2.2.3 Shot-to-shot correction

PLIF intensity is strongly dependent on the laser energy variations. We developed a method to correct both laser inhomogeneities in the intensity profile and global energy differences from one shot to another. We used the ex-situ method developed by Voivenel (2016) and adapted it to our experimental conditions. The method consists in splitting the UV laser sheet into a Rhodamine B cuvette that is observed by another *Princeton Instruments* PIMAX4 camera. Rhodamine is diluted into ethanol at a very low mass concentration. This substance has the property of being fluorescent to 266nm excitation but photolyses after some exposition time. The cuvette is fed by a re-circulation loop, to renew the Rhodamine inside it constantly.

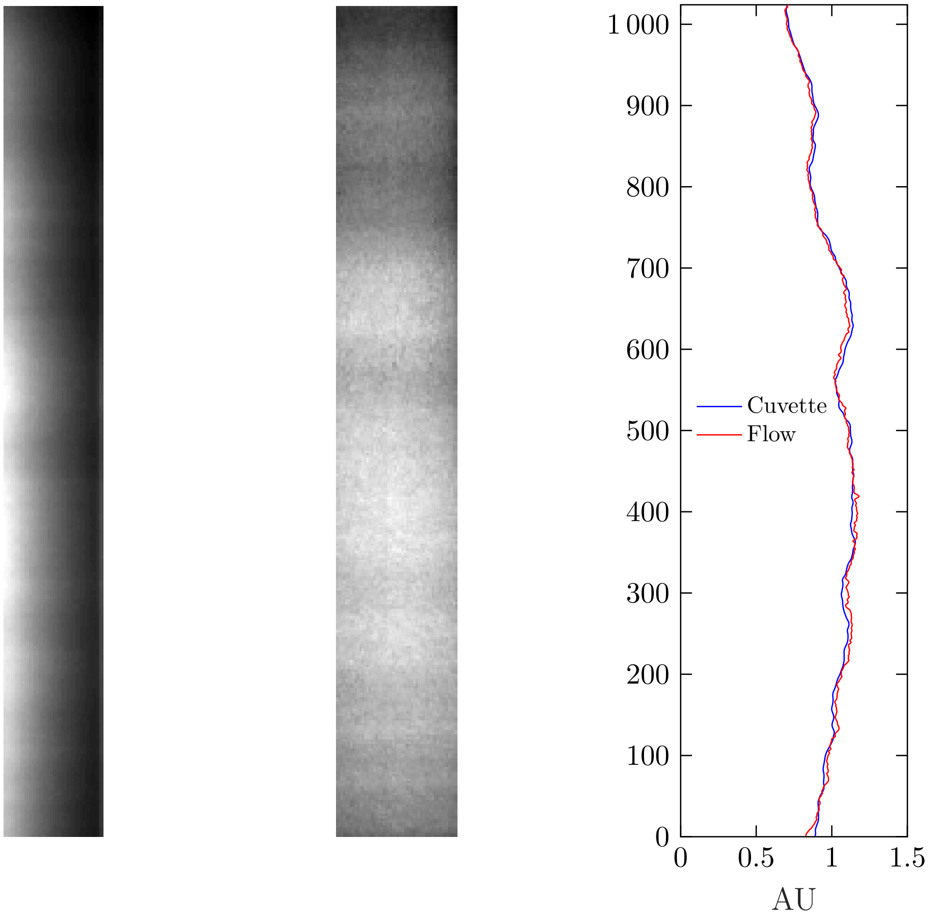

Figure 3.6: Cuvette image (left); laminar jet image (center); aligned intensity profiles (right).

Fig 3.6(left) shows a cuvette fluorescence images. The vertical inhomogeneities are uniquely due to the laser sheet spatial inhomogeneities. We use, at each laser shot individually, a cuvette reference image to correct the raw PLIF images. In order to center the cuvette image on the flow image, we use 100 images of a laminar jet, issuing at Re= 200 (figure 3.6(center)). We wrote a *Matlab* code that establishes the correspondence between the cuvette and the laminar jet images. The algorithm consists in a research of the best alignment of the cuvette image onto the laminar jet image in order to superimpose the intensity profiles (figure 3.6(right)). The best alignment is detected by a least-mean-squared method. When the images are centered, it is straightforward to horizontally normalize the turbulent jet PLIF images.

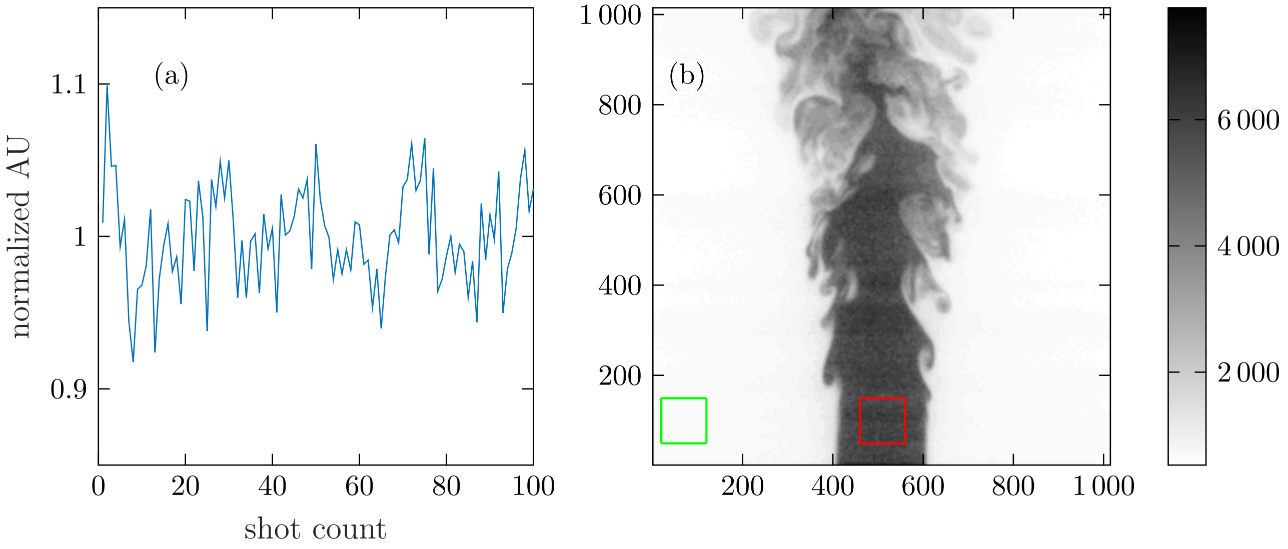

Figure 3.7: Shot-to-shot variations of laser global energy (a) and a typical turbulent jet image (b). The red and green squares are the potential core and background references, respectively.

Figure 3.7(a) shows the evolution of the laser total energy over 100 shots. This variation is random and internal to the laser. In order to correct this uncertainty, we apply another correction to the raw images. We observe that the laser energy oscillates around a steady state intensity level. We use the PLIF images directly, by measuring the intensity of a small square inside the potential core (red square in figure 3.7(b). In this region, the jet concentration is always identically 1, so we can take it as a measure of the Anisole full response to the laser intensity. We also consider a background measurement through as square in the black region of the PLIF images (green square in figure 3.7(b)).

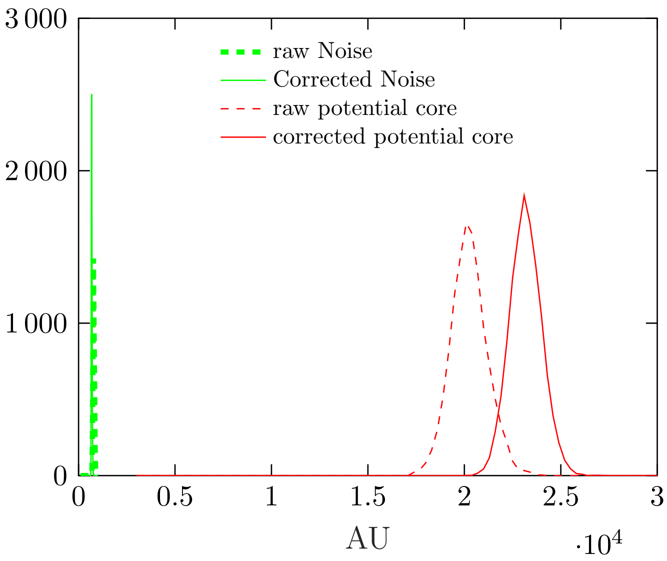

Figure 3.8: Intensity response with and without corrections in the background and in the potential core.

In figure 3.7, we select the green square in the dark to evaluate the background, and the red square to evaluate the potential core. We plot a histogram of the intensity distribution in these squares over 100 frames, with and without the shot-to-shot correction. The results are plotted in figure 3.8. We see a clear improvement of the distribution in the potential core. The histogram is tighter around its mean value after the shot-to-shot correction, as the standard deviation is reduced from 5.5% to 3%. This improvement is very local, and we emphasize that this correction renders the measurements statistically more accurate.

3.2.2.4 Calibration procedure

Anisole quenches with O_2. In measurement conditions where the jet contains the largest mass fraction of Helium $(Re, Ar) = (4000, 20000)$), the oxygen mass fraction varies through the flow. Under these conditions, quenching in the jet core is less intense than in the freshly mixed fluid at the edge of the jet. A dependence of the fluorescence signal to the oxygen concentration would render the signal nonlinear to Helium concentration, and requires an additional calibration step. Pasquier-Guilbert (2004) measured the dependence of Anisole fluorescence signal intensity on oxygen concentration (their Figure 3.43). Using their data, we find that for the highest Helium concentration in our experiment, oxygen variations are small enough. Therefore, this effect can be neglected.

The measured PLIF signal depends on the optical devices used to collect light. The intensified CCD cameras are sensitive to many parameters, including the amount of light they receive and the gain used for the intensification. In order to calibrate all sources of error in our measurements, it is necessary to check the linearity of both fluorescence and CCD sensor. To do so, we vary three parameters, laser energy, Anisole concentration and camera gain. Linearity is required to perform the shot-to-shot correction, as most of the arithmetics are simply based on cross-multiplications. We process by spanning the parameters regularly using 100 images of a laminar jet.

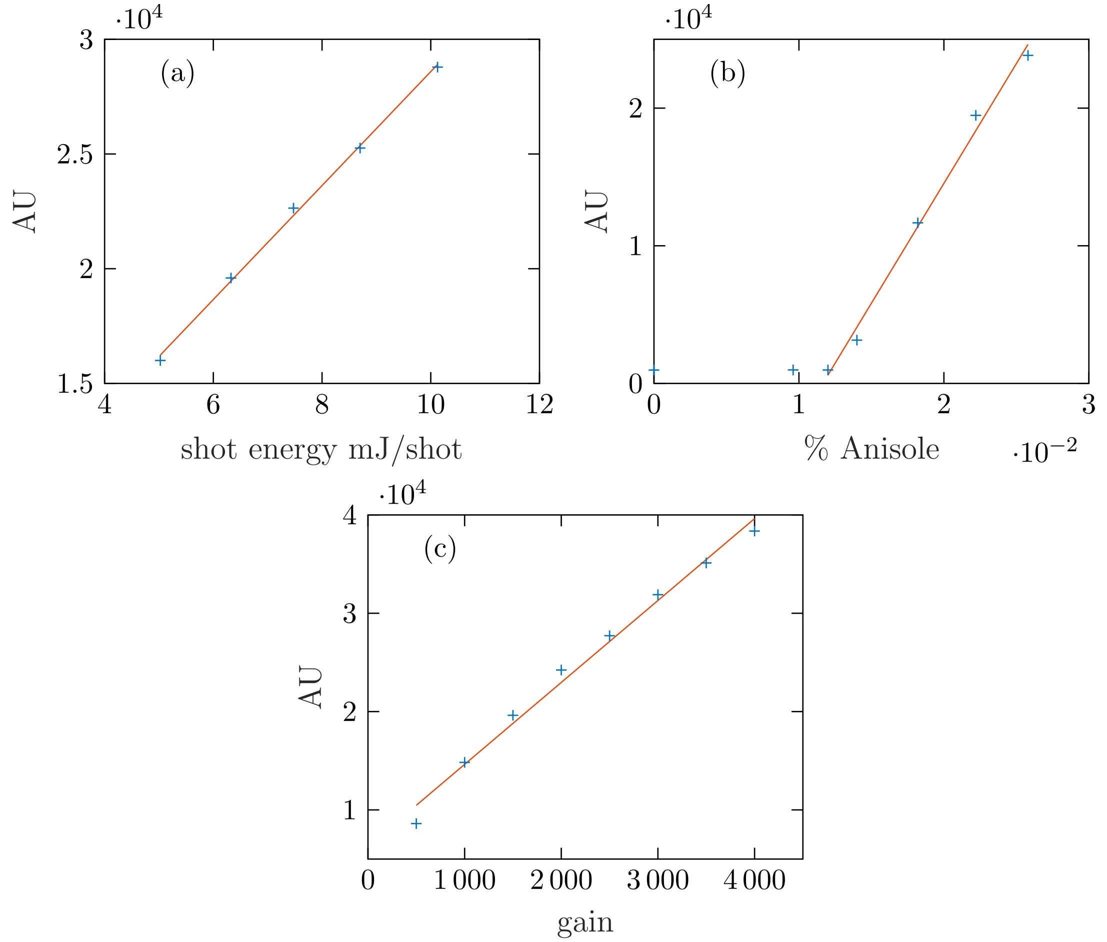

Figure 3.9: Response to Laser intensity (a) Anisole concentration (b) and camera gain (c).

Figure 3.9(a) shows the result of the PLIF linearity calibration to laser energy. In this case, the gain is fixed at 2000 and the Anisole concentration at 0.02%. We clearly see a linear dependency of the response to the laser energy. We limited our measurement to 10 mJ/shot, because larger energy caused photo-dissociation on Anisole. Figure 3.9(b) represents the sensitivity measurement to Anisole mass fraction. In this case, the laser energy is 10 mJ/shot and the gain is 2000. Above 0.03%, the Beer-Lambert effect is non-negligible over the light-path of the UV laser sheet. At very small Anisole mass fractions, no fluorescence signal is observed below a concentration of 0.01%. The PLIF signal linearly depends on the Anisole mass fraction between these limiting values. Figure 3.9(c) shows a weakly nonlinear dependence of the PLIF response to the gain. In this case, the Anisole concentration is 0.02% and the laser intensity is 10 mJ/shot.

We chose the parameters 10 mJ/shot for the laser intensity, 0.02% of Anisole mass concentration and a gain of 2000. During the experiment, we adjusted these parameters to reach the largest possible fluorescence intensity in the potential core of the jet, without exceeding 32000 in pixel intensity, because the CCD response is nonlinear above this value.

When the measurement conditions are reached for a linear response, and all corrections have been applied, the next step consists in converting the PLIF images into concentration fields. The potential core intensity is allocated to $\phi = 1$, and we select the lower-left corner as a reference for the background $\phi = 0$. Both the background and the potential core raw camera responses have wide probability distributions. The corrections tighten the distributions around precise values that we used for the conversion into a concentration field (figure 3.8). The final step consisted in interpolating the concentration fields on the PIV grid.

3.3 Conclusion

In this chapter, we described the design of the experimental facility that allowed us to measure the velocity and scalar fields in the very near field of a variable density round jet. The velocity fields were measured using Stereoscopic Particle Image Velocimetry, whereas the for the scalar field, Planar Laser Induced Fluorescence was used. We described the calibration and the different correction steps to our techniques. In Figure 3.10, we show a typical resulting instantaneous velocity and scalar fields. For clarity, we represent a reduced amount of velocity vectors.

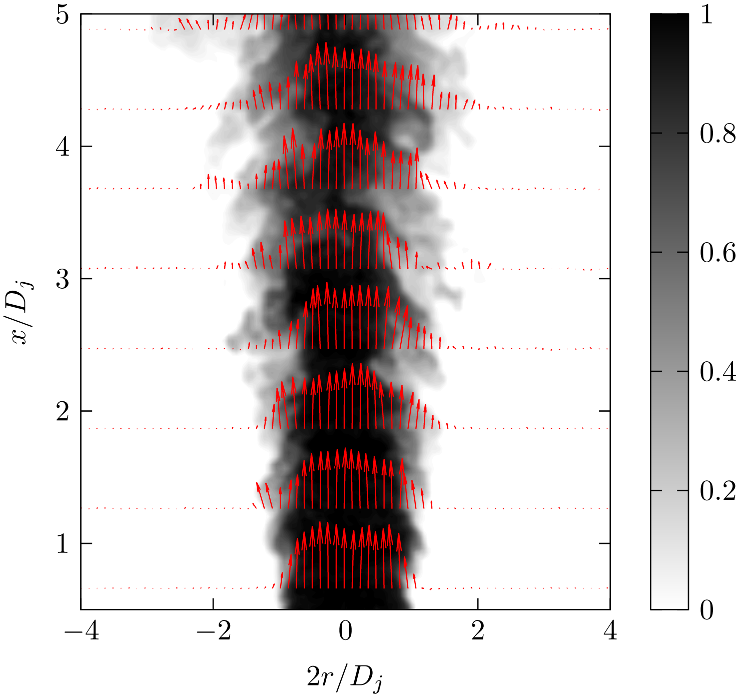

Figure 3.10: Typical instantaneous fields at $(Re, Ar) = (12000, 0)$. Velocity vectors are coarse-grained for clarity.

Chapter 4

Variable density turbulent spatially evolving round jet

In this chapter, we expose the experimental results obtained in our variable density round jet, starting with a validation of mean and second-order statistics, with respect to the literature. Then, we use the one-point statistics approach to explore the (Re, Ar) plane. Motivated by these observations, we focus then on the two-point statistics approach, and evaluate some terms in the variable density Kolmogorov and Yaglom equations that we derived in Section 2.2.4. Finally, we compute conditional statistics for different cases.

4.1 Validation of the measurements

In this section, we present some mean and second-order statistics that are usually presented in the literature. We focus on three cases, $(Re, Ar) = (4000, 0)$, $(24000, 0)$ and $(4000, 20000)$ for which we evaluate momentum and density variations effects.

Figure 4.1 represents the radial variation of the mean velocity and mass fraction fields, at different downstream positions, for the three reference cases. These fields are normalized by their mean value at the axis, whereas the radial distance is normalized by the jet injection radius $D_j/2$.

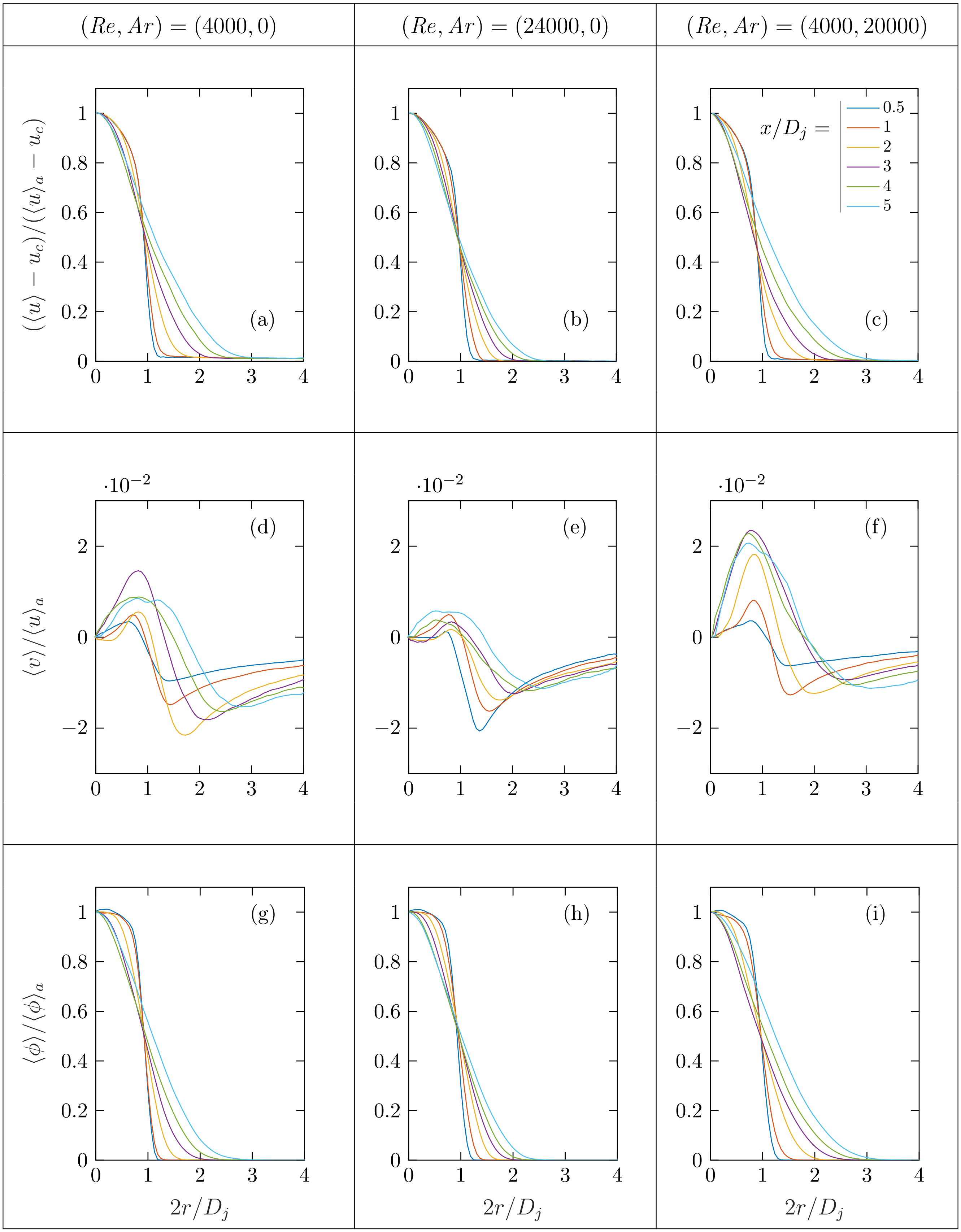

Figure 4.1: Radial variation of normalized mean axial velocity (a)-(c), radial velocity (d)-(f) and mass fraction (g)-(i), for different downstream positions x/D_j.

In all cases, the scalar mean profiles are sharper than the mean axial velocity at the position $x/D_j = 0.5$. This is due to the injection conditions. We recall that the pipe is thermally insulated, and that the jet fluid is very well mixed before entering the pipe. The scalar injection profile is therefore a top-hat. On the contrary, the mean velocity follows a Laufer's fully developed turbulent pipe flow, as shown in Figure 3.4.

Regarding the mean fields, the transitions occurs as follows. The position of inflectional points of the axial velocity and scalar profiles indicate the spreading of the jet. If these inflectional points depart from the radial position $2r/D_j = 1$, the jet widens on average. Also, the mean radial velocity component is negative outside the jet, which is linked to entrainment. By conservation of mass as the jet spreads, the mean radial velocity inside the core is positive.

The low Reynolds number jet $(Re, Ar) = (4000, 0)$ spreads at $x/D_j = 5$, as the mean radial velocity is positive inside the core at that position. Also, the inflectional points of the mean axial velocity and scalar are at radial position $2r/D_j = 1.2$. The left and center columns of Figure 4.1 depict the effect of increasing the Reynolds number on a passive scalar jet. The large Reynolds number jet $(Re, Ar) = (24000, 0)$ does not spread yet at $x/D_j = 5$. This point is located exactly at $2r/D_j = 1$ for the mean axial velocity and scalar profiles. Also, the mean radial velocity is very small, inside the jet. Nevertheless, the mean axial velocity and scalar gradients in the radial direction are smoothed. These quantities do not contaminate the axis of the jet, at $x/D_j = 5$.

The left and right columns of Figure 4.1 show the effect of lowering the density of the jet, when the Reynolds number is kept constant at $Re = 4000$. Density variations cause a stronger spreading of the jet. The mean radial velocity magnitude inside the jet is very large, and the inflectional point of the mean axial velocity and scalar profiles already depart from $2r/D_j = 1$ at $x/D_j = 4$.

Regarding the second-order statistics, the transition takes place as follows. Fluctuations emerge at the mean flow gradients, because of turbulent production. These fluctuations gain in intensity and spread towards the core and the outer-flow. As the fluctuating field contaminates the axis, the peak of turbulence intensity around the shear decays. After transition, the fluctuations profile resembles a Gaussian.

Figure 4.2 represents the radial variation of the turbulence intensity of the axial velocity, radial velocity and scalar, at different downstream positions x/D_j, for the three reference cases. For the low Reynolds number case $(Re, Ar) = (4000, 0)$, the axial velocity and scalar turbulence intensities are the largest at $2r/D_j = 1$, right after the injection. This location corresponds to the largest mean axial velocity and scalar profiles, which are the inflectional points in Figures 4.1(a) and (g) respectively. Farther downstream, the peak magnitude increases, and the fluctuations contaminate the axis of the jet, for both axial velocity and scalar. The radial velocity shows the same behavior, but is delayed as compared to the axial velocity. This is due to the orientation of the shear, which is mostly radial right after the injection.

The turbulence intensities of the axial and radial velocities, together with the scalar follow the same trends with Reynolds and Archimedes numbers variations as their mean counterparts, in Figure 4.1. Increasing the Reynolds number reduces the magnitude of the turbulent fluctuations, whereas increasing the Archimedes number enhances the turbulent fluctuations.

The radial profiles of the mean and second-order velocity and scalar statistics, shown in Figures 4.1, and 4.2 are in agreement with the trends that are observed in the literature, for both scalar and velocity statistics (Pitts, 1991*a*,*b*; Panchapakesan & Lumley, 1993*a*,*b*; Amielh *et al.*, 1996; Djeridane *et al.*, 1996; Darisse *et al.*, 2015). We consider this agreement with literature as a validation of our experimental measurements.

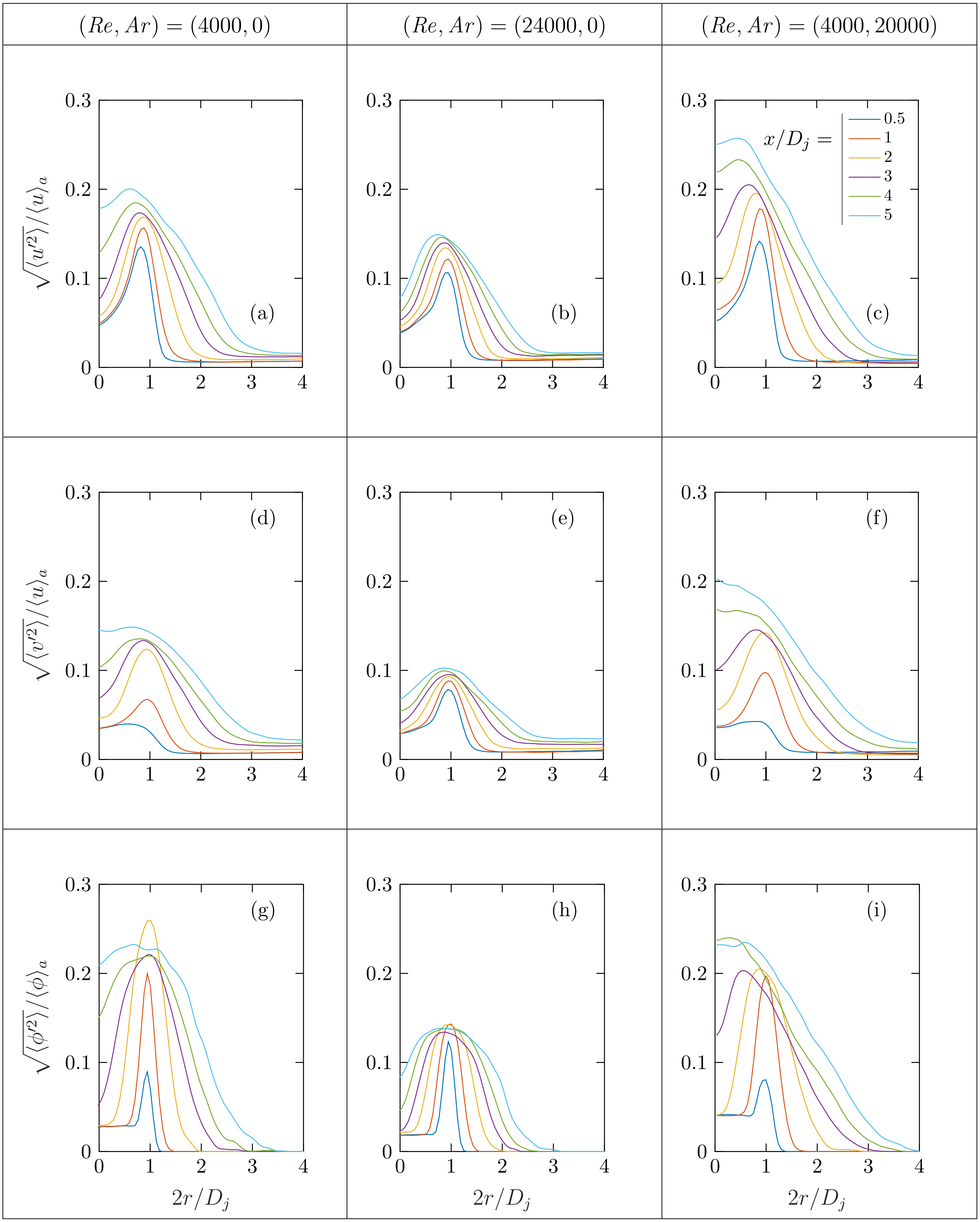

Figure 4.2: Radial variation of normalized turbulence intensity of axial velocity (a)-(c), radial velocity (d)-(f) and mass fraction (g)-(i), for different downstream positions x/D_j.

4.2 One-point statistics

The round jet experiment one-point statistics depend on four parameters, namely the Reynolds and Archimedes numbers and the streamwise and radial distances, Re, Ar, x/D_j and $2r/D_j$ respectively. For clarity, the dependence of statistics on Reynolds and Archimedes numbers will be represented only in localized regions of the flow. First, the axial dependence of low-order statistics is shown. Next, we exopose the radial dependence of these statistics and finally, we discuss our observations with the turbulent mixing literature.

4.2.1 Axial dependence of the conventionally averaged fields

Velocity fields

Figure 4.3(a) shows the mean axial velocity along the axis. We see that in increase of the Reynolds number lengthens the mean potential core, whereas an increase in the Archimedes number shortens this region. This observation is in agreement with the results of Pitts (1991*a*) for density, and Pitts (1991*b*) for momentum, respectively. The self-similar decay in the case $(Re, Ar) = (4000, 20000)$ is already reached at $x/D_j = 4$ (equation (1.2)). Amielh *et al.* (1996) observed the same feature in their pure Helium jet ($(Re, Ar) = (7000, 76000)$).

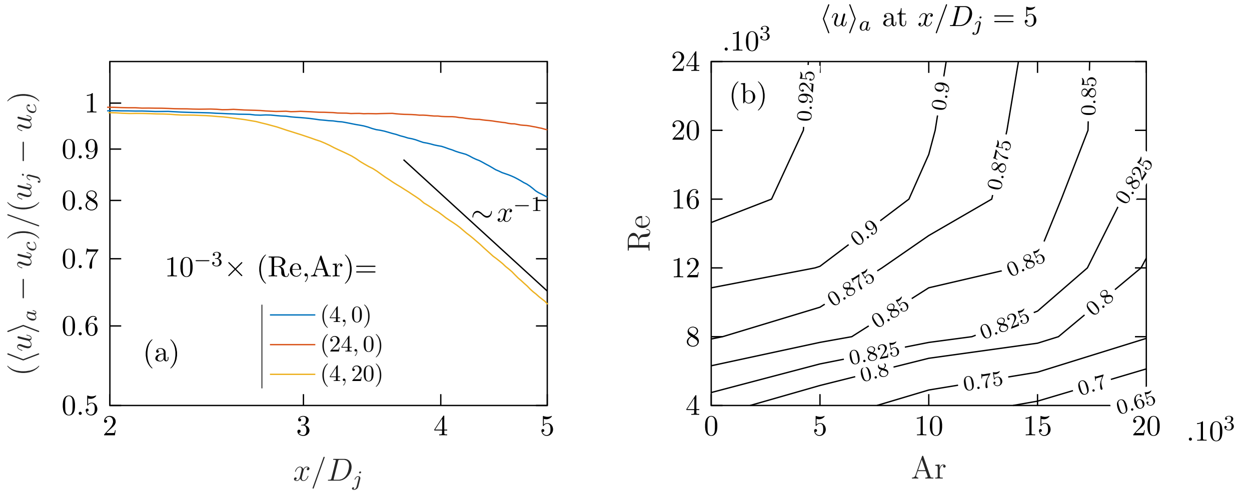

Figure 4.3: Axial variation of the normalized mean axis velocity for some values of (Re, Ar) (a) and for all measured cases at $x/D_j = 5$ (b).

To unravel the competition between momentum and density variations in the transition region of the jet, we represent in Figure 4.3(b) the normalized axis velocity at $x/D_j = 5$, for all measured cases. We notice a dissymmetry of the diagram. In the Boussinesq regime ($Ar < 5000$), the mean axis velocity is more sensitive to Reynolds number variations than to Archimedes number variations, when $Re \geq 16000$. Whereas in the non-Boussinesq regime ($Ar \geq 5000$), this feature is verified for $Re \leq 12000$. For all Ar, this quantity is independent of the Reynolds number when $Re \geq 16000$.

Next, Figure 4.4(a) shows the turbulence intensity of the axial velocity along the axis. This quantity is known to reach a plateau after some distance downstream, but the value of this plateau is subject to debate in the literature. As discussed by Amielh *et al.* (1996), this quantity is very sensitive to the injection conditions and to confinement effects. We consider the recent measurement value of 23% from Mi *et al.* (2013), which we represent by a dashed line in Figure 4.4(a). Similar to the mean axial velocity, a higher Reynolds number lengthens the potential core, and a higher Archimedes number shortens this region. In the case $(Re, Ar) = (4000, 20000)$, the plateau is already reached at $x/D_j = 5$. The injection turbulence intensity is slightly different from one case to another. We find that overall, the quantity $\sqrt{\langle u'^2 \rangle_a}/\langle u \rangle_a$ at $x/D_j = 0.5$ is always between 3% and 6% (figure not shown).

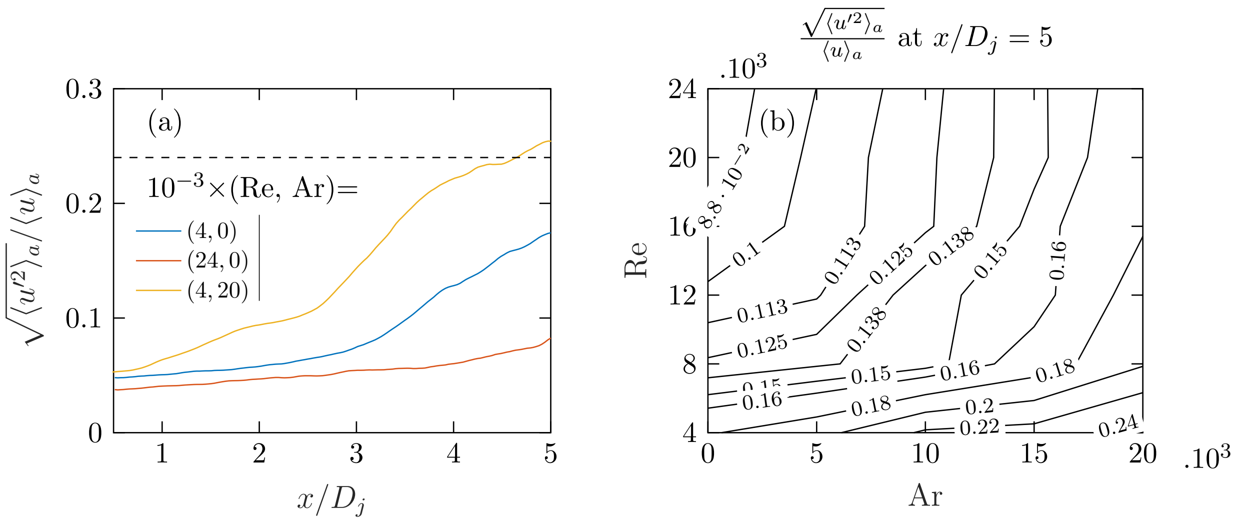

Figure 4.4: Axial variation of axial velocity turbulence intensity for some values of (Re, Ar) (a) and for all measured cases at $x/D_j = 5$ (b).

Figure 4.4(b) represents the axial turbulence intensity at the axis, at $x/D_j = 5$ and for all measured cases. We find that, similarly to the mean axis velocity (Figure 4.3(b)), the axial turbulence intensity shows two distinct regimes, separated by $Re = 12000$ in the Boussinesq regime and $Re = 8000$ in the non-Boussinesq regime, respectively.

Scalar fields

Figure 4.5(a) depicts the mean scalar variation along the axis, for our three reference cases. We observe the same trend as for velocity fields, so that an increase in the Reynolds number delays the transition, whereas an increase in Archimedes number rushes the transition. The self-similar scaling $(x/D_j)^{-1}$ is already reached at $x/D_j = 3.5$ in the case $(Re, Ar) = (4000, 20000)$. The decay of the mean scalar occurs earlier than for the mean axial velocity for this case (Figure 4.3(a)). The faster decay of the scalar is in agreement with the results of Djeridane *et al.* (1996), in the same measurement campaign as Amielh *et al.* (1996) $((Re, Ar) = (7000, 76000))$.

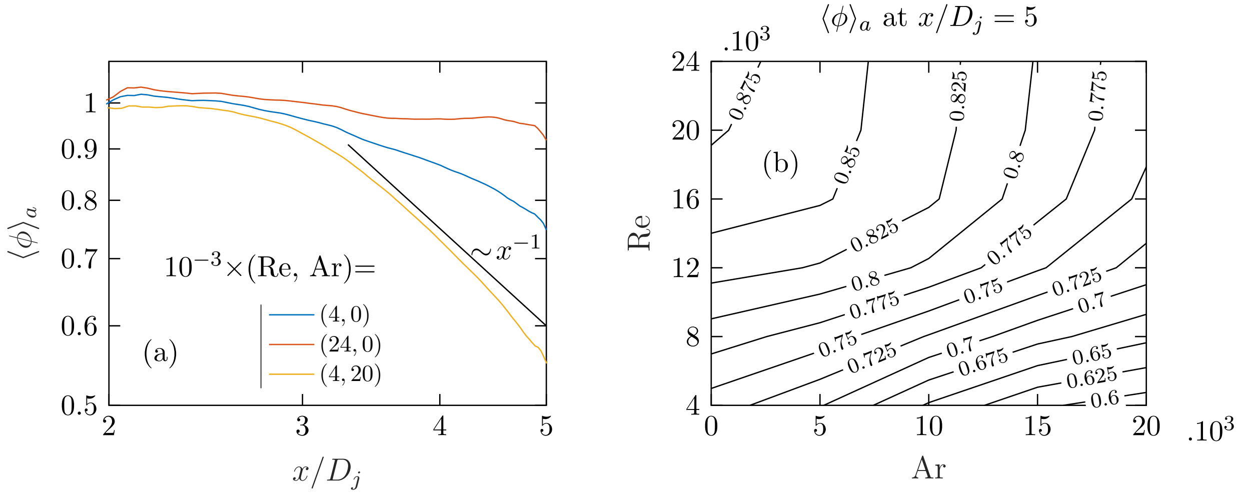

Figure 4.5: Axial variation of the mean scalar field for some values of (Re, Ar) (a) and for all measured cases at $x/D_j = 5$ (b).

Figure 4.5(b) shows the dependence of the mean scalar at the axis at the position $x/D_j = 5$, for all measured cases. We distinguish two regions. In the Boussinesq regime $(Ar < 5000)$, the mean axis scalar is weakly dependent on the Reynolds number. In the non-Boussinesq regime $(Ar \geq 5000)$, this quantity is independent of the Reynolds number when $Re \geq 16000$, as the iso-values become parallel to the Reynolds number axis.

Figure 4.6(a) shows the scalar turbulence intensity variation along the axis, for our three particular cases. This quantity is known for reaching a plateau after some distance. Similarly to the velocity turbulence intensity, there is no agreement in the literature on the magnitude of this plateau (see Mi *et al.* (2001) for exhaustive recent discussion). We choose the reference value of 23% from Pitts (1991*a*) as a reference for the establishment of the second-order plateau, which is represented by the dashed line in Figure 4.6(a). We see that, the plateau is already reached in the variable density case $(Re, Ar) = (4000, 20000)$, whereas the two other cases are still in the transitional regime.

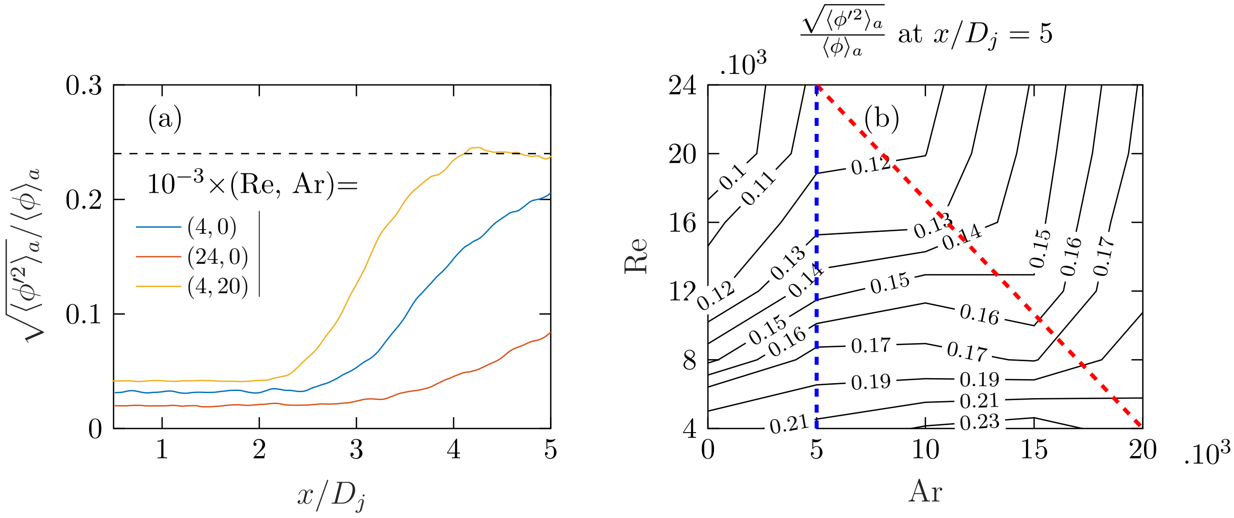

Figure 4.6: Axial variation of the scalar turbulence intensity for some values of (Re, Ar) (a) and for all measured cases at $x/D_j = 5$ (b).

Figure 4.6(b) shows the axis turbulence intensity of the scalar at $x/D_j = 5$ for all measured cases. We observe a strong nonlinear dependence of this quantity on the Reynolds and Archimedes numbers, so that we distinguish three regimes. First, the Boussinesq regime, left to the blue dashed line, is characterized by a gradual transition when increasing the Reynolds numbers from a regime where density variations do not influence the length of the potential core, to a regime that is independent of the Reynolds number above $Re = 20000$. Graphically, the iso-values of scalar turbulence intensity are horizontal at small Reynolds numbers, and gradually become vertical at large Reynolds numbers.

Second, in the non-Boussinesq regime, right to the blue dashed line, we see two very distinct regimes that are separated by the red dashed line. Between the blue and red dashed lines, we find a regime that is independent of the density variations, and above the red dashed line, a regime that is independent of the Reynolds number. The red dashed line is defined by $Re_{crit} = 24000 - \frac{4}{3}(Ar - 5000)$. The transition through this line, from a Archimedes number independent to a Reynolds number independent regime is abrupt, as compared to the Boussinesq regime transition. We also notice a local maximum to the scalar turbulence intensity at the axis for the two points $(Re, Ar) = (4000, 10000)$ and $(Re, Ar) = (4000, 15000)$, where the asymptotic value of 23% is reached already at $x/D_j = 5$.

The pseudo mass fraction φ is naturally suited for the scalar scale-by-scale study (see Section 2.2.4). Performing a Taylor expansion of the state Equation (2.22), the pseudo mass fraction second-order moment is

$$\langle \varphi'^2 \rangle = \langle \rho \rangle^2 \langle \phi'^2 \rangle + o(\langle \phi'^4 \rangle). \tag{4.1}$$

This result is asymptotically true when ϕ' is small in the region where the average is performed. Figure 4.7(a), shows a test of the asymptotic expansion (4.1) at $x/D_j = 5$, for all measured cases. We discuss this figure hereinafter.

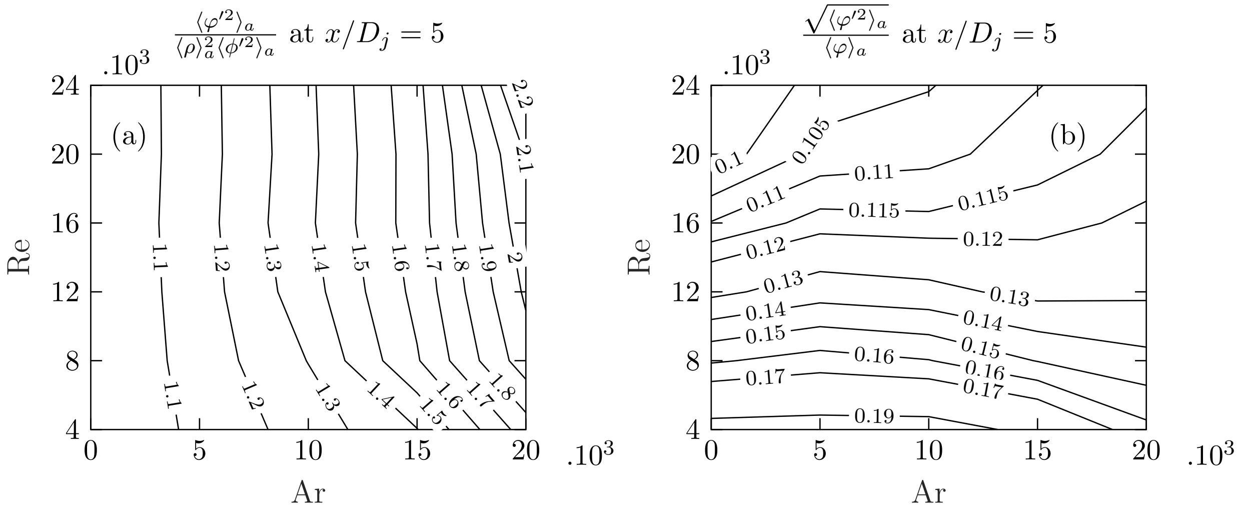

Figure 4.7: Validity test of expansion (4.1) (a) and pseudo mass fraction turbulence intensity (b), at $x/D_j = 5$ for all measured cases.

We find that at this position, the first order approximation of Equation (4.1) is valid only in the Boussinesq regime. Along the $Ar = 0$ axis, the expansion is identically verified, because $\langle \rho \rangle = 1$ and $\varphi = \phi$ locally and instantaneously. As we depart from this axis, the approximation is less and less valid. This departure is caused by factors. The departure through vertical iso-lines, when $Re \geq 8000$, is due to the nonlinearity of the state equation (2.22), that gives more and more weight to the mass fraction fluctuations. In addition, when $Re < 8000$, the departure is enhanced by the accelerated transition to turbulence of the mass fraction field.

The nonlinear dependence of $\langle \varphi'^2 \rangle$ on the Reynolds and Archimedes numbers motivates us to evaluate this quantity as a distinct field, for later comparison with the two-point statistics. Figure 4.7(b) shows the turbulence intensity of the pseudo mass fraction at $x/D_j = 5$ for all measured cases. This quantity does not endure an abrupt transitions like the mass fraction variance $\langle \phi'^2 \rangle_a$ (Figure 4.6(b)). This diagram suggests that the pseudo mass fraction is more robust to density changes, as the injection density inhomogeneity is taken into account in its mathematical definition through the state Equation (2.22).

4.2.2 Radial variation of the conventionally averaged fields

We found, in the (Re, Ar) plane, multiple regimes regarding the scalar mixing. In this part, we focus on two lines within this parameter space, which are defined by $Ar = 10000$ and $Re = 12000$, to evaluate the effect of these regimes on the radial profiles of the second-order statistics.

In Figure 4.8, the turbulence intensity of the velocity components and the scalar at different downstream positions x/D_j, along the two lines in the (Re, Ar) plane that we described. The axis bifurcation is also recovered in the radial profiles. In the left column of Figure 4.8, we see that the axial velocity turbulence intensity decreases from a large magnitude to two distinct curves, depending on the Reynolds number. If $Re \leq 12000$, the turbulence intensity profile reaches the axis value of 14%, whereas this curve is slightly smaller to 12.5% when $Re \geq 16000$. We also notice this effect on the radial velocity turbulence intensity. This result is in agreement with the independence of the velocity turbulence intensity when $Re \geq 20000$ in Figure 4.4(b).

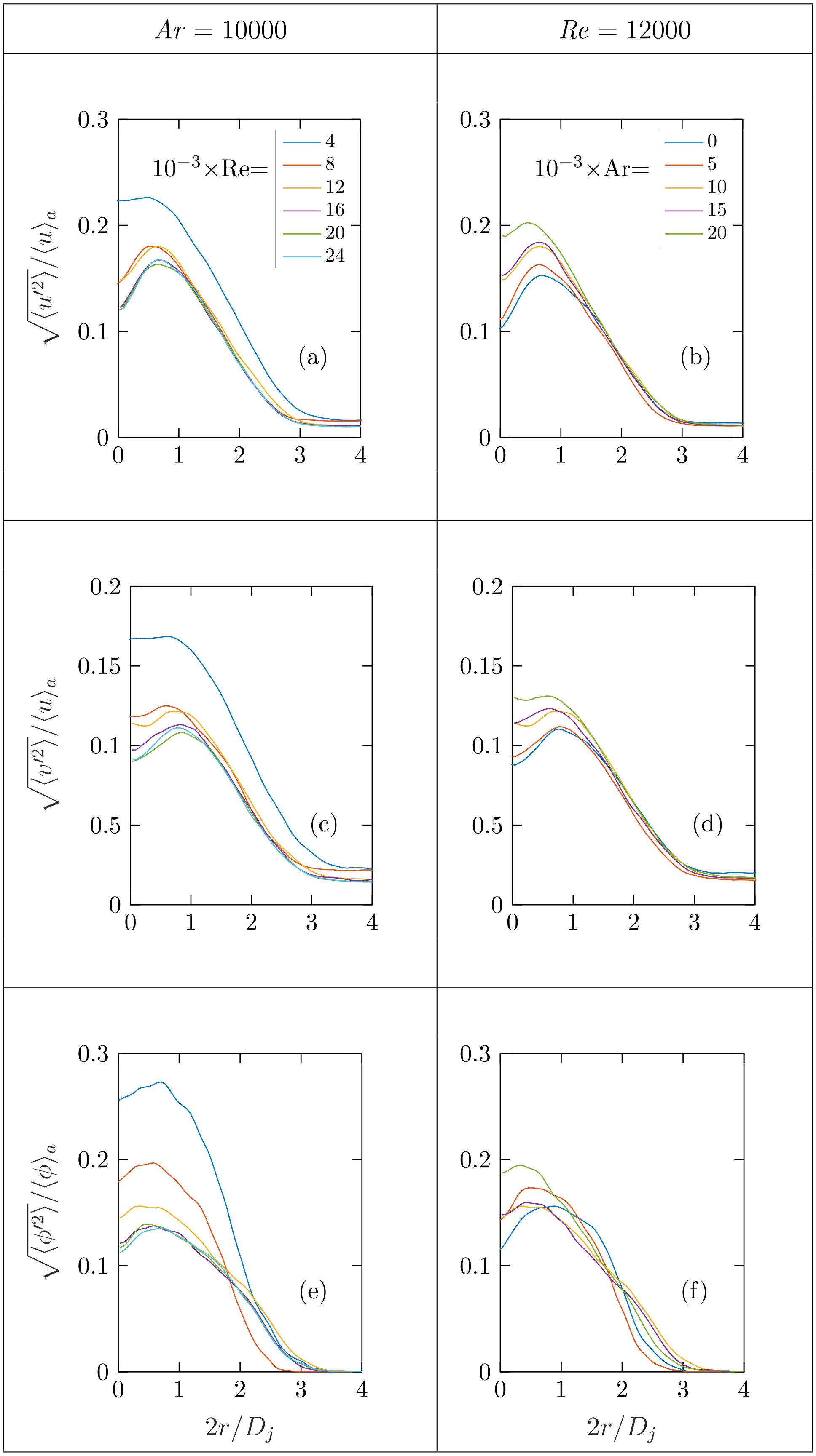

Figure 4.8: Radial variation of the turbulence intensity of axial velocity (a)-(b), radial velocity (c)-(d) and scalar (e)-(f), at different downstream positions x/D_j.

Still on the left column of Figure 4.8, the scalar turbulence intensity behaves differently than the velocity turbulence intensity. We find that above $Re \geq 16000$, all the profiles collapse to a single curve, and therefore become independent of the Reynolds number. This result is in agreement with the two non-Boussinesq regimes that we found, as shown in Figure 4.6(b). The turbulence intensity peaks of all three turbulence intensities considered here is unaffected by the Reynolds number variations.

Let us now focus on the Archimedes number variation effects on the radial turbulence intensities profiles. The right column in Figure 4.8 represents these profiles at different downstream positions x/D_j, for $Re = 12000$. We find that the velocity turbulence intensities stagger around three curves, depending on the Archimedes number. The weak dependence on this number that we found on the axis value of this quantity in Figure 4.4(b) is also present for the corresponding radial profiles. On the contrary, the scalar turbulence intensity does not follow the same trend. Increasing the Archimedes number increases the peak value of the scalar turbulence intensity, and shifts the profile towards the core of the jet. Therefore, the scalar turbulence intensity is more sensitive to density variations than the velocity turbulence intensity radial profile.

4.2.3 Discussion

In this section, we collected many results regarding one-point statistics of the near field or our variable density round jet. The main results from this part can be summarized as follows

1. The mean axial velocity at $x/D_j = 5$ is independent of the Reynolds number above $Re \geq 20000$. Except the mean axial velocity, all the other statistics at x/D_j are independent of the Reynolds number when $Re \geq 16000$.

2. The scalar turbulence intensity has two non-Boussinesq regimes ($Ar \geq 5000$), separated by the curve $Re_{crit} = 24000 - \frac{4}{3}(Ar - 5000)$. When the Reynolds is below this critical value, the near field mixing along the axis depends only on the momentum, whereas when the Reynolds number is above this line, mixing in this region depends only on density variations. This effect is also observed on radial profiles of the scalar turbulence intensity in the Reynolds-independent regime. In the Archimedes-independent regime, the radial profiles variation is not as conclusive.

Regarding the literature on mixing, Dimotakis (2000) states that mixing is most efficient when the Reynolds number is larger than a value comprised between 10000 and 20000, and refers to this feature as the mixing transition. This author observes this transition in many different flows, including jets (Dimotakis *et al.*, 1983). In the variable density configuration, most of the attention has been dedicated to the Rayleigh-Taylor Instability, stably stratified flows and Langmuir circulation (Dimotakis, 2005). To our knowledge, no study considered the mixing transition in non-Boussinesq variable density jets.

The mixing transition is recognizable by the very weak dependence of statistics on Reynolds number variations. We found that except the mean velocity at the axis, all the statistics become independent of the Reynolds number above $Re_{crit} = 16000$ independently of the Archimedes number. The different regimes that we observe in the (Re, Ar) plane are not necessarily related to the mixing transition. In order to confirm that our observations are indeed related to this feature, we need to access the smallest scales of the flow and observe that the scalar variance cascades faster towards the Batchelor length-scale. Unfortunately cannot perform such measurements with the current experimental setup in our round jet.

Our results suggest an enhancement of the transition to turbulence, especially in the non-Boussinesq regime. The scalar second-order moment is independent of density variations at $x/D_j = 5$, when the Reynolds number is below the critical curve $Re_{crit} = 24000 - \frac{4}{3}(Ar - 5000)$. On the other hand, this quantity is independent of the Reynolds number above this curve. We conclude that the scalar variance, and therefore the mixing, undergoes a bifurcation when crossing this critical line in the (Re, Ar) plane. Crossing this line from below, the mixing bifurcates from a density robust regime towards a momentum robust regime. We recall that in our configuration, the flow is inertial, as the momentum length $(x/D_j)_m$ is always larger than 24. Our observation is not a buoyancy effect. Also, we limited our measurements to a downstream distance of $x/D_j = 5$. The results that we obtain concern the initiation of mixing, rather than homogenisation at the molecular level, following the crude definition of mixing (Dimotakis, 2000).

Nevertheless, we aim at giving as much information as possible about mixing. In the next section, we assess the problem of two-point statistics in the very near field of our variable density round jet experiment.

4.3 Two-point statistics

One-point statistics are useful for validation and as a large-scale study of turbulence. In a more elaborate approach, we assess the variable density jet in scale space. To do so, we will evaluate some terms of the variable density Kolmogorov and Yaglom equations, that we derived in Section 2.2.4. First, we describe the numerical method we used to compute the two-point statistics. Second, we evaluate structure functions along the axis of the jet. Then, we compute these quantities in the shear region, along a line that is parallel to the axis and shifted in the radial direction. Finally, we discuss our observations and compare them to the one-point statistics results.

4.3.1 Structure functions post-processing method

Two-point statistics that we evaluate in this section are the temporal, inter-scale and inhomogeneous transport terms for both the variable density Kolmogorov and Yaglom equations. Table 4.1 summarises the these quantities. By virtue of the statistical axisymmetry of the flow, these quantities are functions of the five coordinates (r_r, r_x, X_r, X_x, t), where r and X indicate the scale and space coordinates, whereas subscritps $(.)_r$ and $(.)_x$ indicate the radial and streamwise directions, respectively. Hereinafter, we discuss these terms, and describe the numerical method we used for their evaluation.

	Temporal	Inter-scale transport	Inhomogeneous transport
Yaglom	$\langle(\Delta\varphi')^2\rangle$	$\langle\Delta u'(\Delta\varphi')^2\rangle$	$\langle\Sigma u'\,(\Delta\varphi')^2\rangle/2$
Kolmogorov	$\langle\Sigma\rho\,(\Delta u_i')^2\rangle/2$	$\langle\Sigma\rho\,\Delta u'(\Delta u_i')^2\rangle/2$	$\langle\Sigma\rho\,\Sigma u'(\Delta u_i')^2\rangle/4$

Table 4.1: List of the terms that we compute for variable density Kolmogorov and Yaglom equations, Equation (2.39) and Equation (2.33), respectively

In literature, inter-scale transport terms are generally split into a transport by the mean velocity field $\Delta\langle u_j\rangle\langle(\Delta u_i')^2\rangle$, and a transport due to the velocity fluctuations $\langle\Delta u_j'(\Delta u_i')^2\rangle$ (Gomes-Fernandes *et al.*, 2015; Lai *et al.*, 2018). The former is referred to as linear inter-scale transport, and is seen as a production term. The latter term is referred to as nonlinear inter-scale transport. The same decomposition can also be applied to the inhomogeneous transport terms. In this thesis, we focus on nonlinear transport terms, as the increments in Table 4.1 are all computed using fluctuations.

Pseudo mass fraction φ causes a strong analytical simplification (Equation (2.25)). The computation of the variable density Yaglom equation terms is straightforward, and similar to the terms in the constant density case (Danaila *et al.*, 1999). The measurement techniques we used are stereo-PIV for the velocity field, simultaneously coupled with PLIF for the scalar field (see Chapter 3). The shot-to-shot correction of the laser energy heterogeneity is not perfect, and a slight mistake in this correction can highly alter the resulting scalar structure functions. In particular, the laser energy inhomogeneity mostly influences the large scales of the scalar field. This feature motivated us to evaluate the scalar increments using the fluctuation of the pseudo mass fraction φ'.

On the other hand, the variable density Navier-Stokes equations (2.7) have a higher order of nonlinearity than in the constant density case. This feature leads to third-order and fourth-order structure functions, in the temporal and non-local transport terms of the variable density Kolmogorov equation (2.39), respectively. Numerically, the evaluation of higher-order statistical quantities is more difficult, especially for odd orders. We made sure that the statistics are converged, within the available amount of data we measured. We evaluate the kinetic energy increment using the local instantaneous density, and the velocity fluctuations $\Sigma\rho(\Delta u_i')^2/2$. The Reynolds decomposition of density leads to a larger number of terms, which are related to different physical mechanisms of energy transfer. This decomposition was studied by Dupuy *et al.* (2018), in the one-point statistics context. These considerations are not taken into account in the following two-point results.

Figure 4.9 sketches the regions where structure functions are computed. These regions are defined by $x/D_j \in [3,5]$, at two different radial locations. The blue segment is at the axis $2r/D_j = 0$, and the red segment is shifted from the axis at a position $2r/D_j = 1$. The computation of the two-point quantities is performed using a convolution along these segments, by an increment filter of variable width. The width of this filter is the scale coordinate r_x/D_j. As the spatial resolution of our measurements does not reach the Kolmogorov length-scale, we are limited to moderate to large scales.

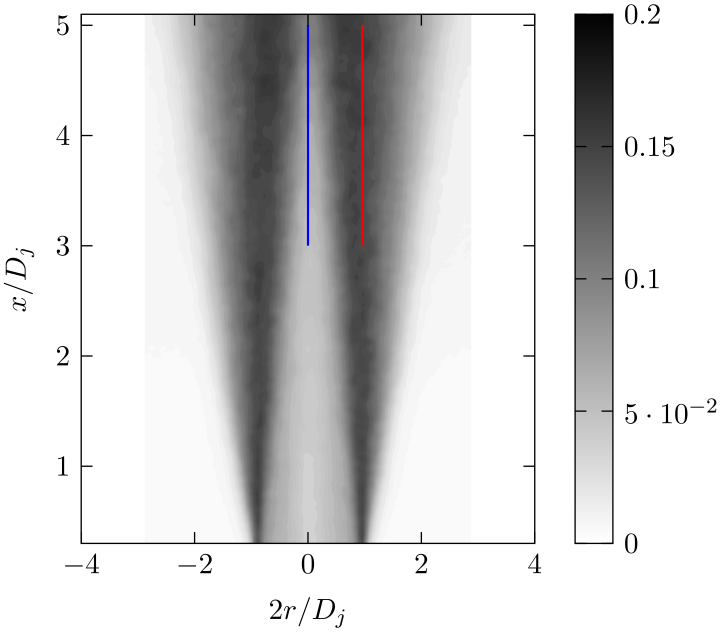

Figure 4.9: Axial velocity turbulence intensity for the case $(Re, Ar) = (12000, 0)$. The colored segments are the regions where structure functions are computed. The blue line is at the axis and the red line is shifted at a radial position $2r/D_j = 1$.

In Section 4.2, we found that scalar turbulence intensity at the axis undergoes a regime transition by crossing the line $Re_{crit} = 24000 - \frac{4}{3}(Ar - 5000)$. In the following, we focus on three regions in this plane, $(Re, Ar) = (4000 - 24000, 0)$ for Reynolds number effects on a passive scalar jet, $(Re, Ar) = (4000 - 24000, 10000)$, for Reynolds number effects on a variable density jet, and $(Re, Ar) = (12000, 0 - 20000)$ for the density variations effects on a turbulent jet. The critical line is crossed at the point $(Re, Ar)_{crit} = (12000, 10000)$. For normalization, we use the notation $(.)_3$ and $(.)_5$ to indicate the quantity taken at $x/D_j = 3$ and $x/D_j = 5$, respectively. As we studied large-scales through one-point statistics, we will normalize the temporal terms by their respective large-scale limits. Non-local terms do not have a preferable normalization, as we do not have access to dissipation rates. We choose to normalize these quantities by their one-point limit at the point $x/D_j = 3$. Regarding scales, we noramlize distances by the jet diameter D_j. The scale dependence will therefore be discussed in the laboratory frame.

4.3.2 Structure functions along the axis

In this part, we focus on the temporal terms. Figure 4.10(a) shows the second-order kinetic energy structure function in the passive scalar case, along the axis, and for different Reynolds numbers. As we normalize using large-scale quantities, all these structure functions converge to unity when r_x/D_j is large. When $Re \geq 16000$, these structure functions collapse, over all accessible ranges of scales. At lower Reynolds numbers, we find a monotonous staggering. Turbulence observed here is reminiscent from the fully developed pipe flow, together with the inhomogeneity due to the decay at the end of the potential core of the jet.

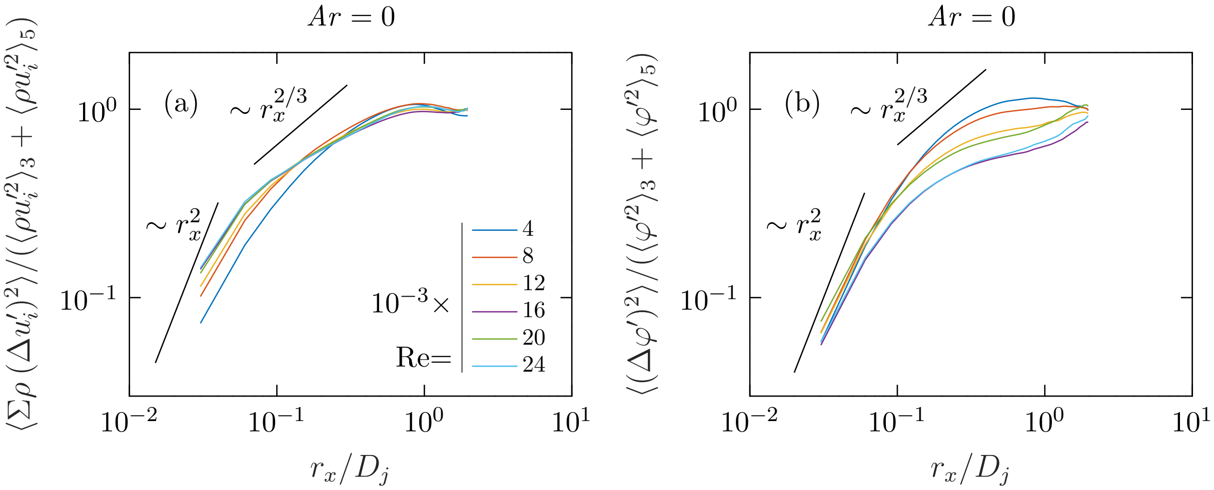

Figure 4.10: Structure function along the axis of kinetic energy (a) and second-order pseudo mass fraction (b), for different Reynolds numbers in the passive scalar case ($Ar = 0$).

Pseudo mass fraction φ is identically equal to the mass fraction ϕ only when density is constant. In the general case, using the same postulates as the Kolmogorov-Obukhov-Corrsin theory (Warhaft, 2000), we can show that

$$\langle (\Delta\varphi')^2\rangle \sim \langle \chi_\varphi\rangle \langle \varepsilon\rangle^{-1/3} r^{2/3}, \tag{4.2}$$

if the Peclet number is high enough, over a restricted range of scales. We recall that $\langle \chi_\varphi\rangle = 2\mathcal{D}^*\langle (\partial_k \varphi')^2\rangle$ is the pseudo mass fraction dissipation rate, defined in Section 2.2.4. For dimensional arguments, we included $\mathcal{D}^*$, which is a reference mass diffusivity. The dissipative range scaling r^2 is valid for any quantity, because it results from a Taylor expansion at the small separation distances.

Figure 4.10(b) represents the axis pseudo mass fraction second-order structure function in the passive scalar case, along the axis and for different Reynolds numbers. We observe the beginning of a dissipative range scaling r_x^2, and no inertial range. Pseudo mass fraction is homogeneous inside the pipe. As the potential core elongates with increasing Reynolds number, pseudo mass fraction fluctuations grow farther in the flow. The staggering of these structure functions is an inhomogeneity effect, that extends the one-point discrepancy in scale-space (Figure 4.6(a)).

Now, we evaluate the effect of Reynolds number on a variable density jet. Figure 4.11(a) represents the kinetic energy second-order structure function along the axis at $Ar = 10000$, and for various Reynolds numbers. When $Re \geq 20000$, these structure functions collapse, and show an inertial scaling range $r_x^{2/3}$, which was not observed in the passive scalar case (Figure 4.10(a)). The cases $Re \in [12000,\ 16000]$ collapse to a different curve, and the lower Reynolds number cases stagger.

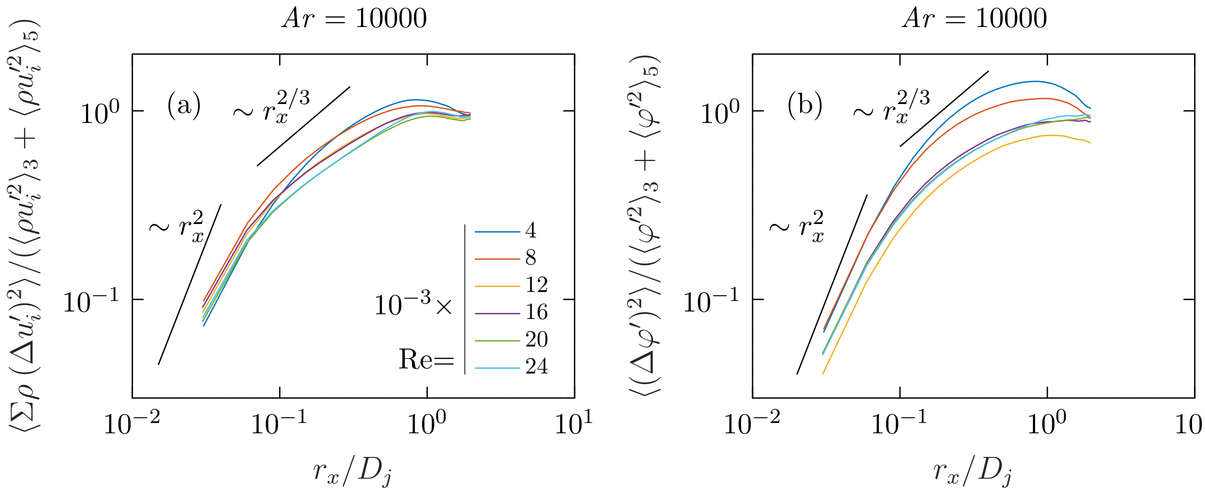

Figure 4.11: Structure functions along the axis of kinetic energy (a) and second-order pseudo mass fraction (b), for different Reynolds numbers at $Ar = 10000$.

Figure 4.11(b) shows the pseudo mass faction second-order structure functions along the axis, at $Ar = 10000$ and for various Reynolds numbers. With increasing Reynolds number, this quantity decreases until $Re = 12000$, and then collapses on a single curve for all larger Reynolds numbers. This single curve presents an inertial range scaling $r_x^{2/3}/D_j$. We notice a pronounced overshoot of the structure functions when $Re \leq 8000$, which is related to the decay of the mean pseudo mass fraction at the axis.

Then, we study the effect of density variations at constant Reynolds number. Figure 4.12(a) shows the kinetic energy increment along the axis for $Re = 12000$, and for various Archimedes numbers. These structure functions monotonously decrease with increasing Archimedes number. When $Ar \geq 5000$, all represented kinetic energy structure functions show a $r_x^{2/3}$ inertial scaling, over a wider range of scales as Ar is larger. Globally, the kinetic energy increment is robust to density variations along the axis at this position downstream.

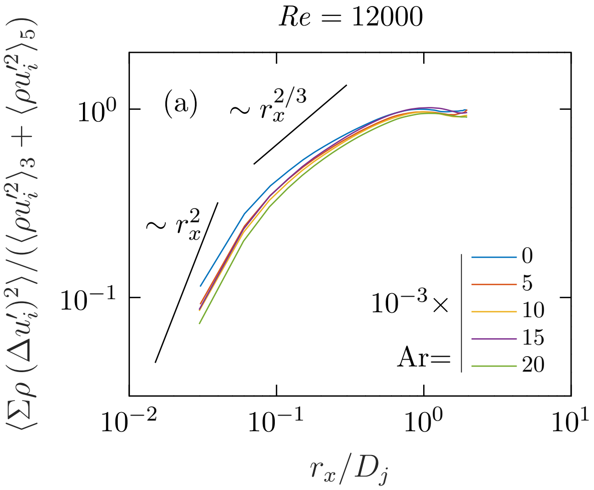

Figure 4.12: Structure functions along the axis of kinetic energy (a) and second-order pseudo mass fraction (b), for different Archimedes numbers at $Re = 12000$.

Figure 4.12(b) shows the pseudo mass fraction second-order increment along the axis, at $Re = 12000$ and for various Archimedes numbers. As the this dimensionless number increases from zero, these structure functions globally decrease until $Ar = 10000$. Then, we see a collapse of when $Ar \geq 15000$ on a larger common curve. In all cases, pseudo mass fraction increments present a dissipative range scaling r_x^2. With increasing Archimedes number, we notice a widening of an inertial range scaling $r_x^{2/3}$.

Mini conclusion

In this part, we evaluated the kinetic energy and pseudo mass fraction second-order structure functions, along the axis of the jet. The purpose is to study the initiation of the jet decay in scale-space. To do so, we browse the (Re, Ar) plane by crossing the different regimes we found in one-point statistics in Section 4.2. We conclude that the pseudo mass fraction is more sensitive than kinetic energy, regarding momentum and density variations, in scale-space along the axis. These aspects will be assessed further in the subsequent discussion. Next, we present the same quantities evaluated in the shear region, along a segment that is parallel to the axis of the jet.

4.3.3 Structure functions in the shear region

Here, we compute all the terms listed in Table 4.1. Figure 4.13 shows these structure functions in the passive case, in the shear region and for various Reynolds numbers. When $Re \geq 12000$, the kinetic energy structure functions collapse with good accuracy on the same curve, as shown in Figure 4.13(a). This common curve does not show an inertial range scaling $r_x^{2/3}$. For lower Reynolds numbers we observe a staggering of these two-point statistics. Figure 4.13(b) depicts the pseudo mass fraction increments, which are almost insensitive to Reynolds number variations, in the passive scalar case in the shear. This common curve shows a dissipative range scaling r_x^2, and an inertial range scaling over a restricted range of scales $r_x^{2/3}$.

Nonlinear inter-scale transport of kinetic energy, shown in Figure 4.13(c), changes with the Reynolds number. We see that this quantity is negative until $r_x/D_j \geq 1$. This indicates a forward cascade (Danaila *et al.*, 2012*b*; Alexakis & Biferale, 2018). These structure functions reach a minimum, which shifts towards smaller scales as the Reynolds number increases. When $Re \geq 12000$, these structure functions become independent to Reynolds number variations, up to the experimental precision. The pseudo mass fraction inter-scale transport is very robust to Reynolds number variations, as shown in Figure 4.13(d).

Figure 4.13(e) shows the inhomogeneous transport of kinetic energy. This quantity is representative of the transport of energy in physical space, and is therefore directly related to the decay at the potential core. The inhomogeneous transport structure function for kinetic energy is here positive for all Reynolds numbers. This indicates that the decay of the flow is accompanied by a strong generation of fluctuations that are transported downstream. When $Re \leq 12000$, increasing the Reynolds number decreases this transport, whereas when $Re \geq 16000$ increases this quantity. We do not observe a collapse of these quantities, as the statistical quality of these structure functions is better for smaller scales. Figure 4.14(f) represents the inhomogeneous transport of the scalar, which is negative at small scales. This indicates a propagation of the pseudo mass fraction fluctuations upstream of the jet. The larger scales values are more difficult to interpret, as these scales suffer from lower statistical quality than small-scales.

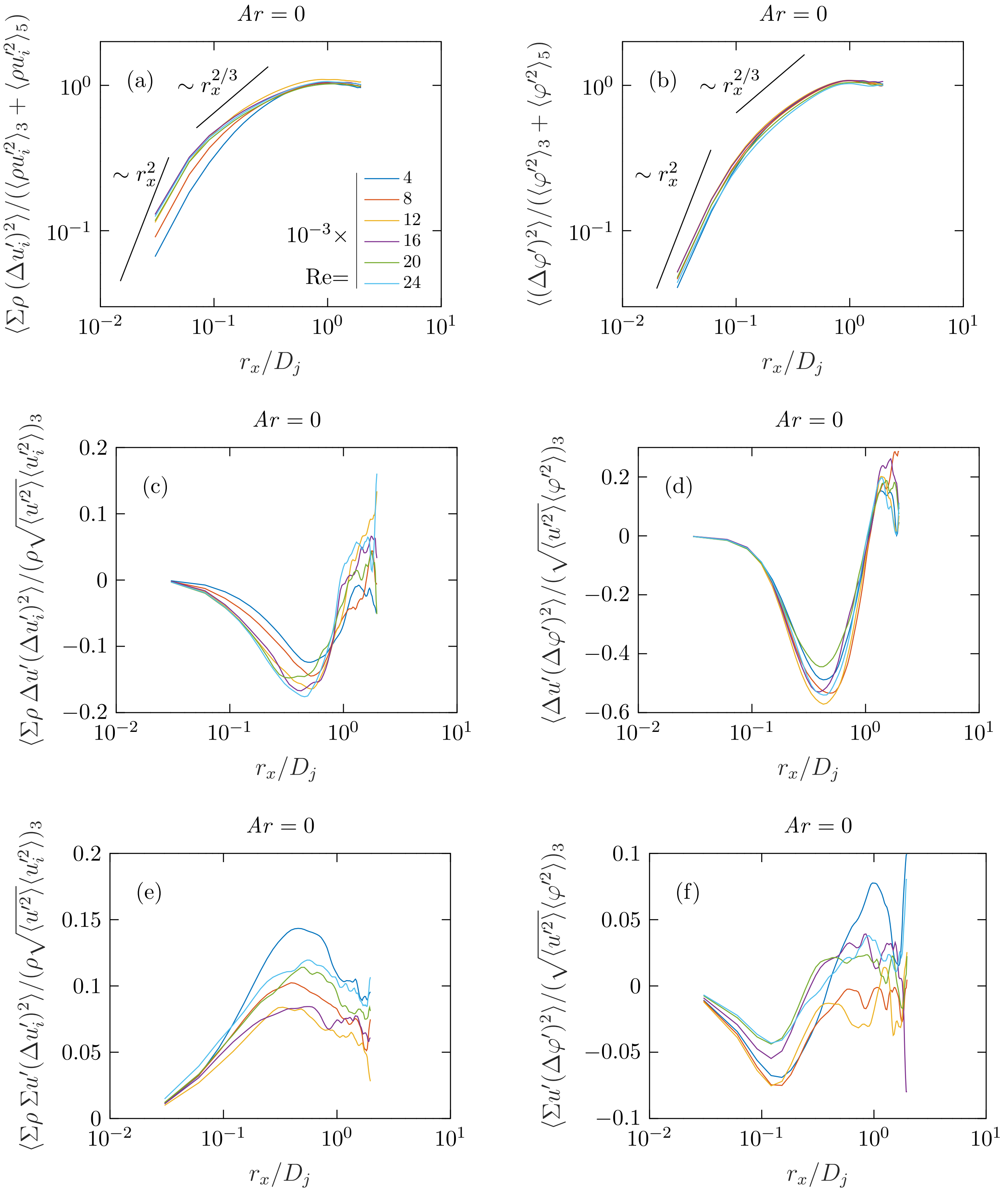

Figure 4.13: Structure functions in the passive scalar case ($Ar = 0$) in the shear region for the temporal terms (a)-(b), nonlinear inter-scale transport (c)-(d) and inhomogeneous transport (e)-(f), and for various Reynolds numbers.

Next, we evaluate the Reynolds number effect on a variable density jet. Figure 4.14 shows all two-point statistics exposed in Table 4.1, in the case $Ar = 10000$, in the shear region and for various Reynolds numbers. The kinetic energy second-order increment, depicted in Figure 4.14(a), collapses on a single curve when $Re \geq 8000$, up to experimental accuracy. An inertial range scaling $r_x^{2/3}$ can be observed in this common structure function. Pseudo mass fraction, shown in Figure 4.14(b) decreases when the Reynolds number increases, and collapses when $Re \geq 12000$. This trend is similar to our observation at the axis in the variable density case (Figure 4.11).

Figure 4.14(c) shows the nonlinear inter-scale transport in the shear for various Archimedes numbers. Here, we observe a forward cascade in all cases. When $Re \geq 8000$, all these structure functions collapse, up to statistical accuracy. The case $Re = 4000$ shows a similar profile, but with a weaker magnitude. The scales at which the minimum is reached is common to all these structure functions. The pseudo mass fraction counter-part, represented in Figure 4.14(d), shows two distinct regimes. When $Re \geq 12000$, all the nonlinear inter-scale transport terms collapse on a single curve, that is therefore independent of the Reynolds number. But, when $Re \leq 8000$, the scale at which this structure function starts to decrease is smaller. This is an indication that the forward cascade transfers energy starting from a different scale.

Inhomogeneous transport of kinetic energy in the variable density case is represented in Figure 4.14(e), for various Reynolds numbers. All these structure functions are positive, which indicates that the fluctuations are nonlinearly transported downstream. The case $Re = 8000$ shows larger structure function. The Yaglom equation counterpart of this term is represented in Figure 4.14(f). When $Re \leq 8000$, these structure functions are very close to zero at small scales, and grow to positive values at larger scales. This indicates a transport of fluctuations towards the downstream direction. On the contrary, when $Re \geq 12000$, the inhomogeneous transport reaches large negative values. Pseudo mass fraction variance is transported upstream.

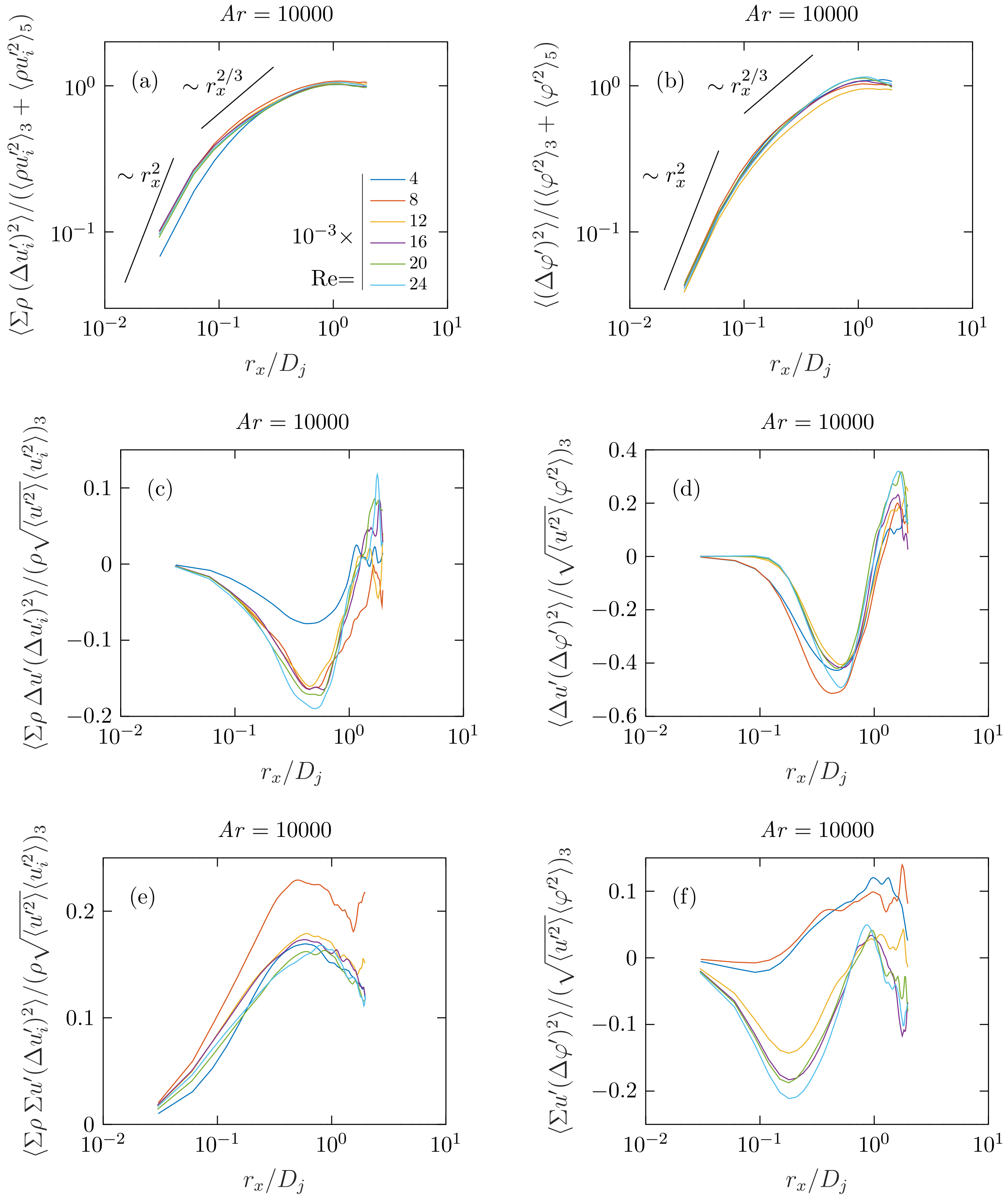

Figure 4.14: Structure functions with $Ar = 10000$ in the shear region for the temporal terms (a)-(b), nonlinear inter-scale transport (c)-(d) and inhomogeneous transport (e)-(f), and for various Reynolds numbers.

Next, we focus on the effect of density variations at fixed Reynolds number, on the scale-space fluxes of kinetic energy and pseudo mass fraction. Figure 4.15 represents the two-point statistics presented in Table 4.1, in the shear at $Re = 12000$ and for various Archimedes numbers. The kinetic energy increment, shown in Figure 4.15(a) follows a weak dependence on the Archimedes number. When $Ar \geq 5000$, these structure functions collapse over all ranges of scales, without showing an inertial range scaling $r_x^{2/3}$. The pseudo mass fraction counterpart of this quantity is represented in Figure 4.15(b). When $Ar \in [5000,\ 10000]$, this structure function collapses on a single curve. Whereas, when $Ar \geq 15000$, we notice a departure at the largest scale. The magnitude of this variation is small, but in agreement with the density variation effect on the same structure function at the axis (Figure 4.11(b)).

Figure 4.15(c) represents the nonlinear inter-scale transport of kinetic energy in the shear, for various Archimedes numbers. These structure functions are independent of density variations, and indicate a forward cascade of energy. The pseudo mass fraction inter-scale transport is depicted in Figure 4.15(d). The scale at which the cascade transfers pseudo mass fraction towards smaller scales depends on density variations. In the non-Boussinesq regime, this flux is zero until an intermediate scale, whereas in the Boussinesq regime, this quantity is non-zero at smaller scales.

Inhomogeneous transport of kinetic energy strongly depends on density variations. Figure 4.15(e) shows this flux, for different Archimedes numbers. We find a transport towards downstream direction that is monotonously proportional to the Archimedes number. The pseudo mass fraction inhomogeneous transport, shown in Figure 4.15(f), presents two distinct regimes. In the Boussinesq case ($Ar \leq 5000$), this quantity is close to zero and then grows. In non-Boussinesq regimes ($Ar \geq 10000$), all these quantities collapse on a single negative curve, which indicates a propagation of fluctuations towards the upstream direction.

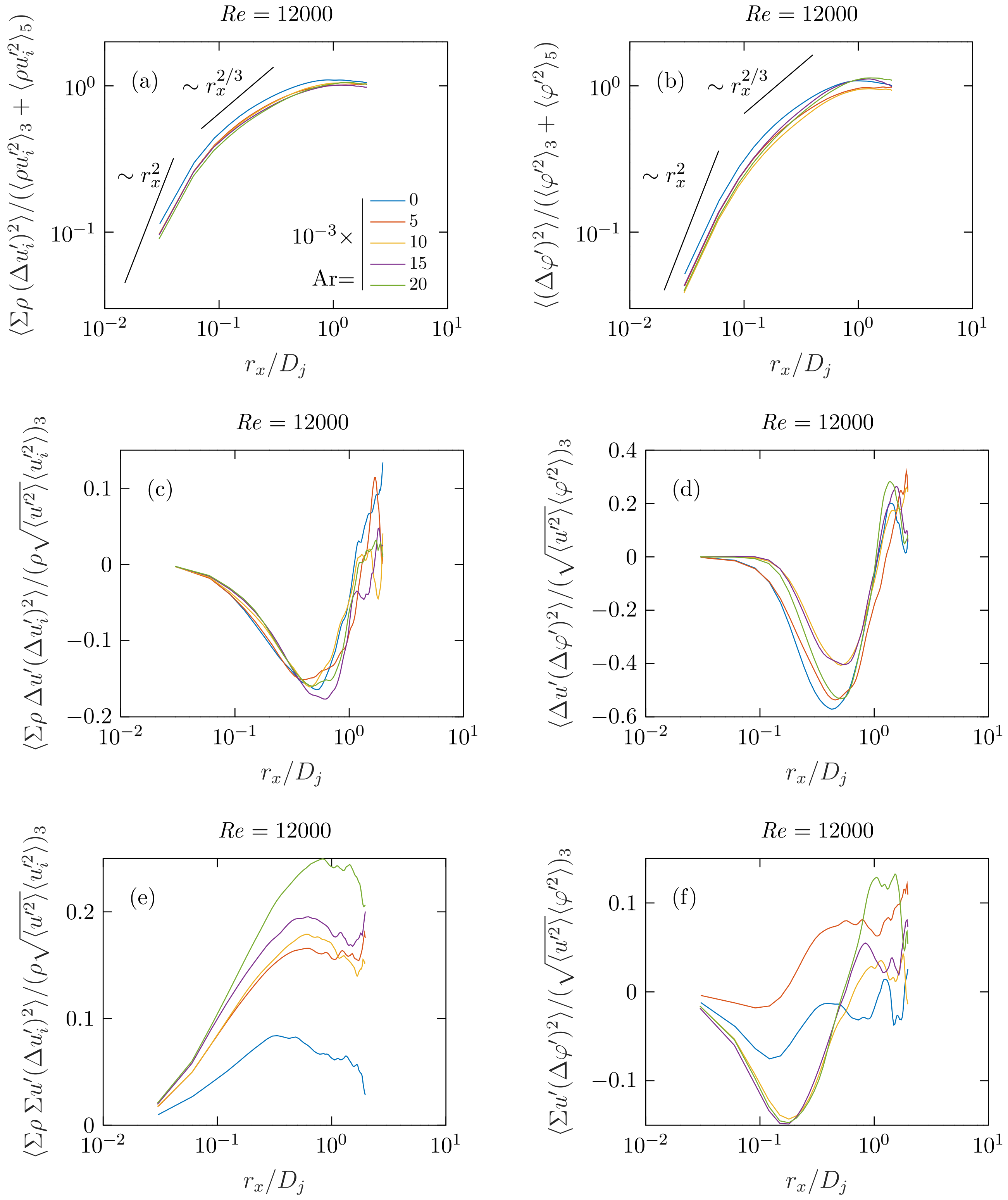

Figure 4.15: Structure functions with $Re = 12000$ in the shear region for the temporal terms (a)-(b), nonlinear inter-scale transport (c)-(d) and inhomogeneous transport (e)-(f), and for various Archimedes numbers.

4.3.4 Discussion

In this part, we evaluated some two-point statistics of both variable density Kolmogorov and Yaglom equations. These quantities were computed in two regions, at the axis to evaluate decay, and at the shear to quantify the fully developed regime. The results of this part can be summarized as follows

- Along the axis
  1. In the passive scalar case, kinetic energy and pseudo mass fraction variance do not show a high turbulence level, as the flow is mostly reminiscent from the pipe flow including the beginning of the decay at the end of the second-order potential core.
  2. In the variable density case, kinetic energy is fully developed at $Re \geq 20000$. The pseudo mass fraction shows a dissimmetric dependence on the Reynolds number. Increasing Re, this quantity first decreases until $Re = 12000$, and then collapses for all cases $Re > 12000$. This dissymmetry occurs when crossing the critical point $(Re, Ar)_{crit} = (12000, 10000)$. Turbulence is globally more developed than the passive scalar case.
  3. Density variations only have a weak influence on kinetic energy increment. The pseudo mass fraction second-order structure functions shows a jump when crossing the critical point $(Re, Ar)_{crit} = (12000, 10000)$. Above this line, these structure functions are invariant to density variations.
- In the shear
  1. In the passive scalar case, the flow is more turbulent than at the axis. The kinetic energy follows a direct cascade, and grows in the downstream direction. The magnitude of this transport is proportional to the Reynolds number. The pseudo mass fraction is more robust to Reynolds number variations, both in the increment and inter-scale transport. The inhomogeneous transport of this quantity shows a propagation of the fluctuations of this quantity towards the upstream direction.
  2. In the variable density case, the flow is globally closer to a fully developed turbulence regime. We found a more pronounced inertial range scaling $r_x^{2/3}$ in

this case. Kinetic energy is transported through scales at larger rates, as the magnitude of the inter-scale transport is larger than in the passive scalar case. Also, fluctuations propagate downstream. Pseudo mass fraction is more turbulent than kinetic energy. The inertial range scaling of this quantity is found to be larger, and almost independent of the Reynolds number. Inter-scale transport occurs at larger scales, when the critical line is crossed from below. The inhomogeneous transport of this quantity is almost null and then grows to positive values for small Reynolds numbers. But, when the critical line is crossed, large negative values of inhomogeneous transport are found, which indicates a strong propagation of pseudo mass fraction fluctuations upstream of the jet.

3. Kinetic energy and its inter-scale transport are robust to density changes. The inhomogeneous transfer of this quantity monotonously increases with increasing Archimedes number. Regarding pseudo-mass fraction, the second-order increment of this quantity shows a weak dissymmetric dependence on density variations. Nonlinear inter-scale and inhomogeneous transports differ between the Boussinesq and non-Boussinesq regimes, in magnitude and in the scales at which these quantities vary.

We conclude from this part that large density variations incorporate an additional length scale in the pseudo mass fraction cascade, when crossing the critical line from below. Consequently, pseudo mass fraction fluctuations are not transported to smaller scales at a higher rate, but their spatial propagation is more intense. These fluctuations spread faster within the flow, when the critical line is crossed from below.

4.4 TNTI statistics

In this section, entrainment of scalar in a round jet with variable density is studied. To do so, we evaluate conditional statistics through the thickness of the TNTI, as discussed in Section 1.2. First, the method that we used to compute the conditional statistics is described. Then, the mean and second-order moments of the mass fraction are exposed, for different values of (Re, Ar). Finally, we discuss our observations with the one and two-point statistics results.

4.4.1 TNTI detection method for spatially developing flows

The velocity measurement spatial resolution is low compared to the scalar measurements alone. The evaluation of conditional statistics using our PIV data is not possible, as the intense gradients at the vicinity of the TNTI are sub-grid to our measurements. Going back to the PLIF calibration procedure, presented in Section 3.2.2.4, we focus on the last calibration steps. Figure 4.16(a) and (b) illustrate the same scalar field with and without interpolation on the PIV grid, respectively. We discuss this figure hereinafter.

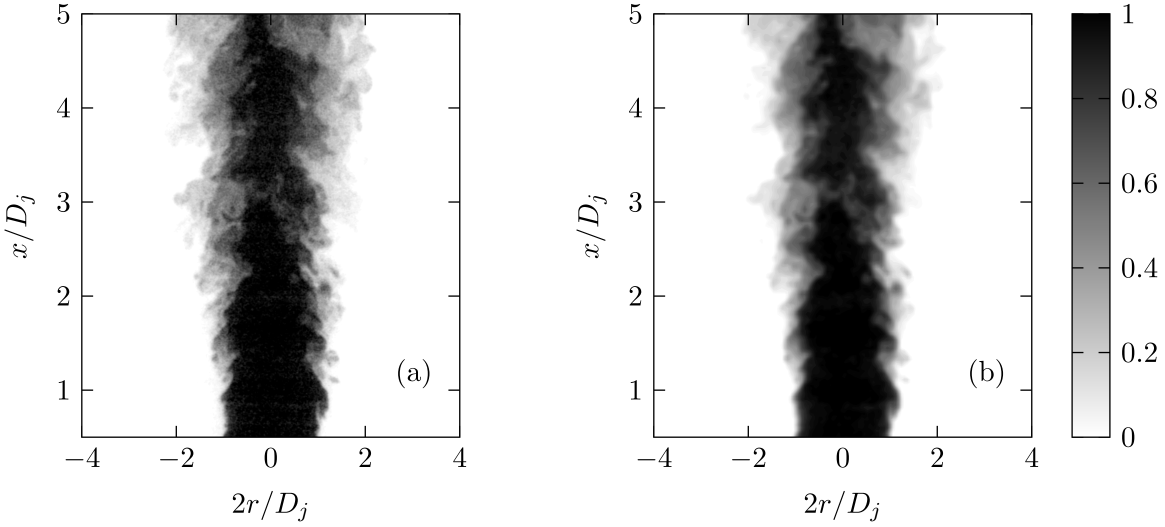

Figure 4.16: Typical raw PLIF measurement after shot-to-shot correction (a) and same image with a stricter filter and the additional step of interpolating on the PIV mesh (b). Here $(Re, Ar) = (12000, 0)$. The two figures share the same color map.

To improve the evaluation of scalar gradients, we apply two changes in the PLIF calibration. First, we do not interpolate the PLIF measurements on the PIV grid. This leads to higher resolution scalar fields, but forbids us from using combined velocity-scalar correlations. Second , we reduce the width of the filter that we used for smoothing the PLIF images. When interpolating, we could afford to use a strict filtering on the scalar field because the final resolution is lower. The scalar gradients in Figure 4.16(a) are clearly better evaluated than in Figure 4.16(b). We made sure that the signal distribution is not very altered by the more compliant filter.

The flow is spatially developing. For comparability with the one-point statistics results, we aim at computing the conditional statistics at $x/D_j = 5$. Doing so, we avoid the potential core contribution that would include a systematic bias in the statistics. The conditional statistics were computed in the interval $x/D_j \in [4.9, 5.1]$, to improve convergence. We make the hypothesis that the flow streamwise inhomogeneity is small, over such a short axial distance interval. The mean conditional mean scalar $\langle \phi \rangle_I$ is normalized by the mean scalar at the axis $\langle \phi \rangle_a$ taken at $x/D_j = 5$, and the turbulence intensity of this quantity $\mathcal{I}_{\phi,I} = \sqrt{\langle \phi'^2 \rangle_I} / \langle \phi \rangle_I$ is normalized by its value at the axis $\mathcal{I}_{\phi,a} = \sqrt{\langle \phi'^2 \rangle_a} / \langle \phi \rangle_a$. Also, we average the left and right TNTI statistics to improve the convergence even more.

The small values of mass fraction are not well enough resolved in our measurements for the Prasad & Sreenivasan (1989) method to be applied. Instead, we choose a threshold $\phi_0 = 0.08$ to detect the interface. We find that the classical Bisset *et al.* (2002) averaging technique, along fixed distances from the TNTI, is suitable for our study. The TNTI thickness is of the order of the Kolmogorov or the Taylor micro scales. This question is still open in the literature (da Silva *et al.*, 2014). In both cases, our spatial resolution for scalar measurements is still not high enough to reach any of these scales. Therefore, large gradients are not resolved. We use the TNTI statistics as an indication of the mixing, and not as a quantitative evaluation of the stresses involved in the vicinity of the TNTI.

We proceeded by performing a sensitivity study to the different parameters of our method. We found that the size of the filtering kernel, the length of the x/D_j interval for TNTI statistics and their normalization, and the value of the threshold to detect the TNTI only weakly influence the conditional statistics, in the neighborhood of the value we chose.

4.4.2 Conditional statistics of the scalar fields

In this part, we evaluate the variation of the scalar conditional statistics along different lines in the (Re, Ar) plane, at the streamwise position $x/D_j = 5$. The purpose is to cross the critical line that we found in the one-point statistics (Figure 4.6(b)). Figure 4.17(a) shows the scalar conditional mean in the passive scalar case $(Ar = 0)$ at $x/D_j = 5$, for various Reynolds numbers. For all Reynolds numbers, we find an abrupt mean scalar increase within a shallow region at the vicinity of the TNTI. Then, these quantities endure a smoother monotonous increase, asymptotically towards 1. In the case $(Re, Ar) = (4000, 0)$, the conditional mean scalar shows an overshoot inside the TNTI. This effect is also present at higher Reynolds numbers, but at a much smaller magnitude. The observed overshoot is in agreement with the literature (Figure 1.8(a)), and will be discussed hereinafter.

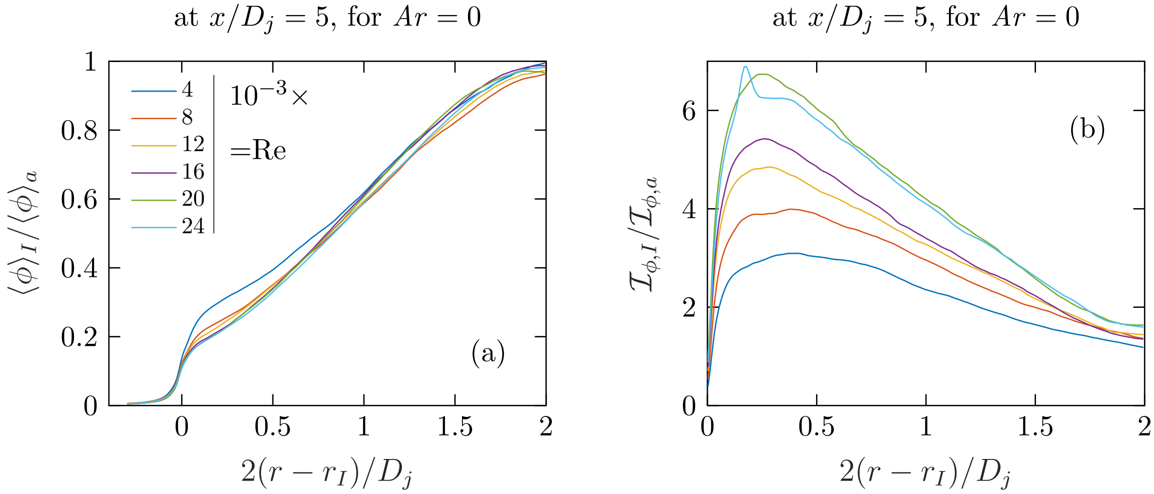

Figure 4.17: Conditionally average normalized scalar mean (a) and scalar turbulence intensity (b), at $x/D_j = 5$ in the passive scalar case $(Ar = 0)$, and for different Reynolds numbers.

Figure 4.17(b) illustrates the conditional scalar turbulence intensity, represented in the same conditions as Figure 4.17(a). Compared to the axis value of the scalar turbulence intensity, this quantity overshoots at a depth of $2(r - r_I)/D_j = 0.25 - 0.35$. The magnitude of this peak is proportional to the Reynolds number. The fluctuations that are generated at the edge of the jet by production mechanisms are transported towards the core, until these fluctuations contaminate totally the jet. The lower peak for the lower Reynolds number indicate a more established scalar turbulence intensity profile, whereas a large peak, like for $Re = 20000$, large fluctuations indicate that the jet is less developed. We notice that at $Re = 24000$, we see a small peak at $2(r - r_I)/D_j = 0.17$. This peak remains from the initial sharp scalar gradient at the injection. Except the small injection peak, we observe that the conditional scalar turbulence intensity is independent of the Reynolds number when $Re \geq 20000$. These observations are in agreement with the fact that larger Reynolds numbers delay the transition.

Now, we focus on the momentum effect on a variable density case. Figure 4.18(a) represents the conditionally averaged mean scalar at $x/D_j = 5$ and for $Ar = 10000$, for various Reynolds numbers. In all cases, this quantity undergoes a steep increase through the TNTI, and then a gradual increase towards the core value of 1. When $Re \geq 12000$, all the profiles collapse, independently of the Reynolds number. The increase in the cases $Re \leq 8000$ occurs at a higher value after the TNTI. The fast increase of the conditionally averaged mean scalar at the vicinity of the TNTI is probably not fully captured by our measurements, and so is the case for the overshoot of the scalar inside the TNTI for the cases $(Re, Ar) = (12000, 10000)$. Nevertheless, the linear variation is precisely evaluated, and we observe an invariance of this profile to the Reynolds number when $Re \geq 12000$.

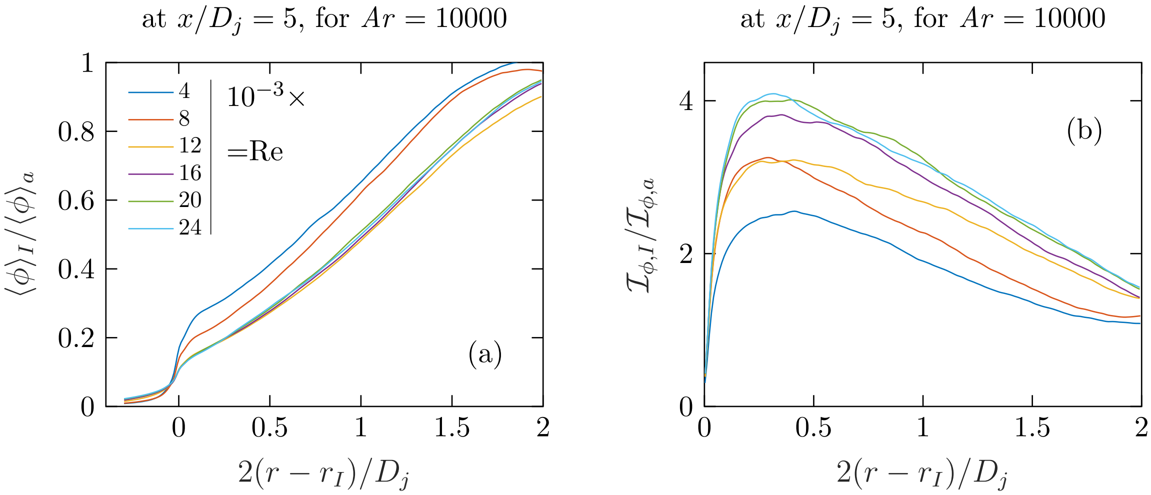

Figure 4.18: Conditionally averaged normalized scalar mean (a) and scalar turbulence intensity (b), at $x/D_j = 5$ in the case $Ar = 10000$, and for different Reynolds numbers.

Figure 4.18(b) represents the scalar turbulence intensity in a conditional averaging approach, in the same conditions as Figure 4.18(a). The behavior of this quantity is similar to the conditionally averaged mean scalar, with a difference for the case $Re = 12000$. The cases $Re \geq 16000$ collapse on the same profile, and show a peak that is four times larger than the axis value of this quantity, at $2(r - r_I)/D_j = 0.35$. When $Re \leq 12000$, we find lower values of the conditioned scalar turbulence intensity, at the same position. The particular case $Re = 12000$ reaches a peak of the same order of the case $Re = 8000$, but then converges towards the same curve as the higher Reynolds number cases. Opposite to the passive scalar case, we do not observe a strong peak at $(Re, Ar) = (24000, 10000)$ (comparing to Figure 4.17(b)).

Now, we focus on the effect of density variations on the scalar conditional statistics. Figure 4.19(a) shows the conditionally averaged mean scalar at $x/D_j = 5$ in the case $Re = 12000$, for various Archimedes numbers. No overshoot is observed, in any considered case. The conditionally averaged mean scalar only shows a weak variability to the Archimedes number, in this configuration. Through the thickness of the TNTI, we notice that the profiles collapse in the Boussinesq regime ($Ar \leq 5000$).

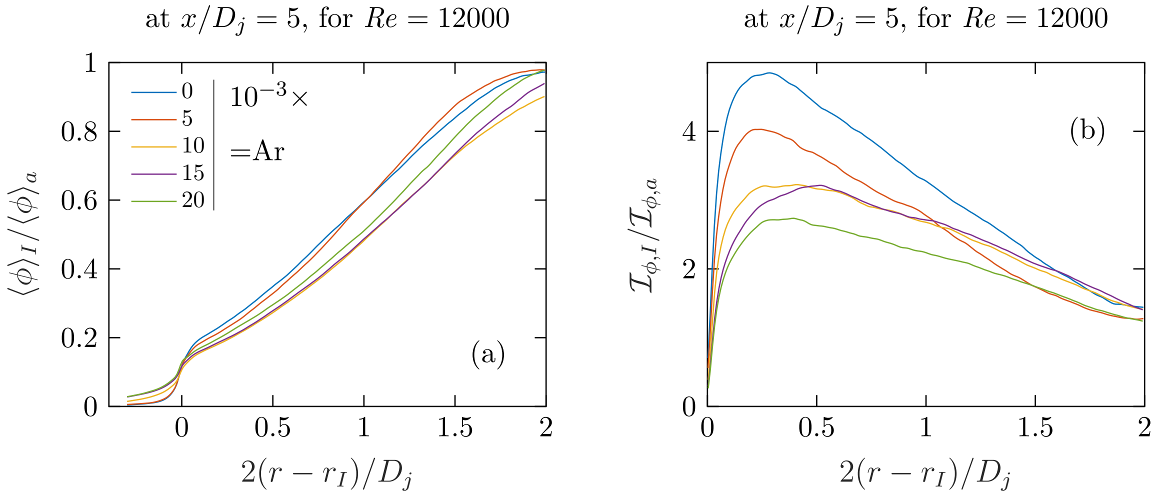

Figure 4.19: Conditionally averaged normalized scalar mean (a) and scalar turbulence intensity (b), at $x/D_j = 5$ in the case $Re = 12000$, and for different Archimedes numbers.

Figure 4.19(b) depicts the variation or the conditioned scalar turbulence intensity, in the same conditions as Figure 4.19(a). In the passive scalar case ($Ar = 0$), this quantity reaches a peak of 4.8 at $2(r - r_I)/D_j = 0.25$, and in the case $Ar = 5000$ a peak of 4 is reached at the same position. For higher Archimedes numbers, the peak is of the order of $2 - 3$, and the fluctuations are overall better distributed inside the jet. This result indicates that the transport of fluctuations towards the core is enhanced, when the jet is in the non-Boussinesq regime.

4.4.3 Discussion

The conventional statistics approach does not capture the local flow dynamics at the vicinity of the jet edge. In this section, we compared the conditional scalar statistics, normalized by their respective axis values. The main results from this section can be summarized as follows

1. The trends that we found in one-point statistics are recovered, so that in increase in the Reynolds number delays the growth of fluctuations, whereas in an increase in Archimedes number enhances this growth.

2. In the TNTI frame of reference, the influence of the Reynolds and Archimedes numbers manifests through the propagation of the fluctuations that are created at the vicinity of the TNTI towards the core. When the transition is delayed, the scalar turbulence intensity is very large in a shallow region inside the TNTI, when compared to its core value. In a jet that is closer to the full establishment of turbulence, the fluctuations are better distributed through the thickness of the jet, which corresponds to the conventional Gaussian profile that is well known in the literature.

3. Crossing the different flow regimes for the scalar turbulence intensity in the (Re, Ar) plane, we find the point $(12000, 10000)$ indeed separates different regimes. But, the conditional profiles show a stronger variability to the flow parameters than the conventionally averaged radial profiles. The Reynolds number variation at $Ar = 10000$ is similar to the conventional radial profile, shown in Figure 4.8(e). On the other hand, the Archimedes number variation at $Re = 12000$ is more conclusive in the conditional frame, than the conventional radial profile, shown in Figure 4.8(f).

4.5 Conclusion

In this chapter, we studied a variable density round jet. Data were aquired using experiemental measurements, as exposed in Chapter 3. Three approaches were used to assess this problem, one-point statistics, two-point statistics and TNTI statistics. We summarize the main results of each approach in the following, focusing on scalar mixing. In the following we summarize the results of these different approaches.

1. One-point statistics allowed us to validate the measurements, comparing with round jets literature. In these flows, increasing the injected momentum delays the growth of fluctuations, whereas lowering the density of the jet has the opposite effect. We explore the combination of these two competing effects, using the Reynolds and Archimedes numbers, to control the injected momentum and density deficit, respectively. We span both Boussinesq and non-Boussinesq regimes. At a fixed downstream position of $x/D_j = 5$, we found that the turbulence intensity of the scalar shows multiple regimes, depending on the dimensionless numbers. In particular, this quantity endures a bifurcation in the non-Boussinesq regime, separated by the critical line $Re_{crit} = 24000 - \frac{4}{3}(Ar - 5000)$. In the Reynolds number is below this value, the scalar turbulence intensity at the axis is very robust to changes in injected density deficit, whereas when the Reynolds number is above this line, this quantity is very robust to injected momentum changes (Figure 4.6(b)).

To further study these regimes, we evaluated statistics following the two lines defined by $Ar = 10000$ and $Re = 12000$ in the parameter space. We focused first on the conventionally averaged radial profile of scalar turbulence intensity. Crossing the critical line by increasing the Reynolds number with $Ar = 10000$, this quantity shows a similar bifurcation as at the axis. On the contrary, crossing the critical line by increasing the Archimedes number with $Re = 12000$ is not as conclusive.

2. In the two-point statistics framework, we evaluated some terms of the variable density Kolmogorov and Yaglom equations. Kinetic energy follows a direct cascade and is transported towards the downstream direction, in all cases considered. Regarding

pseudo mass fraction variance, the scales at which inter-scale transport occurs depend on momentum in the variable density case, and on density variations in the fully developed turbulent regime. Inhomogeneous transport shows a propagation of pseudo mass fraction fluctuations in the shear region towards the upstream direction. This propagation upstream takes place only when the flow conditions are above the critical line.

3. The conventional mean approach is not suitable at the edge of free shear flows, as it considers turbulent and non-turbulent flow under the same average (Section 1.2). To this matter, we evaluated conditional statistics of the mean scalar and scalar turbulence intensity, along reference lines in the (Re, Ar) plane. We found that the general dependence on the Reynolds and Archimedes numbers is in agreement with the one-point statistics observations. Nevertheless, the conditionally averaged profiles of the scalar turbulence intensity show a very large peak, compared to the axis value of this quantity. This peak has a large variability depending on the dimensionless numbers of this study. The conditional averaging unravels scalar dynamics that are smoothed by the conventional averaging approach. We found that mixing in the very near field of variable density round jets mostly occurs in a very shallow region, inside the TNTI.

We conclude from this chapter that momentum and density variations on a turbulent round jet not only change the growth of fluctuations, but also heavily affect the direction of their propagation in scale-space. We found that these fluctuations can propagate by nonlinear inhomogeneous transport towards the upstream direction. Also, the scale at which the forward cascade occurs is very affected. At the vicinity of the TNTI, mixing in this region strongly depends on the Reynolds and Archimedes numbers, and endures different regimes in the non-Boussinesq configuration, that were not observed previously in the literature.

Chapter 5

Variable viscosity and mass diffusivity temporally evolving plane jet

In this chapter, we study a temporally evolving turbulent plane jet, with variable viscosity and mass diffusivity. This work is a followup to Brahami *et al.* (2017), which we include in the discussion hereinafter. First, we briefly describe the simulation setup and the processing method. Then, we evaluate statistics both conventionally and conditionally, focusing on the kinetic energy and scalar dissipation rates. Finally, we include a publication to be submitted, summarizing our most striking results.

5.1 Simulations and post-processing method

Direct numerical simulation (DNS) of a temporally evolving turbulent plane jet was performed by Dr M. Gauding in our group, as described by Gauding *et al.* (2015) and Hunger *et al.* (2016). The DNS solves the dimensionless Navier-Stokes equations with variable viscosity and mass diffusivity, equations (2.48)-(2.51), that we repeat here for the sake of clarity,

$$\begin{aligned}
\partial_j u_j = 0, \quad \psi &= \mathcal{R}_\psi^{\phi-1}, \\
\partial_t u_i + u_j \partial_j u_i &= -\partial_i p + \frac{1}{Re}\partial_j(\psi(\partial_j u_i + \partial_i u_j)), \\
\partial_t \phi + u_j \partial_j \phi &= \frac{1}{Pe}\partial_j(\psi \partial_j \phi),
\end{aligned}$$

where ψ is both the momentum and mass diffusivities, and $\mathcal{R}_\psi$ is a control parameter. To avoid cumbersome terminology, we will refer to ψ as the *diffusivity*, and to $\mathcal{R}_\psi$ as the *diffusivity ratio*. The parameter $\mathcal{R}_\psi$ is the ratio between the outer and inner diffusivities. These simulations were carried out on the supercomputer JUQUEEN at research center Juelich (Germany). In the following, details of the DNS setup are summarized. The computational domain is shown in Figure 5.1. The boundary conditions in stream-wise Ox and span-wise Oy directions are periodic, while free-slip boundary conditions are used in the cross-wise Oz direction. The flow is statistically homogeneous in xOy planes. Conventional statistics are performed over these planes and depend only on time t and the cross-wise coordinate z. The size of the domain is large compared to the integral scales of the jet, thus avoiding confinement effects. The grid width is smaller or equal to the smallest Kolmogorov length scale of the flow. The box grid size is $2048 \times 1024 \times 1024$, in the (x, y, z) directions, respectively.

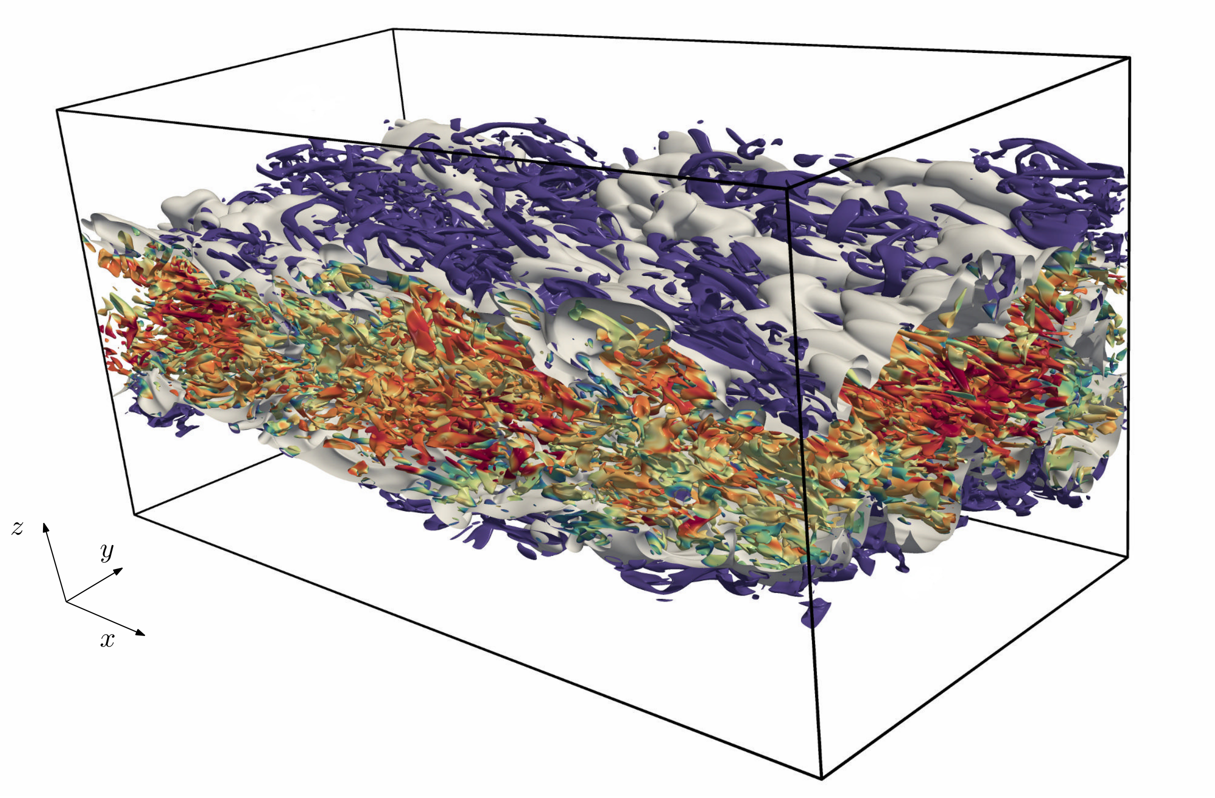

Figure 5.1: A view of the flow simulation, with the computational domain. The iso-surface represents the Q-criterion at a value of 0.7, and the colors are the scalar values at the surface. The gray surface is the TNTI. Figure realised by Dr M. Gauding.

To simplify the definition of the dimensionless numbers, we keep the jet initial conditions unchanged from one case to another, and we modify the external flow conditions. We choose the jet initial center-plane diffusivity $\psi_{0,a}$, velocity $u_{0,a}$ and momentum thickness δ_0 and outer diffusivity $\psi_{0,out}$ as reference quantities. Subscripts 0, a and out indicate the initial, center-plane and outer flow conditions, respectively. The jet width δ_0 is defined as the distance between the points at which the mean streamwise velocity decreases to 50% of its center-line value. As stated in Section 2.3.1, the Schmidt number equals unity, locally and instantaneously, so that the Reynolds and Peclet numbers are $Re = Pe = u_{0,a}\delta_0/\psi_{0,a} = 2000$. The temporal variable in the subsequent simulation is normalized by the characteristic time $\delta_0/u_{0,a}$.

The flow is initialized using hyperbolic tangent profiles that are symmetrized with respect to the center-plane for both velocity and scalar, as shown in Figure 5.2. In the following, we normalize the cross-wise direction z by the instantaneous half-velocity width of the jet $\delta_{1/2}$. We made sure that the forcing is weak enough to avoid by-pass transition. In practical gas flows, $\mathcal{R}_\psi$ rarely exceeds 10, consequently, we consider cases where $\mathcal{R}_\psi = 0.25, 0.5, 1, 2, 4$ (see Figure 5.2 (b)).

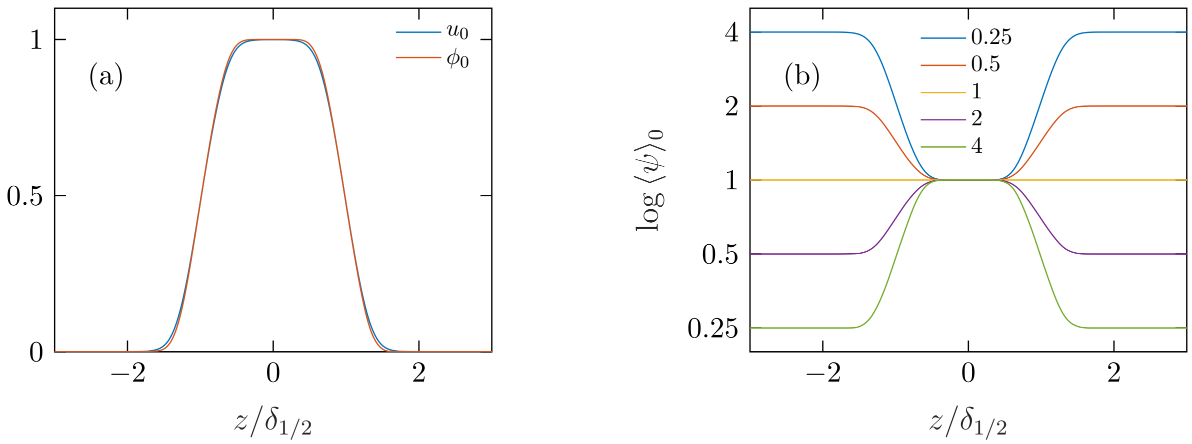

Figure 5.2: Initial profiles of velocity and scalar (a) diffusivity (b), for different diffusivity ratios $\mathcal{R}_\psi$.

As introduced in Section 1.2.1, the classical Prasad & Sreenivasan (1989) method for locating the TNTI was developed for passive scalar flows. It is first necessary to check that the method is not sensitive to diffusivity variations. In our case, variable viscosity and mass diffusivity are additional parameters to the interface detection. Figure 5.3 (a) shows the scalar probability density function over the whole computational domain at the same physical time and for different diffusivity ratios $\mathcal{R}_\psi$. We found that this technique is robust to the diffusivity variations. In particular, the inflectional point of the normalized conditional average of the scalar $\langle \phi | z - z_I \rangle / \langle \phi \rangle_a$ is always located at the TNTI, as shown in Figure 5.3 (b). We recall that the symbol $\langle (.) | z - z_I \rangle$ denotes conditional averaging, and is only a function of the distance to the TNTI $(z - z_I)$. The dependence of this quantity on $\mathcal{R}_\psi$ will be discussed in Section 5.3. The typical threshold values found are comprised between 0.07 and 0.13.

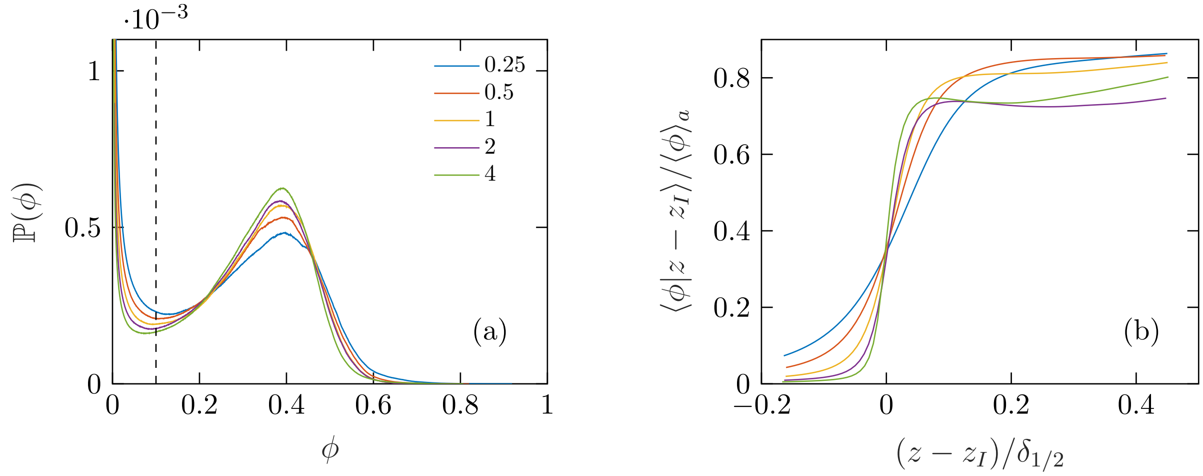

Figure 5.3: Scalar probability density function over the whole computational domain (a) and conditional average of the scalar normalized by the center-plane value (b), for different diffusivity ratios $\mathcal{R}_\psi$.

5.2 Conventional statistics

Turbulent temporal plane jets show, after a long enough time after injection, a self-preserving behavior. In this regime, conventionally averaged mean fields are self-similar in time and decay following analytically predictable laws. This feature has been observed in both spatially and temporally evolving turbulent jets (Sadeghi *et al.*, 2018). Figure 5.4 represents the temporal evolution of the mean streamwise velocity and scalar at the center-plane. These quantities are invariant until $t = 5$, which corresponds to the potential core. Then, a self-preserving decay is very weakly dependent on the diffusivity ratio $\mathcal{R}_\psi$.

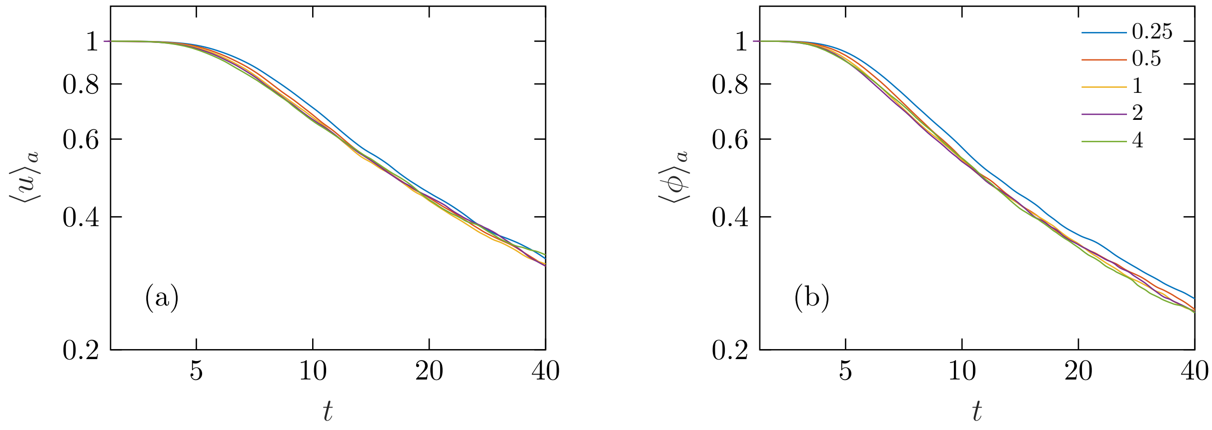

Figure 5.4: Temporal center-plane conventional evolution of mean streamwise velocity (a) and mean scalar (b), for different diffusivity ratios $\mathcal{R}_\psi$.

Turbulent kinetic energy (TKE) $\langle k \rangle_a = \langle u_i'^2 \rangle / 2$ is represented in Figure 5.5 (a). The early evolution of this quantity is affected by diffusivity variations, causing a staggering proportionally to the diffusivity ratio $\mathcal{R}_\psi$. This period of the flow lifespan is characterized by Kelvin-Helmholtz instabilities. The young vorticies grow fast and reach nonlinear saturation, so the TKE reaches a peak. If the jet is less diffusive than the outer flow (i.e. $\mathcal{R}_\psi < 1$), the peak is smaller and occurs later, whereas if the jet is more diffusive (i.e. $\mathcal{R}_\psi > 1$), the peak is larger and occurs sooner, compared to the passive scalar case ($\mathcal{R}_\psi = 1$). This feature is well known in the context of variable viscosity alone (Govindarajan & Sahu, 2014; Harang *et al.*, 2014; Taguelmimt *et al.*, 2016) and is explained by the respective orientation of the shear and viscosity gradients. In our study, we notice that mass diffusivity variations do not alter the variable viscosity effect on the dynamics of TKE, when $\nu = \mathcal{D}$.

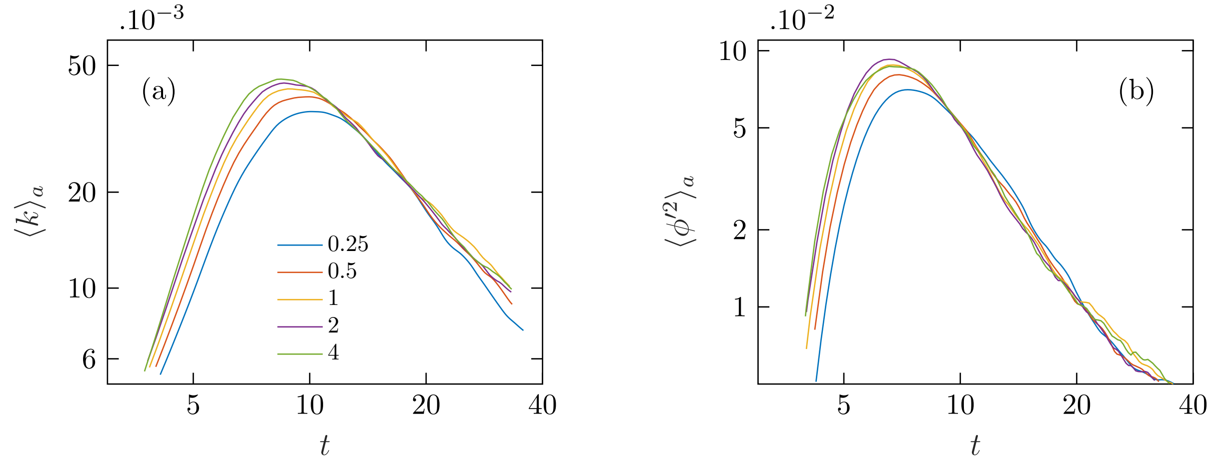

Figure 5.5: Temporal evolution at the center-plane turbulent kinetic energy (a) and scalar variance (b), for different diffusivity ratios $\mathcal{R}_\psi$.

The scalar variance $\langle \phi'^2 \rangle_a$ does not exhibit the same effect as TKE, as shown in Figure 5.5 (b). We find a dissymmetry, so that for $\mathcal{R}_\psi < 1$ the maximum value is weaker and occurs later. Jets with $\mathcal{R}_\psi \geq 1$ behave almost indistinguishably as the passive scalar case. We explain this effect by the early smoothing of the scalar gradient, in the cases $\mathcal{R}_\psi > 1$. The interface diffuses better because of local diffusivity at this location is large enough to weaken the scalar fluctuations.

The later time evolution of both TKE and scalar variance is independent of the initial diffusivity inhomogeneities, and respectively follow a unique temporal power law for all cases. The independence of the mean streamwise velocity and scalar, together with their respective second-order moments at the center-plane of the jet (i.e. Figures 5.4 and 5.5) shows that the self-preserving decay is independent of the diffusivity ratio. The jet core adapts to diffusivity variations, at least as found through low-order statistics. Nevertheless, diffusivity variations are as large as a factor of 4 in the extreme cases we consider. As we focus on mixing, the kinetic energy pseudo dissipation and scalar dissipation rates are of interest. These quantities read

$$\varepsilon = 2\psi A_{ij}^2 \quad \text{and} \quad \chi = 2\psi g^2, \tag{5.1}$$

where $A_{ij}^2 = (\partial_j u_i)^2$ and $g^2 = (\partial_j \phi)^2$, respectively. Strictly speaking, these quantities are the squares of the Frobenius norms of the velocity gradient tensor and scalar gradient vector, respectively. For clarity, we still refer to these quantities as norms, because they appear in this form in the dissipation rates analytical expressions. Next, we focus on the diffusivity field ψ.

Figure 5.6(a) shows the temporal evolution of the conventional mean of diffusivity at the center-plane. Notice that this plot uses logarithmic scales. This quantity departs from its initial value of 1 when the mean scalar decays, starting from $t = 5$ (Figure 5.4(b)). The departure from the center-plane value is symmetric and inversely proportional to $\mathcal{R}_\psi$, in the logarithmic frame of reference. On the other hand, Figure 5.6 (b) represents the diffusivity turbulence intensity $\langle \mathcal{I}_\psi \rangle_a = \sqrt{\langle \psi'^2 \rangle_a} / \langle \psi \rangle_a$ at the center-plane. At early times, this quantity presents a dis-symmetric dependence on diffusivity ratio, so that the $\mathcal{R}_\psi = 4$ and $\mathcal{R}_\psi = 0.25$ cases respectively reach a maximum at 40% and 35%. This discrepancy vanishes quickly, and the diffusivity turbulence intensity converges towards two common decay curves, starting from $t = 8$. Hereinafter, we give an explanation for the collapse of this quantity on two curves.

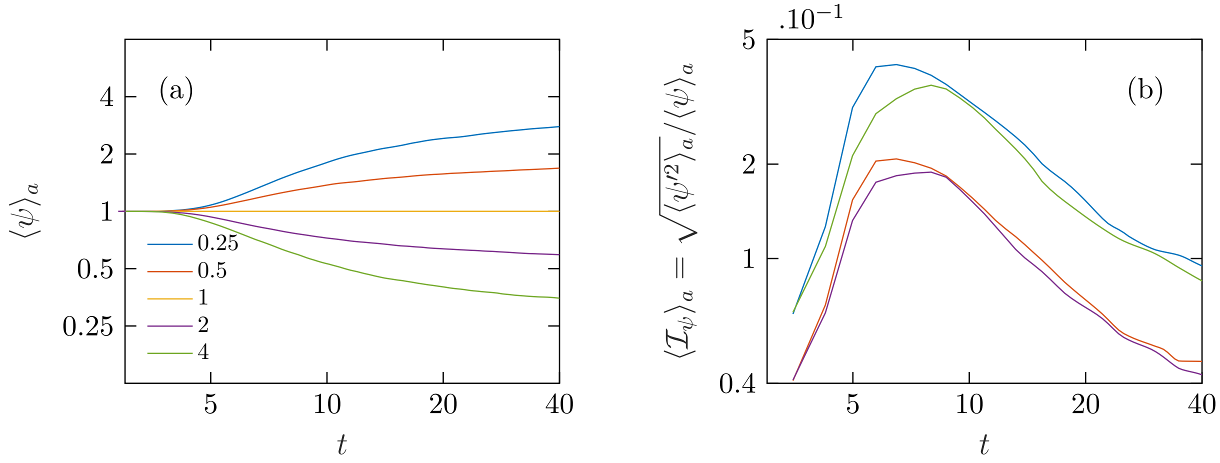

Figure 5.6: Temporal center-plane conventional evolution of mean diffusivity (a) and diffusivity turbulence intensity (b), for different diffusivity ratios $\mathcal{R}_\psi$.

The diffusivity turbulence intensity asymptotic variation at large times can be estimated using the averaged state equation (2.51). A Taylor expansion for the scalar fluctuation leads to

$$\langle \psi \rangle = f(\langle \phi \rangle) + o(\langle \phi'^2 \rangle) \quad \text{and} \quad \langle \psi'^2 \rangle = \left(d_\phi f \Big|_{\phi = \langle \phi \rangle} \right)^2 \langle \phi'^2 \rangle + o(\langle \phi'^4 \rangle), \tag{5.2}$$

where $f(\phi;\mathcal{R}_\psi)$ is the state equation. The only necessary condition for this relation to be valid is that the scalar turbulence intensity is small enough over the region where the averaging is performed. We find that the mean scalar, and scalar variance decay following temporal power laws. When applied to our case, we find the large time asymptotic expressions

$$\langle\psi\rangle_a \sim \frac{1}{\mathcal{R}_\psi}(1+\log\mathcal{R}_\psi\, t^{-n}) \quad \text{and} \quad \langle\mathcal{I}_\psi\rangle_a = \frac{\sqrt{\langle\psi'^2\rangle_a}}{\langle\psi\rangle_a} \sim \sqrt{(\log\mathcal{R}_\psi)^2}\, t^{-m/2}, \tag{5.3}$$

where n and m are the decay exponents of the mean and second-order scalar, respectively. From these simulations, we find $n = 1/2$ and $m = 1$, which is in agreement with the self-preservation predictions (Sadeghi *et al.*, 2018). At later times, we observe indeed that $\mathcal{I}_{\psi,a}$ decay depends only on $|\log\mathcal{R}_\psi|$. The diffusivity field asymtotically decorrelates from the dynamic field, and the effects of variable diffusivity that we see are mostly due to mean diffusivity gradients.

Next, we evaluate the gradient magnitude of the velocity and scalar fields, represented in Figures 5.7 (a) and (b), respectively. These quantities exhibit a large dependence on the diffusivity variations, even in the self-preserving regime. In the first stage, the gradients grow until $t = 10$, reaching a peak value that is proportional to $\mathcal{R}_\psi$. Then, the flow decays from that peak, with a temporal exponent that is independent of $\mathcal{R}_\psi$. This trend is similar to TKE and scalar variance, with the difference that the decay curves stagger.

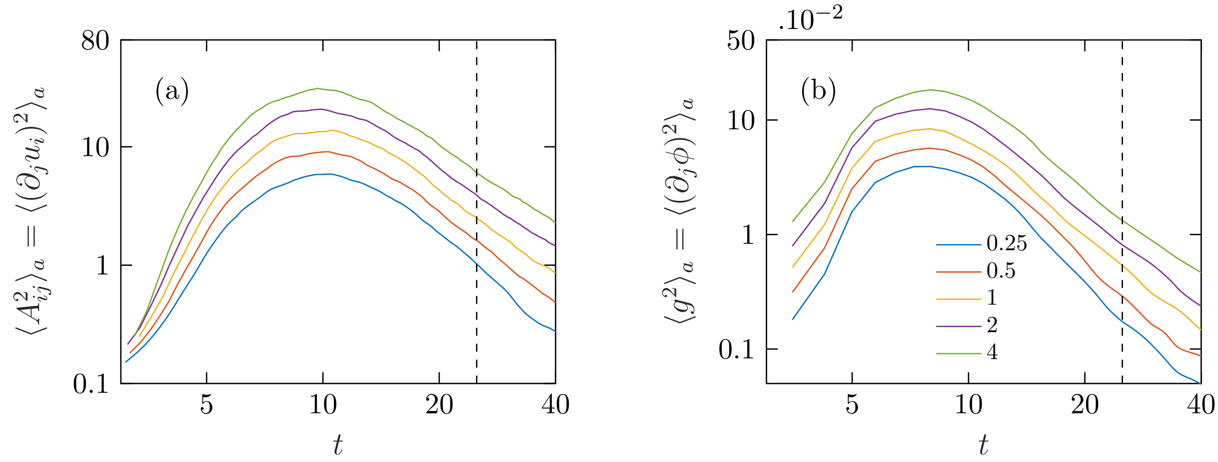

Figure 5.7: Temporal center-plane conventional evolution of velocity gradient norm (a) and scalar gradient norm (b), for different diffusivity ratios $\mathcal{R}_\psi$. The dashed lines correspond to the time-step considered in Figure 5.8.

The spatial profile of the velocity and scalar gradients at $t = 25$, are shown in Figures 5.8 (a) and (b) respectively. The overall dependence of these fields is similar to the center-plane temporal evolution (Figure 5.7), so that the gradient magnitude is proportional to the diffusivity ratio $\mathcal{R}_\psi$. We explain this feature as follows. The local low values of viscosity (respectively mass diffusivity) permit the turbulent cascade to transfer kinetic energy (respectively scalar variance) towards smaller scales, and consequently the velocity gradients (respectively scalar gradients) are locally larger. Also, the scalar gradient shows a peak around $z/\delta_{1/2} \sim 1$.

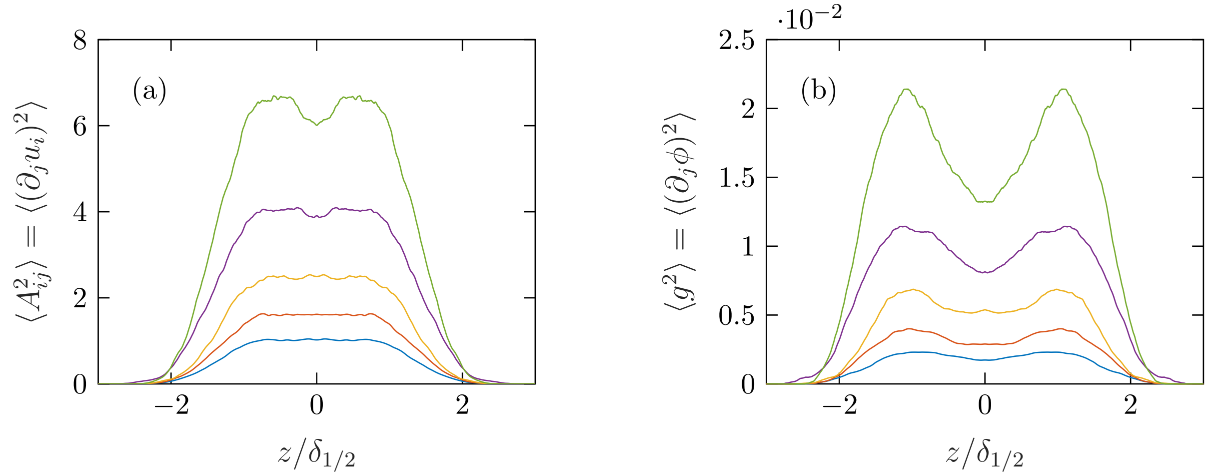

Figure 5.8: Spatial conventional average of the velocity gradient norm (a) and scalar gradient norm (b), at $t = 25$, for different diffusivity ratios $\mathcal{R}_\psi$. See Figure 5.7 (b) for legend.

Figures 5.9 (a) and (b) represent the center-plane temporal evolution of the kinetic energy pseudo dissipation rate $\langle \varepsilon \rangle_a = 2\langle \psi A_{ij}^2 \rangle_a$ and scalar dissipation $\langle \chi \rangle_a = 2\langle \psi g^2 \rangle_a$ rate, respectively. These quantities show the same dependence as the second-order velocity and scalar one-point statistics (Figure 5.5). It is well known that the flow *adapts* to the viscosity variations Lee *et al.* (2008); Kumar *et al.* (2011); Gréa *et al.* (2014); Gauding *et al.* (2018). We find that, in the self-preserving regime, the scalar gradient field also adapts to the diffusivity variations.

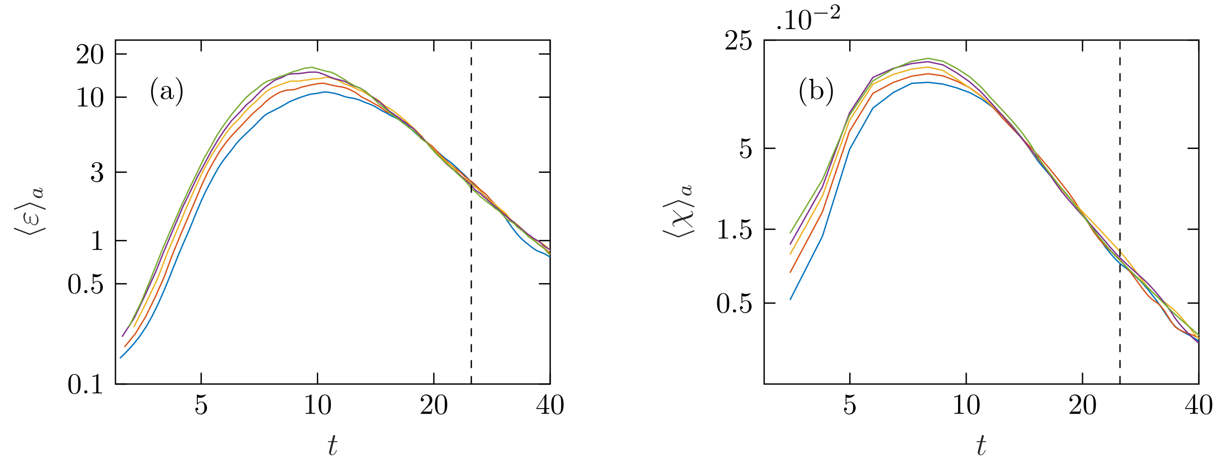

Figure 5.9: Temporal center-plane conventional evolution of kinetic energy pseudo dissipation rate (a) and scalar dissipation rate (b), for different scalar ratios $\mathcal{R}$. The dashed line represents the considered time-step in Figure 5.10.

Figures 5.10 (a) and (b) depict the conventionally averaged spatial profile of the kinetic energy pseudo dissipation and scalar dissipation rates at time $t = 25$, respectively. At this time, the flow is fully developed and all the low-order statistics are in the self-preserving regime in the core. From Figures 5.9 and 5.7, it is clear that, when conventionally averaged, the flow adapts completely to the active scalar variations, within numerical accuracy.

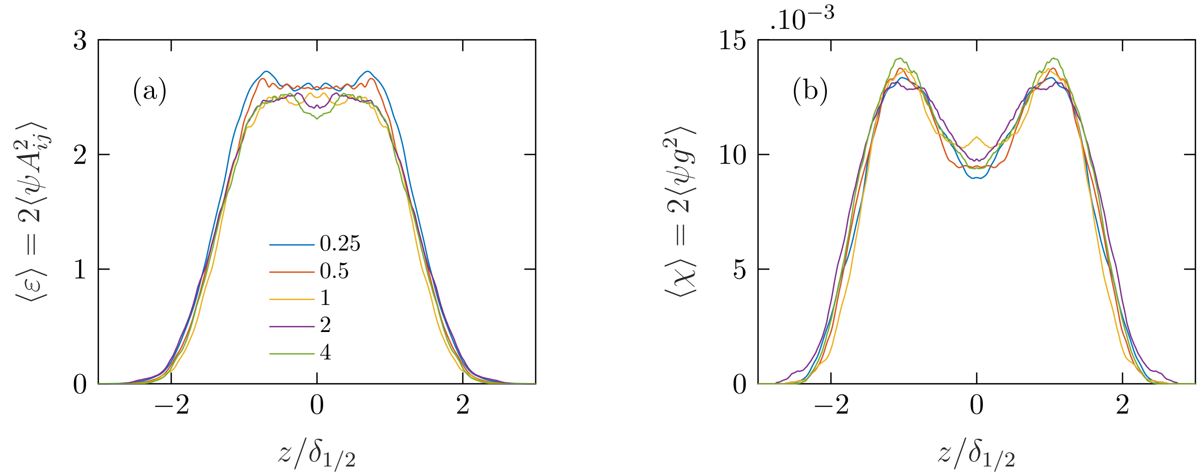

Figure 5.10: Spatial conventional average of kinetic energy pseudo dissipation rate (a) and scalar dissipation rate (b), at $t = 25$.

Mini conclusion

Until this section, we introduced the temporally evolving turbulent jet, with variable viscosity and mass diffusivity. We discussed the particular choice of unity Schmidt number and the state equation for both diffusivities. Then, we exposed conventional statistics of the flow, and demonstrated that a self-preserving regime is reached early in the simulations.

As we are interested in the mixing properties of this flow, we focused on the kinetic energy pseudo dissipation and scalar dissipation rates. We conclude from this part that we can write

$$\langle\varepsilon\rangle(t, z/\delta_{1/2}) \sim \underbrace{\langle\varepsilon\rangle_a(t)}_{\text{temporal}}\ \underbrace{h_\varepsilon(z/\delta_{1/2})}_{\text{spatial}}, \tag{5.4}$$

$$\langle\chi\rangle(t, z/\delta_{1/2}) \sim \underbrace{\langle\chi\rangle_a(t)}_{\text{temporal}}\ \underbrace{h_\chi(z/\delta_{1/2})}_{\text{spatial}}, \tag{5.5}$$

where $\langle\varepsilon\rangle_a = 2\langle\psi\rangle_a\langle A_{ij}^2\rangle_a$ and $\langle\chi\rangle_a = 2\langle\psi\rangle_a\langle g^2\rangle_a$ are the center-plane temporal evolution of the dissipation rates, and the terms denoted as spatial are the cross-wise profiles normalized by the center-plane value of these quantities. We found that in self-preserving regime and when Equations (5.4)-(5.5) are written in a conventional averaging sens, that temporal variations of the dissipation rates are independent of the diffusivity ratio $\mathcal{R}_\psi$. We also find that the spatial profiles h_ε and h_χ are very near to a single curve, within numerical accuracy.

The conventional averaging approach is unnatural, as we use the Cartesian coordinates for their computational convenience. Next, we focus on the same quantities that we computed in the last section, but averaged in a conditional manner, in the vicinity of the TNTI. This location is important in a shear flow, because it is the region where most momentum and mass exchanges with the outer-flow occur.

5.3 Conditional statistics

Conventional averaging is an artificial point of view to the turbulent statistics. The natural frame of reference that is felt by a flow is the local velocity gradient tensor eigen-frame. In order to use a less artificial frame of reference, we consider conditional statistics through the thickness of the TNTI in the self-preserving regime found earlier, i.e. for $t \geq 8$.

Figure 5.11(a) shows the normalized conditional mean active scalar $\langle \psi | z - z_I \rangle / \langle \psi \rangle_a$ in the self-similar regime. This quantity shows an dissymmetry at the vicinity of the TNTI, with respect to the scalar ratio $\mathcal{R}_\psi$. The conventional center-plane value $\langle \psi \rangle_a$ is reached monotonously, through a shallow region inside the TNTI. The jet is therefore mainly composed of a statistically homogeneous core with an abrupt active scalar gradient in the vicinity of the TNTI. The thickness of the transition layer between outer and inner flow is inversely proportional to the diffusivity ratio $\mathcal{R}_\psi$. There is a sustained mean diffusivity gradient very locally at the vicinity of the TNTI. This feature is not revealed by the conventional averaging approach.

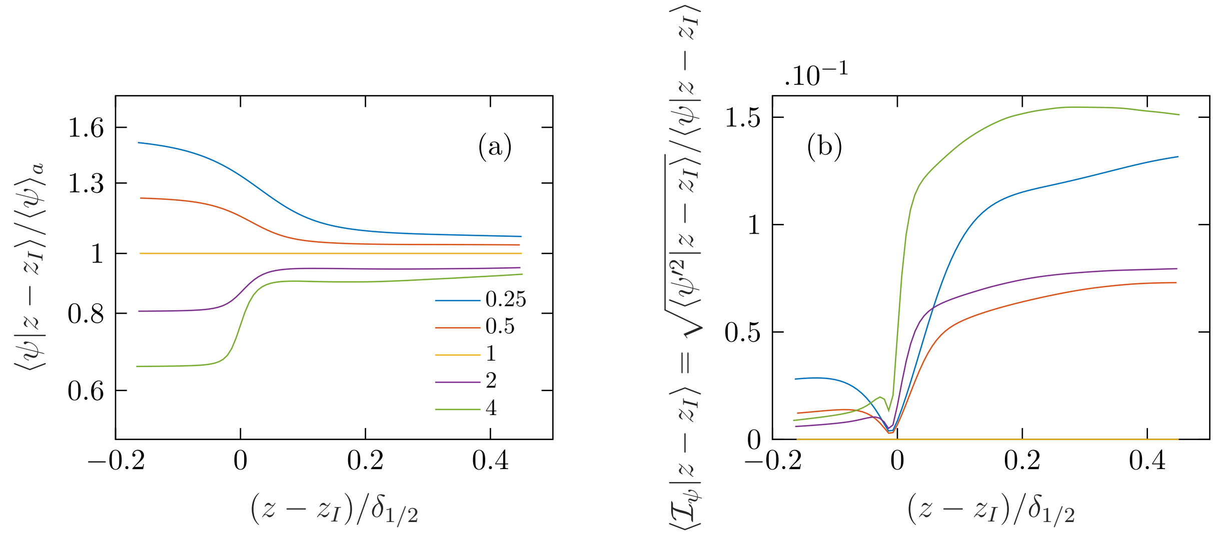

Figure 5.11: Conditional average of mean diffusivity (a) and diffusivity turbulence intensity (b), at $t = 25$. Both quantities are suitably normalized.

The diffusivity turbulence intensity, represented in Figure 5.6(b), shows an early dissymmetry that vanishes at $t \geq 8$. Figure 5.11(b) depicts the same quantity conditionally averaged, at $t = 25$. We find that the early center-plane dissymmetry persists for a longer time in the vicinity of the TNTI. Also, the diffusivity turbulence intensities at this time step at the center-plane are 11% and 5% for the cases $|\log \mathcal{R}_\psi| = 4$ and $|\log \mathcal{R}_\psi| = 2$, respectively. The local diffusivity turbulence intensity at the vicinity of the TNTI is of the same magnitude, but the increase of these quantities is sharper for large $|\log \mathcal{R}_\psi|$. The dissymmetry that we observe at the vicinity of the TNTI eventually decays after some time, when the diffusivity of the jet is close enough to the diffusivity of the outer flow. This trend is not revealed by the conventional averaging approach.

Figures 5.12(a) and (b) respectively represent the conditional average of the gradient norm of both velocity and scalar in the self-preserving regime. The velocity gradients show a sharp increase through the TNTI. The core value is reached, similarly to the mean diffusivity, monotonously and in a shallow region inside the TNTI. The thickness and magnitude of the jump between the outer flow and the jet core are inversely proportional to the scalar ratio $\mathcal{R}_\psi$. The scalar gradient presents a peak at the vicinity of the TNTI. The magnitude and thickness of this peak region is inversely proportional to the scalar ratio $\mathcal{R}_\psi$. In the case $\mathcal{R}_\psi = 4$, the peak is one order of magnitude larger than the core value.

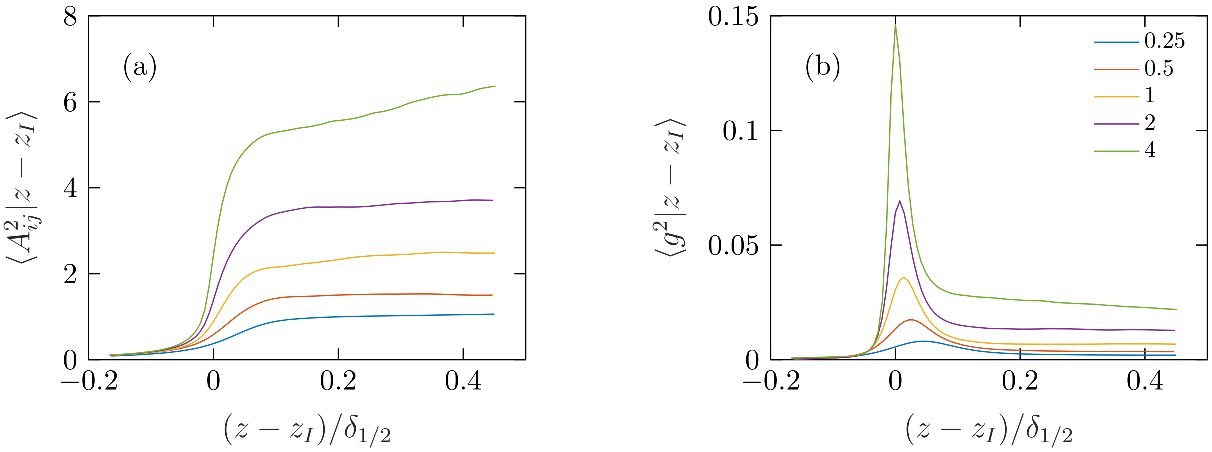

Figure 5.12: Conditional average of the velocity gradient norm (a) scalar gradient norm (b), at $t = 25$, for different diffusivity ratios $\mathcal{R}_\psi$.

Figures 5.13 (a) and (b) show the conditional average of the kinetic energy pseudo dissipation and scalar dissipation rates, in the self-preserving regime, respectively. The kinetic energy pseudo dissipation rate $\langle\varepsilon\rangle_I$ presents a jump at the vicinity of the TNTI, and then slowly increases towards its core value. The diffusivity variations have only a weak effect on this quantity, as we find a staggering of these conditional statistics depending on the diffusivity ratio $\mathcal{R}_\psi$. On the contrary, the scalar dissipation is very sensitive to the diffusivity ratio $\mathcal{R}_\psi$. This quantity shows a very large overshoot at the edge of the TNTI. This effect is known in passive scalar flows (Westerweel *et al.*, 2009; Taveira & da Silva, 2013). We find that the peak thickness inversely proportional to $\mathcal{R}_\psi$, whereas the magnitude is proportional to this parameter. Compared to the passive scalar peak ($\mathcal{R}_\psi = 1$), the peak is twice larger when $\mathcal{R}_\psi = 4$, even in the self-preserving regime.

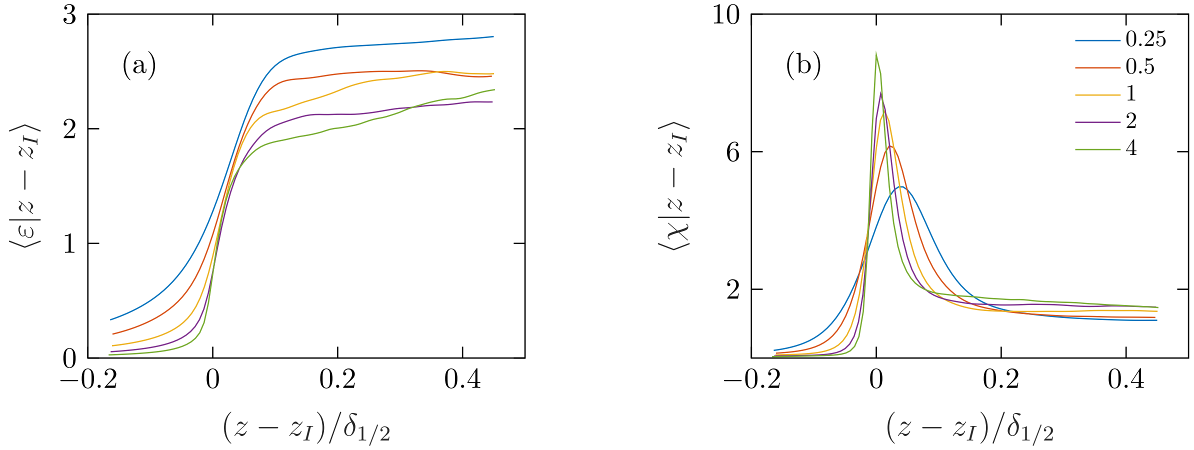

Figure 5.13: Conditional average of pseudo kinetic energy dissipation rate (a) and scalar dissipation rate (b) at $t = 25$, and for different diffusivity ratios $\mathcal{R}_\psi$.

The turbulence intensity of the diffusivity is of the order of 10% at the vicinity of the TNTI, as shown in Figure 5.11(b). The staggering of the conditional scalar dissipation rate is due to the local generation of diffusivity fluctuations, and also to the persistent mean diffusivity gradient, at the vicinity of the TNTI. The turbulent field, does not adapt fast enough to the diffusivity variations at the edge of the flow, even when the diffusivity fluctuations are not very intense. This result is opposite to the fully developed core scalar dissipation rate, and cannot be revealed with a conventional averaging approach.

Mini conclusion

In this section, we computed conditional statistics of diffusivity, velocity and scalar gradients and dissipation rates. The main results of this section can be summarized as follows

1. The early conventional statistics dissymmetries with respect to the diffusivity ratio $\mathcal{R}_\psi$ are found to be persistent at the vicinity of the TNTI.
2. This discrepancy causes a large variability of the mean scalar gradient $g^2 = (\partial_k \phi)^2$ depending on the diffusivity ratio $\mathcal{R}_\psi$.
3. The modified scalar gradient norm causes a staggering of the conditional scalar dissipation, which peak can have twice its value in the passive scalar case, even late in the self-preserving regime.

Next, we discuss the results of both the conventional and conditional statistics sections, compared to the literature on variable diffusivty flows.

5.4 Discussion

This study is a followup to set of simulations that we performed. In these first DNSs, we computed a similar flow, with variable viscosity and constant mass diffusivity. The results are summarized in Brahami *et al.* (2017), which is in Appendix C. We found that the conventionally averaged center-plane scalar dissipation rate staggers in such a flows, even in the self-preserving regime. We interpreted this feature as a lack of a physical mechanism that allows the scalar field to adapt to diffusivity variations. Consequently, we decided to perform a new run of simulations, with both viscosity and mass diffusivity variations.

Taylor's postulate consists in the hypothesis that at large enough Reynolds numbers, the constant $C_\varepsilon = u'^3/(L\langle\varepsilon\rangle)$, is universal (Taylor, 1935). In this context, the kinetic energy dissipation rate $\langle\varepsilon\rangle$ is the viscous pseudo dissipation $\langle 2\psi A_{ij}^2\rangle$, L is the integral length-scale and u' a characteristic velocity at that scale. In other words, Taylor's postulate states that the kinetic energy dissipation rate at small and large scales are proportional in value by a factor C_ε, when the Reynolds number is sufficiently high. The scalar counterpart of this postuale is the hypothesis of the universality of $C_\chi = \phi'^2 u'/(L\langle\chi\rangle)$ at very large Peclet number. Similarly, ϕ' is a characteristic scalar concentration at the integral length-scale.

In literature, Donzis *et al.* (2005) compiled experimental and numerical data on the dependence of C_ε and C_χ, in HIT with a passive scalar. These authors showed that a plateau is reached for both quantities, at large enough Reynolds numbers. In the variable diffusivity context, Lee *et al.* (2008), Kumar *et al.* (2011) and Gréa *et al.* (2014) evaluated the effect of diffusivity variations on the numerical value of viscous dissipation rates in HIT, without evaluating the dependence of C_ε and C_χ on the Reynolds number. Strictly speaking, none of these authors confirmed Taylor's postulate in a variable diffusivity flow. Nevertheless, the common result from these studies is the independence of the small-scale dissipation rates to initial diffusivity inhomogeneities. The velocity and scalar gradient fields adapt quickly to viscosity and mass diffusivity variations, respectively.

In our study, we approached the problem in a similar way to Lee *et al.* (2008), Kumar *et al.* (2011) and Gréa *et al.* (2014). We consider a single injection Reynolds number Re_0, and evaluate the value of the kinetic energy pseudo dissipation and scalar dissipation rates, with the only focus on the dependence of this value to diffusivity inhomogeneities. The constant diffusivity values $\langle \varepsilon \rangle$ and $\langle \chi \rangle$ at $\mathcal{R}_\psi = 1$, are finite Reynolds number quantities, and are far from the asymptotic value that might be reached if Taylor's postulate was valid in a jet. The active scalar cases ($\mathcal{R}_\psi \neq 1$), the Taylor-based Reynolds number departs from the passive scalar value. Including a diffusivity variation is another way of changing the jet Reynolds number, dynamically as mixing occurs.

These results are introductory to the evaluation of the scalar gradient norm budget, in a conditional averaging approach. Next, we present a paper, that is to be submitted in the near future.

5.5 Paper

Version August 31, 2020
Work in progress, to be submitted

Temporal space/scale transport due to variable momentum and mass diffusion at the Turbulent/non-Turbulent Interface

Y. Brahami,[1] E. Varea,[1] L. Danaila,[1] and M. Gauding[1]
[1]*CORIA, CNRS UMR 6614, Normandie Université, 76821 St. Etienne du Rouvray, France*

(Dated:)

G.I. Taylor postulated that the mean energy dissipation rate may be insensitive to viscosity variations and that it depends only upon the large-scale properties, in particular on the energy injected in the flow. The counterpart of Taylor's postulate for turbulent mixing hinges on the assumption that the mean dissipation rate of the scalar variance is independent of the local value of molecular properties (mass diffusivity, or thermal conductivity). Whilst different forms of Taylor's postulate have been assessed for time decaying homogeneous isotropic turbulence, its validity for: i) flows with both variable viscosity and mass diffusivity, and ii) time decaying shear flows, has never been investigated. It is the gap that this study aims filling.

We prospect the classical turbulent mixing paradigm for the case of inhomogeneous fluid media, with variable viscosity and mass diffusivity, for the particular case of Schmidt=1. We use DNS of a temporally evolving jet, that mixes with a different fluid, R times more viscous and diffusive. The ratio R varies between 0.25 and 4.

Of specific interest is the dependence of scalar dissipation, and the norm of the scalar gradient, on the ratio R and of large-scale properties of the jet (initial Reynolds number). The validity of the classical paradigm would entail that scalar dissipation be spatially uniform, despite strong variations in both viscosity and mass diffusivity.

(1) In the jet core, it is found that fluctuating scalar gradients do adapt to the imposed diffusivity variations, rendering scalar dissipation nearly insensitive to these fluctuations. (2) However, when statistics are conditioned on the distance to the so called Turbulent/Non-Turbulent Interface, we find an intense and persistent effect of the diffusivity variations on the conditional scalar dissipation, on the scalar gradient magnitude in physical space. The orientation of these additional fluxes depends on the viscosity and diffusivity gradients alignment with shear. Therefore, the classical mixing paradigm is not tenable at the T/NT interface, as mixing progressively includes new, unmixed yet, fluid.

PACS numbers:

A scalar transported in a turbulent flow can be either passive (when it does not influence at all the velocity field, it is therefore a tracer), or active. Active scalars are created by: i) strong gradients of temperature in the same fluid; ii) mixing fluids with different chemical composition (often inducing vastly contrasting physical properties). Sometimes, both cases i) and ii) occur. We consider here an isothermal temporal plane jet, mixing two fluids with vastly different mass and momentum diffusivities, for the particular case of unity Schmidt number (the kinematic viscosity and the mass diffusivity are equal).

An active scalar influences the velocity field through variations of either density, or viscosity. The variable-density case has been extensively studied in the literature [8, for a recent review]. Variable-viscosity turbulent flows received much less attention. Some such studies have been carried out numerically in statistically homogeneous and isotropic turbulence (HIT) [4–7], temporally evolving shear layer [11] and experimentally in round jets [2, 13]. All of them dealt with temporally decaying flows and pointed out the quick independence of the mean energy dissipation rate with respect to viscosity fluctuations.

The scalar counterpart of this problem remains untreated. As stated by Lee *et al.* [7] in their HIT, it is not clear whether or not the scalar dissipation rate is independent of mass diffusivity variations. Nevertheless, viscosity variations can either enhance or diminish the energy transfer, both locally in physical space [11] and non-locally, in scale space [4].

Most traditional theories on turbulence are formulated for sufficiently large Reynolds numbers. Under these conditions, small scales are supposed to exhibit universal properties and should be locally isotropic. However, real flows face what we can generally call 'Finite Reynolds number' effects, including impact of initial and boundary conditions, very specific of each flow. In particular, free shear flows consist on a turbulent region, surrounded by an irrotational fluid. These two regions are separated by a thin layer, the Turbulent/Non-Turbulent Interface (TNTI), where mass and momentum exchanges occur [10]. Most studies regarding the TNTI focus on passive scalar flows. To the authors knowledge, no study considers active scalar effects on the scalar dissipation rate, with both variable viscosity and mass diffusivity in a free incompressible shear flow. In this letter, we analyse this type of flows in a temporally evolving jet.

We perform Direct numerical simulation (DNS) of a temporally evolving turbulent plane jet as described by Gampert *et al.* [3]. The DNS solves the following non-dimensional incompressible Navier-Stokes equations with variable viscosity and mass diffusivity

$$\partial_j u_j = 0, \tag{1}$$

$$\partial_t u_i + u_j \partial_j u_i = -\partial_i p + \frac{1}{Re_0} \partial_j \left[\psi \left(\partial_j u_i + \partial_i u_j \right) \right], \tag{2}$$

$$\partial_t \phi + u_j \partial_j \phi = \frac{1}{Pe_0} \partial_j \left[\psi \partial_j \phi \right], \tag{3}$$

$$\psi = f(\phi; \mathcal{R}) = \mathcal{R}^{\phi - 1}, \tag{4}$$

Here, ϕ is the scalar, and ψ is either the momentum and mass diffusivities, which couples the scalar to the velocity field. To avoid cumbersome terminology, we will refer to ψ as *diffusivity*, and $\mathcal{R} = \psi_{0,c}/\psi_{0,out}$ is the *diffusivity ratio* that we use as an external control parameter. Subscripts 0, c and *out* indicate the initial, center-plane and outer flow conditions, respectively. In practical gas flows, $\mathcal{R}$ rarely exceeds 5, consequently, we consider the cases $\mathcal{R} = 0.25, 0.5, 1, 2, 4$. The streamwise velocity and scalar are initialized using hyperbolic tangent profiles, symmetrized with respect to the center-plane. From one case to the other, we keep the jet initial conditions unchanged and modify the outer flow conditions, through $\mathcal{R}$ only. We choose the jet initial center-plane diffusivity $\psi_{c,0}$, velocity $u_{c,0}$ and momentum thickness h_0 as reference quantities. The initial Reynolds and Peclet numbers are $Re_0 = Pe_0 = u_{c,0} h_0 / \psi_{0,c} = 2000$. The computational domain has periodic boundary conditions in stream-wise Ox and span-wise Oy directions, while free-slip boundary conditions are used in the cross-wise Oz direction. The size of the domain is large compared to the largest integral scales of the jet to avoid confinement effects and the grid size was chosen in order to resolve the smallest Kolmogorov length scale in each flow. Large-scale quantities are used for normalization, because the definition of small scale quantities is delicate when diffusivities vary.

Turbulent temporal plan jets show, after a long enough time after injection, a self-preservation behavior [12]. In our simulations, the mean streamwise velocity and scalar, together with their respective second-order moments, are in agreement with the self-preservation predictions. Moreover, these fields are independent of the initial diffusivity distribution, after a time as short as $t = 8$ for the mean fields, and $t = 12$ for the variance fields, respectively.

Figure 1 shows the time evolution of the scalar dissipation rate $\langle \chi \rangle_c = 2 \langle \psi g^2 \rangle_c$ spatially averaged over the center-plane. Here, $g^2 = (\partial_j \phi)^2$ is the square of scalar gradient vector magnitude. This quantity becomes independent of $\mathcal{R}$ in the self-preserving regime, which proves that scalar gradients adapt to diffusivity variations in the fully turbulent core. At $t = 25$, the magnitude of $\langle \psi'^2 \rangle_c$ is of the order of 10%, and decays quickly [15]. The quantity $\langle g^2 \rangle_c$ dynamically compensates diffusivity variations. This result is also valid for the spatial distribution of these fields, averaged over cross-stream planes (figures not shown).

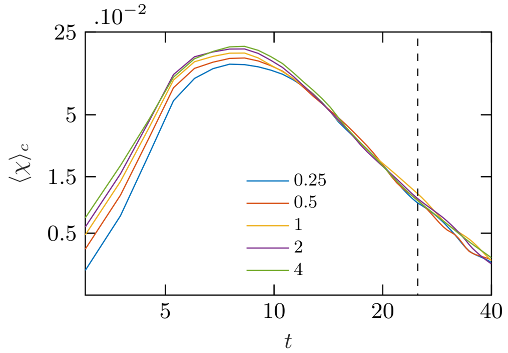

FIG. 1: Temporal evolution of the scalar dissipation spatially averaged over the center-plane, for different scalar ratios $\mathcal{R}$.

The conditioned fields are averaged along the homogeneous directions at crosswise distance to the TNTI [1], and denoted $\langle . \rangle_I$. In order to detect the TNTI, we use the technique suggested by Prasad & Sreenivasan [9]. This method consists in using the lower local minimum of the scalar distribution over the whole computational domain. Choosing this local minimum as a threshold value guarantees that this scalar iso-surface is at the edge of the flow. Conditional averaging consists in performing a mean over a surface that is shifted from the TNTI by a distance $(z - z_I)$ where z_I is the TNTI crosswise position. In this study, we consider conditional averaging in the cross-stream direction.

It is known in the literature that in passive scalar flows, the conditionally averaged scalar dissipation rate endures a large overshoot in passive scalar flows [14]. Figure 2 depicts the conditionally averaged scalar dissipation rate. Noticeable is a strong dependence of this overshoot on the diffusivity ratio $\mathcal{R}$, even in the self-preserving regime. The peak is thinner, more intense, and shifts towards to the TNTI, as $\mathcal{R}$ increases.

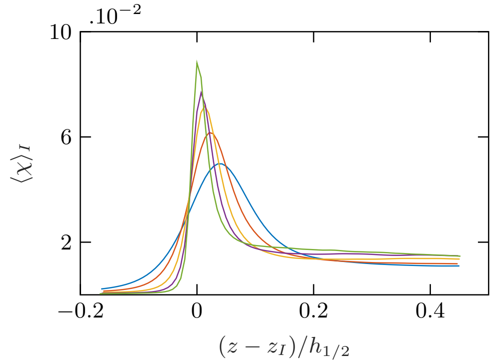

FIG. 2: Conditional average of the scalar dissipation rate at $t = 25$ (dashed line in FIG.1), for different scalar ratios $\mathcal{R}$.

The conditionned diffusivity turbulence intensity $\sqrt{\langle \psi'^2 \rangle_I} / \langle \psi \rangle_I$ at $t = 25$ is the order of 15% at worst.

Figure 3 depicts the conditioned mean diffusivity, normalized by its core value. A dissymmetric dependence on the diffusivity ratio $\mathcal{R}$ is revealed, suggesting that the scalar is very nearly homogeneous inside the jet. This strongly contrasts with enhances scalar gradients present at the TNTI. The jet is therefore composed of a statistically homogeneous turbulent core, surrounded by intense and persistent gradients at the vicinity of the TNTI. This result demonstrates that the scalar at the TNTI remains active for a very long time, even if it is readily mixed inside the jet core, as soon as self-preservation is achieved.

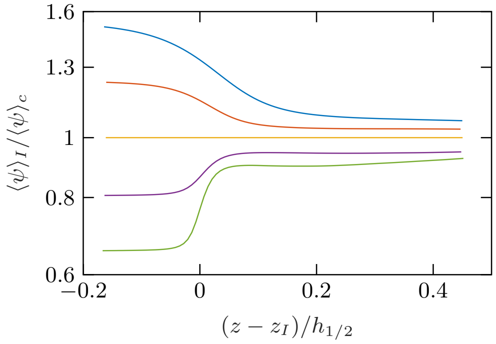

FIG. 3: Conditional average of the diffusivity at $t = 25$ (dashed line in FIG.1), for different scalar ratios $\mathcal{R}$.

In order to give a physical explanation to the scalar dissipation rate dissymmetry, we evaluate the one-point budget of the scalar gradient $g^2 = g_k^2$, generalized for variable diffusivity. We make an extensive use of the chain rule on the state equation (4), and obtain

$$\partial_t g^2 = -\underbrace{u_j \partial_j g^2}_{\mathcal{A}} - \underbrace{2 g_k g_j \partial_k u_j}_{\mathcal{P}} + \frac{1}{Pe_0}\Big[\underbrace{\psi \partial_j^2 g^2}_{\mathcal{D}_1} - \underbrace{2\psi(\partial_j g_k)^2}_{\mathcal{D}_2}\Big]$$

$$+\frac{2}{Pe_0}\log\mathcal{R}\,\psi\Big[\underbrace{g^2\partial_j g_j}_{\mathcal{A}cc} + \underbrace{g_j\partial_j g^2}_{\mathcal{D}r} + \underbrace{\log\mathcal{R}(g^2)^2}_{\mathcal{VD}iss}\Big] \qquad (5)$$

In Eq. (5), terms on the first line of the right-hand-side represent, from left to right, advection, production, diffusion and dissipation, respectively. On the second line are the variable diffusivity terms. We name these terms from left to right accretion, drift and variable diffusivity dissipation, respectively. We normalized all these terms by the large scale quantity $\mathcal{N}_c = \langle g^2\rangle_c\langle u\rangle_c/h_{1/2}$.

Figure 4 presents the sum the advection, production, diffusion and dissipation terms, conditionally averged. We find that the constant diffusivity terms mostly vary in the vicinity of the TNTI. We notice that the scalar gradients are generated outside the TNTI, and destroyed inside. In the core, the decay of this quantity is homogeneous, which is in agreement with our observations.

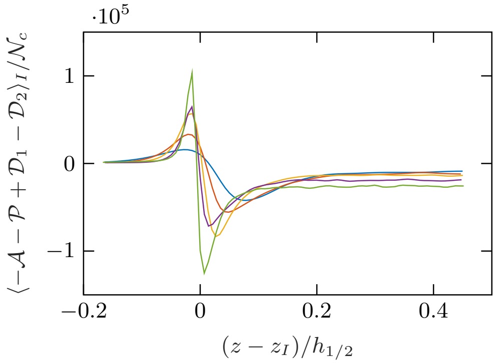

FIG. 4: Conditional average of constant diffusivity terms in Equation (5) at $t = 25$, for different diffusivity ratios $\mathcal{R}$.

Regarding the diffusivity gradient terms, Fig. 5 the sum of the accretion and drift terms. These quantities are null inside the jet. In the vicinity of the TNTI, we find that these terms peak at an order of 40% of the constant diffusivity terms. The diffusivity gradient terms highly contribute to the dynamics of the scalar gradient. The accretion and drift terms are multiplied by $\log\mathcal{R}$, and are expected to change sign whether the jet is more or less diffusive than the outer-flow. Depending on the orientation of the mean diffusivity gradient, the diffusivity gradient terms are either aligned or opposed to the constant diffusivity terms. This variable alignement is a direct source for the conditional scalar dissipation rate dissymmetry. This behavior can be explained by the fact that the accretion and drift terms are multiplied by $\log\mathcal{R}$. The variable diffusivity dissipation $\mathcal{VD}iss$ is found to be two orders of magnitude smaller than the accretion and drift terms, but remains always positive, as it depends on $(\log\mathcal{R})^2(g^2)^2$.

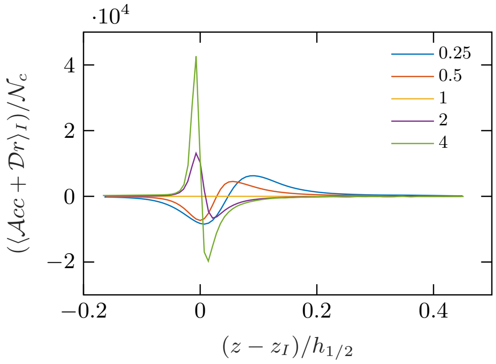

FIG. 5: Conditional average of $\mathcal{A}cc + \mathcal{D}r$ in equation (5) at $t = 25$, for different scalar ratios $\mathcal{R}$.

When diffusivity is locally smaller, the local Kolmogorov and Batchelor length scales are smaller, and the kinetic energy together with the scalar variance cascade towards smaller scales. This effect generates sharper structures, and therefore locally larger velocity and scalar gradients.

In conclusion, we analysed a variable viscosity and mass diffusivity temporal turbulent jet. The core scalar dissipation is unaffected by the diffusivity variations in the self-preserving regime, which confirms the scalar counterpart of Taylor's postulate in the fully developed region. Nevertheless, when conditionally averaged on the distance to the Turbulent/Non-Turbulent Interface (TNTI), we find an intense and persistent effect of the mean diffusivity gradient on the scalar dissipation, even in the self-preserving regime. This result demonstrates that the scalar at the TNTI remains active for a very long duration, even if it is passive inside the jet core as soon at self-preservation is reached.

To find a physical explanation to this discrepancy, we further investigate the two-point transport equation of the scalar second-order strauture function, for the particular case of variable diffusivity case. We further assess this budget conditioned on the TNTI. We find that the diffusivity gradient related terms contribute to the one-point budget only in a very shallow region in the vicinity of the TNTI. Depending on the respective orientation of the initial diffusivity gradient with respect to the shear, these terms are either source or sink terms. We find a non-local counterpart to the diffusivity gradients that are also asymmetric with the diffusivity profile at the initial time.

Acknowledgments

Financial support from the French National Research Agency, under the project 'EMCO2Re' is gratefully acknowledged. We thank the computing centers CRIANN and Jüelich for computation time.

---

[1] Bisset, D.K., Hunt, J.C.R. & Rogers, M.M. 2002 The turbulent/non-turbulent interface bounding a far wake. *J. Fluid Mech.* **451**, 383–410.

[2] Danaila, L., Voivenel, L. & Varea, E. 2017 Self-similarity criteria in anisotropic flows with viscosity stratification. *Phys. Fluids* **29** (2).

[3] Gampert, M., Boschung, J., Hennig, F., Gauding, M. & Peters, N. 2014 The vorticity versus the scalar criterion for the detection of the turbulent/non-turbulent interface. *J. Fluid Mech.* **750**, 578–596.

[4] Gauding, M., Danaila, L. & Varea, E. 2018 One-point and two-point statistics of homogeneous isotropic decaying turbulence with variable viscosity. *Int. J. Heat Fluid Flow* **72** (December 2017), 143–150.

[5] Gréa, B.J., Griffond, J. & Burlot, A. 2014 The effects of variable viscosity on the decay of homogeneous isotropic turbulence. *Phys. Fluids* **26** (3).

[6] Kumar, G., Girimaji, S.S. & Kerimo, J. 2011 Preconditions and limitations of the postulate of scalar-dissipation- conductivity independence in a variable conductivity medium. *Phys. Rev. E - Stat. Nonlinear, Soft Matter Phys.* **84** (4), 1–10.

[7] Lee, K., Girimaji, S.S. & Kerimo, J. 2008 Validity of Taylor's dissipation-viscosity independence postulate in variable-viscosity turbulent fluid mixtures. *Phys. Rev. Lett.* **101** (7), 1–4.

[8] Livescu, D. 2020 Turbulence with Large Thermal and Compositional Density Variations. *Annu. Rev. Fluid Mech.* **52** (1), 309–341.

[9] Prasad, R.R. & Sreenivasan, K.R. 1989 Scalar interfaces in digital images of turbulent flows. *Exp. Fluids* **7** (4), 259–264.

[10] da Silva, C.B., Hunt, J.C.R., Eames, I. & Westerweel, J. 2014 Interfacial layers between regions of different turbulence intensity. *Annu. Rev. Fluid Mech.* **46** (1), 567–590.

[11] Taguelmimt, N., Danaila, L. & Hadjadj, A. 2016 Effect of viscosity gradients on mean velocity profile in temporal mixing layer. *J. Turbul.* **17** (5), 491–517.

[12] Townsend, A.A.R. 1980 *The structure of turbulent shear flow*. Cambridge university press.

[13] Voivenel, L., Varea, E., Danaila, L., Renou, B. & Cazalens, M. 2017 Variable viscosity jets: Entrainment and mixing process. In *Whither Turbul. Big Data 21st Century?*, pp. 147–162. Springer.

[14] Westerweel, J., Fukushima, C., Pedersen, J.M. & Hunt, J.C.R. 2009 Momentum and scalar transport at the turbulent/non-turbulent interface of a jet. *J. Fluid Mech.* **631**, 199–230.

[15] Invoking the self-preservation of the mass fraction field and a Taylor expansion and in the state equation (4), we can show that the large time asymptotic behavior of the diffusivity variance is: $<\psi'^2>_c \sim (\log \mathcal{R})^2 <\psi>_c^2 t^{-2}$.

5.6 Conclusion

In this chapter, we studied a temporally evolving turbulent plane jet, with variable viscosity and mass diffusivity. We focused on the kinetic energy pseudo dissipation and scalar dissipation rates. These quantities are directly linked to mixing, and especially to turbulence closure modeling. We assessed this problem using two statistical approaches. First, conventional statistics consist in averaging over planes at fixed cross-wise direction. Second, conditional statistics focus on averaging by conditioning on the distance to the so-called Turbulent/Non-Turbulent Interface (TNTI). The behavior of this flow was studied with respect to the initial viscosity and mass diffusivity distribution, which we refer to as diffusivity, for simplicity. The results can be summarized as follows.

1. Using the conventional statistics approach, we found that the flow is self-preserving after some time. The mean and second-order one-point statistics of velocity and scalar were found to follow temporal power laws at the center-plane of the jet. Then, we computed the diffusivity statistics temporal evolution at the center-plane, and found an early dissimmetric behavior on the turbulence intensity of this quantity. This discrepancy is smoothed as the self-preserving regime is reached. Then, we evaluated the kinetic energy pseudo dissipation and scalar dissipation rates in a conventional manner temporally at the center-plane. We found that these quantities quickly become independent of the initial diffusivity inhomogeneities, and they respectively collapse towards the same self-preserving decay curves. The spatial profiles of these dissipation rates in the cross-wise direction were also found to collapse, within the numerical accuracy.

2. The statistics are then computed in a conditional manner, in the self-preserving regime. We found that all the statistics vary by large magnitudes over a very shallow region inside the TNTI. The jet therefore consists of a very homogeneous turbulence core, surrounded by sharp gradients at the vicinity of the TNTI. Also, the thickness of the region over which the statistics vary from the outer flow to the fully developed core depends on the initial diffusivity inhomogeneity. The gradients are found to be thinner and more intense when the jet is initially more viscous than the surrounding fluid.

> Moreover, we found that the conditional mean and second-order moment of diffusivity remains dissimmetric, even in the self-preserving regime. The early dissymmetry that was observed to vanish in the conventional center-plane average persist for a much longer time, at the vicinity of the TNTI. The conditional scalar dissipation rates are equal in value in the fully turbulent core of the jet, but can largely differ at the vicinity of the TNTI.

Finally, we presented a paper that is to be submitted in the near future. In this paper, we evaluated the one-point budget of the scalar gradient vector norm, in a conditional manner. We found that the variable diffusivity terms contribute differently to this budget, depending on the local orientation of the diffusivity gradient with respect to shear. We conclude from this part that the scalar can remain active intensely and persistently at the vicinity of the TNTI. This feature manifests through scalar gradients at the edge of the flow, which cause a strong dependence of scalar dissipation rate on the initial diffusivity distribution.

General conclusion and perspectives

In turbulent mixing, temperature and chemical concentration can actively contribute to the flow dynamics, through density and/or viscosity variations. In free jets, a noticeable effect of active scalars is the enhancement of the growth of turbulence after the injection in two cases. When the jet fluid is lighter, or more viscous.

The aim of this thesis was to explore two different types of active scalar jets. First, a spatially evolving variable density round jet, and second, a temporally evolving variable viscosity and mass diffusivity plane jet. We started, in Chapter 2, by setting the theoretical ground for incompressible flows, in general. A discussion of active scalar flows was presented, considering the role of temperature and chemical species concentration. We highlighted the subtle differences between these two fields, and the mechanism by which they couple to the velocity fields. In the following, we summarize the results obtained for each of the active scalar flows studied in thesis, separately.

Variable density round jet

In Chapter 2, we chose chemical species as an active scalar. Considering isochoric mixing, a natural change of variable is derived to take large density variations into account in the chemical species conservation equation. We refer to this new field as *pseudo mass fraction*. We derived generalized scale-by-scale Kolmogorov and Yaglom equations, in this type of flows. These budgets are written in such form that the constant density case is recovered, as a control parameter tends to zero. In particular, the Yaglom equation is written using pseudo mass fraction, and the Kolmogorov equation is written for a specific form for the kinetic energy.

We designed an experiment that allows to simultaneously measure the velocity and scalar fields, in the very near field of the jet. The details of the experimental measurements are given in Chapter 3. Momentum and density variations were adjusted through the Reynolds and Archimedes numbers, respectively. In Chapter 4, we assessed the combined effect of momentum and density deficit on the one-point, two-point and TNTI statistics of the very-near field of the jet. The main results of this part are summarized in the following.

1. Focusing on low-order statistics at fixed downstream position in the very near field, we found that most velocity and scalar quantities depend nonlinearly on momentum and density variations. In particular in the non-Boussinesq regime, the scalar turbulence intensity at the axis follows two very distinct regimes, separated by the critical line $Re_{crit} = 24000 - \frac{4}{3}(Ar - 5000)$. Below this line, the axis scalar turbulence intensity is insensitive to changes in Archimedes numbers. Whereas above the critical line, this quantity at the axis is independent of the Reynolds number. These regimes also manifest in the conventionally and conditionally averaged radial statistics of the scalar turbulence intensity.

2. Based on our finding, we computed the two-point statistics at fixed Archimedes number, for different Reynolds numbers, and at fixed Reynolds number for different Archimedes numbers. In both cases, the critical line is crossed. We found that large density variations incorporate an additional length scale in the pseudo mass fraction cascade, when crossing the critical line from below. Consequently, pseudo mass fraction fluctuations are not transported to smaller scales at a higher rate, but their spatial propagation is more intense. These fluctuations spread faster within the flow, when the critical line is crossed from below.

We conclude from the variable density jet study that the combined effect of momentum and density variations on the initiation of mixing is non trivial. In the non-Boussinesq regime ($Ar > 5000$), the critical line defined by $Re_{crit} = 24000 - \frac{4}{3}(Ar - 5000)$ delimits two regimes that show different dynamics in scalar turbulence intensity. We identified these regimes in conventional axial and radial averages, TNTI conditional averages, and in scale-space through nonlinear inter-scale and inhomogeneous transports of pseudo mass fraction.

Variable viscosity and mass diffusivity plane jet

In Chapter 2, we derived a variable viscosity and mass diffusivity set of equations. The wide variety of state equations for these quantities is discussed, and we make a justified choice. This flow was assessed by Direct Numerical Simulations (DNS) of temporally evolving plane turbulent jets, in Chapter 5. Here, we chose to equate viscosity and mass diffusivity, and refer to this quantity as the *diffusivity*. These simulations were performed by Dr M.Gauding in our research group. The focus was put on kinetic energy and scalar dissipation rates. Statistics were evaluated in two different manners. First, conventional statistics, where we averaged over cross-wise planes. Second, conditional statistics where the average is performed in the vicinity of the TNTI. Here, we summarize the results of this part.

1. We found, by conventional averaging at the center-plane, that the jet reaches a self-preserving regime kinetic energy and scalar dissipation rates collapse in this regime at the center-plane, independently of initial diffusivity inhomogeneities. In the self-preserving regime, we found that the conventionally averaged spatial profiles of these quantities also collapse, within reasonable accuracy.

2. The conditionally averaged kinetic energy and scalar dissipation rates do not collapse in the self-preserving regime, for different initial diffusivity distributions. To assess this discrepancy, we focused on the diffusivity and velocity and scalar gradient norms, conditioned on the TNTI. These quantities were found to remain affected to diffusivity variations, even in the self-preserving regime. Depending on whether the outer-flow is more or less diffusive than the jet, gradients of diffusivity and scalar show an intense peak in the vicinity of the TNTI.

We conclude from this part, that gradient fields, in the vicinity of the TNTI, do not adapt fast enough to diffusivity variations. We add physical insights to this effect by deriving the scalar gradient norm transport equation, and evaluating its different terms in a conditional manner. These results are attached in a paper that is soon to be submitted.

General conclusion

It is well known that active scalar flows show a dissymmetric response compared to passive scalar flows. This dissymmetry depends on whether the injected fluid is more or less dense and/or viscous than the host fluid. It is also believed that these discrepancies are quickly smoothed by the turbulent flow.

In a variable density jet, we found that combinations of momentum and density variations lead to new dynamics, compared to momentum or density variations taken separately. These nonlinear variations manifest through conventional axial and radial averages, TNTI conditional averages, and in scale-space through nonlinear inter-scale and inhomogeneous transports of pseudo mass fraction.

In the variable viscosity and mass diffusivity case, we found a localized active scalar effect that is intense and persistent, in the self-preserving regime. This effect manifests at the vicinity of the TNTI through statistics of kinetic energy and scalar dissipation rates, velocity and scalar gradient norms, and viscosity and mass diffusivity together with their gradients.

We conclude from this thesis two main results. First, a dissymmetry is a simplistic view of active scalar flows, because momentum also has to be considered as a free parameter. Second, active scalar effects persist at the edge of a free shear flow, even at late times when the scalar is almost passive inside the core.

Perspectives

In the variable density jet experiment, we did not have access to the smallest scales of the flow. This is due to the limited scale separation that PIV offers. A potential solution would be to combine the same configuration that we retained with an additional stereo-PIV set of cameras. This new pair of cameras would be zoomed in a smaller region of the flow, in order to have a better estimate of smaller scales. Doing so, we could apply the same method that we used in the temporally evolving jet DNS, on the variable density experiment. Also, in our study, we measured very close to the injection. In order to match our measurements with literature, we need to measure up to twenty jet diameters downstream. Realizing this new experimental setup would allow us to measure precisely the Taylor based Reynolds number.

In the DNS, we made multiple arbitrary choices. We equated the viscosity and mass diffusivity, and chose a specific form of the state equation. This choice led to unity Schmidt number, locally and instantaneously over the computational domain. Nonlinearity of the state equation is a key ingredient for active scalar flows. As a perspective, we could consider a wider set of simulations, with the same state equation but with a prescribed Schmidt number. This choice would lead to difficulties in locating the TNTI, and requires the development of a new method. Another approach would be to choose a different state equation, and study the effect of state equation on the TNTI statistics. In our study, we considered a single Reynolds number, which is relatively small. As a perspective, a more systematic study, as a function of the Reynolds and Schmidt numbers would lead to an analogous problem to what we performed in the variable density jet experiment.

The more general case, which is the combination of density and viscosity variations. In the single active scalar case, such a flow depends on the Reynolds number, the Archimedes number, the viscosity ratio, the Peclet number and the Froude number. In this thesis, we assessed only particular sets of this general problem. The main experimental difficulty is to find chemical substances that combine all the correct thermo-physical properties to fit in such a parameter space. On the other hand, performing DNS is too expensive. The perspective procedure consists in combining experiments and DNS to cover wide regions in small regions of the parameter space, like fixing the Schmidt and Froude numbers.

Finally, as an additional study, linear stability analysis could be considered to predict the very first structures that appear after the injection of the jet. This approach could provide a link to the forcing mechanism that occurs at the largest scales at the end of the potential core of the jet. Regarding active scalar flows, many studies considered this method. In the following, we provide a perspective in the shape of a small chapter about linear stability analysis in active scalar flows.

A perspective: Linear stability analysis of active scalar jets

This study is motivated by the observation that, in Figure 1.9, two annular vorticies can be observed near the potential core. Therefore, we considered LSA as an eventual prediction for the early coherent structures jets with active scalars. In this section, we first briefly present LSA. Second, a small literature review on variable density jets is presented. Finally, we describe some results concerning the stability of variable density jets, and discuss their consequences as a perspective to this thesis.

LSA and its relationship to turbulence

The large variety of empirical observations of the transition from laminar to non-laminar states sets a very fertile ground for hydrodynamic stability. To do so, we start from a fixed point of the dynamical system that is called a base flow U_i. LSA consists in testing the robustness of this fixed point to infinitely small perturbations. If the perturbations grow, the flow is linearly unstable. On the contrary, if the perturbations decay and the flow goes back the fixed point, it is said to be linearly stable.

The LSA literature is almost as old as the Navier-Stokes equations themselves. We do not aim at performing a review of such a literature. We will focus on recent developments on the stability of round jets. But, we recall that there are two mechanisms in the LSA formalism that are responsible for the transfer of energy from the base flow to the perturbed field. The Orr mechanism, that generates the so-called Kelvin-Helmholtz vorticies in shear layers, and the lift-up mechanism, that is responsible for streaks in a boundary layer.

Figure 6.1 sketches Kelvin-Helmholtz vorticies. This instability is believed to be the main mechanism that generates the first large structures in free shear flows. The structures break down through secondary instabilities farther downstream an feed a turbulent cascade, when the Reynolds number is large enough. Such a mechanism is represented in the textbook of Green (2012).

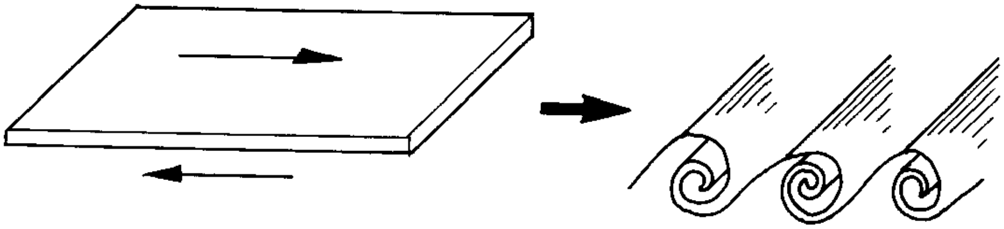

Figure 6.1: Kelvin-Helmholtz instability sketch. Figure from Davidson (2004).

In the turbulence formalism, after performing a Reynolds decomposition on a fully turbulent signal $u_i = \langle u_i \rangle + u'_i$, one can derive a transport equation for the kinetic energy of the velocity fluctuating field (TKE) noted $k_t = \langle u'^2_i \rangle / 2$. Analogously, in the stability frame, we perform a perturbation of the base flow, $u_i = U_i + \tilde{u}_i$. We can derive a transport equation for the perturbation kinetic energy (PKE) notes $k_p = \tilde{u}_i^2/2$. Considering, for the TKE, a statistically homogeneous shear flow on a cubic volume of size V, and for the PKE a deterministic periodic flow over the same volume, one can spatially integrate the equations. The volume averaged TKE k_{tV} and PKE k_{pV} dimensionless transport equations read,

$$\text{TKE,} \quad \frac{d\,k_{tV}}{dt} = -2\int_V \langle u'_k u'_i \rangle \partial_k \langle u_i \rangle dv - \int_V \frac{2}{Re} \langle (\partial_k u'_i)^2 \rangle dv, \tag{6.6}$$

$$\text{PKE,} \quad \frac{d\,k_{pV}}{dt} = -2\int_V \tilde{u}_k \tilde{u}_i \partial_k U_i dv - \int_V \frac{2}{Re} (\partial_k \tilde{u}_i)^2 dv. \tag{6.7}$$

The apparent similarity of Equations (6.6) and (6.7) is only due to the resemblance between the Reynolds decomposition and the perturbation around a base flow, even so the mathematical and physical significance of the fully turbulent and linear stability approaches are diametrically opposed. The former is statistical, fully non-linear, two-way coupled between the mean and fluctuating fields, unstationnary and focuses on the large time chaotic dynamics, whereas the latter is deterministic, linear, one-way coupled between the base and perturbed fields, stationary and valid on the very short times only.

In order to illustrate the LSA described in the previous section, we briefly proceed to the derivation of the classical Orr-Sommerfeld equation in Cartesian coordinates. We will list the hypotheses during the derivation, in order to discuss the implications of each of them regarding the LSA we will perform in active scalar shear flows.

H1, Suppose the existence a fixed point of the Navier-Stokes equations in the form of a parallel base flow $(U(y), 0, 0)$. When the flow is indeed parallel, this type of laminar solutions can always be built by adjusting the pressure gradient in the streamwise direction.

H2, Linearize around the base flow through a very small perturbation, so that $u = (U(y) + \tilde{u}, \tilde{v}, \tilde{w})$, where $(\tilde{u}, \tilde{v}, \tilde{w}) \ll U$. The quadratic perturbation terms are neglected.

H3, We suppose that the perturbations are periodic, in the form of normal modes $\tilde{u} = \hat{u}(y)e^{i(\alpha x+\beta z-\alpha ct)}$. This hypothesis allows to perform a Fourier-Laplace transform, which converts the linear differential operators ∂_t, ∂_x and ∂_z into multiplications by $-ic$, $i\alpha$ and $i\beta$, respectively. The result is a set of ordinary differential equations in the cross-wise direction only d/dy.

H4 Next, we make use of the Squire theorem (Squire, 1933), that states that there is a preferential direction in which the system is most unstable. This theorem reduces the problem to a 2-D flow in the least stable direction $k = \sqrt{\alpha^2 + \beta^2}$.

H5 The usual procedure at this stage is to eliminate the pressure and to reduce all the system to a single equation on the crosswise velocity perturbation $\hat{v}$. This last step results in the Orr-Sommerfeld equation Orr (1907*a*,*b*); Sommerfeld (1908)

$$\left((U-c)\left[\frac{d^2}{dy^2} - k^2\right] - \frac{d^2U}{dy^2}\right)\hat{v} = \frac{1}{ik\mathrm{Re}}\left[\frac{d^2}{dy^2} - k^2\right]^2 \hat{v}. \tag{6.8}$$

H6 The usual approach to solve this equation consists in considering that $k \in \mathbb{R}$ and $c \in \mathbb{C} : c = c_r + i\, c_i$. The sign of c_i controls the exponential growth of the periodic perturbations through time. For a given velocity profile $U(y)$ and boundary conditions, we perturb the system at a certain real wave length k and test the sign of c_i, so that $c_i > 0$ implies that the system is linearly unstable, and $c_i < 0$ the system is linearly stable. Solving the Orr-Sommerfeld equation leads to a dispersion relation $c_i(k; \mathrm{Re})$ that represents the stability of the base flow.

This approach has proven to fail in many situations. This is due to the oversimplifications of the above listed hypotheses. We will discuss briefly the reasons of this failure, by listing the hypotheses, starting from the last one

- **H6**, The true problem is spatio-temporal $(k, c) \in \mathbb{C}^2$. This feature leads to the concept of convective and absolute instabilities (Huerre & Monkewitz, 1990).

- **H5**, The combination of the equations hides part of the problem. The Orr-Sommerfeld equation is one-way coupled to the equation that governs $\hat{u}$, which is referred to as the Squire equation Squire (1933). This equation is responsible for the lift-up effect, that is inherently three dimensional.

- **H4**, Rayleigh (1878) claimed that at a macroscopic scale, only the most unstable mode is observable because the growth is exponential. Nevertheless, when the purpose is to find patterns in the unstable flow, it is necessary to compute the whole spectrum. In boundary layers, the perturbation has to be studied in the (α, β) plane, because the most unstable mode can be oblique.

- **H3**, The normal mode hypothesis, which is referred to as the modal approach, has two consequences. First, if a system is found to be linearly stable, the perturbations can reach a large amplitude before decaying to the base state, which could trigger a non-linear transition in finite time. In order to correct this, non-modal stability was developed Schmid (2007). Second, the perturbations are supposed to be spatially periodic, this is called local stability analysis. In order to allow the perturbations to grow locally, the global stability analysis was developed Theofilis (2011).

- **H2**, In many flows, the validity of the linearization is narrow. For example, in boundary layers, the transition is nonlinear above a perturbation intensity of 0.8%. In order to capture these effects, a weakly-nonlinear stability analysis is necessary Wu (2019).

- **H1**, A jet spreads with the streamwise coordinate as $\delta \sim x$. The base flow is slowly varying in the streamwise direction. In order to take this variation into account, weakly non-parallel Crighton & Gaster (1976) and fully non-parallel Shtern & Hussain (2003) methods were developed.

Relationship to turbulence

Recently, a new kind of LSA has been developed, since the work of Barkley (2006). This author proposed to use a turbulent mean flow velocity profile as a base state for LSA of a cylinder wake. The Reynolds number of this wake flow was just above the critical value for the von-Kármán street to appear. Using this approach, this author was able to predict some features of the nonlinear regime, using a LSA approach.

The question of the comparability of LSA and turbulent flows has important implications, both fundamentally and for applications. This topic receives a lot of attention since a few years. Beneddine *et al.* (2016) give a general criterion for the validity of such a comparison. One of the results of this study is the error is a strong function of the turbulence intensity in the flow, when performing LSA using a statistical averaged profile. More precisely, if in some flow coherent structures are present, the departure of the predictions depend on the intensity of the fluctuations around these coherent structures.

Particular cases where LSA of statistical fields give strikingly good results exist. Combining this approach with the global stability analysis theory Chomaz *et al.* (1991); Theofilis (2011) gave rise to a large amount of work. In confined flows, with persists coherent motion, this method has been proven to be very efficient. For example, Paredes *et al.* (2016) compared predictions from global stability analysis, with Proper Orthogonal Decomposition of PIV data inside a combustor. The LSA was performed using a closure model for the Reynolds stresses, and the purpose was to evaluate the dynamics of the persistent coherent structure that is present inside the combustor. The eigen-vectors of the globally unstable modes were found to collapse almost perfectly with the PIV measurements, and the turn-over time of the coherent structure was estimated with an error of only 17%.

The purpose is a of this discussion is to give a perspective to comparisons between LSA predictions and experimental measurements of our round jet. Such an approach is out of the scope of the present thesis, but as shown in Figure 1.9, we clearly distinguish large vortical structures on some frames of our PIV measurements, at our lowest Reynolds numbers. In this perspective, we perform a small study of a variable density jet. Next, we review some literature on this topic.

Review of the LSA of variable density jets

The literature on free shear flows LSA is very rich. Here, we present a brief review of round jets with passive scalar and variable density jets, focusing on the points that are related to our study.

Passive scalar round jets

This problem is treated in cylindrical coordinates (r, θ, x), where the base flow is parallel along the axial direction, and inhomogeneous in the radial direction $(0, 0, U(r))$. The perturbations take the form $\tilde{u}(r, \theta, x, t) = \hat{u}(r)e^{i(kx+m\theta-kct)}$, where k and m are the axial and azimuthal wave numbers, respectively. It is worth noticing that there is no equivalent to the Squire theorem in cylindrical coordinates, because of the form of the differential operators in this frame of coordinates. The perturbations are necessarily two-dimensional. Depending on the shape of the base velocity profile, the most unstable spatial mode can either be axisymmetric $(m = 0)$, or helical $(m = 1)$. The main parameter that influences the azimuthal wave number of the most unstable mode is the momentum thickness of the injection velocity profile. The procedure to evaluate the effect of the momentum thickness was introduced by Michalke (1964),

$$U(r) = \frac{1}{2}\left(1 + \tanh\left[\frac{D_j}{8\delta_m}\left(\frac{1}{r} - r\right)\right]\right), \text{ where, } \quad \delta_m = \int_0^\infty \left[1 - \frac{U(r)}{U_k}\right]\frac{U(r)}{U_k}dr, \tag{6.9}$$

δ_m is the momentum thickness. When the momentum thickness is small, the dominant mode is axisymmetric, whereas when the momentum thickness is large the dominant mode is helical. Figure 6.2 shows the destabilization of a very this vorticity sheet. Jimenez-Gonzalez *et al.* (2015) showed that the critical value $\delta_{m,crit}$ for the transition between axisymmetric and helical modes is a function of the jet Reynolds number. These authors provide the empirical correlation $\delta_{m,crit}/D_j = 1/(720/(\mathrm{Re} - 33.8) + 19.12)$. For a fixed inlet geometry, the momentum thickness depends on the development of the boundary layer in the nozzle, which in turn is affected by the injection Reynolds number. To take this effect into account, Garnaud *et al.* (2013*a*,*b*) include the inner laminar boundary layer in their numerical computational domain, whereas Kyle & Sreenivasan (1993); Hallberg *et al.* (2006) measure the momentum thickness for different Reynolds numbers or nozzle length in their experiments.

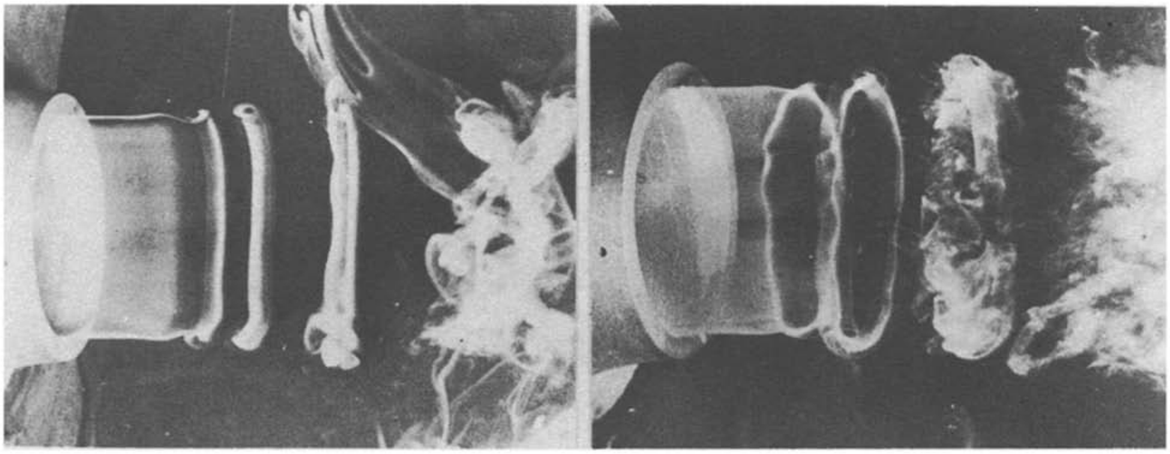

Figure 6.2: Axisymmetric instability of a cylindrical vorticity sheet, from Wille (1963).

Abid *et al.* (1993) showed that, in the modal approach, it is possible to make an asymptotic expansion of the cylindrical problem in the limit of vanishing momentum thickness $\delta_m/D_j \to 0$. These authors demonstrated that in this limit, the cylindrical problem can be approximated by the Cartesian problem with an error of the order $\mathcal{O}(\delta_m/D_j)$. This result allows us to restrict our study to plane jets. The advantage of this simplification is the use of the Squire theorem and the use of Orszag (1971) method in Cartesian coordinates[1].

In Cartesian coordinates, the equivalent of the cylindrical vorticity sheet is the pair of parallel vorticity sheets. Applying the Squire theorem, the azimuthal mode ($m = 1$) does not have a plane jet counterpart in the modal approach. On the contrary, the analogues of the axisymmetric ($m = 0$) mode in Cartesian frame are the varicose and sinuous modes. These modes are characterized by the symmetry of their respective vertical velocity eigen-functions. The varicose mode velocity is odd, which represents a symmetric oscillation of the vorticity sheets. On the contrary, the sinuous mode velocity is even, and represents an oscillation of the flow in a snake like movement. Many recent studies focus on non-modal (Boronin *et al.*, 2013; Garnaud *et al.*, 2013*a*; Jimenez-Gonzalez *et al.*, 2015; Jimenez-Gonzalez & Brancher, 2017; Montagnani & Auteri, 2019) and non-parallel (Shtern & Hussain, 2003; Mullyadzhanov *et al.*, 2019) effects on the linear stability of jets.

---

[1] The cylindrical formulation of the Orszag algorithm requires a lot more caution (Jimenez-Gonzalez *et al.*, 2015, Appendix B).

Variable density jets

Light jets issuing into a quiescent fluid can show a self-sustained oscillation close to the injection, when the density ratio is low enough (Monkewitz & Sohn, 1986). This oscillation is linked to a convective/absolute transition. Many experimental investigations determined a critical value of the density ratio for this transition to occur. The experimental results showed a large scattering from an author to another. Hallberg *et al.* (2006) showed that this problem depends on the jet Reynolds number, the momentum thickness δ_m of the velocity profile, and on the density ratio $\mathcal{R}_\rho = \rho_j/\rho_c$, giving a general law for the oscillation frequency that was able to collapse all the available experimental data.

Hallberg *et al.* (2007) suggest that a very weak co-flow can dramatically change the absolute instability appearance. Srinivasan *et al.* (2010) confirmed, through LSA, that small co-flow velocities can highly alter the absolute instability. In addition, these authors showed that the density gradient thickness is also a parameter to this problem, when the base profiles are not top-hat like.

For an inviscid parallel pair of vorticity sheets with density jumps, Yu & Monkewitz (1990) gave an analytical dispersion relation that comprises both jets and wakes. This result was generalized by Juniper (2006) to the case of a confined geometry and for two-phase jets. Ravier *et al.* (2006) studied variable density Bickley jets, using a classical Taylor-Goldstein equation. These authors, as most of the variable density jets literature, focused on the prediction of the convective/absolute transition, as a function of the density ratio and for different velocity base profiles. They performed both a temporal and spatial approaches, using a shooting method to follow the modes in spectral space. We will use some of these authors results as validation for our linear stability study.

More recently, some studies consider the global stabiltiy analysis of compressible jets (Lesshafft *et al.*, 2019; Pickering *et al.*, 2020). The purpose of these studies is to identify the dominant linear amplification mechanism as a function of the Reynolds and Mach numbers. This approach is out of the scope of our work.

Study of a variable density jet

In this section, we derive a new variable density LSA equation. We expose a preliminary study on the stability analysis of variable density jets, together with the relationship with experimental measurements.

Generalized Taylor-Goldstein equation

We employ the set (2.23)-(2.25) in the local modal linear stability framework. We linearize this set of equations around a base state as follows $(u, v, w, p) = (U+\tilde{u}, \tilde{v}, \tilde{w}, P+\tilde{p})$ and for the pseudo mass fraction $\varphi = \Phi + \tilde{\varphi}$, and apply the procedure described for the Orr-Sommerfeld equation. In order to simplify, we consider an inviscid fluid ($Re \to +\infty$). We find

$$\left[\mathcal{A}_1 + a\left(\mathcal{A}_2 + \frac{1}{Pe}\mathcal{A}_3\right)\right]\hat{v} + a\left[\frac{1}{Pe^2}\mathcal{A}_4 + Fr^2(\mathcal{A}_5 + \mathcal{A}_6)\right]\hat{\varphi} = c(\mathcal{B}_1 + a\mathcal{B}_2)\hat{v}, \tag{6.10}$$

$$\mathcal{A}_7\hat{v} + \left[\mathcal{A}_8 + \frac{1}{Pe}\mathcal{A}_9\right]\hat{\varphi} = c\mathcal{B}_3\hat{\varphi}, \tag{6.11}$$

with

$$\begin{aligned}
&\mathcal{A}_1 = \alpha\Big(U\Big[\frac{d^2}{dy^2} - (\alpha^2+\beta^2)\Big] - \frac{d^2U}{dy^2}\Big)\ ; \quad \mathcal{A}_2 = \alpha\left(\frac{d\Phi}{dy}\frac{dU}{dy} - U\frac{d\Phi}{dy}\frac{d}{dy}\right);\\
&\mathcal{A}_3 = i\frac{d^4\Phi}{dy^4} + i\frac{d^3\Phi}{dy^3}\left(3\frac{d}{dy} - a\frac{d\Phi}{dy}\right) + i\frac{d^2\Phi}{dy^2}\left(5\frac{d^2}{dy^2} - 2a\frac{d\Phi}{dy}\frac{d}{dy} - (\alpha^2+\beta^2)\right)\\
&\qquad + i\frac{d\Phi}{dy}\left(2\frac{d}{dy} - a\frac{d\Phi}{dy}\right)\Big[\frac{d^2}{dy^2} - (\alpha^2+\beta^2)\Big]; \quad \mathcal{A}_4 = i\left(\frac{d}{dy} - a\frac{d\Phi}{dy}\right)\Big[\frac{d^2}{dy^2} - (\alpha^2+\beta^2)\Big]^2;\\
&\mathcal{A}_5 = -(\alpha g_x + \beta g_z)\left(a\frac{d\Phi}{dy} + \frac{d}{dy}\right)\ ; \quad \mathcal{A}_6 = i(\alpha^2+\beta^2)g_y; \quad \mathcal{A}_7 = -i\frac{d\Phi}{dy}\ ; \quad \mathcal{A}_8 = U\alpha\ ;\\
&\mathcal{A}_9 = i\Big[\frac{d^2}{dy^2} - (\alpha^2+\beta^2)\Big]; \quad \mathcal{B}_1 = \alpha\Big[\frac{d^2}{dy^2} - (\alpha^2+\beta^2)\Big]\ ; \quad \mathcal{B}_2 = -\alpha\frac{d\Phi}{dy}\frac{d}{dy}\ ; \quad \mathcal{B}_3 = \alpha,
\end{aligned}$$

where g_i is the projection of the gravity direction on axis x_i. The set of equations (6.10)-(6.11) is a generalization of the non-Boussinesq Taylor-Goldstein equation (Drazin & Reid, 2004). Notice that the linear differential operators $\mathcal{A}_i$ and $\mathcal{B}_i$ do not always commute with the base flow so that $\mathcal{A}_i\Phi$ means the application of the operator to Φ, whereas $\Phi\mathcal{A}_i$ indicates a multiplication. To avoid misleading notation, all operators have been suitably applied to the base flow.

This generalized Taylor-Goldstein equation is valid for binary mixing of diffusive and buoyant chemical species, with arbitrarily oriented gravity and three dimensional perturbations. The derivation of Equations (6.10)-(6.11) follows the same procedure as for the Orr-Sommerfeld equation, with an explicit accounting of the time derivative of the pseudo mass fraction perturbation in Equation (6.10). Because we started with the set of equations (2.23)-(2.25), the state equation (2.21) is implicitly used through the term $e^{-a\varphi}$. Next, we discuss the relationship between our generalized equation and its particular cases.

In comparison with the usual Rayleigh equation, all the additional terms are due to density variations. If $a \to 0$, the only terms that remain are $\mathcal{A}_1$ and $\mathcal{B}_1$ in equation (6.10), and the pseudo mass fraction becomes a passive scalar, i.e. the system is one-way coupled and equation (6.11) can be removed. When the density is variable $a \neq 0$, some sub-cases can be identified, depending on the magnitude of the dimensionless numbers of the problem.

When molecular diffusion is neglected, $Pe \to +\infty$, and the operators $\mathcal{A}_3$, $\mathcal{A}_4$ and $\mathcal{A}_9$ are dropped, and the velocity perturbations are divergence free. In addition, if buoyancy is also neglected, $Fr \to 0$, and $\mathcal{A}_5$ and $\mathcal{A}_6$ are dropped. Notice that density variations still have an impact on the stability of the flow through $\mathcal{A}_2$ and $\mathcal{B}_2$, even in a non-diffusive non-buoyant flow. These particular operators can only be removed if the density variations are very small in a buoyant flow, and by applying the Boussinesq approximation. The non-diffusive and non-buoyant case has been studied in the literature for plane jets (Monkewitz & Sohn, 1986; Yu & Monkewitz, 1990; Raynal *et al.*, 1996; Ravier *et al.*, 2006, among many others).

When buoyancy is considered $Fr \neq 0$, the orientation of the gravity vector g_i plays a role on the dynamics. If the gravity is oriented in the crosswise direction y, $\mathcal{A}_5$ drops. This case has extensively been studied in the literature through the Rayleigh-Taylor instability when ($\Phi' < 0$) (Kull, 1991; Boffetta & Mazzino, 2020), and through the stably stratified flows ($\Phi' > 0$) (Mashayek & Peltier, 2012*a*,*b*). If the gravity vector is oriented in the (x, z) plane $\mathcal{A}_6$ drops, and the perturbations are two-dimensional in general.

If molecular diffusion is taken into account $Pe \in \mathbb{R}$, the velocity field is not divergence free. This effect has been taken into account in the Rayleigh-Taylor configuration, but received much fewer attention for shear flows (Duff *et al.* (1962), for shear layers, Nichols *et al.* (2007), for round jets).

Considered flow configuration

We consider a temporally evolving variable density Bickley jet. The velocity and pseudo mass fraction base profiles are,

$$U(y) = \frac{1}{1+\sinh^2(y)}, \quad \text{and} \quad \Phi(y) = -\frac{1}{a}\log\left(1-\frac{a}{1+a}U(y)\right), \tag{6.12}$$

respectively. When $a = 0$, the pseudo mass fraction converges to a passive scalar, and it is set to be equal to the velocity profile. Figures 6.3(a) and (b) represent the base velocity profile that we consider, together with some pseudo mass fraction profiles for various values of $\mathcal{R}_\rho$, respectively.

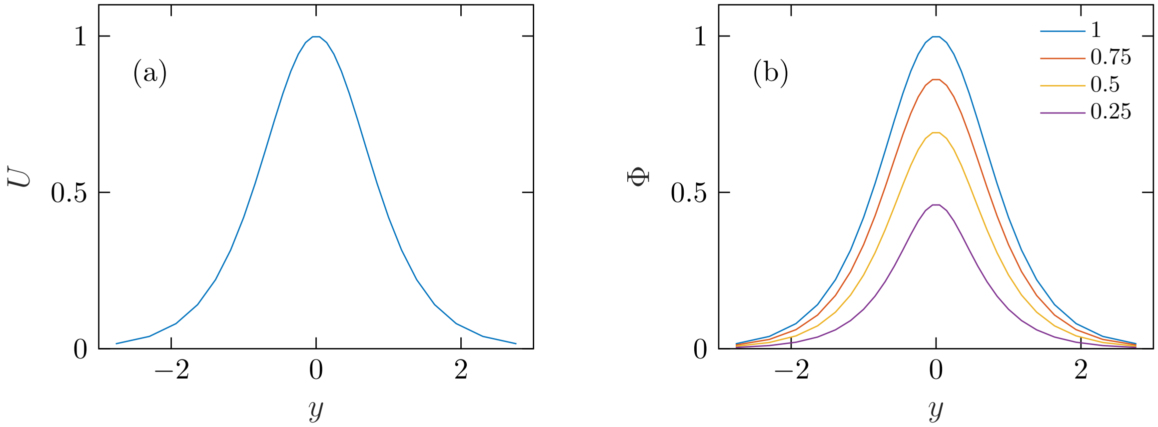

Figure 6.3: Base velocity (a) and pseudo mass fraction (b), for various density ratios $\mathcal{R}_\rho$.

In our study, we will consider the effect of variable density coupled with mass diffusivity, on an inertial plane jet, with cross-wise perturbations only.

Resolution method and validation

In order to resolve the generalized Taylor-Goldstein equation (6.10)-(6.11), we make use of a spectral collocation method to discretize the differential operators, as developed by Orszag (1971). This method consists in projecting the equations with Tchebychev polynomials as test functions, and solving using Gauss-Lobatto quadrature to evaluate the projection. The algorithm that we developed is very similar to (Schmid & Henningson, 2001, Appendix A).

The procedure consists in the choice of a mapping function between spectral space and physical space. We choose $y = \tan(\pi s/2)/2$, where $s \in [-1, 1]$ is in spectral space. For validation of our code, we compare our results to Ravier *et al.* (2006). Figure 6.4 shows the variation of the two most unstable modes in a constant density Bickley jet, namely the sinuous and varicose modes.

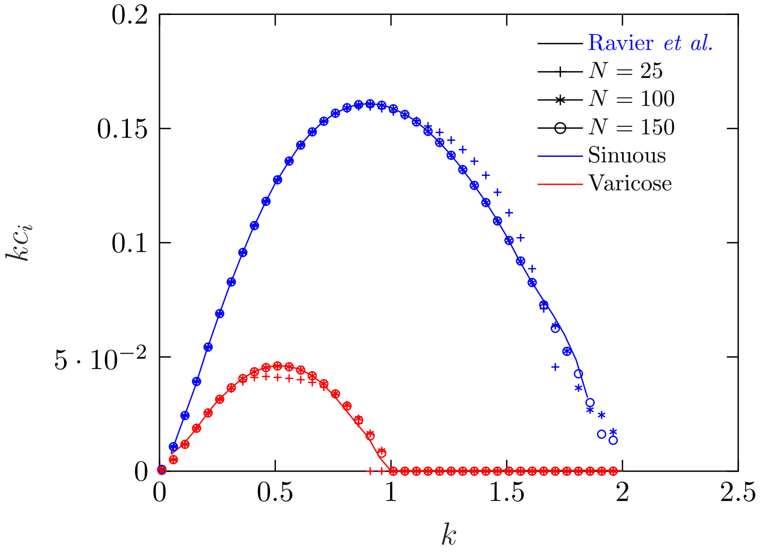

Figure 6.4: Sinuous and varicose instability modes dependence on the real perturbation wave number, for different number of collocation points. Here, $\mathcal{R}_\rho = 1$. We also reproduced data from Figure 2(a) of Ravier *et al.* (2006).

We find that the two most unstable modes, namely the varicose and sinuous modes, are well evaluated when $N = 100$, as shown in Figure 6.4. We see a slight lack of convergence around $k = 0.5$ for the varicose mode. In order to ensure the quality of the resolution, Figure 6.5 (a) and (b) represent the associated eigen-vectors to the sinuous and varicose modes, respectively, at $k = 0.5$. The sinuous $\hat{v}$ velocity eigen-mode is even, whereas the varicose $\hat{v}$ velocity eigen-mode is odd. We confirm this feature in Figures 6.5, and validate that these functions are well converged when $N = 100$.

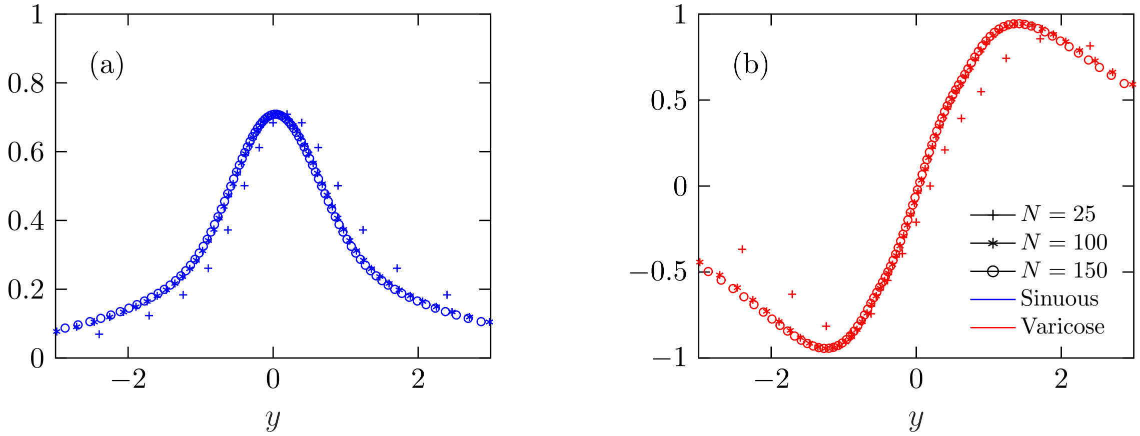

Figure 6.5: Eigen-vectors associated with the sinuous mode (a) and the varicose mode (b), for $k = 0.5$ and $\mathcal{R}_\rho = 1$, for different number of collocation points.

To show the validity of the density variations part of equations (6.10)-(6.11), we reproduce, in Figure 6.6, the density ratio dependence of the two most unstable eigen-modes in this flow. We find a good agreement between the results and the literature, which validates our code.

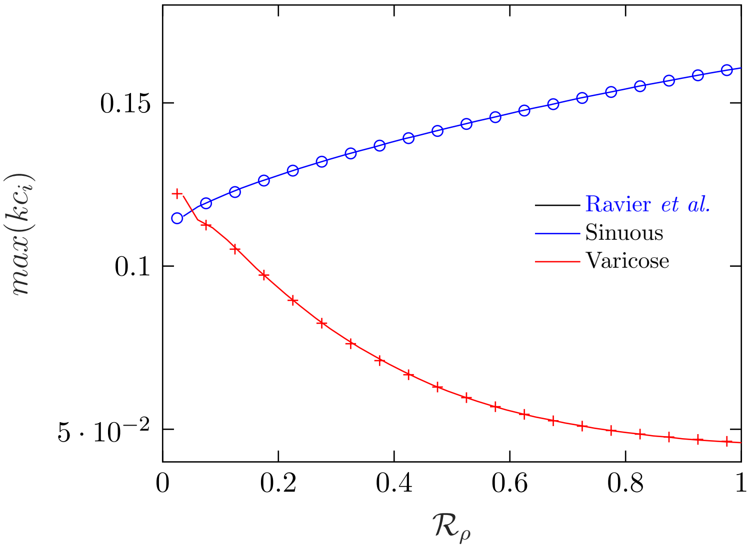

Figure 6.6: Maximum growth rate of the two most unstable modes with $\mathcal{R}_\rho$. We also reproduced Figure 3(a) from Ravier *et al.* (2006).

Stability analysis of a diffusive variable density jet

Let us now consider the case of finite Peclet number. As a preliminary approach, we evaluate the full spectrum of the generalized Taylor-Goldstein equation in the inertial case $Fr = 0$. Figure 6.7 shows such a spectrum for $k = 1$ and $\mathcal{R}_\rho = 0.3$, for various Peclet numbers. This spectrum is associated with the most unstable sinuous mode at $\mathcal{R}_\rho = 0.3$. The case $Pe \sim 10^9$ is in consistent with the non-diffusive predictions (Figure 6.6). In this case, the sinuous and varicose modes are depicted by the blue dots that are above the neutral axes, respectively at $kc_i = 0.1308$ and $kc_i = 0.0404$.

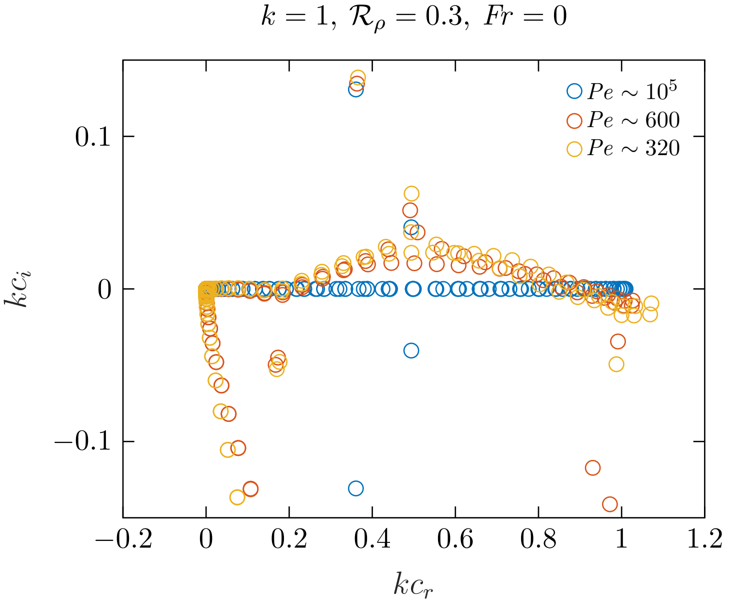

Figure 6.7: Full spectrum of the generalized Taylor-Goldstein equation, for $k = 1$, $\mathcal{R}_\rho = 0.3$ and $Fr = 0$, for various Peclet numbers.

When the Peclet number is lowered to $Pe \sim 600$, a large amount of unstable modes rise from the neutral curve. The sinuous and varicose modes become more unstable, as represented by the red dots in their upper neighborhood. This tendency increases as the Peclet number is lowered even more to $Pe \sim 320$. We notice an increase in the imaginary part of the sinuous and varicose modes. This effect is stronger on the varicose mode.

The sinuous mode remains the most unstable mode, for the three Peclet numbers we show. We focus now on the eigen-functions associated with this mode. The corresponding cross-wise velocity eigen-function $\hat{v}$ is depicted in Figure 6.8(a). This function presents a monotonous decrease in magnitude with decreasing Peclet number. On the other hand, the pseudo-mass fraction eigen-function $\hat{\varphi}$, associated with the same mode is shown in Figure 6.8(b). We find that this eigen-function is odd, in all cases. The sign of this function is to be interpreted as a sinuous mode, as this quantity is not a vector like the velocity. When $Pe \sim 10^9$, pseudo mass fraction is passive, even if density variations influence the velocity through pure inertial terms ($\mathcal{A}_2$ in Equation (6.10)). In this case, $\hat{\varphi}$ is kinematically transported by $\hat{v}$, through Equation (6.11), showing sharp gradients at the edge of the jet. For lower Peclet numbers, the pseudo mass fraction gradients are globally smoother, at the edge and inside the core.

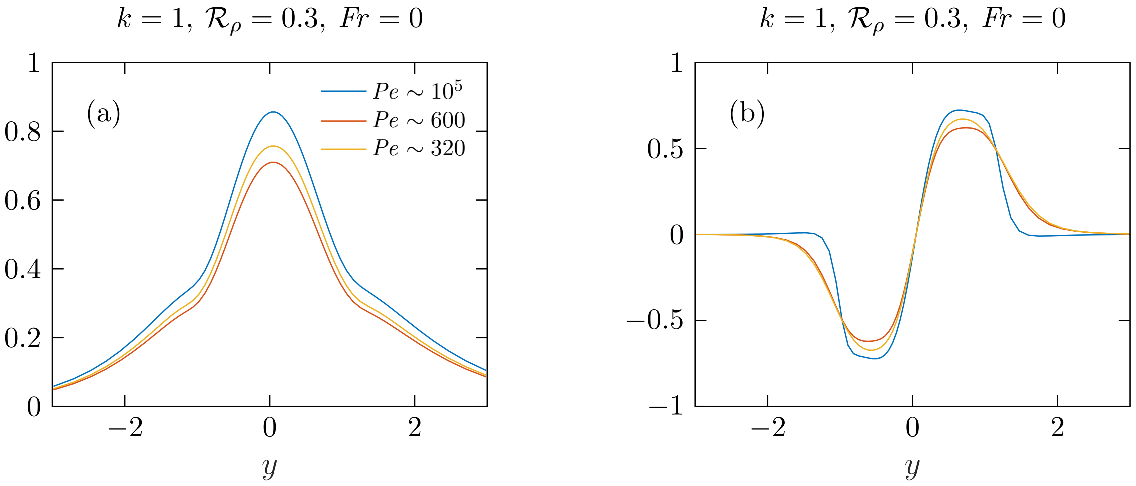

Figure 6.8: Eigen-vectors associated with the sinuous mode of cross-wise velocity $\hat{v}$ (a) and pseudo mass fraction $\hat{\varphi}$ (b), in the case $k = 1$, $\mathcal{R}_\rho = 0.3$ and $Fr = 0$, for various Peclet numbers.

The purpose of this discussion is to illustrate the effect of finite diffusivity on the LSA of a variable density jet. In a more systematic way, we now focus on a large variation of density ratio and Peclet number, by performing a LSA in a $(\mathcal{R}_\rho, Pe)$ plane. Figure 6.9 shows such a stability diagram, where we represented the most unstable growth rate $max(kc_i)$, normalized by the maximum growth rate at the same density ratio but in the non-diffusive case $max(kc_i, \text{non-diffusive})$, in a logarithmic scale.

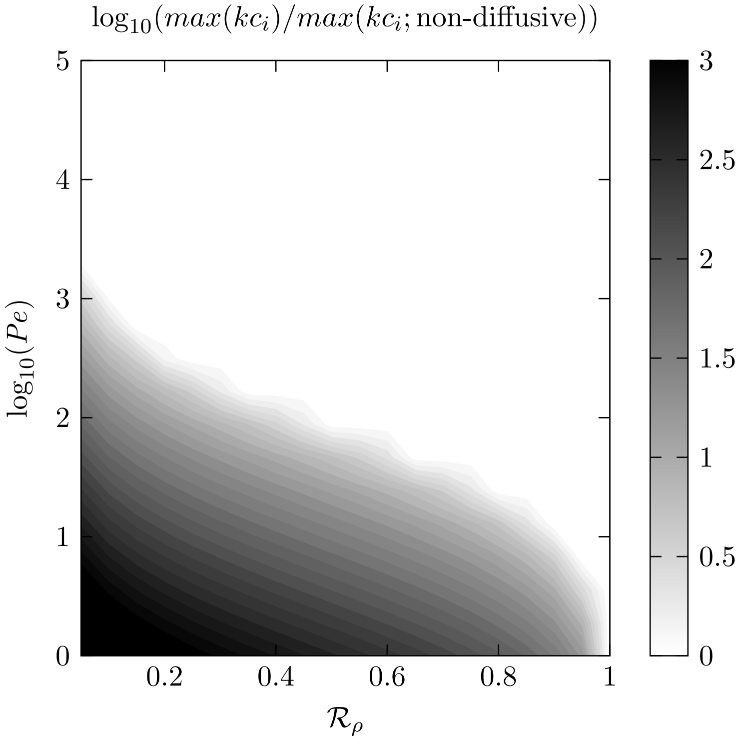

Figure 6.9: Stability diagram of the variable density diffusive Bickley jet.

On this diagram, the horizontal line defined by $Pe = 10^5$, the quantity depicted equals unity, and corresponds to the blue line in Figure 6.6. We see two very distinct regimes, separated by a line in the middle of the diagram. Above this line, diffusivity does not contribute at all the stability of the problem, which is completely determined by the non-diffusive response. Below this line, mass diffusivity dominates the instability. Also, the shape of the separation line indicates that diffusivity does not influence the instability asymptotically at the density tends to unity $\mathcal{R}_\rho \to 1$. In this limit, pseudo mass fraction is fewer and fewer coupled to the dynamics, and the inertial contribution of density variations vanish as well (though $\mathcal{A}_2$ in Equation (6.10)).

The clear separation of these two regimes does not imply that the flow dynamics is totally independent of mass diffusivity after the very short time where LSA is valid. The very first Kelvin-Helmholtz vorticies can get damped by diffusivity, even above the line in the diagram 6.9.

Conclusion and perspectives

In this part, we made a small review linear stability analysis of active scalar flows. Then, we derived a new equation to take mass diffusivity variations in a non-Boussinesq variable density jet into account. This equation, and the algorithm that we wrote to solve it, were validated by reproducing some results from literature for a non-diffusive jet. We showed the consistency of our method by a highly non-diffusive case. Finally, we evaluated the effect of mass diffusivity on a variable density Bickley jet, and found two distinct regimes in a density ratio-Peclet number stability diagram.

In a more general context, active scalar LSA can be assessed directly using the full incompressible set (2.1)-(2.5). Performing a linearization, and then combining the resulting equation leads to a generalization of both the Orr-Sommerfeld and Taylor-Goldstein equations, that would contain all active scalar effects in one eigen-value problem. To our knowledge, no study in the literature assessed the stability of an incompressible flow in this point of view. Nevertheless, viscosity variations were taken into account using the thermal Orr-Sommerfeld equation (Wazzan *et al.*, 1968; Wall & Wilson, 1996; Govindarajan, 2004; Govindarajan & Sahu, 2014). This problem has mainly been considered in confined flows, as it directly related to oil industry applications.

Regarding our jet, Figure 1.9 illustrates a typical scalar field measurement. This particular image was chosen on purpose to illustrate that turbulence that occurs at $3D_j$ downstream can be fed by young vorticies at the injection. This picture is a bit simplistic, as the jet issues from a fully turbulent pipe regime, and turbulent fluctuations already exist in the flow. We do not observe vortices in all measurement images. But, at lower Reynolds numbers, we saw more sustained and persistent vorticies, that could be predictable by LSA. The base velocity profile is a laminar Hagen-Poiseuille flow, and pseudo mass fraction is a top-hat like profile.

Recently, a lot of work is dedicated to global stability analysis of compressible round jets (Lesshafft *et al.*, 2019; Pickering *et al.*, 2020). Finally, a long term perspective to this thesis is to adapt these stability approaches to incompressible jets with variable density and/or viscosity, together with mass and heat diffusivities. The generalized Taylor-Goldstein equation (6.10)-(6.11) is a small step in this direction.

Appendices

Appendix A

Computation of flow conditions

The aim is to find the jet inlet velocity, co-flow velocity and jet density (u_j, ρ_j, u_c), that correspond to the dimensionless numbers (Re, Ar, Ct_{ni}) that we choose. Then, to find the mass flow distribution over the six mass flow meters that control the seeding and jet density. To do so, we solve the nonlinear set of equations

$$Re = \frac{\rho_j (u_j - u_c) D_j}{\mu_j} \tag{A.1}$$

$$Ar = \frac{g \rho_j (\rho_c - \rho_j) D_j^3}{\mu_j^2} \tag{A.2}$$

$$Ct_{ni} = \frac{u_k}{(u_d^2 - \frac{1}{2} u_k^2)^{1/2}} \tag{A.3}$$

$$u_k = \frac{\rho_j u_j D_j^2 + \rho_c u_c (D_c^2 - D_j^2)}{\rho_0 D_c^2} \tag{A.4}$$

$$u_d^2 = \frac{\rho_j u_j^2 D_j^2 + \rho_c u_c^2 (D_c^2 - D_j^2)}{\rho_0 D_c^2} - \frac{1}{2} \frac{\rho_c}{\rho_0} u_c^2 \tag{A.5}$$

$$\rho_0 = \frac{\rho_j u_j D_j^2 + \rho_c u_c (D_c^2 - D_j^2)}{u_j D_j^2 + u_c (D_c^2 - D_j^2)} \tag{A.6}$$

The jet and co-flow diameters $D_j = 10$ mm and $D_c = 800$ mm respectively. The co-flow is composed of air at $T = 50°C$, therefore $\rho_c = 1.09$. The jet is composed of a Helium-Air mixture. The dynamic viscosity ratio pure Helium and pure air is $\mathcal{R}_\mu \sim 0.93$. We evaluated the viscosity of this mixture when the jet contains the largest Helium mass fraction, using a Wilke law (Wilke, 1950). We found that this quantity is always very close to the viscosity of air at $T = 50°C$, which we will consider in our study $\mu_j = 1.796.10^{-5}$ Pa.s.

The Archimedes number depends only on the jet target density. We exploit this feature by solving the jet density ρ_j directly. Then, the problem (Re, Ct_{ni}) is numerically solved by fixing $\mathrm{Ct}_{ni} = 0.7$ and the desired Reynolds number. This resolution was performed by the Matlab function *fsolve* through a Newton-Raphson method. This algorithm requires a first guess, and the convergence is not guaranteed because the problem is not parabolic. We make sure that the solution is correct, by recomputing the dimensionaless quantities with the solution. If the algorithm does not converge, we manually try a different guess, exploiting the information that the jet velocity is one order of magnitude larger than the co-flow velocity. We typically use a guess of 1 m/s for u_j and 0.1 m/s for u_c.

Once the velocities are computed, it is necessary to adjust the six flow meters for the optical diagnostics, namely for the jet, pure air, pure Helium, DEHS air for PIV, Anisole air for PLIF, and for the co-flow, pure air and DEHS air for PIV. Both jet and co-flow are heated up to $T = 50^\circ$, to ensure a precise control of the density variations. In the jet, the heating system is placed on the pure air inflow, because this fluid has the largest mass flow rate in most of the flow conditions. Also Anisole is highly flammable, so it was injected far from the jet pure air. The method that we employed is fixing first an air/Helium ratio in the jet. The air mass flow rate is then distributed between the three sources, heating, DEHS, Anisole. We adjusted manually these three mass flow rates to have enough DEHS droplets for PIV, enough mass flow rate for the heating system not to blow up and enough Anisole for the PLIF to emit enough signal.

It is important to notice that Anisole is 4 times heavier than Air, so the Archimedes number decreases when more Anisole is injected in the jet. The mass flow rate of Anisole depends strongly on the temperature of the seeding device, through its vapor pressure. As Anisole evaporates, this seeding device cools down. We corrected the injected mass flow rate of Anisole in real time with a temperature measurement within the seeding device, and computed the vapor pressure with an Antoine equation from Dreisbach & Spencer (1949).

More generally, we coded a LabView algorithm that computes the Reynolds and Archimedes numbers in real time, using the measured temperatures and mass flow rates.

Appendix B

List of conferences

Here, we enumerate the attended conferences, symposia and graduate schools during this thesis.

1. *Pacific Symposium on Flow Visualisation and Image Processing-11*, 1-3 December 2017, Kumamoto, Japan. We wrote a conference paper attached in Appendix C. This paper is based on our first variable viscosity DNS, realised by DR M. Gauding.
2. *John Von-Neumann Institute for Computing Symposium 2018*, 22-23 February 2018, Jülich, Germany. Realized a poster about variable viscosity flows, based on Brahami *et al.* (2017).
3. *LxLaser-19*, 16-19 July 2018, Lisbon, Portugal, gave a presentation on entrainment in variable viscosity flows, based on the experimental measurements of Voivenel (2016) in our group.
4. *GDR Turbulence*, 16-18 October 2018, Nice, France.
5. *New Challenges in Turbulence Research V*, 7-12 April 2019, Ecole de Physique des Houches, Les Houches, France.
6. *European Turbulence Conference- 17*, 3-6 September 2019, Turin, Italy. We gave a presentation on two-point statistics in variable density round jets, based on our measurements.

Appendix C

Publications

In this appendix, we attach two papers. First, a conference paper on a variable viscosity temporally evolving jet. Second, an accepted paper on a temporally evolving jet flame.

CONDITIONAL AND CONVENTIONAL STATISTICS OF VARIABLE VISCOSITY JET FLOWS

Y. Brahami[1], M. Gauding[1], E. Varea[1], and L. Danaila[1]

[1]*CORIA UMR 6614, University of Rouen, St Etienne du Rouvray, France*

Abstract

This study aims to evaluate the effect of variable viscosity a planar temporal jet, computed with direct numerical simulation (DNS). Classical turbulence quantities are treated using both conventional and conditioned statistics. This study shows that the conventional statistics are mostly unable to divulge the effects of variable viscosity, whereas the conditioned statistics are more suited to reveal these subtle effects.

Introduction

Theoretical developments in hydrodynamic turbulence assume constant thermo-physical properties for the studied fluid. In realistic situations, this consideration is rarely reached. Mixing two fluids may involve density and/or viscosity differences. The case of variable density turbulent flows has been studied extensively in the literature Chassaing et al. [2002]. In contrary, the case of variable viscosity flows did not rise so much interest. Because turbulence mixes the fluids very strongly, it has been assumed that the asymptotic case where the scalar field is close to homogeneity is reached fast, hence variable viscosity has a negligible effect on the fully turbulent fields. In industrial applications, the encountered flows rarely have enough time to reach this fully established state, and most of the relevant phenomena occur during the transition phase. On the purpose of understanding the mixing processes including the transition phase, it is of great interest to evaluate the effect of variable viscosity.

The first study of the effects of viscosity is due to Campbell and Turner [1986]. They studied the case of the injection of a fluid into a more viscous fluid. The purpose was to evaluate the effect of different viscosities on the mixing of magmas. It has been noticed in Cabra et al. [2005], Voivenel et al. [2017] that the morphology of a variable viscosity flow can be very different from that of a constant viscosity flow. The influence of viscosity stratification in channel flows has been studied in the frame of linear stability analysis by Govindarajan [2004], Govindarajan and Sahu [2014]. Variable viscosity effects compete with the destabilization due to the shear, and it can have a stabilizing or even more destabilizing effect on the flow.

When a shear flow develops inside a laminar flow, two regions distinguish by their turbulence intensity. These two regions are separated by a thin layer that is called the turbulent/non-turbulent interface (T/NT or interface). The improvement of DNS in the past decades has permitted to access very precise information about the phenomena that occur at the T/NT. As reviewed in detail by da Silva et al. [2014], the detection of the interface is arbitrary and based on a threshold criterion, generally on the vorticity or the scalar fields. Studies have shown that the evolution of one point turbulent quantities through the T/NTI are of high relevance to explain mass entrainment and the development of turbulence, [Phillips, 1955, Westerweel et al., 2009, Taveira and da Silva, 2013]. This method has been applied to a wide variety of turbulent flows, as shear layers and boundary layers, but always with constant viscosity. As shown by Bisset et al. [2002], conditioned statistics approach reveals a particular evolution of the statistics through the interface. This evolution is not unrevealed by the conventional averaging. The thickness of the T/NT in jets is of the order of the Taylor length-scale λ, da Silva et al. [2014].

This study aims to highlight the influence of varying viscosity on turbulence by using conventional and conditioned statistics. This article is structured as follows. First, we introduce the DNS that we used. Second, a detailed post-processing technique is described, and the considered cases presented. Then, one point turbulent quantities are examined, focusing on the scalar fields. The conventional and conditional approaches are applied to the scalar concentration and scalar dissipation, then compared. Finally, concluding remarks are exposed.

Post-processing technique

DNS details

Direct numerical simulation (DNS) of a temporally evolving turbulent plane jet flow was performed as described by Gampert et al. [2014], Gauding et al. [2015] and Hunger et al. [2016]. The DNS solves the non-dimensional incrompressbile Navier-Stokes equations and was carried out on the supercomputer

JUQUEEN at research center Juelich (Germany) with a hybrid MPI/OpenMP parallelization. The high resolution of the DNS captures local gradients of the viscosity and velocity fields and allows to detect the turbulent/non-turbulent interface with high accuracy. In the following, details of the DNS algorithm are summarized. The non-linear term of the momentum equation is formulated in skew-symmertic form to reduce aliasing errors. Spatial derivatives are computed by a sixth-order implicit finite difference scheme Lele [1992]. Temporal integration is performed by a low storage, fourth order Runge-Kutta scheme and the Poisson equation is solved in spectral space by employing a Helmholtz equation. The computational domain has periodic boundary conditions in stream-wise Ox and span-wise Oy directions, while free-slip boundary conditions are used in the cross-wise Oz direction. The flow is statistically homogeneous in xOy planes. Conventional statistics are averaged over these planes and depend only on time t and the cross-wise coordinate z. The non-dimensional size of the domain is $L_x = 6\pi$, $L_y = 6\pi$ and $L_z = 12.5$, discretized by $2816 \times 2816 \times 1500$ grid points. The size of the domain is large compared to the integral scales of the jet to reduce confinement effects. A uniform equidistant mesh is used for the inner part of the domain, while the outer part is slightly coarsened towards the cross-wise boundaries. The DNS is well resolved, since the grid width is smaller or equal the Kolmogorov length scale. Initially the interfacial layer at the edge of the jet is well resolved by 14 grid points. The Navier-Stokes equations are solved in non-dimensional form, and read:

$$\frac{\partial u_j}{\partial x_j} = 0 \tag{1}$$

$$\frac{\partial u_i}{\partial t} + u_j \frac{\partial u_i}{\partial x_j} = -\frac{\partial p}{\partial x_i} + \frac{1}{Re_0} \frac{\partial}{\partial x_j}\left[\nu\left(\frac{\partial u_i}{\partial x_j} + \frac{\partial u_j}{\partial x_i}\right)\right] \tag{2}$$

$$\frac{\partial \phi}{\partial t} + u_j \frac{\partial \phi}{\partial x_j} = \frac{1}{Sc\, Re_0} \frac{\partial^2 \phi}{\partial x_j^2} \tag{3}$$

$$\nu = e^{\phi log(R_\nu)} \tag{4}$$

For non-dimensionalization the initial centerline velocity $u_{c,0}$ and the initial jet thickness δ_0 are used. For the dissipative term, the initial centerline viscosity ν_1 is chosen as a reference. The initial Reynolds number is defined as $Re_0 = u_{c,0}\delta_0/\nu_1$ and equals 2200. The jet width δ is defined as the distance between the points at which the mean streamwise velocity decreases to 50% of its centerline value. The parameter $R_\nu = \nu_2/\nu_1$ is the initial viscosity ratio between the jet (subscript 1) and the host (subscript 1) viscosities. The third parameter to be specified is the Schmidt number defined as $Sc = \nu_1/\mathcal{D}_1$, where $\mathcal{D}_1$ is a diffusion coefficient. We set $\mathcal{D}_1$ equal to ν_1 which results in a unity Schmidt number. Additional, an equation that links the local viscosity to the mixture fraction is necessary to close the system. This choice depends on the thermodynamic of the fluids. The choice of equation (4) is suitable for isothermal perfect gases. In real isothermal gas flows, R_ν rarely exceeds 10, consequently, we consider cases where $R_\nu = 0,25; 0,5; 1; 2; 4$. The velocity and viscosity initial profiles are build using hyperbolic tangents that are symmetrized with respect to the mid-plane.

Post-processing

The considered fields are evaluated by conventional and conditioned statistics. The conventional approach consists in averaging the fields, that depends on (x, y, z), over the xOy planes at each time step. This is done by averaging all the values of the field on a fixed z. We then obtain an averaged field, noted $< . >$, that is a function of the crosswise coordinate z only.

The conditioned approach consists on computing the fields over a region that surrounds the T/NT. In figure .1, we show a schematic view of the procedure detailed hereinafter. This systematic approach was suggested by Bisset et al. [2002]. First, a threshold is chosen to locate the interface (blue line in Fig. 1). Then, the field is evaluated over a certain distance through the thickness of the interface, in and out of the turbulent region (red region in Fig. 1). We obtain a field that is a function of the separation distance from the interface $(x, y, z - z_I)$. The new coordinates are a set of surfaces that have the same shape as the T/NTI, but at translated crosswise coordinates. Finally, an averaging over this new set of curvilinear coordinates is performed on each interface shaped surface, by fixing $z - z_I$. The result is an average field, noted $< .|z - z_I >$, that is a function of the crosswise separation distance to the interface position $z - z_I$ only.

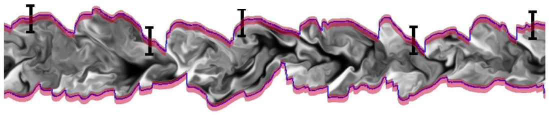

Figure 1: Schematic view of the conditional averaging.

The localization of the interface has been done by different thresholds, on different fields. In a flow with constant thermo-physical properties, the vorticity or the scalar fields are mostly used. The study from Gampert et al. [2014] shows that the interface position is not very sensitive to the field considered, except for low Schmidt numbers. The choice of unity Schmidt number is valid, and in this case the two approaches converge towards the same T/NT position. In order to compare the results, the interface position should not be very sensitive on the threshold value. The technique suggested by Prasad and Sreenivasan [1989] evaluates a threshold using a histogram of the field distribution. This histogram generally shows a plateau, and choosing a threshold value close to this plateau ensures the interface position to be almost independent of the threshold value. In our case, variable viscosity is an additional parameter to the interface detection. The interface position has to be independent of the viscosity ratio. To do so, we compared different methods to detect the T/NT. This comparison has been done by comparing the high order moments of the pdf of the interface position. We checked that the scalar Prasad and Sreenivasan [1989] technique is suitable for this problem.

Results

Turbulent plan jets show, far enough form the injection, a self-similar behavior. In this regime, turbulence is self-preserving and the turbulent quantities decay following precise exponents. In this section, we check the time evolution of conventional one point statistics at the mid-plan of the jet. Then, we take a closer look at the scalar quantities, with both conventional and conditioned approaches. We show through figures 2 and 3 the time evolution at the mid-plan (noted with a subscript c) of classical turbulence quantities, for different viscosity ratios.

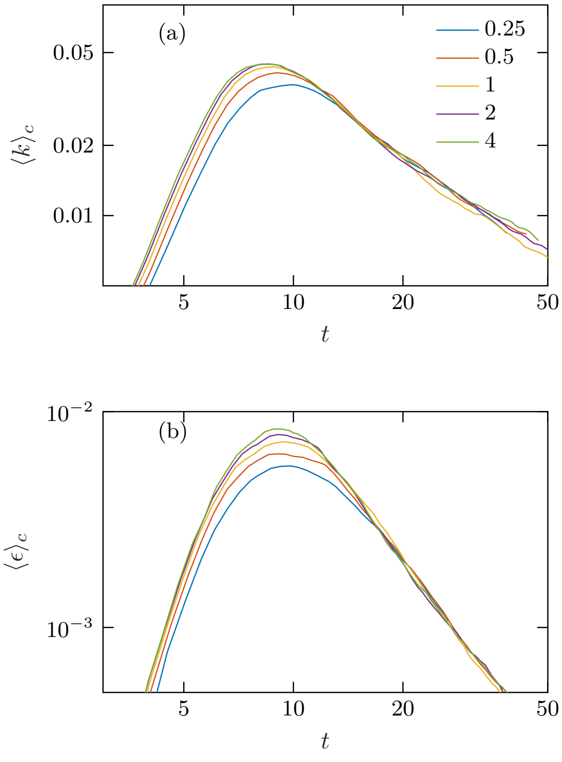

Figure 2: Temporal evolution of mid-plan conventional averages of (a) turbulent kinetic energy and (b) dissipation. The legend represent R_ν values.

We show on Fig. 2 (a) and (b) that for turbulent kinetic energy and dissipation at the mid-plan the very early and late times are not affected by the viscosity ratio. But in the transition phase where the flow is destabilized and the energy is withdrawn from the mean velocity field, we see that the higher the viscosity ratio, the more turbulent the flow is. Compared to the constant viscosity case, we see that if $R_\nu < 1$, the peak is lower and happens later in time, and if $R_\nu > 1$ the peak is higher and is reached earlier. R_ν is defined as the ratio of outer to the inner viscosities. This means that the injection of a less viscous fluid into a more viscous one has a different behavior than the opposite case. This phenomenon has been observed by in a spatial round jet experiment. Viscosity variation can either have a stabilizing of destabilizing effect on the initial flow. In the far field, the curves collapse and we do not see any effect of the viscosity anymore. This asserts the argument that viscosity does not have any effect on the decay, which is Taylor's postulate Taylor [1935]. The turbulent field smooths the viscosity variations so strongly that no effect is seen inside the fully turbulent core in the far field.

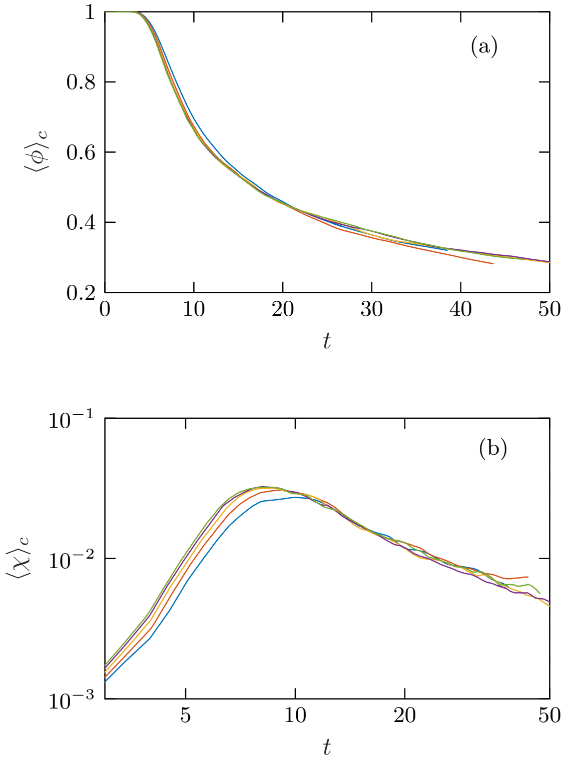

Figure 3: Temporal evolution of mid-plan conventional averages of (a) scalar concentration (mean + fluctuation) and (b) scalar dissipation. The legend is shared with Fig. 2.

The mid-plan scalar concentration and scalar dissipation are shown if Fig. 3 (a) and (b), respectively. The decay of the mid-plan scalar concentration shows no dependence on the viscosity ratio for all times. The scalar dissipation shows the same dependency as the dynamic quantities. Figure. 2 (a),(b) concern the evolution second order moments of the fluctuating fields, and Figure. 3 (a) and (b) the evolution of the mean scalar and scalar dissipation full fields (mean + average). The independence of the mid-plan scalar concentration is an indication that viscosity variations do not affect the mean fields. The scalar dissipation, Fig.3, is a quantity that depends on $\nabla\phi$, which is a small scale quantity. This lack of influence on mean fields and strong influence on gradients shows that viscosity is indeed affecting only the small scales of the flow. This result is in agreement with the well known Kolmogorov similarity hypotheses Kolmogorov [1941], and more precisely: Taylor's postulate Taylor [1935]. The scalar dissipation is an important quantity in mixing modeling, and a precise estimation is necessary to ensure the efficiency of the models predictions.

In order to assert the influence of variable viscosity on the conventional scalar field statistics, we show the conventional statistics of $<\phi>$ and $<\chi>$ in Fig.4:

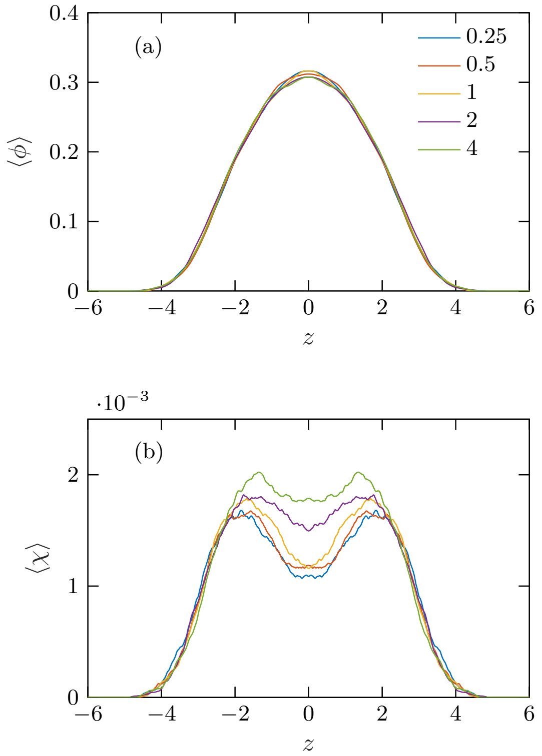

Figure 4: Crosswise profiles of conventional (a) mean scalar concentration and (b) mean scalar dissipation. All the curves are plotted at $t = 25$. The legend represents R_ν values.

We see from Fig.4(a) that viscosity variations do not have any effect on the scalar concentration conventional mean, across the jet. This result was shown in Fig.3(a) at the mid-plan for all times. Moreover, all the information about the jet edge is smoothed by the conventional approach. On this figure, the plotted variables are not normalized. It is not possible to exhibit the exchanges between the turbulent core and the laminar region by this approach. The scalar dissipation crosswise profile, Fig.4(b), is strongly affected by viscosity variations. In particular, we see that close to the edge of the jet, peaks of this quantity appear. These peak regions are monotonically depending on R_ν, so that high values of R_ν engender higher peaks. We see the same dependence for the scalar dissipation in the turbulent core. Compared to the constant viscosity flow, the scalar dissipation in the core is larger if $R_\nu > 1$, and smaller if $R_\nu < 1$. This is an indication that the mixing is indeed affected by viscosity variations. This information is crucial for the understanding of mass exchange processes between the turbulent core and the laminar region. In order to unravel the local behavior of mass transfer at the T/NT, Fig.5 illustrates the conditional average of ϕ and χ:

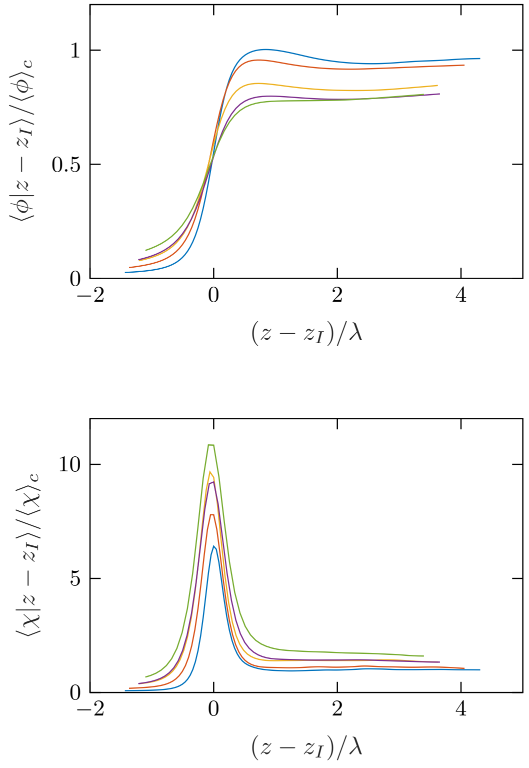

Figure 5: Condition average of: (a) the scalar concentration and (b) the scalar dissipation at $t = 25$. The legend is shared with Fig.4.

The quantities shown in Fig.5 are conditional averages normalized by the conventional average of the same field at the mid-plan. The variation is plotted against a crosswise separation distance to the T/NT normalized by the mid-plan average Taylor length-scale λ_c. The conditioned scalar concentration is plotted on Fig.5(a). We see a very abrupt jump from 0 in the laminar region (corresponding to the negative values of the x-axis) to a value close to 1 inside the core. This asymptotic value of 1 is reached at different speeds depending on the viscosity ratio. This result is commonly known in the literature for constant viscosity, Bisset et al. [2002]. Very close inside core, we see an overshoot of the scalar concentration, that is stronger with decreasing R_ν. In particular, for the case $R_\nu = 0.25$, the overshoot is so strong that the local conditional average of ϕ is larger than the mean mid-plan value. The interface thickness is also changed by R_ν. This effect is due to the fact that, for different R_ν, the Taylor length-scale is not the same at equal time. Because the transition to turbulence is different, the Taylor-bases Reynolds numbers have different values for each case, if compared at the same physical time. This does not contradict the self-similarity on the decay. The Taylor-based Reynolds number follows the same power law for all cases in the fare-field, but shifted in time.

The scalar dissipation is plotted on Fig.5(b). This quantity varies from a value close to 0 in the laminar region, to a value close to 1 in the core. Through the T/NTI, the scalar dissipation sustains a very large bump. The amplitude of this bump is strongly affected by R_ν. Compared to the constant viscosity case, where the maximum value is $8 \times \langle\chi\rangle_c$, we see that for $R_\nu = 4$ this value is of the order of $11 \times \langle\chi\rangle_c$ and that for $R_\nu = 0.25$ the maximum is $6 \times \langle\chi\rangle_c$. The scalar dissipation is a central quantity is many mixing models, and an error on its estimation could lead to wrong predictions. More importantly, the scalar dissipation is very often used in turbulent reactive flows models. In this phenomenon, the chemical reactions occur at very localized regions, very similarly to mass exchanges in non-reactive turbulence. As we saw, the conditional average shows a miss-evaluation of the scalar dissipation at the T/NTI that can be of the order of 2 if variable viscosity effects are not taken into account.

Conclusion

In this paper, we studied the influence of viscosity variations of a temporal plan jet, computed with DNS. Conventional statistical averaging has been used to evaluate the turbulent kinetic energy, dissipation, scalar concentration and scalar dissipation variations. In addition, the conditional statistics of the scalar concentration and scalar dissipation are computed. We show that self-similarity of the decaying turbulence is not broken for this kind of flows. The conventional averages of mean scalar concentration is not affected by viscosity variations, but the scalar dissipation is. This is an indication that the viscosity variations mostly affect the small scales of the flow. The conditional statistics of the scalar dissipation reveal a strong dependence on viscosity variations, especially crossing the T/NT. This tendency is detectable using the conventional approach, but highly underestimated. Scalar dissipation is a central quantity in many mixing models, and its precise estimation is required to guarantee good predictions for these models.

References

D.K. Bisset, J.C.R. Hunt, and M.M. Rogers. The turbulent/non-turbulent interface bounding a far wake. *Journal of Fluid Mechanics*, 451:383–410, 2002.

R. Cabra, J. Y. Chen, R. W. Dibble, A. N. Karpetis, and R. S. Barlow. Lifted methane-air jet flame in vitiated co-flow. *Combust. Flame*, 143 (4):491–506, 2005.

I. H. Campbell and J. S. Turner. The influence of viscosity on fountains in magma chamber. *Journal of Petrology*, 27:1–30, 1986.

P. Chassaing, R.A. Antonia, F. Anselmet, L. Joly, and S. Sarkar. *Variable density fluid turbulence, Kluwer.* Cépadues Editions, 2002.

C.B. da Silva, J.C.R. Hunt, I. Eames, and J. Westerweel. Interfacial layers between regions of different turbulence intensity. *Annual Review of Fluid Mechanics*, 46:567–590, 2014.

M. Gampert, J. Boschung, F. Hennig, M. Gauding, and N. Peters. The vorticity versus the scalar criterion for the detection of the turbulent/non-turbulent interface. *Journal of Fluid Mechanics*, 750:578–596, 2014. doi: 10.1017/jfm.2014.280.

M. Gauding, J.H. Goebbert, C. Hasse, and N. Peters. Line segments in homogeneous scalar turbulence. *Physics of Fluids*, 27(9):095102, 2015.

R. Govindarajan. Effect of miscibility on the linear instability of two-fluid channel flow. *Int. J. Multiphase Flow*, 30:1177–1192, 2004.

R. Govindarajan and K.C. Sahu. Instabilities in viscosity-stratified flow. *Ann. Rev. Fluid Mech.*, 46: 331–353, 2014.

F Hunger, M Gauding, and C Hasse. On the impact of the turbulent/non-turbulent interface on differential diffusion in a turbulent jet flow. *Journal of Fluid Mechanics*, 802, 2016.

A.N. Kolmogorov. The local structure of turbulence in incompressible viscous fluid for very large reynolds numbers. In *Dokl. Akad. Nauk SSSR*, volume 30, pages 299–303, 1941.

S.K. Lele. Compact finite difference schemes with spectral-like resolution. *Journal of computational physics*, 103(1):16–42, 1992.

O. M. Phillips. The irrotational motion outside a free turbulent boundary. *Mathematical Proceedings of the Cambridge Philosophical Society*, 51(1):220–229, 1955. doi: 10.1017/S0305004100030073.

R.R. Prasad and K.R. Sreenivasan. Scalar interfaces in digital images of turbulent flows. *Experiments in Fluids*, 7(4):259–264, 1989.

R.R. Taveira and C.B. da Silva. Kinetic energy budgets near the turbulent/nonturbulent interface in jets. *Physics of Fluids*, 25(1):015114, 2013.

G.I. Taylor. Statistical theory of turbulence. In *Proceedings of the Royal Society of London A: Mathematical, Physical and Engineering Sciences*, volume 151, pages 421–444. The Royal Society, 1935.

L. Voivenel, E. Varea, L. Danaila, B. Renou, and M. Cazalens. Variable viscosity jets: Entrainment and mixing process. In *Whither Turbulence and Big Data in the 21st Century?*, pages 147–162. Springer, 2017.

J. Westerweel, C. Fukushima, J.M. Pedersen, and J.C.R. Hunt. Momentum and scalar transport at the turbulent/non-turbulent interface of a jet. *Journal of Fluid Mechanics*, 631:199–230, 2009.

On the combined effect of internal and external intermittency in turbulent non-premixed jet flames

M. Gauding[a,*], M. Bode[b], D. Denker[b], Y. Brahami[a], L. Danaila[a], E. Varea[a]

[a] *CORIA – CNRS UMR 6614, Saint Etienne du Rouvray, France*
[b] *Institute for Combustion Technology, RWTH Aachen University, Germany*

Abstract

This paper analyzes the combined effect of internal intermittency and external intermittency on the dynamics of small-scale turbulent mixing in a turbulent non-premixed jet flame. The phenomenon of external intermittency in turbulent jet flames originates from a very thin layer, known as turbulent/non-turbulent interface, that separates the inner turbulent core from the outer irrotational surrounding fluid. The impact of external intermittency on turbulence is evaluated across the jet flame by the self-similarity scaling of higher-order structure functions of the mixture fraction. It is shown that the scaling of structure functions exhibits a growing departure from the prediction of classical scaling laws toward the edge of the flame. Empirical evidence is provided that this departure is primarily due to external intermittency and the associated break down of self-similarity. External intermittency creates local gradients that are significantly more intense compared to those created by internal intermittency alone. As chemical reactions usually take place in thin layers in the vicinity of the turbulent/non-turbulent interface, an accurate statistical description of these intense events is necessary to predict the turbulence-chemistry interaction. The study is based on data from a highly-resolved direct numerical simulation of a temporally evolving planar jet flame.

---

[*] Corresponding author
Email address: `michael.gauding@coria.fr`
(M. Gauding)

Preprint submitted to Proc. Comb. Inst. *May 30, 2020*

1. Introduction

Turbulent non-premixed flames are characterized by strong spatio-temporal fluctuations over a wide range of different length and time scales [1]. In many applications of turbulent non-premixed flames, chemistry is relatively fast and the turbulent mixing between fuel and oxidizer is the rate determining process. Reliable predictions of turbulence are therefore necessary to develop a fundamental understanding of the turbulence-chemistry coupling and to improve the accuracy of models. An important example is the flamelet model, which relies on an accurate prediction of the small-scale turbulent mixing statistics [2]. In non-premixed flames, the mixing state can be uniquely quantified by the mixture fraction Z, defined as the local mass fraction of the fuel stream in a given fuel-oxidizer mixture

$$Z = \frac{\dot{m}_{\mathrm{fuel}}}{\dot{m}_{\mathrm{fuel}} + \dot{m}_{\mathrm{oxidizer}}} \,. \tag{1}$$

Profound predictions of small-scale turbulence have been provided by Kolmogorov's similarity theory [3, 4] and its extension for turbulent mixing by Obukhov [5] and Corrsin [6] (henceforth referred to as KOC). The central element of the KOC theory is the increment of the mixture fraction, defined as $\Delta Z = Z(\boldsymbol{x} + \boldsymbol{r}) - Z(\boldsymbol{x})$, which describes mixture fraction fluctuations between two points separated by the distance $\boldsymbol{r}$. The statistical moments of ΔZ are known as structure functions. The KOC theory postulates that the entire distribution function of ΔZ depends only on the molecular diffusivity D, the mean energy dissipation rate $\langle \varepsilon \rangle$, and the mean scalar dissipation rate $\langle \chi \rangle$. As only three scaling parameters are necessary, this was understood as a claim for small-scale universality. While the KOC theory has been confirmed to be generally valid for low-order statistics of many turbulent flows, there are numerous experimental and numerical studies that have reported substantial deviations for higher-order statistics [7]. These deviations occur even when the condition of sufficiently high Reynolds number is met, and originate from very strong fluctuations of the energy dissipation and the scalar dissipation. These strong fluctuations, known as internal intermittency, are non-universal and thus invalidate the KOC self-similarity hypotheses [8]. Internal intermittency is created by the non-linear dynamics of the vortex stretching mechanism and occurs predominantly at the smallest scales of any turbulent flow.

For turbulent reactive flows, the situation is more delicate, and there are objections that the KOC theory may not hold for these flows. Firstly, the KOC postulates were formulated for fully developed turbulence in flow regions independent of boundary or initial conditions. Secondly, spatio-temporal variations of the fluid's thermo-physical properties were assumed to be negligible. However, turbulent jet flames are exposed to the phenomenon of external intermittency [9]. External intermittency, occurs predominantly at the edge of the jet flame and is linked to the turbulent/non-turbulent interface (TNTI). The TNTI is a thin, highly contorted layer that separates the inner turbulent core from the outer irrotational surrounding fluid. Different from internal intermittency, external intermittency has its origin in the larger scales and is caused by the alternation between fully developed turbulent fluid and irrotational outer fluid at the outer boundary of the jet flame. Kuznetsov et al. [10] demonstrated that external intermittency can affect the statistics and universality of small-scale turbulence. Moreover, Mi and Antonia [11] found that statistics of scalar fields are more sensitive to external intermittency than velocity statistics. Consequently, the application of turbulence models developed for homegenoeus isotropic turbulence is limited for non-premixed jet flames.

The TNTI plays an important role for the dynamics of turbulent non-premixed flames because it is the place where the fuel stream and the oxidizer stream meet. For most technical relevant flames, the TNTI is located in the vicinity of stoichiometric mixture, where most chemical reactions occur [12]. Turbulent fluctuations at the TNTI enhance local mixing, which increases the heat release, but strong turbulent fluctuations may also trigger local extinction when radicals are transported out of the reaction zone and heat loss exceeds heat release [13]. Classical turbulence theories underestimate these very intense bursts of the mixture fraction field and it is not fully understood how turbulence at the TNTI differs from fully developed turbulence in the core of the jet. Analyzing and predicting these strong fluctuations of the mixture fraction field is essential for modeling turbulent non-premixed flames.

The objective of the present study is to assess the impact of external intermittency on small-scale motion in a turbulent non-premixed jet flame. The analysis is based on structure functions of the mixture fraction field. Structure functions are non-local statistical quantities, which can provide scale-sensitive information about the dynamics of turbulence. Specifically, Chien et al. [14] observed that the scaling of structure functions can unveil the signature of large-scale fluctuations.

The paper is structured as follows. In section 2, we present the direct numerical simulation data on which the analysis is based. In section 3, we introduce the methodology to detect the TNTI and define an intermittency factor that quantifies external intermittency. In section 4, we study structure functions of the mixture fraction in the dissipative and inertial range. The structure functions are evaluated at different crosswise positions and their dependence on the external intermittency factor is analyzed. Concluding remarks are given in section 5.

2. Data set description

The analysis is performed by means of direct numerical simulation data of a turbulent temporally evolving planar non-premixed jet flame [15]. The oxidizer stream is air, consisting of oxygen $Y_{\mathrm{O_2},2} = 0.232$ and nitrogen $Y_{\mathrm{N_2},2} = 0.768$. The fuel stream is methane ($Y_{\mathrm{CH_4},1} = 0.07$), which is highly diluted by nitrogen in a way that the stoichiometric mixture fraction Z_{st} equals 0.45. The DNS was carried out with the high-fidelity in-house code CIAO, which solves the unsteady Navier-Stokes equations in a low Mach number approximation with a fourth-order explicit spatial discretization and semi-implicit Crank-Nicholson scheme for time integration [17]. Species and temperature equations are discretized with a fifth-order WENO scheme and temporally advanced by the symmetric operator split of Strang [16]. The combustion process was considered by finite rate chemistry employing a reaction mechanism with 30 species and 102 reactions. The kinematic viscosity ν and the molecular diffusivity D depend on temperature and the local composition. The Schmidt number $Sc = \nu/D$ is approximately constant and close to 0.7.

The three-dimensional DNS domain was discretized by a rectangular structured mesh with $768 \times 512 \times 768$ points in order to resolve small-scale turbulence and the inner-structure of the flame sufficiently. The Kolmogorov length-scale equals approximately half the grid size, which is considered to be sufficient to accurately compute statistics of small-scale quantities [18]. The grid is uniform and equidistant in regions where flame structures appear, and gradually stretched toward the boundaries in the crosswise direction. The size of the computational domain equals $8.2H_0 \times 5.5H_0 \times 10.2H_0$, where H_0 denotes the initial jet width. The initial velocity field in the jet core was initialized with an instantaneous realization of a turbulent channel flow in order to facilitate a physical transition. The jet Reynolds number, defined with H_0, the initial mean velocity difference ΔU_1 between the center-line and the co-flow, and the kinematic viscosity of the fuel ν_{fuel}, equals 4,500. Velocity and scalar fields are periodic in the stream-wise and span-wise directions (denoted by x_1 and x_2). Non-periodic (outlet) boundary conditions are used in the crosswise direction (denoted by x_3).

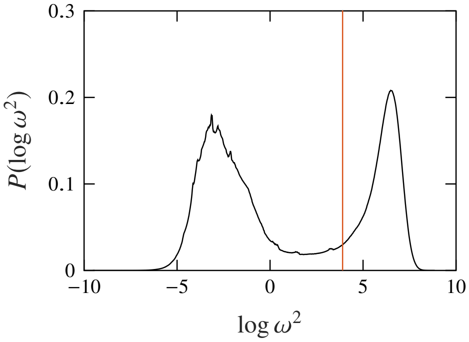

Figure 1: Probability density function $\log\omega^2$. The vertical line indicates the threshold $\log\omega_0^2$, which is used to distinguish between turbulent and non-turbulent regions.

As the setup is statistically homogeneous in (x_1, x_2) planes, it allows a statistical analysis at different crosswise positions $x_3/h_{1/2}$, with $h_{1/2}$ being the half-width, defined as the distance between the centerplane and the position at which the mean velocity decreased to 50% of its center value. The following analysis is based on one time-step, at which the jet is decaying and chemistry interacts with fully developed turbulence.

3. External fluctuations in turbulent flames

External intermittency can be quantified by an intermittency function $I(\boldsymbol{x})$ that is defined by a threshold criterion of the enstrophy ω^2 as

$$I(\boldsymbol{x}) = H(\omega^2 - \omega_0^2)\,, \tag{2}$$

where H is the Heaviside function. Following Townsend [19], the intermittency factor γ is then defined as the probability that the flow at a certain crosswise position x_3 is turbulent, i.e.

$$\gamma(x_3) = \langle I(\boldsymbol{x})\rangle\,, \tag{3}$$

where the angular brackets denote an ensemble-average, which is approximated by averages over (x_1, x_2)-planes. Specifically, the definition of γ based on the enstrophy is able to account for engulfment pockets with high heat release, where turbulence is locally damped by an increase of kinematic viscosity [20]. Other threshold criteria, such as the mixture fraction field, have been used as a surrogate to define the intermittency factor. However, an intermittency factor defined in such a way is not suitable for flows with heat release [21].

The intermittency factor γ is linked to the position of the TNTI and its definition requires a specific

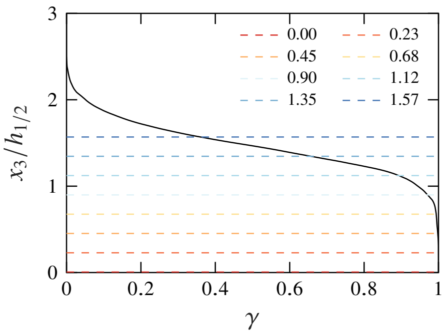

Figure 2: Variation of the intermittency factor γ with the crosswise direction $x_3/h_{1/2}$. The dashed lines indicate different crosswise positions $x_3/h_{1/2}$ that are used for the analysis.

threshold ω_0^2 to distinguish between turbulent and non-turbulent fluid. Following Silva et al. [22], the threshold ω_0^2 is defined as the local minimum of the global probability density function (pdf) of $\log \omega^2$, shown in Fig. 1. As a signature of the TNTI, this pdf has a bimodal shape, where the peak at low ω^2 corresponds to the irrotational region, and the peak at high ω^2 corresponds to the turbulent region. As the two peaks are considerably separated, the position of the TNTI is largely insensitive to the specific choice for ω_0^2.

Figure 2 shows the intermittency factor γ across the jet flame. At the center, there is a fully turbulent core region, which extends up to $x_3/h_{1/2} \approx 0.5$, where γ is nearly constant and close to unity. A steep decrease of γ is observed at the edge of the flame, which originates from an alternating flow structure at the TNTI. In the irrotational co-flow, the intermittency factor tends to zero. The TNTI defined by the threshold ω_0^2 is visualized for a snapshot of the flame in Fig. 3. It can be observed that a threshold criteria is suitable to distinguish between the turbulent and non-turbulent fluid. Moreover, Fig. 3 shows that the zone of stoichiometric mixture with $Z_{\mathrm{st}} = 0.45$ is frequently located in the vicinity of the TNTI.

4. Structure function analysis

The analysis in this paper is built upon the longitudinal structure functions, defined as the moments of the mixture fraction increment ΔZ in stream-wise direction $\boldsymbol{e}_1$

$$\langle \Delta Z^n \rangle (r; x_3) = \langle (Z(\boldsymbol{x} + r\boldsymbol{e}_1) - Z(\boldsymbol{x}))^n \rangle \,. \qquad (4)$$

In turbulent flows exposed to external intermittency, there are three different possibilities for the distribution of the ending points $\boldsymbol{x}$ and $\boldsymbol{x} + r\boldsymbol{e}_1$ of ΔZ. More precisely,

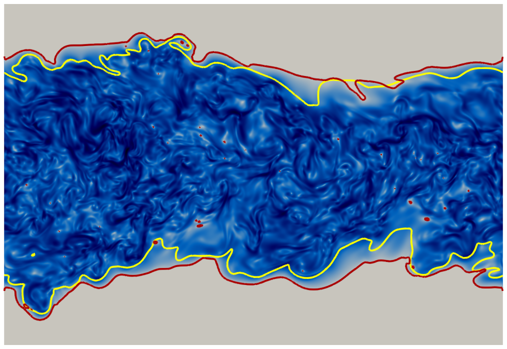

Figure 3: Two-dimensional snapshot of the enstrophy field, with the colormap increasing in the sequence gray-blue-back. Additionally, the position of the turbulent/non-turbulent interface (red solid line) and the position of the stoichiometric mixture fraction $Z_{\mathrm{st}} = 0.45$ (yellow solid line) are shown.

both points can be either located within the fully turbulent or within the non-turbulent regime, or one point is in the turbulent and the other point is in the non-turbulent regime. Kuznetsov et al. [10] predicted the corresponding probabilities as $\gamma_{tt} = \gamma - \frac{1}{2} D_{\gamma\gamma}$, $\gamma_{nn} = 1 - \gamma - \frac{1}{2} D_{\gamma\gamma}$, and $\gamma_{nt} = D_{\gamma\gamma}$, where

$$D_{\gamma\gamma} = \langle (I(\boldsymbol{x} + r\boldsymbol{e}_1) - I(\boldsymbol{x}))^2 \rangle \qquad (5)$$

Of special interest is the probability γ_{tt}/γ that quantifies the likelihood that one ending point of the structure functions is in a turbulent regime given that the other ending point also lies in a turbulent regime. The probability γ_{tt}/γ is shown in Fig. 4 for different crosswise positions $x_3/h_{1/2}$ between 0 and 1.57. In the proximity of the centerplane, γ_{tt}/γ is close to unity and nearly independent of the separation distance r, which reflects the fact that the core region of the jet is fully turbulent. Toward the edge of the jet (i.e. for $x_3/h_{1/2} > 0.9$), γ_{tt}/γ equals unity only for $r \longrightarrow 0$, and drops quickly at larger separation distances when turbulent fluid is mixed with non-turbulent fluid.

4.1. *Structure functions in the dissipative range*

The KOC theory predicts that the structure functions of the mixture fraction are universal functions and scale in the dissipative range as

$$\frac{\langle \Delta Z^{2n} \rangle}{\langle \chi \rangle^n \tau_\eta^n} = C_n \left(\frac{r}{\eta} \right)^{2n} , \qquad (6)$$

where C_n is an order-dependent pre-factor. The Kolmogorov time-scale and the Kolmogorov length-scale are defined as $\tau_\eta = (\langle \nu \rangle / \langle \varepsilon \rangle)^{1/2}$ and $\eta = (\langle \nu \rangle^3 / \langle \varepsilon \rangle)^{1/4}$,

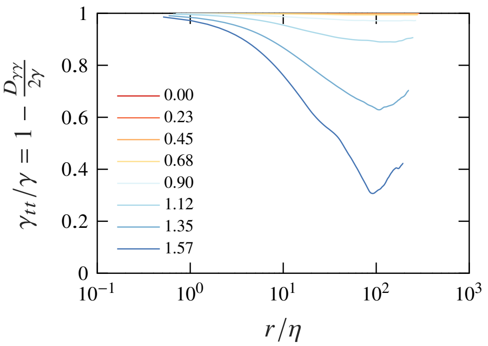

Figure 4: Probability γ_{tt}/γ that both endpoints of structure functions at different crosswise positions $x_3/h_{1/2}$ (as indicated in the legend) are located in turbulent fluid.

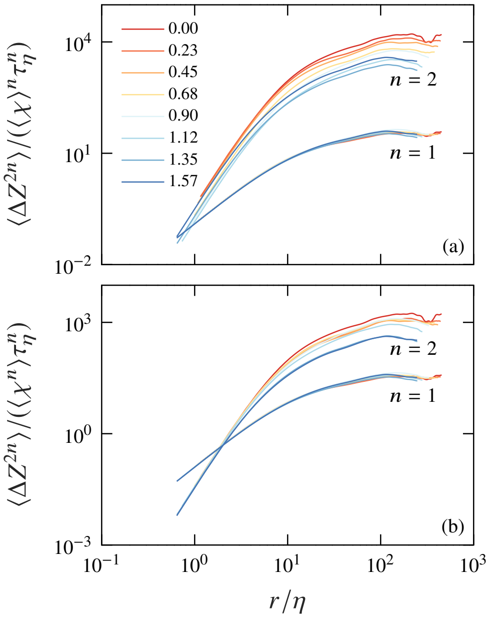

Figure 5: Normalized second and fourth-order structure functions $\langle \Delta Z^{2n} \rangle$ of the mixture fraction field for different crosswise positions $x_3/h_{1/2}$ (as indicated by the legend). The structure functions are normalized with the KOC scales $\langle \chi \rangle$ and τ_η (a) and the generalized scales $\langle \chi^n \rangle$ and τ_η (b) according to Eq. (9).

respectively. The instantaneous energy dissipation rate is defined as $\varepsilon = 2\nu S_{ij}^2$, where $S_{ij} = (\partial u_i/\partial x_j + \partial u_j/\partial x_i)/2$ is the strain rate tensor and u_i the fluctuating velocity field. The instantaneous scalar dissipation rate is defined as $\chi = 2D(\partial Z/\partial x_i)^2$. Repeated indices imply summation.

Figure 5(a) presents the mixture fraction structure functions normalized according to Eq. (6) for the second and fourth order at different crosswise positions x_3. There is good support for the KOC scaling for the second-order $\langle \Delta Z^2 \rangle$, which means that an adequate collapse of the structure functions at different x_3 can be observed after normalization with $\langle \chi \rangle$ and τ_η. This finding is surprising and clearly highlights the validity of the KOC scaling for second-order structure functions, despite heat release, finite Reynolds number effects, and external intermittency. Interestingly enough, the KOC scaling is not limited to the smallest scales but extends up to the intermediate scales.

Next, we inspect the scaling of the fourth-order structure functions $\langle \Delta Z^4 \rangle$. Figure 5(a) reveals a staggered, clearly non-universal arrangement after normalization with the KOC scales. Hence, we can conclude that the KOC scales are not a consistent choice for normalization of higher-order structure functions. This observation agrees with the standard paradigm that higher-order statistics are non-universal and highly sensitive to intermittency [7, 23].

As higher-order statistics are not in agreement with the KOC scaling, a correction of Eq. (6) is necessary. A generalization of the KOC scaling for higher orders can be obtained by expanding $\langle \Delta Z^n \rangle$ as

$$\langle \Delta Z^{2n} \rangle = \langle \left(\frac{\partial Z}{\partial x_1} \right)^{2n} \rangle r^{2n} + O(r^{2n+2}) , \qquad (7)$$

where the series is truncated after the first non-negative term. To proceed, the assumptions of local isotropy and decorrelation between the molecular diffusivity and the gradient of the mixture fraction are made. A justification of these assumptions is given in the next paragraph. In that case, the moments of χ can be written as

$$\langle \chi^n \rangle \propto \langle D \rangle^n \langle \left(\frac{\partial Z}{\partial x_1} \right)^{2n} \rangle . \qquad (8)$$

Combining Eqs. (7) and (8) yields the dissipative range scaling of structure functions

$$\frac{\langle \Delta Z^{2n} \rangle}{\langle \chi^n \rangle \tau_\eta^n} = \hat{C}_n \left(\frac{r}{\eta} \right)^{2n} , \qquad (9)$$

where $\hat{C}_n$ is an order-dependent prefactor. Equation (9) is an exact generalization of the KOC scaling theory for higher-order structure functions that does not require a high Reynolds number. Moreover, Eq. (9) signifies that $\langle \chi^n \rangle$ is the relevant scaling parameter instead of $\langle \chi \rangle^n$. As the exponent and the averaging operator do not commute, Eqs. (6) and (9) are generally different. Higher-order scales have been introduced before by Boschung et al. [24] for the scaling of velocity structure functions.

Schumacher et al. [25] showed that the existence of higher-order scaling parameters is a direct consequence from anomalous scaling.

A test of the new scaling relation proposed by Eq. (9) is shown in Fig. 5(b). Compared to the classical KOC scales, a normalization with $\langle \chi^n \rangle$ improves clearly the collapse of the fourth-order structure functions in the dissipative range. This implies that we have found a generalized solution for the structure functions of the mixture fraction that accounts for both internal and external intermittency effects. The collapse of the structure functions in the dissipative range also justifies the assumption of small-scale isotropy and the statistical independence of D with the mixture fraction gradients made by Eq. (8).

In summary, the classical KOC scales are not a consistent choice for the normalization of higher-order structure functions. This can be further demonstrated by expressing Eq. (9) as

$$\frac{\langle \Delta Z^{2n} \rangle}{\langle \chi \rangle^n \tau_\eta^n} \propto \frac{\langle \chi^n \rangle}{\langle \chi \rangle^n} \left(\frac{r}{\eta} \right)^{2n} , \tag{10}$$

where the non-dimensional moments

$$F_{2n,\chi} = \frac{\langle \chi^n \rangle}{\langle \chi \rangle^n} \tag{11}$$

represent the non-universality of small-scale turbulence. If $F_{2n,\chi}$ were constant, the classical KOC scales would be valid similarity scales for any order n. In Fig. 6, we present the flatness factor $F_{4,\chi}$ as a function of the intermittency factor γ. It can be seen that $F_{4,\chi}$ increases from a centerplane value close to 6 to a value close to 20 when the intermittency factor γ equals to 0.2. This increase of $F_{4,\chi}$ originates from a combined effect of strong gradients over the thickness of TNTI, and the alternating flow structure of turbulent and non-turbulent fluid. The dependence of $F_{4,\chi}$ on γ violates the standard paradigm of turbulence that small scale quantities decouple from the larger scales, but instead signifies that external fluctuations can have a striking impact on the small-scales. We note that internal intermittency can be ruled out as the reason for the increase of $F_{4,\chi}$ because the Taylor-scale based Reynolds number Re_λ (see Fig. 6) decays toward the edge of the flame [23].

To further study the role of external intermittency, we define the conditional moments

$$F_{2n,\chi}^t = \frac{\langle I \chi^n \rangle}{\langle I \chi \rangle^n} , \tag{12}$$

that considers only the fully turbulent portion of the flow located inside the turbulent envelope. Figure 6 shows that unlike $F_{4,\chi}$, the conditional flatness factor $F_{4,\chi}^t$, is significantly less sensitive to variations of the intermittency factor γ. Physically, this indicates that strong turbulent transport leads to a rapid homogenization of turbulent regions. In summary, the analysis of $F_{4,\chi}$ and $F_{4,\chi}^t$ provides conclusive evidence for the coupling between external intermittency and small-scale turbulence. This also means that external intermittency plays an important role for the break-down of self-similarity of the fourth-order structure functions in the dissipative range.

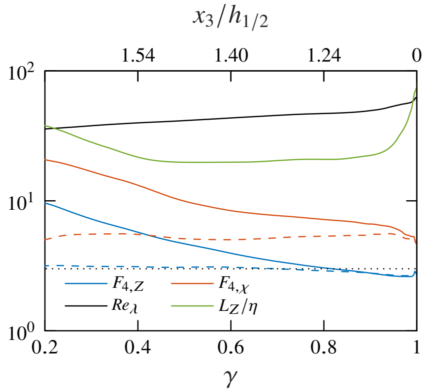

Figure 6: Variation of the flatness factors $F_{4,Z}$ and $F_{4,\chi}$ of the mixture fraction and the mixture fraction gradients, respectively, with the intermittency factor γ and the crosswise position $x_3/h_{1/2}$. The dashed lines corresponds to the conditioned flatness factor $F_{4,Z}^t$ and $F_{4,\chi}^t$, computed for solely turbulent regions with $I(\boldsymbol{x}) = 1$. Additionally, the Taylor-scale Reynolds number Re_λ and the length-scale L_Z are shown. The black dotted line represents the flatness factor of a Gaussian distribution.

While $F_{2n,\chi}$ represents the small-scale limit of structure functions, it is of interest to define analogously the non-dimensional moments of the mixture fraction fluctuations

$$F_{2n,Z} = \frac{\langle z^{2n} \rangle}{\langle z^2 \rangle^n} \quad \text{and} \quad F_{2n,Z}^t = \frac{\langle I z^{2n} \rangle}{\langle I z^2 \rangle^n}, \tag{13}$$

with $z = Z - \langle Z \rangle$, to evaluate the large-scale limit of structure functions. Figure 6 shows that $F_{4,Z}$ grows similarly to $F_{4,\chi}$ from the core to the edge of the jet. The conditional flatness factor $F_{4,Z}^t$ is likewise virtually independent of γ and close to the flatness of a Gaussian distribution over the entire range. This observation further supports the assertion of rapid mixing and homogenization of turbulent regions as postulated by Jahanbakhshi and Madnia [20] and Corrsin and Kistler [26].

As external intermittency is entangled with other large-scale effects, such as anisotropy, inhomogeneity, or finite Reynolds number effects, it is necessary to quantify the impact of the large scales on small-scale turbulent mixing. To this end, we follow Thiesset et al. [27] and define the length-scale

$$L_Z = \frac{\langle \chi \rangle^{3/4}}{\langle \varepsilon \rangle^{1/4} \Gamma_Z^{3/2}}\,, \tag{14}$$

where Γ_Z is the mean mixture fraction gradient. For length-scales smaller than L_Z, statistical properties of turbulence are expected to be independent of large-scale effects. Figure 6 shows that L_Z is nearly constant for $0.4 < \gamma < 0.9$. This means that there is a relatively broad region in crosswise direction, which is subject to a strong variation of the intermittency factor γ, but a comparably much smaller variation of large-scale effects. Similarly, Mi and Antonia [11] found for a turbulent jet that variations of the intermittency factor have a much stronger impact on the scaling of structure functions than local variations of the Reynolds number or the mean shear.

4.2. *Structure functions in the inertial range*

In this section, we present empirical evidence for the link between external intermittency and the inertial-range scaling exponents of structure functions. Provided that an inertial subrange exists, we expect that the pth-order mixture fraction structure function can be expressed as

$$S_p = \langle |\Delta Z|^p \rangle \propto r^{\zeta_p}\,, \tag{15}$$

where ζ_p is the inertial-range scaling exponent. Absolute values of the increments in Eq. (15) permit even and odd moments. The KOC theory predicts for sufficiency large Reynolds numbers from dimensional grounds $\zeta_p = p/3$. However, numerous experimental and numerical studies have provided conclusive evidence for anomalous scaling of structure functions [28], which refers to a discrepancy from that linear law, i.e. $\zeta_p < p/3$ for $p > 2$. For homogeneous isotropic turbulence, this discrepancy has been explained by internal intermittency, which breaks the similarity scaling of turbulence [7]. However, at finite Reynolds numbers and in flows exposed to external intermittency, an increased deviation from the KOC prediction is expected. Therefore, the dependence of the scaling exponents on the crosswise position x_3 and the external intermittency factor γ is of interest.

As the Reynolds number of the considered jet flame is relatively low, a well developed inertial-range does not exist. For this reason, we determine the scaling exponents ζ_p by the so-called extended self-similarity (ESS) framework [29]. Instead of evaluating the scaling directly via Eq. (15), a relative scaling exponent, ζ_p/ζ_2 is obtained by plotting the pth-order structure function against the second-order structure function. Specifically, the relative scaling exponents equal

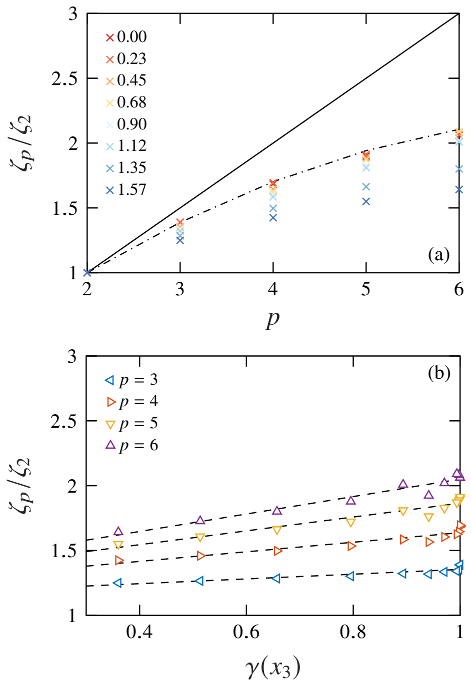

Figure 7: Scaling exponents ζ_p of the structure functions S_p^Z of the mixture fraction field up to the sixth-order for different crosswise positions $x_3/h_{1/2}$ (a). The back solid line indicates the analytical KOC scaling. The dash-dotted line corresponds to the log-normal model, see Eq. (17), with $\rho = 0.5$ and $\mu = 0.25$. Dependence of ζ_p on the intermittency factor γ (b). The dashed lines correspond to a least-square fit.

$$\frac{\zeta_p}{\zeta_2} = \frac{\mathrm{d}\log S_p(r; x_3)}{\mathrm{d}\log S_2(r; x_3)}\,. \tag{16}$$

The ESS approach increases the width of the so-called restricted scaling range and enables us to obtain reliable scaling exponents even at moderate Reynolds numbers. In general, the scaling exponents of structure functions exhibit a small dependence on the Reynolds number, unless the Reynolds number is very large [30]. By defining the scaling exponents in Eq. (16) relative to S_2, this Reynolds number dependence is masked. Here, we take advantage of this feature, since local variations of the Reynolds number across the jet flame do not affect the relative scaling exponents.

The relative scaling exponents ζ_p/ζ_2 obtained by this approach are shown in Fig. 7(a) up to the sixth-order for different crosswise positions. For comparison, we display the KOC prediction and the log-normal model, originally developed by Atta [31], i.e.

$$\zeta_p = \frac{p}{3} - \mu p \left[(10 - 6\rho)p - 12 \right] / 72 \,. \qquad (17)$$

Antonia et al. [28] showed that Eq. (17) is able to predict the scaling exponents of scalar structure functions in homogeneous isotropic turbulence with good accuracy for $p < 8$, when $\rho = 0.5$ and $\mu = 0.25$.

Figure 7(a) shows that the relative scaling exponents at the centerplane of the flame depart increasingly from the KOC prediction with increasing order, but are consistent with the prediction from the log-normal model. In other words, the relative centerplane scaling exponents reflect the effect of internal intermittency but are virtually not influenced by large-scale effects. With increasing distance from the centerplane, the relative scaling exponents decrease below the prediction of the log-normal model, which signifies a growing level of intermittency compared to homogeneous isotropic turbulence. To link this increase to external intermittency, we show in Fig. 7(b) the relative scaling exponents as a function of the external intermittency factor γ. As anticipated, the relative scaling exponents decrease with decreasing γ. From these observations we may conclude that external fluctuations amplify the break-down of small-scale similarity, which manifests itself in a pronounced departure from the KOC prediction.

5. Conclusion

In this paper, the impact of external intermittency on turbulent small-scale mixing in a non-premixed jet flame was studied. It was demonstrated that external intermittency has a similarity-breaking effect on higher-order structure functions. The similarity-breaking effect becomes more pronounced toward the edge of the flame, and has its origin in a combination of strong mixture fraction gradients over the thickness of the TNTI and the alternating flow structure of turbulent and non-turbulent fluid.

External intermittency has strong implications for turbulent combustion, as classical scaling theories underestimate intense fluctuations at the edge of the jet flame. We found that external intermittency creates fluctuations that are significantly more intense compared to those created by internal intermittency alone. As chemical reactions in most hydrogen and hydrocarbon flames usually take place in the proximity of the TNTI, an accurate statistical description of these intense events is necessary to predict the turbulence-chemistry interaction.

The analysis of the non-premixed jet flame revealed that the KOC theory is suitable to predict second order statistics in the entire flame. However, the KOC theory is not an appropriate choice for the prediction of strong fluctuations, represented by higher-order statistics. Therefore, a correction of the KOC theory was proposed that accounts for these fluctuations. The new scaling incorporates the higher-order moments of the scalar dissipation and is an exact generalization of the classical KOC theory to flows that are exposed to both internal and external intermittency. The proposed scaling does not require a large Reynolds number.

The consequences for combustion models are twofold. Firstly, the flatness factor $F_{4,\chi}$ is a function of the intermittency factor γ, which quantifies the impact of the large, non-universal scales on the small-scales. Secondly, following Mellado et al. [12], the moments of the scalar dissipation can be predicted by a zonal approach that distinguishes between turbulent and non-turbulent layers. Hereby, the independence of the conditional flatness factors $F^t_{4,\chi}$ and $F^t_{4,Z}$ from the intermittency factor γ can be exploited to simplify mixing models. Specifically, a mixing model that is built with the conditional flatness factors may reveal a reduced dependence on the large, non-universal scales.

Acknowledgment

Financial support was provided by EMCO2RE. The authors gratefully acknowledge the computing time granted through JARA on JURECA (jhpc55).

References

[1] N. Peters, Multiscale combustion and turbulence, Proceedings of the Combustion Institute 32 (2009) 1–25.

[2] N. Peters, Turbulent combustion, Cambridge university press, 2000.

[3] A. N. Kolmogorov, in: Dokl. Akad. Nauk SSSR, volume 32, pp. 16–18.

[4] A. N. Kolmogorov, in: Dokl. Akad. Nauk SSSR, volume 30, pp. 299–303.

[5] A. Obukhov, Temperature field structure in a turbulent flow, Izv. Acad. Nauk SSSR Ser. Geog. Geofiz 13 (1949) 58–69.

[6] S. Corrsin, On the spectrum of isotropic temperature fluctuations in an isotropic turbulence, Journal of Applied Physics 22 (1951) 469–473.

[7] Z. Warhaft, Passive scalars in turbulent flows, Annual Review of Fluid Mechanics 32 (2000) 203–240.

[8] L. Landau, E. Lifshitz, Fluid mechanics, 1963.

[9] J. Hunt, I. Eames, C. Da Silva, J. Westerweel, Interfaces and inhomogeneous turbulence, Philosophical Transactions of the Royal Society A 369 (2011) 811–832.

[10] V. Kuznetsov, A. Praskovsky, V. Sabelnikov, Fine-scale turbulence structure of intermittent shear flows, Journal of Fluid Mechanics 243 (1992) 595–622.

[11] J. Mi, R. Antonia, Effect of large-scale intermittency and mean shear on scaling-range exponents in a turbulent jet, Physical Review E 64 (2001) 026302.

[12] J. P. Mellado, L. Wang, N. Peters, Gradient trajectory analysis of a scalar field with external intermittency, Journal of fluid mechanics 626 (2009) 333–365.

[13] M. Ihme, H. Pitsch, Prediction of extinction and reignition in nonpremixed turbulent flames using a flamelet/progress variable model: 1. a priori study and presumed pdf closure, Combustion and Flame 155 (2008) 70–89.

[14] C.-C. Chien, D. B. Blum, G. A. Voth, Effects of fluctuating energy input on the small scales in turbulence, Journal of Fluid Mechanics 737 (2013) 527–551.

[15] D. Denker, A. Attili, S. Luca, F. Bisetti, M. Gauding, H. Pitsch, Dissipation element analysis of turbulent premixed jet flames, Combustion Science and Technology 0 (2019) 1–16.

[16] G. Strang, On the construction and comparison of difference schemes, SIAM journal on numerical analysis 5 (1968) 506–517.

[17] O. Desjardins, G. Blanquart, G. Balarac, H. Pitsch, High order conservative finite difference scheme for variable density low mach number turbulent flows, Journal of Computational Physics 227 (2008) 7125–7159.

[18] D. Donzis, P. Yeung, K. Sreenivasan, Dissipation and enstrophy in isotropic turbulence: resolution effects and scaling in direct numerical simulations, Physics of Fluids 20 (2008) 045108.

[19] A. Townsend, The fully developed wake of a circular cylinder, Australian Journal of Chemistry 2 (1949) 451–468.

[20] R. Jahanbakhshi, C. K. Madnia, The effect of heat release on the entrainment in a turbulent mixing layer, Journal of Fluid Mechanics 844 (2018) 92–126.

[21] T. Watanabe, T. Naito, Y. Sakai, K. Nagata, Y. Ito, Mixing and chemical reaction at high Schmidt number near turbulent/nonturbulent interface in planar liquid jet, Physics of Fluids 27 (2015) 035114.

[22] T. S. Silva, M. Zecchetto, C. B. da Silva, The scaling of the turbulent/non-turbulent interface at high Reynolds numbers, Journal of Fluid Mechanics 843 (2018) 156–179.

[23] M. Gauding, L. Danaila, E. Varea, High-order structure functions for passive scalar fed by a mean gradient, International Journal of Heat and Fluid Flow 67 (2017) 86–93.

[24] J. Boschung, F. Hennig, M. Gauding, H. Pitsch, N. Peters, Generalised higher-order Kolmogorov scales, Journal of Fluid Mechanics 794 (2016) 233–251.

[25] J. Schumacher, K. R. Sreenivasan, V. Yakhot, Asymptotic exponents from low-Reynolds-number flows, New Journal of Physics 9 (2007) 89.

[26] S. Corrsin, A. L. Kistler, Free-stream boundaries of turbulent flows (1955).

[27] F. Thiesset, V. Schaeffer, L. Djenidi, R. Antonia, On self-preservation and log-similarity in a slightly heated axisymmetric mixing layer, Physics of Fluids 26 (2014) 075106.

[28] R. Antonia, E. Hopfinger, Y. Gagne, F. Anselmet, Temperature structure functions in turbulent shear flows, Physical Review A 30 (1984) 2704.

[29] R. Benzi, S. Ciliberto, R. Tripiccione, C. Baudet, F. Massaioli, S. Succi, Extended self-similarity in turbulent flows, Physical review. A 48 (1993) R29–R32.

[30] S. Tang, R. Antonia, L. Djenidi, L. Danaila, Y. Zhou, Finite Reynolds number effect on the scaling range behaviour of turbulent longitudinal velocity structure functions, Journal of Fluid Mechanics 820 (2017) 341–369.

[31] C. Atta, Sampling techniques in turbulence measurements, Annual Review of Fluid Mechanics 6 (1974) 75–91.

Bibliography

Abid, M., Brachet, M. & Huerre, P. 1993 Linear hydrodynamic instability of circular jets with thin shear layers. *Eur. J. Mech. Ser. B FLUIDS* **12**, 683.

Aihara, Y., Koyama, H. & Morishita, E. 1974 Effects of an air stream on turbulent diffusion of a helium jet from a small nozzle. *Phys. Fluids* **17** (4), 665–673.

Alexakis, A. & Biferale, L. 2018 Cascades and transitions in turbulent flows. *Phys. Rep.* **767-769**, 1–101.

Aleyasin, S.S., Tachie, M.F. & Koupriyanov, M. 2017 PIV Measurements in the Near and Intermediate Field Regions of Jets Issuing from Eight Different Nozzle Geometries. *Flow, Turbul. Combust.* **99** (2), 329–351.

Amielh, M., Djeridane, T., Anselmet, F. & Fulachier, L. 1996 Velocity near-field of variable density turbulent jets. *Int. J. Heat Mass Transf.* **39**, 2149–2164.

Antonia, R.A. & Bilger, R.W. 1973 An experimental investigation of an axisymmetric jet in a co-flowing air stream. *J. Fluid Mech.* **61** (4), 805–822.

Antonia, R.A. & Zhao, Q. 2001 Effect of initial conditions on a circular jet. *Exp. Fluids* **31** (3), 319–323.

Barkley, D. 2006 Linear analysis of the cylinder wake mean flow. *Europhys. Lett.* **75** (5), 750–756.

Becker, H.A., Hottel, H.C. & Williams, G.C. 1963 Mixing and flow in ducted turbulent jets. *Symp. Combust.* **9** (1), 7–20.

Beneddine, S., Sipp, D., Arnault, A., Dandois, J. & Lesshafft, L. 2016 Conditions for validity of mean flow stability analysis. *J. Fluid Mech.* **798**, 485–504.

Berlman, I. 2012 *Handbook of florescence spectra of aromatic molecules*. Elsevier.

Bisset, D.K., Hunt, J.C.R. & Rogers, M.M. 2002 The turbulent/non-turbulent interface bounding a far wake. *J. Fluid Mech.* **451**, 383–410.

Boffetta, G. & Mazzino, A. 2020 Rayleigh-Taylor turbulence. *Ann. Rev. Fluid Mech.* .

Boronin, S.A., Healey, J.J. & Sazhin, S.S. 2013 Non-modal stability of round viscous jets. *J. Fluid Mech.* **716**, 96–119.

Brahami, Y., Gauding, M., Varea, E. & Danaila, L. 2017 Conditional and conventional statistics of variable viscosity jet flows. *PSFVIP-11* .

Broze, G. & Hussain, F. 1994 Nonlinear Dynamics of Forced Transitional Jets: Periodic and Chaotic Attractors. *J. Fluid Mech.* **263**, 93–132.

Burattini, P., Antonia, R.A. & Danaila, L. 2005 Similarity in the far field of a turbulent round jet. *Phys. Fluids* **17** (2), 1–14.

Buresti, G. 2015 A note on Stokes' hypothesis. *Acta Mech.* **226** (10), 3555–3559.

Campagne, A., Gallet, B., Moisy, F. & Cortet, P.P. 2014 Direct and inverse energy cascades in a forced rotating turbulence experiment. *Phys. Fluids* **26** (12), 125112.

Campbell, I.H. & Turner, J.S. 1985 Turbulent mixing between fluids with different viscosities. *Nature* **313** (5997), 39–42.

Campbell, I.H. & Turner, J.S. 1986*a* The influence of viscosity on fountains in magma chamber. *J. Petrol.* **27**, 1–30.

Campbell, I.H. & Turner, J.S. 1986*b* The influence of viscosity on fountains in magma chambers. *J. Petrol.* **27** (1), 1–30.

Chapman, S., Cowling, T.G. & Burnett, D. 1990 *The mathematical theory of non-uniform gases: an account of the kinetic theory of viscosity, thermal conduction and diffusion in gases*. Cambridge university press.

Chassaing, P. 1979 Melange turbulent de gaz inertes dans un jet de tube libre. *These Doc. Sci. Inst. Nat. Poly. Toulouse.* **42**.

Chassaing, P., Antonia, R.A., Anselmet, F., Joly, L. & Sarkar, S. 2002 *Variable Density Fluid Turbulence*.

Chassaing, P., Harran, G. & Joly, L. 1994 Density Fluctuation Correlations in Free Turbulent Binary Mixing. *J. Fluid Mech.* **279**, 239–278.

Chen, C.J. & Rodi, W. 1980 Vertical turbulent buoyant jets: a review of experimental data. *Oxford, U.K., Pergamon Press. 1980* **4**).

Chomaz, J.M., Huerre, P. & Redekopp, L.G. 1991 A Frequency Selection Criterion in Spatially Developing Flows. *Stud. Appl. Math.* **84** (2), 119–144.

Cook, A.W. & Dimotakis, P.E. 2001 Transition stages of Rayleigh-Taylor instability between miscible fluids. *J. Fluid Mech* **443**, 69–99.

Corrsin, S. & Kistler, A. 1955 Free-stream boundaries of turbulent flows. *Tech. Rep.* 5.

Cotel, A.J. & Breidenthal, R.E. 1997 Jet detrainment at a stratified interface. *J. Geophys. Res. Atmos.* **102** (D20), 23813–23818.

Craya, A. & Curtet, R. 1955 Sur l'évolution d'un jet en espace confiné. *Compte Rendu Hebd. des Séances l'Académdie des Sci.* **251**, 621–622.

Crighton, D.G. & Gaster, M. 1976 Stability of slowly diverging jet flow. *J. Fluid Mech.* **77** (2), 397–413.

Cussler, E.L. 2009 *Diffusion: mass transfer in fluid systems*. Cambridge university press.

Danaila, L., Anselmet, F., Zhou, T. & Antonia, R.A. 1999 A generalization of Yaglom's equation which accounts for the large-scale forcing in heated decaying turbulence. *J. Fluid Mech.* **391**, 359–372.

Danaila, L., Anselmet, F., Zhou, T. & Antonia, R.A. 2001 Turbulent energy scale budget equations in a fully developed channel flow. *J. Fluid Mech.* **430**, 87–109.

Danaila, L., Antonia, R.A. & Burattini, P. 2004 Progress in studying small-scale turbulence using 'exact' two-point equations. *New J. Phys.* **6**, 1–23.

Danaila, L., Antonia, R.A. & Burattini, P. 2012*a* Comparison between kinetic energy and passive scalar energy transfer in locally homogeneous isotropic turbulence. *Phys. D Nonlinear Phenom.* **241** (3), 224–231.

Danaila, L., Krawczynski, J.F., Thiesset, F. & Renou, B. 2012*b* Yaglom-like equation in axisymmetric anisotropic turbulence. *Phys. D Nonlinear Phenom.* **241** (3), 216–223.

Danaila, L., Voivenel, L. & Varea, E. 2017 Self-similarity criteria in anisotropic flows with viscosity stratification. *Phys. Fluids* **29** (2).

Darisse, A., Lemay, J. & Benaïssa, A. 2015 Budgets of turbulent kinetic energy, Reynolds stresses, variance of temperature fluctuations and turbulent heat fluxes in a round jet. *J. Fluid Mech.* **774**, 95–142.

Davidson, P.A. 2004 *Turbulence An Introduction for Scientists and Engineers*.

Dimotakis, P.E. 2000 The mixing transition in turbulent flows. *J. Fluid Mech.* **409**, 69–98.

Dimotakis, P.E. 2005 Turbulent Mixing. *Annu. Rev. Fluid Mech.* **37** (1), 329–356.

Dimotakis, P.E., Miake-Lye, R.C. & Papantoniou, D.A. 1983 Structure and dynamics of round turbulent jets. *Phys. Fluids* **26** (11), 3185–3192.

Djeridane, T., Amielh, M., Anselmet, F. & Fulachier, L. 1996 Velocity turbulence properties in the near-field region of axisymmetric variable density jets. *Phys. Fluids* **8** (6), 1614–1630.

Donzis, D.A., Sreenivasan, K.R. & Yeung, P.K. 2005 Scalar dissipation rate and dissipative anomaly in isotropic turbulence. *J. Fluid Mech.* **532**, 199–216.

Drazin, P.G. & Reid, W.H. 2004 *Hydrodynamic stability*. Cambridge university press.

Dreisbach, R.R. & Spencer, R. S. 1949 Simple Equations for Vapor and Liquid Densities. *Ind. Eng. Chem.* **41** (7), 1363–1366.

Dubrulle, B. 2019 Beyond kolmogorov cascades. *J. Fluid Mech.* **867**.

Duff, R.E., Harlow, F.H. & Hirt, C.W. 1962 Effects of diffusion on interface instability between gases. *Phys. Fluids* **5** (4), 417–425.

Dupuy, D., Toutant, A. & Bataille, F. 2018 Equations of energy exchanges in variable density turbulent flows. *Phys. Lett. Sect. A Gen. At. Solid State Phys.* **382** (5), 327–333.

Echols, W.H. & Young, J.A. 1963 Studies of portable air-operated aerosol generators. *Tech. Rep.*. NAVAL RESEARCH LAB WASHINGTON DC.

Elsinga, G.E. & da Silva, C.B. 2019 How the turbulent/non-turbulent interface is different from internal turbulence. *J. Fluid Mech.* **866**, 216–238.

Friehe, C.A., Van Atta, C.W. & Gibson, C.H. 1971 Jet turbulence: dissipaion rate measurements and correlations. *AGARD Turbul. Shear Flows* **18**, 1–7.

Frisch, U. 1995 *Turbulence, The Legacy of A.N. Kolmogorov*. Cambridge University Press.

Galtier, S. & Banerjee, A. 2011 Exact relation for correlation functions in compressible isothermal turbulence. *Phys. Rev. Lett.* **107** (13), 134501.

Gampert, M., Boschung, J., Hennig, F., Gauding, M. & Peters, N. 2014 The vorticity versus the scalar criterion for the detection of the turbulent/non-turbulent interface. *J. Fluid Mech.* **750**, 578–596.

Garnaud, X., Lesshafft, L., Schmid, P.J. & Huerre, P. 2013*a* Modal and transient dynamics of jet flows. *Phys. Fluids* **25** (4), 44103.

Garnaud, X., Lesshafft, L., Schmid, P.J. & Huerre, P. 2013*b* The preferred mode of incompressible jets: linear frequency response analysis. *J. Fluid Mech.* **716**, 189–202.

Gauding, M., Danaila, L. & Varea, E. 2018 One-point and two-point statistics of homogeneous isotropic decaying turbulence with variable viscosity. *Int. J. Heat Fluid Flow* **72** (December 2017), 143–150.

Gauding, M., Goebbert, J.H., Hasse, C. & Peters, N. 2015 Line segments in homogeneous scalar turbulence. *Phys. Fluids* **27** (9), 95102.

George, W.K. 1989 The Self-Preservation of Turbulent Flows and Its relation to Initial Conditions and Coherent Structures. *Adv. Turbul.* .

Gomes-Fernandes, R., Ganapathisubramani, B. & Vassilicos, J.C. 2015 The energy cascade in near-field non-homogeneous non-isotropic turbulence. *J. Fluid Mech.* **771**, 676–705.

Govindarajan, R. 2004 Effect of miscibility on the linear instability of two-fluid channel flow. *Int. J. Multiph. Flow* **30**, 1177–1192.

Govindarajan, R. & Sahu, K.C. 2014 Instabilities in viscosity-stratified flow. *Ann. Rev. Fluid Mech.* **46**, 331–353.

Gréa, B.J., Griffond, J. & Burlot, A. 2014 The effects of variable viscosity on the decay of homogeneous isotropic turbulence. *Phys. Fluids* **26** (3).

Green, S. 2012 *Fluid vortices*, , vol. 30. Springer Science & Business Media.

Guillén-González, F., Damázio, P. & Rojas-Medar, M.A. 2007 Approximation by an iterative method for regular solutions for incompressible fluids with mass diffusion. *J. Math. Anal. Appl.* **326** (1), 468–487.

Hallberg, M.P., Srinivasan, V., Gorse, P. & Strykowski, P.J. 2007 Suppression of global modes in low-density axisymmetric jets using coflow. *Phys. Fluids* **19** (1), 14102.

Hallberg, M.P., Strykowski, P J & Srykowski, P. J. 2006 On the universality of global modes in low-density axisymmetric jets. *J. Fluid Mech.* **569**, 493–507.

Harang, A., Thual, O., Brancher, P. & Bonometti, T. 2014 Kelvin-Helmholtz instability in the presence of variable viscosity for mudflow resuspension in estuaries. *Environ. Fluid Mech.* **14** (4), 743–769.

Hill, R.J. 2002 Exact second-order structure-function relationships. *J. Fluid Mech.* **468**, 317–326.

Holzner, M., Liberzon, A., Nikitin, N., Kinzelbach, W. & Tsinober, A. 2007 Small-scale aspects of flows in proximity of the turbulent/nonturbulent interface. *Phys. Fluids* **19** (7).

Huerre, P. & Monkewitz, P.A. 1990 Local and global instabilities in spatially developing flows. *Annu. Rev. Fluid Mech.* **22** (1), 473–537.

Hunger, F, Gauding, M. & Hasse, C. 2016 On the impact of the turbulent/non-turbulent interface on differential diffusion in a turbulent jet flow. *J. Fluid Mech.* **802**.

Hunt, G.R. & Burridge, H.C. 2015 Fountains in Industry and Nature. *Annu. Rev. Fluid Mech.* **47** (1), 195–220.

Jahanbakhshi, R. & Madnia, C.K. 2016 Entrainment in a compressible turbulent shear layer. *J. Fluid Mech.* **797**, 564–603.

Jahanbakhshi, R., Vaghefi, N.S. & Madnia, C.K. 2015 Baroclinic vorticity generation near the turbulent/non-turbulent interface in a compressible shear layer. *Phys. Fluids* **27** (10).

Jimenez-Gonzalez, J.I. & Brancher, P. 2017 Transient energy growth of optimal streaks in parallel round jets. *Phys. Fluids* **29** (11), 114101.

Jimenez-Gonzalez, J.I., Brancher, P. & Martínez-Bazán, C. 2015 Modal and non-modal evolution of perturbations for parallel round jets. *Phys. Fluids* **27** (4).

Juniper, M.P. 2006 The effect of confinement on the stability of two-dimensional shear flows. *J. Fluid Mech.* **565**, 171–195.

Kármán, T. & Howard, L.N. 1938 On the statistical theory of isotropic turbulence. *Proc. R. Soc. Lond. A. Math. Phys. Sci.* **164** (917), 192–215.

Keagy, W.R. & Weller, A.E. 1949 A study of freely expanding inhomogeneous jets. In *Heat Transf. Fluid Mech. Inst.*, , vol. 2, pp. 89–98. American Society of Mechanical Engineers.

Kelso, R.M., Lim, T.T. & Perry, A.E. 1996 An experimental study of round jets in cross-flow. *J. Fluid Mech.* **306**, 111–144.

Kolmogorov, A.N. 1941*a* Dissipation of energy in locally isotropic turbulence. In *Dokl. Akad. Nauk SSSR*, , vol. 32, pp. 16–18.

Kolmogorov, A.N. 1941*b* The local structure of turbulence in incompressible viscous fluid for very large Reynolds numbers. In *Dokl. Akad. Nauk SSSR*, , vol. 30, pp. 299–303.

Kull, H.J. 1991 Theory of the Rayleigh-Taylor instability. *Phys. Rep.* **206** (5), 197–325.

Kumar, G., Girimaji, S.S. & Kerimo, J. 2011 Preconditions and limitations of the postulate of scalar-dissipation- conductivity independence in a variable conductivity medium. *Phys. Rev. E - Stat. Nonlinear, Soft Matter Phys.* **84** (4), 1–10.

Kyle, D.M. & Sreenivasan, K.R. 1993 The instability and breakdown of a round variable-density jet. *J. Fluid Mech* pp. 619–664.

Lai, Chris C.K., Charonko, J.J. & Prestridge, K. 2018 A Kármán-Howarth-Monin equation for variable-density turbulence. *J. Fluid Mech.* **843**, 382–418.

Laufer, J. 1954 The structure of turbulence in fully developed pipe flow.

Lee, K., Girimaji, S.S. & Kerimo, J. 2008 Validity of Taylor's dissipation-viscosity independence postulate in variable-viscosity turbulent fluid mixtures. *Phys. Rev. Lett.* **101** (7), 1–4.

Lesshafft, L., Semeraro, O., Jaunet, V., Cavalieri, A.V.G. & Jordan, P. 2019 Resolvent-based modeling of coherent wave packets in a turbulent jet. *Phys. Rev. Fluids* **4** (6), 1–29.

Lighthill, M.J. 1952 On sound generated aerodynamically I. General theory. *Proc. R. Soc. London. Ser. A. Math. Phys. Sci.* **211** (1107), 564–587.

Lighthill, M.J. 1954 On sound generated aerodynamically II. Turbulence as a source of sound. *Proc. R. Soc. London. Ser. A. Math. Phys. Sci.* **222** (1148), 1–32.

Livescu, D. 2020 Turbulence with Large Thermal and Compositional Density Variations. *Annu. Rev. Fluid Mech.* **52** (1), 309–341.

Livescu, D. & Ristorcelli, J.R. 2007 Buoyancy-driven variable-density turbulence. *J. Fluid Mech.* **591**, 43–71.

Lozano, A., Yip, B. & Hanson, R.K. 1992 Acetone: a tracer for concentration measurements in gaseous flows by planar laser-induced fluorescence. *Exp. Fluids* **13** (6), 369–376.

Mashayek, A. & Peltier, W.R. 2012*a* The zoo of secondary instabilities precursory to stratified shear flow transition. Part 1 Shear aligned convection, pairing, and braid instabilities. *J. Fluid Mech.* **708**, 5–44.

Mashayek, A. & Peltier, W.R. 2012*b* The zoo of secondary instabilities precursory to stratified shear flow transition. Part 2 the influence of stratification. *J. Fluid Mech.* **708**, 45–70.

Matsumoto, R., Kimoto, K. & Tsuchimoto, N. 1973 Study on double concentric jets. *Bull JSME* **16** (93), 529–540.

Mi, J., Nobes, D.S. & Nanthan, G.J. 2001 Influence of jet exit conditions on the passive scalar field of an axisymmetric free jet. *J. Fluid Mech.* **432** (May), 91–125.

Mi, J., Xu, M. & Zhou, T. 2013 Reynolds number influence on statistical behaviors of turbulence in a circular free jet. *Phys. Fluids* **25** (7), 75101.

Michalke, A. 1964 On the inviscid instability of the hyperbolictangent velocity profile. *J. Fluid Mech.* **19** (4), 543–556.

Mistry, D., Philip, J. & Dawson, J.R. 2019 Kinematics of local entrainment and detrainment in a turbulent jet. *J. Fluid Mech.* **871**, 896–924.

Monkewitz, P.A. & Sohn, K.D. 1986 Absolute instability in hot jets and their control. In *10th Aeroacoustics Conf.*, p. 1882.

Montagnani, D. & Auteri, F. 2019 Non-modal analysis of coaxial jets. *J. Fluid Mech.* **872**, 665–696.

Morton, B.R., Taylor, G.I. & Turner, J.S. 1956 Turbulent gravitational convection from maintained and instantaneous sources. *Proc. R. Soc. London. Ser. A. Math. Phys. Sci.* **234** (1196), 1–23.

Mullyadzhanov, R., Yavorsky, N. & Oberleithner, K. 2019 Linear stability of Landau jet: Non-parallel effects. *J. Phys. Conf. Ser.* **1268** (1).

Nahme, R. 1940 Beiträge zur hydrodynamischen Theorie der Lagerreibung. *Ingenieur-Archiv* **11** (3), 191–209.

Nelkin, M. 1994 Universality and scaling in fully developed turbulence. *Adv. Phys.* **43** (2), 143–181.

Nichols, J.W., Schmid, P.J. & Riley, J.J. 2007 *Self-sustained oscillations in variable-density round jets*, , vol. 582.

Orr, W.M. 1907*a* The Stability or Instability of the Steady Motions of a Perfect Liquid and of a Viscous Liquid . Part I : A Perfect Liquid Author .

Orr, W.M. 1907*b* The stability or instability of the steady motions of a perfect liquid and of a viscous liquid. Part II: A viscous liquid. In *Proc. R. Irish Acad. Sect. A Math. Phys. Sci.*, , vol. 27, pp. 69–138. JSTOR.

Orszag, S.A. 1971 Accurate solution of the Orr–Sommerfeld stability equation. *J. Fluid Mech.* **50** (4), 689–703.

Panchapakesan, N.R. & Lumley, J.L. 1993*a* Turbulence Measurements in Axisymmetric Jets of Air and Helium. Part 1. Air jet. *J. Fluid Mech.* **246**, 197–223.

Panchapakesan, N.R. & Lumley, J.L. 1993*b* Turbulence Measurements in Axisymmetric Jets of Air and Helium. Part 2. Helium Jet. *J. Fluid Mech.* **246**, 225–247.

Papantoniou, D.A. & List, E.J. 1988 Investigations of round vertical turbulent buoyant jets. *J. Fluid Mech.* **195**, 341–391.

Paredes, P., Terhaar, S., Oberleithner, K., Theofilis, V. & Paschereit, C.O. 2016 Global and Local Hydrodynamic Stability Analysis as a Tool for Combustor Dynamics Modeling. *J. Eng. Gas Turbines Power* **138** (2), 1–7.

Pasquier-Guilbert, N. 2004 Mesures couplées de richesse et de vitesse pour la combustion instationnaire en écoulement stratifié .

Pickering, E., Rigas, G., Nogueira, P.A.S., Cavalieri, A.V.G., Schmidt, O.T. & Colonius, T. 2020 Lift-up, Kelvin–Helmholtz and Orr mechanisms in turbulent jets. *J. Fluid Mech.* **896**.

Pitts, W.M. 1986 *Effects of Global Density and Reynolds Number Variations on Mixing in Turbulent, Axisymmetric Jets*, , vol. 1. National Bureau of Standards.

Pitts, W.M. 1991*a* Effects of global density ratio on the centerline mixing behavior of axisymmetric turbulent jets. *Exp. Fluids* **11** (2-3), 125–134.

Pitts, W.M. 1991*b* Reynolds number effects on the mixing behavior of axisymmetric turbulent jets. *Exp. Fluids* **11** (2-3), 135–141.

Politano, H. & Pouquet, A. 1998 von Kármán–Howarth equation for magnetohydrodynamics and its consequences on third-order longitudinal structure and correlation functions. *Phys. Rev. E* **57** (1), R21.

Pope, S.B. 2000 *Turbulent flows*. Cambridge University Press, Cambridge, UK.

Prasad, R.R. & Sreenivasan, K.R. 1989 Scalar interfaces in digital images of turbulent flows. *Exp. Fluids* **7** (4), 259–264.

Rao, P., Caulfield, C.P. & Gibbon, J.D. 2017 Nonlinear effects in buoyancy-driven variable-density turbulence. *J. Fluid Mech.* **810**, 362–377.

Ravier, S., Abid, M., Amielh, M. & Anselmet, F. 2006 Direct numerical simulations of variable-density plane jets. *J. Fluid Mech.* **546**, 153–191.

Rayleigh, J.W.S. 1878 On the instabilities of jets. *Proc. London Math. Soc.* **14** (June 1873), 4–13.

Raynal, L., Harion, J. L., Favre-Marinet, M. & Binder, G. 1996 The oscillatory instability of plane variable-density jets. *Phys. Fluids* **8** (4), 993–1006.

van Reeuwijk, M., Krug, D. & Holzner, M. 2018 Small-scale entrainment in inclined gravity currents. *Environ. Fluid Mech.* **18** (1), 225–239.

Reid, R.C., Prausnitz, J.M. & Poling, B.E. 1987 The properties of gases and liquids .

Ricou, F.P. & Spalding, D B 1961 Measurements of entrainment by axisymmetrical turbulent jets. *J. Fluid Mech.* **11**, 21–32.

Risso, F. & Fabre, J. 1997 Diffusive turbulence in a confined jet experiment. *J. Fluid Mech.* **337**, 233–261.

Sadeghi, H., Oberlack, M. & Gauding, M. 2018 On new scaling laws in a temporally evolving turbulent plane jet using Lie symmetry analysis and direct numerical simulation. *J. Fluid Mech.* **854**, 233–260.

Sandoval, D.L. 1995 The dynamics of variable-density turbulence. *Tech. Rep.*. Los Alamos National Lab.

Schmid, P.J. 2007 Nonmodal stability theory. *Annu. Rev. Fluid Mech.* **39**, 129–162.

Schmid, P.J. & Henningson, D.S. 2001 *Stability and transition in Shear Flows*.

Schulz, C. & Sick, V. 2005 Tracer-LIF diagnostics: quantitative measurement of fuel concentration, temperature and fuel/air ratio in practical combustion systems. *Prog. energy Combust. Sci.* **31** (1), 75–121.

Shaabani-Ardali, L., Sipp, D. & Lesshafft, L. 2019 Vortex pairing in jets as a global Floquet instability: modal and transient dynamics. *J. Fluid Mech.* **862**, 951–989.

Shih, T.H., Lumley, J.L. & Janicka, J. 1987 Second-order modeling of a variable-density mixing layer. *J. Fluid Mech.* **180**, 93–116.

Shtern, V. & Hussain, F. 2003 Effect of deceleration on jet instability. *J. Fluid Mech.* **480** (480), 283–309.

da Silva, C.B., Hunt, J.C.R., Eames, I. & Westerweel, J. 2014 Interfacial layers between regions of different turbulence intensity. *Annu. Rev. Fluid Mech.* **46** (1), 567–590.

Sommerfeld, A. 1908 Ein Beitrag zur hydrodynamischen Erklärung der turbulenten Flüssigkeitsbewegung. G. Castelnuovo, ed. In *Atti del IV Congr. internazionale dei Mat.*, pp. 116–124.

Squire, H.B. 1933 On the Stability for Three-Dimensional Disturbances of Viscous Fluid Flow between Parallel Walls. *Proc. R. Soc. A Math. Phys. Eng. Sci.* **142** (847), 621–628.

Sreenivasan, K.R. & Antonia, R.A. 1997 The phenomenology of small-scale turbulence. *Annu. Rev. Fluid Mech.* **29** (1), 435–472.

Srinivasan, V., Hallberg, M.P. & Strykowski, P. J. 2010 Viscous linear stability of axisymmetric low-density jets: Parameters influencing absolute instability. *Phys. Fluids* **22** (2), 1–7.

Steward, F.R. & Guruz, A.G. 1977 Aerodynamics of a confined jet with variable density. *Combust. Sci. Technol.* **16** (1-2), 29–45.

Straughan, B. 2007 A note on convection with nonlinear heat flux. *Ric. di Mat.* **56** (2), 229–239.

Sutherland, W. 1893 The viscosity of gases and molecular force. *London, Edinburgh, Dublin Philos. Mag. J. Sci.* **36** (223), 507–531.

Taguelmimt, N, Danaila, L. & Hadjadj, A. 2016 Effects of Viscosity Variations in Temporal Mixing Layer. *Flow, Turbul. Combust.* **96** (1), 163–181.

Talbot, B. 2009 Mélange et dynamique de la turublence en écoulement libre à viscosité variable. PhD thesis.

Taveira, R R & da Silva, C.B. 2013 Kinetic energy budgets near the turbulent/nonturbulent interface in jets. *Phys. Fluids* **25** (1), 15114.

TAYLOR, G.I. 1935 Statistical theory of turbulence. In *Proc. R. Soc. London A Math. Phys. Eng. Sci.*, , vol. 151, pp. 421–444. The Royal Society.

THEOFILIS, V. 2011 Global linear instability. *Annu. Rev. Fluid Mech.* **43**, 319–352.

THRING, M W & NEWBY, M.P. 1953 Combustion length of enclosed turbulent jet flames. *Symp. Combust.* **4** (1), 789–796.

TROPEA, C. & YARIN, A.L. 2007 *Springer handbook of experimental fluid mechanics*. Springer Science & Business Media.

VICICONTE, G. 2019 Turbulent mixing driven by variable density and transport coefficients effects. PhD thesis.

VIGNES, A. 1966 Diffusion in binary solutions: Variation of Diffusion Coefficient with Composition. *Ind. Eng. Chem. Fundam.* **5** (2), 189–199.

VOIVENEL, L. 2016 Influence des paramètres hydrodynamiques sur le mélange turbulent des fluides hétérogènes. Etude expérimentale et analytique. PhD thesis.

VOIVENEL, L., VAREA, E., DANAILA, L., RENOU, B. & CAZALENS, M. 2017 Variable viscosity jets: Entrainment and mixing process. In *Whither Turbul. Big Data 21st Century?*, pp. 147–162. Springer.

WALL, D.P. & WILSON, S.K. 1996 The linear stability of channel flow of fluid with temperature-dependent viscosity. *J. Fluid Mech.* **323**, 107–132.

WALL, D.P. & WILSON, S.K. 1997 The linear stability of flat-plate boundary-layer flow of fluid with temperature-dependent viscosity. *Phys. Fluids* **9** (10), 2885–2898.

WARHAFT, Z. 2000 Passive scalars in turbulent flows. *Annu. Rev. Fluid Mech.* **32** (1), 203–240.

WATANABE, T., RILEY, J.J., DE BRUYN KOPS, S.M., DIAMESSIS, P.J. & ZHOU, Q. 2016*a* Turbulent/non-turbulent interfaces in wakes in stably stratified fluids. *J. Fluid Mech.* **797**, 1–11.

Watanabe, T., Riley, J.J. & Nagata, K. 2016*b* Effects of stable stratification on turbulent/nonturbulent interfaces in turbulent mixing layers. *Phys. Rev. Fluids* **1** (4), 44301.

Watanabe, T., Riley, J.J. & Nagata, K. 2017 Turbulent entrainment across turbulent-nonturbulent interfaces in stably stratified mixing layers. *Phys. Rev. Fluids* **2** (10), 104803.

Watanabe, T., Riley, J.J., Nagata, K., Onishi, R. & Matsuda, K. 2018 A localized turbulent mixing layer in a uniformly stratified environment. *J. Fluid Mech.* **849**, 245–276.

Watanabe, T., Sakai, Y., Nagata, K., Ito, Y. & Hayase, T. 2014 Enstrophy and passive scalar transport near the turbulent/non-turbulent interface in a turbulent planar jet flow. *Phys. Fluids* **26** (10).

Way, J. & Libby, Paul A. 1971 Application of hot-wire anemometry and digital techniques to measurements in a turbulent helium jet. *AIAA* **9** (8), 1567–1573.

Wazzan, A.R., Okamura, T. & Smith, A.M.O. 1968 The Stability of Water Flow Over Heated and Cooled Flat Plates. *J. Heat Transfer* **90** (1), 109–114.

Westerweel, J., Fukushima, C., Pedersen, J.M. & Hunt, J.C.R. 2005 Mechanics of the Turbulent-Nonturbulent Interface of a Jet. *Phys. Rev. Lett.* **95** (17), 174501.

Westerweel, J., Fukushima, C., Pedersen, J.M. & Hunt, J.C.R. 2009 Momentum and scalar transport at the turbulent/non-turbulent interface of a jet. *J. Fluid Mech.* **631**, 199–230.

Wilke, C.R. 1950 A viscosity equation for gas mixtures. *J. Chem. Phys.* **18** (4), 517–519.

Wille, R. 1963 *Beiträge zur Phänomenologie der Freistrahlen*.

Williams, F.A. 2018 *Combustion theory*. CRC Press.

Winterbone, D.E. & Turan, A. 2015 *Advanced Thermodynamics for Engineers: Second Edition*.

Wolf, M., Holzner, M., Lüthi, B., Krug, D., Kinzelbach, W. & Tsinober, A. 2013 Effects of mean shear on the local turbulent entrainment process. *J. Fluid Mech.* **731**, 95–116.

Wolf, M., Lüthi, B., Holzner, M., Krug, D., Kinzelbach, W. & Tsinober, A. 2012 Investigations on the local entrainment velocity in a turbulent jet. *Phys. Fluids* **24** (10).

Wu, X.Z. 2019 Nonlinear Theories for Shear Flow Instabilities: Physical Insights and Practical Implications. *Annu. Rev. Fluid Mech.* **51** (1), 451–485.

Xu, G. & Antonia, R.A. 2002 Effect of different initial conditions on a turbulent round free jet. *Exp. Fluids* **33** (5), 677–683.

Yaglom, A.M. 1949 On the local structure of a temperature field in a turbulent flow. In *Dokl. Akad. Nauk SSSR*, , vol. 69, pp. 743–746.

Yoda, M. & Fiedler, H.E. 1996 The round jet in a uniform counterflow: flow visualization and mean concentration measurements. *Exp. Fluids* **21** (6), 427–436.

Yu, M. H. & Monkewitz, P.A. 1990 The effect of nonuniform density on the absolute instability of two-dimensional inertial jets and wakes. *Phys. Fluids A Fluid Dyn.* **2** (7), 1175–1181.

Zhao, D. & Aluie, H. 2018 Inviscid criterion for decomposing scales. *Phys. Rev. Fluids* **3** (5), 1–20.